SIGNAL PROCESSION OF SINGLE MEASURAND

FOR DYNAMICAL SYSTEM IDENTIFICATION

A Dissertation Presented to the Faculty of the Graduate School

at the University of Missouri-Columbia

In Partial Fulfillment

of the Requirements for the Degree

Doctor of Philosophy

---

by

XUEWEI RUAN

Dr. P. Frank Pai, Dissertation Supervisor

Dr. Ming Xin, Dissertation Co-Supervisor

JULY 2017

The undersigned, appointed by the dean of the Graduate School, have examined the [thesis or dissertation] entitled

SIGNAL PROCESSION OF SINGLE MEASURAND

FOR DYNAMICAL SYSTEM IDENTIFICATION

Presented by Xuewei Ruan

A candidate for the degree of Doctor of Philosophy in Mechanical & Aerospace Engineering

And hereby certify that, in their opinion, it is worthy of acceptance.

Professor P. Frank Pai

Professor Ming Xin

Professor Craig Kluever

Professor Roger Fales

Professor Steven Neal

Professor Stephen Montgomery-Smith

ACKNOWLEDGEMENTS

I would like to express my sincere appreciation and thanks to my advisor, Dr. P. Frank Pai and my co-advisor, Dr. Ming Xin. Even with his inconvenience situation, Dr. Pai still tried his best to help me with my research; he has been a tremendous mentor for me. I would like to thank Dr. Xin steps up for me to be my co-advisor. His advice on my thesis work as well as my career has been priceless. I would also like to thank my committee members, Dr. Craig Kluever, Dr. Steven Neal, Dr. Roger Fales and Dr. Stephen Montgomery-Smith for serving on my thesis committee and providing me valuable comments and suggestions.

A special thanks go to my husband, Tiancheng Xu. Words cannot express how grateful I am to him for all of his support and sacrifices for my study and life. I would also like to thank my family for being supportive of my study and always being my strong backup. I would also like to thank all of my friends who supported my study and encouraged me to strive towards my goal. Haoguang Deng, Xiaopeng Li, Yu Shao and Hao Peng have been giving me their personal and professional unwavering support during my stay at the University of Missouri.

TABLE OF CONTENTS

LIST OF ILLUSTRATIONS

Figure Page

Table Page

ABSTRACT

Accurate damage inspection and reliable health monitoring of dynamical systems rely on accurate dynamical data computation. In theory, if all three variables (i.e., displacement, velocity, and acceleration) of each point on a dynamical system are available from measurement, system identification/damage detection methods can be easily and accurately performed. In the experiment, however, there is often only one variable is measured because collocating three different sensors at a point is too difficult even if the sensors are small enough not to affect the system's dynamic characteristics. Numerical investigations reveal that velocity is the best choice because the corresponding acceleration and displacement can be estimated by numerical differentiation and integration and because today's laser vibrometers can provide very accurate measurements of velocities. Therefore, with the velocity signal as the single measurand, efficient and accurate numerical computation methods are needed to compute the corresponding displacement and acceleration signals.

Ideally, an intelligent structure will be able to realize real-time monitoring that the occurrence of damage can be identified at a very early stage. Then, by localizing the existed damage, a detailed analysis of the damaged structure section can be carried out such as determine the severity of the damage or the remaining service life of the structure. Two direct time-domain methods and two indirect time-domain methods for system identification are reviewed in this thesis. The feasibility of using these system identification methods for level 1 damage detection has been discussed in this thesis. While some of the methods can realize a real-time monitoring and quick feedback, some can only realize periodic inspections or cannot reflect small change in modal parameters.

Two origin methods as stiffness-characteristic matrix method (stiffness-CMM) and mass characteristic matrix method (mass-CMM) for damage localization are proposed in this thesis, and it is the concentration of the thesis. Different from traditional damage detection methods, proposed methods do not require the corresponding intact beam structure for comparison. While measured signals only processed in the spatial domain, a weighting matrix developed from the finite element model of the beam structure is used for computing the damage index on each measured location. The largest (filtered) damage index indicate the actual damage location. Two different weighting matrixes are used in proposed methods and the mass-CMM is more robust to measuring noise. Application of the two methods is demonstrated through numerical examples. In addition, experimental vibration data of damaged beam structure measured using a PSV-200 scanning laser vibrometer are also used to verify the accuracy of these methods.

Chapter 1 INTRODUCTION

1.1 Background

The interest in the ability to monitor a structure and detect damage at the earliest possible stage is pervasive throughout the civil, mechanical and aerospace engineering communities [1]. Engineers and researchers, particularly in the aerospace and offshore oil industries, began to utilize vibration based damage detection during the late 1970s and early 1980s [2] because vibration-based methods are more globally sensitive to damage than localized methods such as ultrasonic and eddy current methods [3]. In the offshore oil industry, research objectives included the detection of near-failing drilling equipment and the prevention of expensive oil pumps from becoming inoperable [4]. According to Farrar and Doebling, the most mature and successful application of vibration-based damage detection technology has been in the monitoring of rotating machinery [2]. Moreover, the infrastructure monitoring in the civil engineering community is also a vibrant area of current research [5]. Therefore, the vibration-based damage detection problem is fundamentally one of statistical pattern recognition [2].

The time history response of a structure can be measured by a variety of sensors, e.g. accelerometers, strain gauges, etc. While measurements are always made in the time domain, the condition monitoring analyst may choose to analyses the data in the time, frequency or modal domains [5]. Doebling and Farrar [1] has presented an extensive survey of damage detection methods in 1996, and a categorization based on the type of measured data used, and/or the technique used to identify the damage from the measured data was given in the survey and has been mostly referred in later literature. However, with more and more damage detection

methods proposed in past decades, some new category may be necessary to classify the new methods [5-7]. On the other hand, based on with different results from different damage detection methods, Rytter [8] has proposed a classification of damage detection methods as following:

Level 1 The method gives a qualitative indication that damage might be present in the structure. (DETECTION)

Level 2 The method gives information about the probable location of the damage. (LOCALIZATION)

Level 3 The method gives information about the size of the damage. (ASSESSMENT)

Level 4 The method gives information about the actual safety of the structure given a certain damage state. (CONSEQUENCE)

It has been widely used to classify the feature of different damage detection methods [5, 9, 10]. And most literature concentrating on level 1 to 3 of damage detection. With discussed damage detection methods focusing on level 1 and 2, the literature of methods also for level 1 and 2 will be reviewed in next section.

1.2 Literature Review and Discussions

Based on the type of measured data used, and/or the technique used to identify the damage from the measured data, methods reviewed in Doebling's survey [1] has been categorized as:

A. Natural Frequency Based Methods

B. Mode Shape Based Methods

C. Mode Shape Curvature/Strain Mode Shape Based Methods

D. Dynamically Measured Flexibility Based Methods

E. Matrix Update Based Methods

F. Non-linear Methods

G. Neural Network Based Methods

H. Other Methods

The amount of literature related to damage detection using shifts in natural frequencies is quite large [1]. That is because the natural frequencies can be conveniently measured from just a few accessible points on the structure and are usually less contaminated by experimental noise [10]. The observation that changes in structural properties can cause changes in vibration frequencies was the impetus for using modal methods for damage identification and health monitoring [1]. And related methods can be divided as 'the forward problem' and 'the inverse problem'. The forward problem is about determining the natural frequency changes of a given structure based on damage location and severity, and it serves as a theoretical foundation for natural frequency-based methods [10]. The inverse problem is about determining the damage location and size of a given structure based on natural frequency measurement [10]. Therefore, the first three levels of damage detection can all be realized by natural frequency based methods.

However, there existed a few laminations of natural frequency based methods. Since almost every natural frequency method is model-based [10], the used simplification in its numerical model can cause errors in predicted natural frequency when the actual structure has any difference from the assumption. On the other hand, since the change of natural frequency is relatively small, it can be buried by the changes caused by environmental and operational conditions. Moreover, even without noise pollution, solutions of damage location and severity has a problem of nonuniqueness. Therefore, it can be only successfully applied to simple

structures with small cracks (typically, a slender beam-type structure with an artificially induced crack) in a controlled laboratory condition [10].

On the contract, the mode shape which contains local information can be more sensitive to damage location then natural frequency as a global property of the structure. In the past three decades, many damage identification methods have been developed based on measured mode shapes. These methods can be categorized into two types: 1) the traditional 'mode shape change methods' that establish a relationship between damage location/severity and modal shape change through a finite element model or experimental test and 2) the modern 'signal processing methods' that can be applied to either mode shape change or mode shape data from damaged structures alone [10].

West [11] presents what is possibly the first systematic use of mode shape information for the location of structural damage without the use of a prior FEM. The author uses the modal assurance criteria (MAC) to determine the level of correlation between modes from the test of an undamaged structure and the modes from the test of the damaged structure. The development of the MAC has led to a number of similar assurance criteria used in the area of experimental and analytical structural dynamics [12-17]. However, the intact structures are not always available, and the numerical model must be established through careful model verification and validation [18], it is hard to get an accurate identification result from model-based methods. And some other limitations also exist such as they are only sensitive to damage in the certain area of the structures [19] or cannot give a preliminary damage location rather than an accurate location [20].

On the other hand, the 'signal processing methods' that don't require an intact structure/model can be more flexible when it comes to in *in-situ* structures. However, with only data from the damaged structure,

these methods cannot realize a level 3 damage detection (damage quantification) due to its inherent limitation [10]. Moreover, it has been shown by many researchers that the displacement mode shape itself is not very sensitive to small damage, even with high-density mode shape measurement [21-23].

An alternative to using mode shapes to obtain spatial information about vibration changes is using curvature. And it can also be divided into traditional ‘modal curvature change methods’ and the modern ‘signal processing methods.' Pandey [24] first demonstrated that absolute changes in mode shape curvature could be a good indicator and central difference approximation is used to calculate the curvature mode shapes. However, Chance [25] found that numerically calculating curvature from mode shapes resulted in unacceptable errors. They used measured strains instead to measure curvature directly, which dramatically improved results. On the other hand, Ratcliffe [26] developed a response-based method without requiring a baseline mode shape. Wavelet transform technique has been applied to enhance the sensitivity and accuracy of curvature based methods [27, 28]. However, like mode shape based methods, curvature based methods also have a few problems such as the selection of the mode [22] and the accuracy of extracted mode shape. Moreover, curvature based methods also suffer from the similar limitations as cannot locate small damages [29] and require a fine mesh [30].

Such uncertainty has led to the investigation of other methods such as the use of operational deflection shapes (ODSs), which have many similarities to mode shapes [5]. And since developed methods are proposed after the survey of Doebling, there was no such category as listed. ODSs depends on the location and relative magnitudes of the forces applied to the structure and can be similar to mode shape when it is excited at a single location near resonance. However, since the ODSs are the actual structural response from all modes

combined that can be more sensitive in detecting damage [3]. It can provide a visual interpretation of the vibration patterns of a structure [5] and has been used for damage detection on bridges, wind turbines and other structures [24, 31-34]. With ODSs of the beam structure generated by piezoceramic actuators and measured by a scanning Laser Doppler Vibrometer [3], ODSs based methods can be easily verified.

In addition to ODSs based methods, there existed some other categories of widely used damage identification methods didn't include in Doebling's survey such as modal strain energy method, residual force vector method, FRF based methods, FRF based methods, wavelet transform methods, genetic algorithm methods and statistical methods [5]. And damage detection methods in rest of listed categories have also been developed during the past few decades.

1.3 Motivations and Goals

To numerically simulate the process of damage detection of a structure, a mathematical structural model is needed, and the sensor needs to be modeled. In order to obtain more information about the certain structure, it is better to use more sensors at more locations and even more than one sensor at each location. But collocating several sensors at one point is too difficult even if the sensors are very tiny. Moreover, the accuracy and sensitivity of the chosen sensor play an important role for accurate damage inspection and monitoring of structures. The scanning laser vibrometer is probably today's most sensitive and accurate instrument for measuring velocities of structures. Hence, the dynamical signal to be experimentally obtained is velocity. Meanwhile, noise contained in the measured velocity will be simulated by adding normal random numbers to the simulated velocity. On the other hand, the accuracy of numerical computation methods used

for computing displacement and acceleration signals will influence the accuracy of applied damage detection methods. And considering the large amount of data required from a fine grid measuring for damage localization, the efficiency of applied numerical computation methods are also important. Therefore, different numerical computation methods need be compared to find the more accurate and efficient one for signal processing.

Ideally, a robust damage detection scheme will be able to identify that damage has occurred at a very early stage (level 1 damage detection), locate the damage within the sensor resolution being used (level 2 damage detection), provide some estimate of the severity of the damage (level 3 damage detection), and predict the remaining useful life of the structure (level 4 damage detection). Based on the direct time-domain methods and indirect time-domain methods for system identification studied in my master research, level 1 damage detection can be easily realized by recognizing the change of system properties. Damage localization (level 2 damage detection) will be the emphasis in this thesis. Since the ODSs are the actual structural response from all modes combined that can be more sensitive in detecting damage[3]. Meanwhile, with both piezoceramic actuators and scanning Laser Doppler Vibrometer available from the lab, accurate ODS can be measured/computed. Damage detection methods based on the ODSs are considered. Both numerical analysis and experimental validation will be performed to verify the feasibility and accuracy of proposed methods. And since the majority of civil and mechanical structure and their main components can be simplified as a beam or plate [10], the beam structure can be used as the example in both numerical simulation and experimental validation.

1.4 Thesis Overview

Chapter 2 starts with an introduction of the benefit of using velocity as the single measurand and principles of later methods comparison. Section 2.2 reviewed three different numerical differentiation methods and compared them with a linear/nonlinear model with/without simulated noise. Section 2.3 gives three different numerical integration methods, compared them with the same models from the previous section. In addition, three methods of computing the integration constant have been discussed.

Chapter 3 introduces the detailed understanding of four levels of damage detection. Section 3.2 reviews two direct time-domain methods and section 3.3 reviews two indirect time-domain methods. A linear model with an occurrence of damage has been used for verifying the ability of real-time monitoring/level 1 damage detection for discussed methods.

As the numerical model of the beam structure change from single degree-of-freedom system (for level 1 damage detection) to a continuous system (for level 2 damage detection), chapter 4 reviews the finite element model of the beam structure and introduces three major categories of used numerical model for damaged beam structure. One example of each categorize is given in following sections, and the advantage of disadvantage of each numerical model has been discussed.

Chapter 5 introduced two origin damage detection methods for damage localization called the stiffness characteristic matrix method and the mass characteristic matrix method. Challenges in proposed methods have been discussed through numerical model.

Chapter 6 presents the experimental validation of proposed methods from chapter 5. It discussed the operability of different types of experiments and the choice of exciting frequency for steady state vibration.

Chapter 2 COMPUTATION OF DYNAMICAL DATA BASED ON SINGLE MEASURAND

2.1 Introduction

The process of implementing a damage detection strategy for aerospace, civil and mechanical engineering infrastructure is referred to as Structural Health Monitoring (SHM) [35]. And the data acquisition portion of the structural health monitoring process involves selecting the types of sensors to be used, the locations where the sensors should be placed, the number of sensors to be used, and the data acquisition/storage/transmittal hardware [35].Using more sensors at different locations and even more than one sensor at each location would be better to obtain information of a structure. However, since displacement and acceleration sensor usually asks for contact, it is difficult to set up several sensors at the same location even if the sensors are small enough. Hence, a practical approach is to use only one sensor at each location to measure one dynamic signal (as single measurand), and then use differentiation and/or integration to obtain the other two.

The accuracy and sensitivity of the sensor play an important role for accurate signal measuring. Since measuring displacement and acceleration usually asks for contact, it would not only introduce noise to measured signal but also influence the structure's feature. Thus, measured velocity signals usually contain less noise than measured displacement or acceleration. Also, today's scanning laser vibrometer can provide a very accurate measurement of velocities. Velocity would be the best option for measuring. On the other hand, since measuring noise can be accumulated by numerical integration and aggravated by numerical differentiation. If the displacement signal $u(t)$ (t is time) is measured, $\dot{u}(\equiv du/dt)$ and $\ddot{u}$ can be obtained by one and two times of numerical differentiation, respectively. But the second numerical differentiation

always introduces serious errors because of the noise. If $\ddot{u}(t)$ is measured, $\dot{u}$ and u can be obtained by one and two times of numerical integration, respectively. But it involves two unknown integration constants as initial displacement and velocity. On the contract, if $\dot{u}$ is measured, u and $\ddot{u}$ can be obtained by one-step numerical integration and differentiation, respectively. It would have less problem of noise accumulating. And with relative less measuring noise, velocity will be the best option for the single measurand, and we will use it as our single measurand in later numerical simulation and experimental validation.

Based on measured velocity, displacement and acceleration can be obtained through numerical integration/differentiation methods. However, numerical integration/differentiation methods would not only accumulate noise from measured data through calculation but also contain calculation errors. A higher order method can have a smaller calculation error but also have noise from more data points tangled in its calculation. On the contract, a lower order method can efficiently calculate a large amount of data with less noise tangling, but the calculation error will be relatively large. In following sections, different methods of numerical integration and differentiation will be compared to find the relative more accurate one. Meanwhile, the efficiency of the method is also a focal point. For a single-DOF system, u and $\ddot{u}$ of only one point is required, it is acceptable if it takes a relative longer time for computing the signals for the entire time trace. But when it comes to a continuous system, u and $\ddot{u}$ of all measured points along the structure need to be computed, different efficiency would result in a big difference in calculation time. For displacement computation, the measuring noise can result in an inaccurate moving average. Therefore, a method with the ability of noise filtering will be an advantage that not only noise from the measured signal can be filtered and the inaccurate moving average from the computed displacement signal can be filtered. And since the

numerical integration of velocity can only result in the relative displacement, computation of unknown initial displacement will also be discussed.

Because real-world dynamical systems often have a nonlinear behavior when they are damaged/aged. Therefore, dynamical signals of both linear and nonlinear systems will be considered. Meanwhile, both accurate signals and signals with added noise will be used to reflect both accuracy and noise tolerance of applied methods. On the other hand, since dynamic characteristics of a nonlinear system such as modal frequencies and damping ratio change with time, it requires system identification methods need to be capable of extracting such time-varying system characteristics. Moreover, real-time health monitoring also requires online tracking of system's properties even for linear systems. Therefore, it requires the computed dynamic signals as displacement/acceleration only based on data from the past.

2.2 Numerical Differentiation Methods

2.2.1 Finite Difference Approximation

Finite difference approximation would be the most basic method we know for computing acceleration. Centered and backward finite difference method can be performed to observed time instant t_j as shown below:

$$\ddot{u}(t_j) = \frac{\dot{u}_{j+1} - \dot{u}_{j-1}}{2\Delta t} \tag{2.1a}$$

$$\ddot{u}(t_j) = \frac{\dot{u}_{j} - \dot{u}_{j-1}}{\Delta t} \tag{2.1b}$$

where Δt is the time interval, $\dot{u}_j$ represents data point from measured velocity signal and $\ddot{u}(t_j)$ is the computed acceleration of the observed time instant t_j. With only two data points involved in the calculation,

this method is very efficient and has relative less noise tangled in it. Moreover, the backward differentiation formula (Eq. (2.1b)) only requires data from the current time instant and previous time instant. It can be applied to signal processing for real-time healthy monitoring methods. However, the calculation error depending on the time interval Δt is relatively large. Based on Eq. (2.1a) and (2.1b), the calculation error is about $O(\Delta t^2)$ and $O(\Delta t)$, respectively. Equation (2.2) gives a higher order backward differentiation formula that can be applied for real-time monitoring with a relative higher accuracy. Notice with measuring noise existed in velocity signal, the tangled noise will result in an extra error. A higher order accuracy cannot ensure a higher order accuracy.

$$\ddot{u}(t_j) = \frac{3\dot{u}_j - 4\dot{u}_{j-1} + \dot{u}_{j-2}}{2\Delta t} \tag{2.2}$$

2.2.2 Curve Fitting Method

While finite difference method directly using data points from measured velocity signal in its calculation, a more analytical way to get acceleration is to perform curve fitting on velocity signal first, and then get the acceleration as the first derivative of the fitted velocity function. For observed time instant t_j, curve fitting can be applied to compute the velocity function $\dot{u}_j(t)$ based on data points around it. For example, a symmetrical section involves $\dot{u}_i$ $(i = j-n,\ j-n+1, \ldots, j+n)$ can be applied. Data $\dot{u}_i$ variance from $\dot{u}_j(t)$ is defined as the error *E*. Weighting factor α_i can be added to the definition of error in the form of $\alpha_i = 1/(1+|9i/n|)$ to give an emphasis on the observed data point $\dot{u}_j$. And a simpler fitting can be realized having all α_i to be 1.

$$
\begin{aligned}
&For\ t_j : \dot{u}_j(t) = \sum_{k=0}^{M} a_k t^k \\
&E = \sum_{i=j-n}^{j+n} \alpha_i (\dot{u}_j(t_i) - \dot{u}_i)^2 \\
&\partial E / \partial a_k = \sum_{i=j-n}^{j+n} \alpha_i (\dot{u}_j(t_i) - \dot{u}_i) t_i^k = 0 \\
&\Rightarrow \ddot{u}_j(t) = \frac{d\dot{u}_j(t)}{dt} = \sum_{k=0}^{M} k a_k t^{k-1}
\end{aligned}
\tag{2.3}
$$

The accuracy of the result acceleration function $\ddot{u}_j(t)$ depends on the accuracy of the fitted velocity function $\dot{u}_j(t)$. And based on the time interval and vibrating frequency of the measured signal, a more accurate velocity function can be achieved with different applied section length and polynomial order M. For certain signal, with a longer section length, a more 'average' will be taken by the curve fitting. While some of the existed noise can be filtered out during the calculation, time-localized transient events will be smoothed out too. On the contract, with a shorter section length for certain signal, the time instant of any abnormal transient event can be localized more clearly. Literature suggests the used section length as $2n \times \Delta t$ should cover at least quarter of the lowest vibration period to capture the characteristic of velocity data [36]. And for high sampling rate signals, to reduce the amount of calculation, besides of using successional points, one can also use skipped data points such as t_{j-2}, t_j and t_{j+2}.

While a symmetrical section can achieve a smaller calculation error, an asymmetric section with only data points from the past can be used in signal processing for real-time health monitoring methods. Notice that for the first several points, without enough data points from the past, online tracking cannot be applied. More importantly, although the curve fitting method can give a flexible option for applied differentiation, an inverse calculation is included in determining the coefficients for each observed data point. With this step repeated through the entire time trace and for each measured signal, it requires a relative longer

computation time to compute all acceleration signals. However, this data processing algorithm can be dramatically accelerated by using the Savitzky-Golay filter [37].

2.2.3 Savitzky-Golay Filter Method

Savitzky and Golay proposed a method of data smoothing based on local least-squares polynomial approximation. They showed that fitting a polynomial to a set of input samples and then evaluating the resulting polynomial at a single point within the approximation interval is equivalent to discrete convolution with a fixed impulse response. The lowpass filters obtained by this methods are widely known as Savitzky-Golay (SG) filters [38]. The simplest type of filter works as replacing each data value f_i at point j by g_j as a linear combination of itself and some number of nearby neighbors. And it can be written as [39]:

$$g_j = \sum_{i=j-n_L}^{j+n_R} c_i \cdot f_i \tag{2.4}$$

where g_j is the replacing value, n_L is the number of data points used from the left of j, n_R is the number of data points used from the right of j, c_i is a factor, and f_i is the respective data value [39]. Instead of using a polynomial function of the independent variable j to fit the data function and substituting the j back, SG filter uses constant coefficient c_i with the data value directly. And the constant coefficients are also generated from a curve fitting procedure, but without involving actual data points. For example, if we want to use a polynomial $G_j(i)$ with order of M to fit data point f_j:

$$G_j(i) = \sum_{k=0}^{M} a_k i^k \tag{2.5}$$

And we want to use data points from f_{j-n_L} to f_{j+n_R} for the observed data point f_j. We will have

$n_L + n_R + 1$ points satisfy the function $G_j(i)$, and an equation set can write as below:

$$\begin{cases} f_{j-n_L} = G_j(j-n_L) = a_0(j-n_L)^0 + a_1(j-n_L)^1 + \cdots + a_M(j-n_L)^M \\ \vdots \\ f_j = G_j(j) = a_0 j^0 + a_1 j^1 + \cdots + a_M j^M \\ \vdots \\ f_{j+n_R} = G_j(j+n_R) = a_0(j+n_R)^0 + a_1(j+n_R)^1 + \cdots + a_M(j+n_R)^M \end{cases} \tag{2.6}$$

It can be simplified as $[f] = [A] \cdot [a]$, where $[a]$ is a vector of coefficients of polynomial $G_j(i)$, $[f]$ is a vector of data values on the left side in Eq. (2.6) and $[A]$ is as listed in Eq. (2.7).

$$[A] = \begin{bmatrix} (j-n_L)^0 & (j-n_L)^1 & \cdots & (j-n_L)^M \\ \vdots & \vdots & \cdots & \vdots \\ i^0 & i^1 & \cdots & i^M \\ \vdots & \vdots & \ddots & \vdots \\ (j+n_R)^0 & (j+n_R)^1 & \cdots & (j+n_R)^M \end{bmatrix} \tag{2.7}$$

Then coefficient vector $[a]$ can be easily computed by the following procedure:

$$\begin{aligned} [A] \cdot [a] &= [f] \\ ([A]^T \cdot [A]) \cdot [a] &= [A]^T \cdot [f] \\ [a] &= ([A]^T \cdot [A])^{-1} \cdot ([A]^T \cdot [f]) \end{aligned} \tag{2.8}$$

which can be simplified as $[a] = [C] \cdot [f]$ where:

$$[C] = ([A]^T \cdot [A])^{-1} \cdot [A]^T \tag{2.9}$$

As shown in Eq. (2.9), here $[C]$ is a matrix of coefficients being independent of $[f]$ [39]. Approximation value and its first derivative at the point j can be calculated as:

$$\begin{aligned} G_j(j) &= [j^0 \quad j^1 \quad \cdots \quad j^M] \cdot [a] \\ G_j'(j) &= \sum_{k=0}^{M} a_k k j^{k-1} = [0 \quad 1 \cdot j^0 \quad 2 \cdot j^1 \quad \cdots \quad M \cdot j^{M-1}] \cdot [a] \end{aligned} \tag{2.10}$$

When it applied to the velocity signal, the acceleration signal can be computed as the first derivative of the velocity signal as in Eq. (2.10). However, the $[A]$ and $[C]$ still depend on j which means the

$[A]$ and $[C]$ need to be calculated for each observed data point repeatedly. The efficiency of calculation has not been improved. Change the independent variable from $i's$ to $t_i's$ to suit our case, for each observed data point $\dot{u}_j$, the time axis of data points used for its curve fitting can be shifted as $\tilde{t} = t - t_j$. Then, the $[A]$ matrix can be adjusted to be $\left[\tilde{A}\right]$ and the corresponding $\left[\tilde{C}\right], [\tilde{a}]$ can be calculated as:

$$\begin{aligned}
\left[\tilde{A}\right] &= \begin{bmatrix} (-n_L\Delta t)^0 & (-n_L\Delta t)^1 & \cdots & (-n_L\Delta t)^M \\ \vdots & \vdots & \cdots & \vdots \\ (t_i - t_j)^0 & (t_i - t_j)^1 & \cdots & (t_i - t_j)^M \\ \vdots & \vdots & \ddots & \vdots \\ (n_R\Delta t)^0 & (n_R\Delta t)^1 & \cdots & (n_R\Delta t)^M \end{bmatrix} \\
\left[\tilde{C}\right] &= \left(\left[\tilde{A}\right]^T \cdot \left[\tilde{A}\right]\right)^{-1} \cdot \left[\tilde{A}\right]^T \\
[\tilde{a}] &= \left[\tilde{C}\right] \cdot [\dot{u}]
\end{aligned} \tag{2.11}$$

Then, the fitted velocity function can be determined as: $\tilde{\dot{u}}_j(\tilde{t}) = \sum_{k=0}^{M} \tilde{a}_k \tilde{t}^k$. From the definition of the $\left[\tilde{A}\right]$ in Eq. (2.11) we can see it is independent with t_j. And as long as n_L, n_R and M stays the same the $\left[\tilde{A}\right]$ stays the same. Then, the $\left[\tilde{C}\right]$ stays the same and the $[\tilde{a}]$ of different time instants can be calculated with the same $\left[\tilde{C}\right]$, no repeated inverse calculation is required. Moreover, with the shifting procedure, the formula of fitted velocity value and computation of acceleration will also be simplified. By substituting t_j as $\tilde{t} = 0$ back to $\tilde{\dot{u}}_j(\tilde{t})$, fitted velocity at time instant t_j would equal to coefficient $\tilde{a}_0$ and the result acceleration would equal to $\tilde{a}_1$ as shown in Eq. (2.12). Thus, one even doesn't need to calculate out all the coefficients but only the first two to get the fitted velocity and computed acceleration.

$$\begin{aligned}
\dot{u}_j(0) &= \sum_{k=0}^{M} \tilde{a}_k 0^k = \tilde{a}_0 = \left[\tilde{C}(1,:)\right] \cdot [\dot{u}] \\
\ddot{u}_j(0) &= \frac{d\tilde{\dot{u}}_j}{dt}(0) = \sum_{k=0}^{M} k\tilde{a}_k 0^{k-1} = \tilde{a}_1 = \left[\tilde{C}(2,:)\right] \cdot [\dot{u}]
\end{aligned} \tag{2.12}$$

Notice the first and last several data points cannot be processed with the same n_L, n_R and M as the rest data

points since there is no enough points to use on left/right side. Usually, more points from the other side will be used to keep the number of points involved the same as $n_L + n_R + 1$. Then, only $n_L + n_R + 1$ different $\left[\tilde{C}\right]$ are needed for computing the acceleration signal through the entire time trace.

As we can see, the SG filter method has basically the same basic procedure with the curve fitting method. They both gives a point-by-point curve fitting of the velocity signal and then get the acceleration signal as its first derivative. The only difference is instead of doing inverse calculation repeatedly through the entire time trace in curve fitting method, the SG filter method only asks for $n_L + n_R + 1$ times of the inverse calculations. Therefore, as long as the same n_L, n_R and M used for the curve fitting method and the SG filter method, they will give the same result, but the SG filter method will cost much less computation time. And in the next section of methods comparison, we will only compare the result of the finite difference approximation and the SG filter method.

2.2.4 Methods Comparison

As introduced before, accuracy, efficiency, the ability of real-time monitoring and tolerance to noise would be our focus for comparison. Since no complex calculation involved in the finite difference approximation and only $n_L + n_R + 1$ times of the inverse calculation is involved in the SG filter method, there would not be much difference in the efficiency of these two methods. The accuracy of methods will be compared based on accurate velocity signals from both linear and nonlinear systems, and the ability of noise tolerance will be compared based on velocity signals with added simulated noise. Meanwhile, to simulate the situation of real-time monitoring, only backward differentiation method and the SG filter method with $n_R = 0$ will be

applied to later cases. Here is the governing equation of a single-degree-of-freedom (single-DOF) linear dynamic system:

$$m\ddot{u} + c\dot{u} + ku = f(t) \tag{2.13a}$$

$$2\ddot{u} + 1.0053\dot{u} + 78.9568u = 0 \tag{2.13b}$$

where its accurate velocity and displacement signal can be obtained from Runge-Kutta integration. And accurate acceleration signal can be calculated by:

$$\ddot{u} = \left(f(t) - c\dot{u} - ku \right) / m \tag{2.14a}$$

$$\ddot{u} = \left(-1.0053\dot{u} - 78.9568u \right) / m \tag{2.14b}$$

Figs. 2.1a&2.1b present accurate displacement and velocity signal obtained from Runge-Kutta integration with a sampling rate of $40Hz$ and the initial condition of $u(0) = 2, \dot{u}(0) = 0$. Fig. 2.1c presents the accurate acceleration signal obtained based on displacement and velocity signal in Figs. 2.1a&2.1b by Eq. (2.14b).

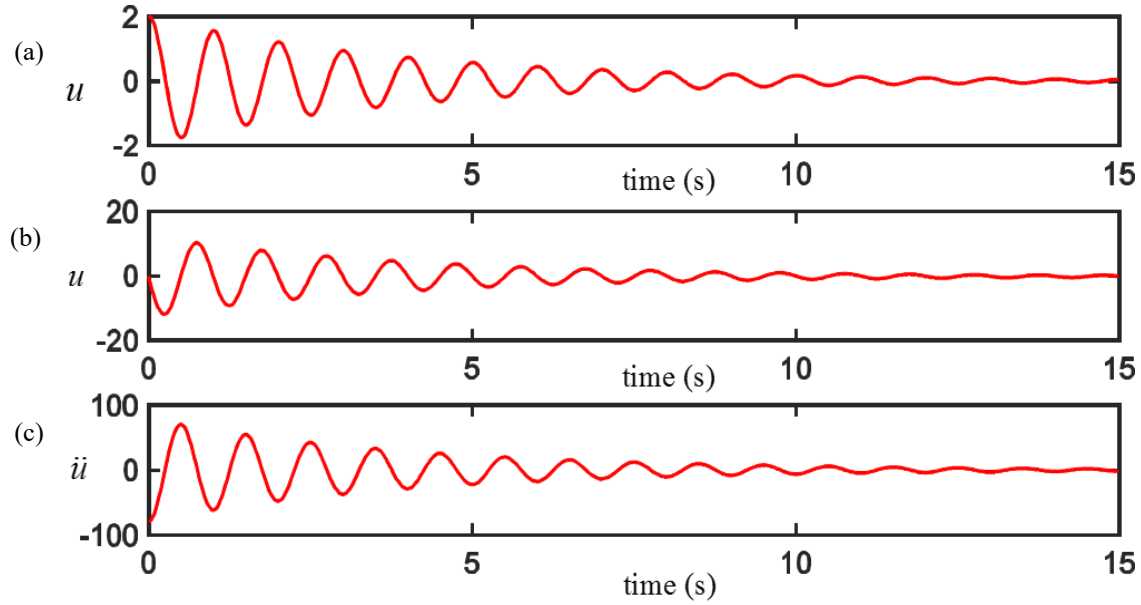

Fig. 2.1 Accurate dynamic signals of the linear system in Eq. (2.13b): (a) the displacement signal, (b) the velocity signal and (c) the acceleration signal.

Based on the accurate velocity signal from Fig. 2.1b, acceleration signals can be computed by the two discussed differentiation methods. The green curve in Fig. 2.2a presents the computed acceleration signal based on the backward differentiation formula in Eq. (2.1b) and the blue curve in Fig. 2.2a presents the computed signal based on the SG filter method with $n_L = 3, n_R = 0$ and $M = 3$. Without enough data points from the past, a forward finite difference method is applied to the first data point, and the SG filter method with shifted sections are applied to first 3 data points. While the difference of the applied differentiation methods does not show clearly in Fig. 2.2a, the relative errors can show the difference. The relative true error can be calculated by:

$$Error_1 = \left| \frac{\ddot{u}(t_i) - \ddot{u}_i}{\ddot{u}_i} \right| \times 100\% \tag{2.15}$$

where $\ddot{u}(t_i)$ is the computed acceleration signal and $\ddot{u}_t$ is the accurate acceleration signal. Then, the relative true error of two applied methods can be calculated and are given in Fig. 2.2b with the same color notation.

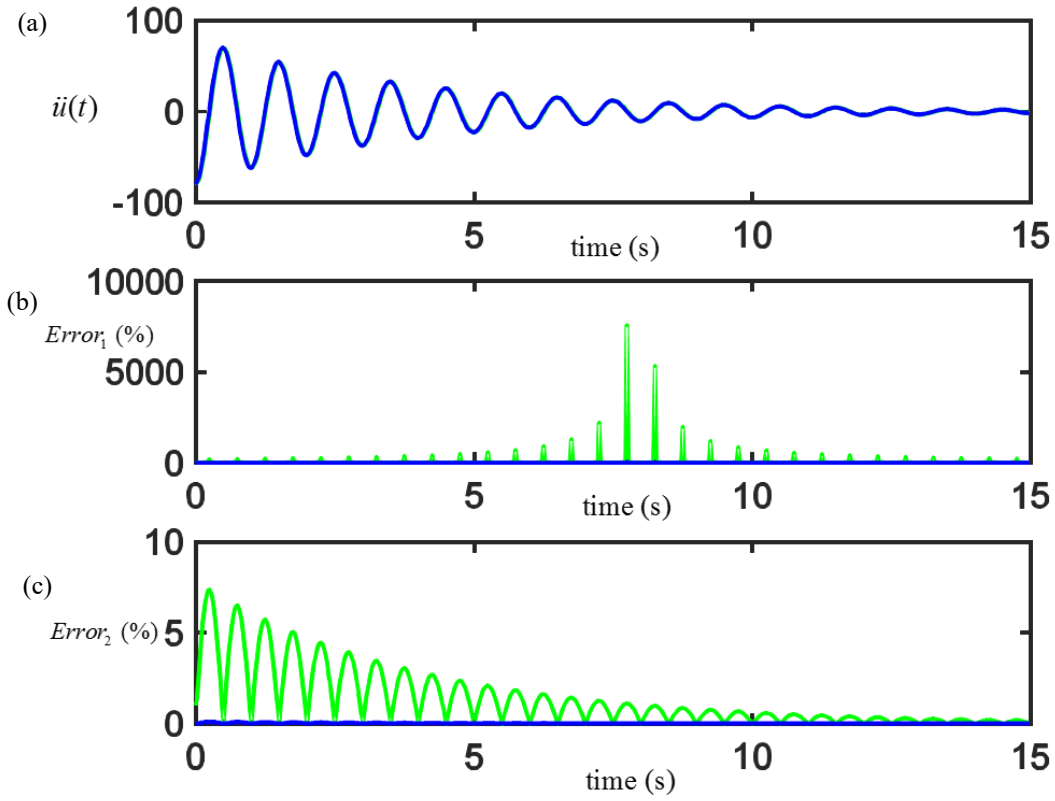

Fig. 2.2 Comparison of applied differentiation methods based on the velocity signal in Fig. 2.1b: (a) computed acceleration signals, (b) errors of Fig. 2.2a defined by Eq. (2.15) and (c) errors of Fig. 2.2a defined by Eq. (2.16).

For both computed errors, there exist some peaks with certain intervals. It doesn't mean the result acceleration is less accurate at those points but caused by nearly zero accurate acceleration at those points. With the denominator close to zero, the value of error would blow up and cannot represent the true error appropriately. Hence, we modified the definition of error to be:

$$Error_2 = \left| \frac{\ddot{u}(t_i) - \ddot{u}_i}{\max(|\ddot{u}_i|)} \right| \times 100\% \tag{2.16}$$

By using the maximum magnitude of accurate acceleration as the denominator, the problem of singularity in $Error_1$ has been avoided. And Fig. 2.2c gives the corresponding errors based on Eq. (2.16). With the

constant denominator, $Error_2$ is more like a 'true error' but not 'relative true error'. As shown in Fig. 2.2c, with vibration signal has its value oscillating around zero, the value of error also oscillates above zero periodically. And with vibration amplitude decrease through the time trace, the amplitude of calculated errors also decreases through the time trace. Thus, although the shape of $Error_2$ influenced by the shape of the acceleration signal, it gives a more appropriate expression about how big error existed in the signal than $Error_1$. It is a better option for accuracy comparison. Based on accurate velocity data from a linear system, while the backward differentiation formula gives the error up to 7% in Fig. 2.2c, the SG filter method with the choice of $n_L = 3, n_R = 0$ and $M = 3$ only has its value up to 0.1%.

However, although the applied SG filter method has a much higher accuracy than the appliedbackward differentiation formula based on the accurate velocity signal. When it comes to velocity signals with measuring noise, with a longer section used in the SG filter method, the existing noise can be tangled more in the SG filter method and result in extra errors. And the accuracy of the SG filter method and the finite difference method can be relative close. To simulate the noise introduced by the measuring in the numerical model, a vector of pseudorandom numbers drawn from the standard normal distribution usually can be added to the numerical data.

$$noise_1 = 0.01 \times randn(N,1) \times \max(|\dot{u}_i|) \tag{2.17}$$

where a standard deviation $\sigma = 0.01$ is assumed. Thus, magnitude of simulated noise will mostly fall in range of 1% of the largest velocity. However, in real cases, the noise range can change respect to the velocity value. To have a more realistic simulation, we have another noise model as:

$$noise_2 = 0.01 \times randn(N,1) \times |\dot{u}_i| \tag{2.18}$$

where for each time instant, simulated noise keep the same deviation, but fall in the range proportional to the magnitude of the velocity. Adding $noise_1$ and $noise_2$ to velocity signal in Fig. 2.1b respectively, we can get simulated measured velocity with added noise as shown in Figs. 2.5a&2.5b.

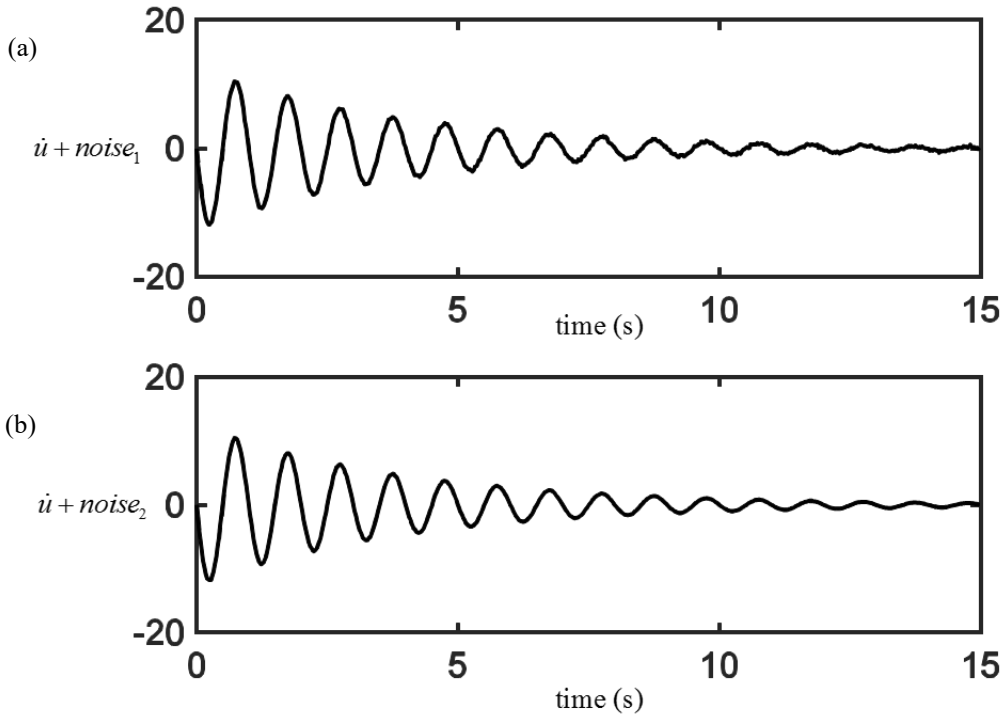

Fig. 2.3 Simulation of the measured velocity: (a) the velocity from Fig. 2.1b with simulated noise defined in Eq. (2.17) and (b) the velocity from Fig. 2.1b with simulated noise defined in Eq. (2.18).

Applying the same differentiation methods from the previous case, we can get result accelerations and corresponding errors (defined by Eq. (2.16)) as shown in Fig. 2.4. Result accelerations in Fig. 2.4a are calculated based on velocity signal in Fig. 2.3a (with $noise_1$). Green/blue curve present result based on the backward differentiation formula/SG filter method, respectively. Fig. 2.4b gives the corresponding errors of result acceleration signals in Fig. 2.4a with the same color notation. Result acceleration signals in Fig. 2.4c are calculated based on the velocity signal in Fig. 2.3b (with $noise_2$). And Fig. 2.4d gives the corresponding

errors of the result acceleration signals in Fig. 2.4c.

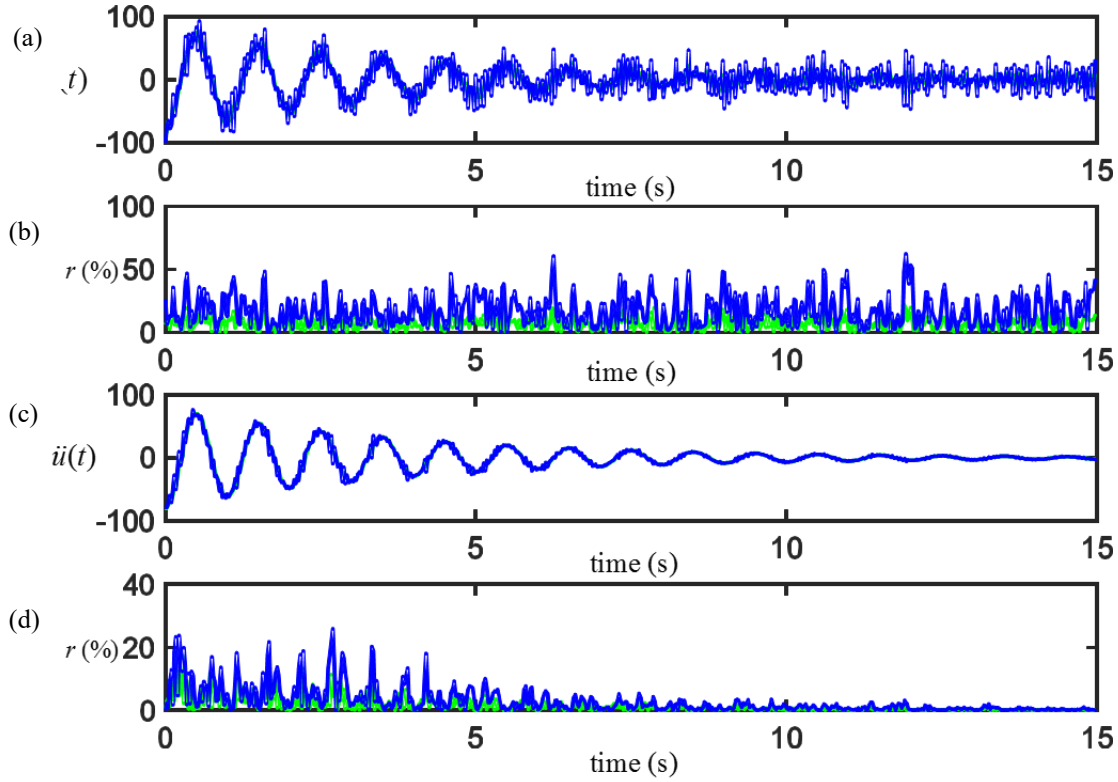

Fig. 2.4 Comparison of added simulated noise and comparison of applied differentiation methods: (a) computed acceleration based on velocity in Fig. 2.3a, (b) corresponding errors of Fig. 2.4a, (c) computed acceleration based on velocity in Fig. 2.3b and (d) corresponding errors of Fig. 2.4c.

Despite the different accuracy between applied differentiation methods, let's consider the rationality of these two definitions of noise first. Based on velocity signal with noise defined in Eq. (2.17), errors from both methods keep a relative stable amplitude as shown in Fig. 2.4b. While based on velocity signal with noise defined in Eq. (2.18), errors from both methods have a decreasing amplitude through the time trace as shown in Fig. 2.4d. However, with the error defined in Eq. (2.16), the computed signal with a consistent accuracy should have its corresponding error proportional to the magnitude of the data point as shown in Fig.

2.2c. Even with measuring noise and noise tangling in the calculation, a realistic noise simulation should have kept the situation that the error of computed acceleration signal is about proportional to the magnitude of the data point. Therefore, noise defined in Eq. (2.18) is more realistic and it will be used in the later numerical simulation.

And with added noise in the velocity signal, not only the accuracy of both methods has decreased, the SG filter method even has a larger noise than the finite difference method. As shown in the Fig. 2.4d, while the error of the used backward differentiation formula is up to 20%, the corresponding error of the applied SG filter method is up to 25%. That is because although longer section length for each observed data point can have a smaller calculation error, the coupled noise from those data points can result in a larger error. Thus, considering the calculation error and the coupled noise, and the applied section length of each observed point cannot be either too long or too short.

However, the accuracy of computed acceleration signal can be improved by using the SG filter method as a filter before acceleration computation. As discussed, a relative longer section length can be a more 'average' and filter out the existing noise. Therefore, choice of $n_L = n_R = 10$ and $M = 4$ is used for the filtering in this case. Here data points from the right side have been involved to show the feature of the applied filter. And the same $n_L = 3, n_R = 0$ and $M = 3$ is used for the acceleration computation. Figure 2.5 gives the calculated acceleration signal and Fig. 2.5b gives the corresponding error. Based on the filtered velocity signal, the computed acceleration signal becomes a lot smoother, and the error has been decreased dramatically to only 3%. Therefore, the extra step of noise filtering is necessary for measured data with noise. And by involving relative short time period in the computation, the accuracy of the computed acceleration

can have a significant increase.

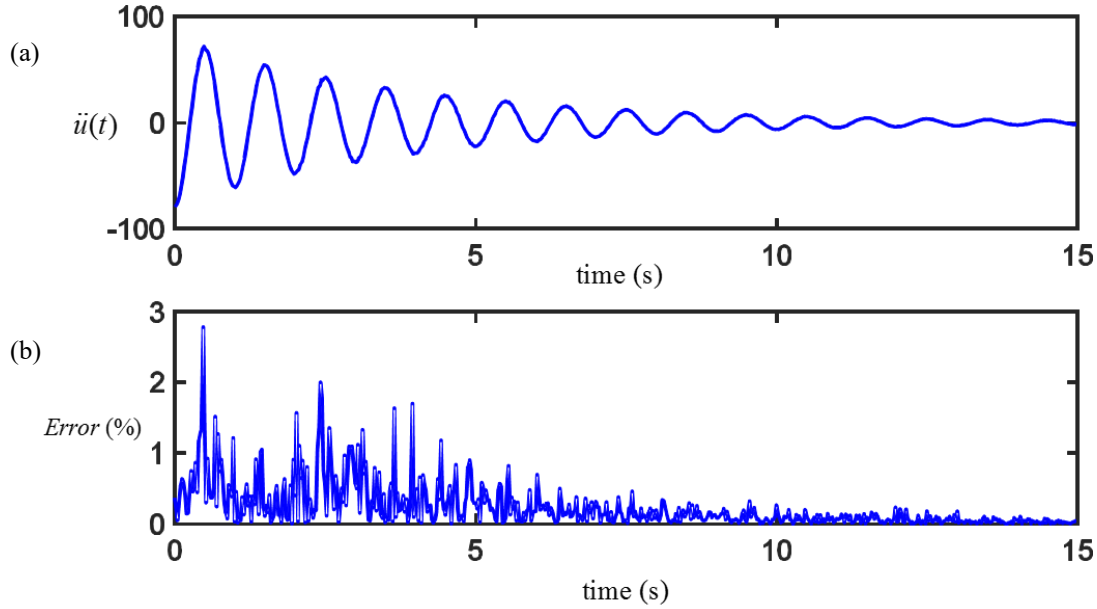

Fig. 2.5 Computed acceleration and error by the SG filter method with the extra step of noise filtering: (a) computed acceleration based on velocity in Fig. 2.3b and (b) corresponding errors of Fig. 2.5a.

When it comes to a nonlinear system, the behavior of velocity and acceleration signal can be more complicated. Consider a nonlinear single DOF system as:

$$\ddot{u} + 0.05\dot{u} + u + 20u^3 = 0 \tag{2.19}$$

Accurate displacement and velocity signal can be obtained from Runge-Kutta integration with a sampling rate of and the initial condition of $u(0) = 1, \dot{u}(0) = 0$. Accurate acceleration signal can be calculated by Eq. (2.14a). Figure 2.6 represents the accurate dynamic data of the nonlinear system in Eq. (2.19).

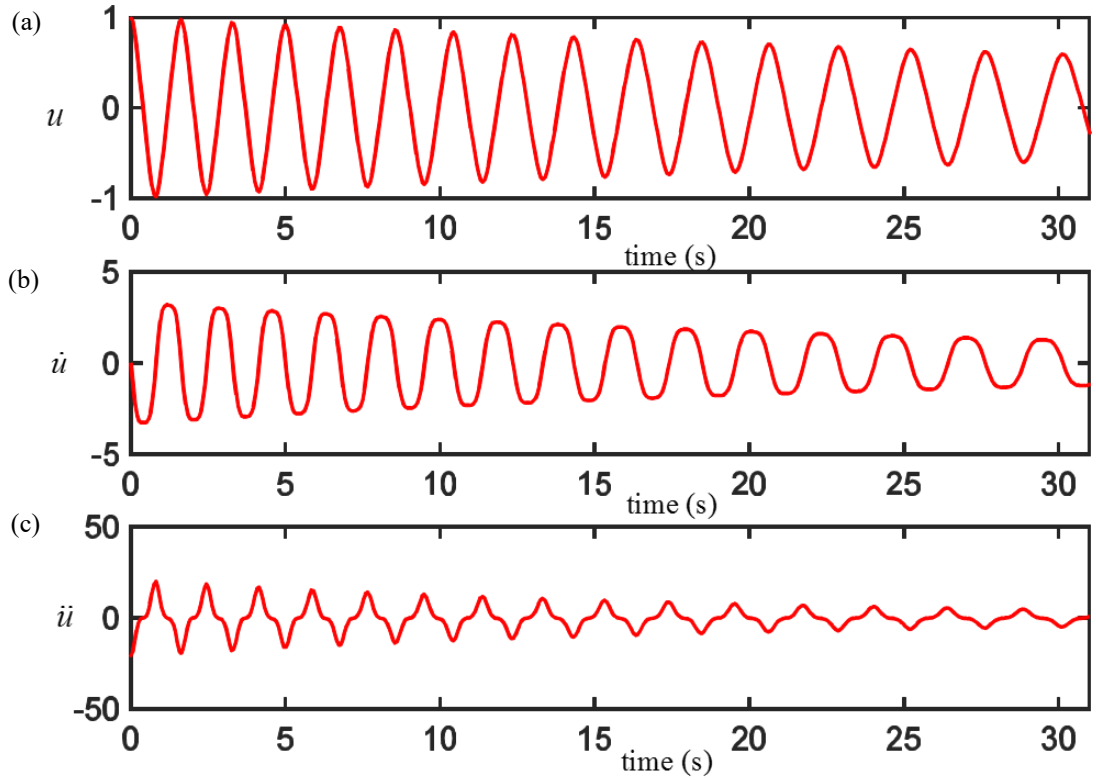

Fig. 2.6 Accurate dynamic signal of the nonlinear system in Eq. (2.19): (a) the displacement signal, (b) the velocity signal and (c) the acceleration signal.

Based on the accurate velocity signal in Fig. 2.6b, the backward differentiation formula in Eq. (2.1b) and SG filter with $n_L = 4, n_R = 0$ and $M = 4$ can applied for comparison. The green curve in Fig. 2.7a presents the result acceleration signal of the applied finite difference method, and blue curve in Fig. 2.7a presents the result acceleration signal of the applied SG filter method. The corresponding errors are given in Fig. 2.7b with the same color notation. While the accuracy of two applied methods does not show clearly in Fig. 2.7a, it shows a relative big difference in Fig. 2.7b. And the applied SG filter method has a higher accuracy.

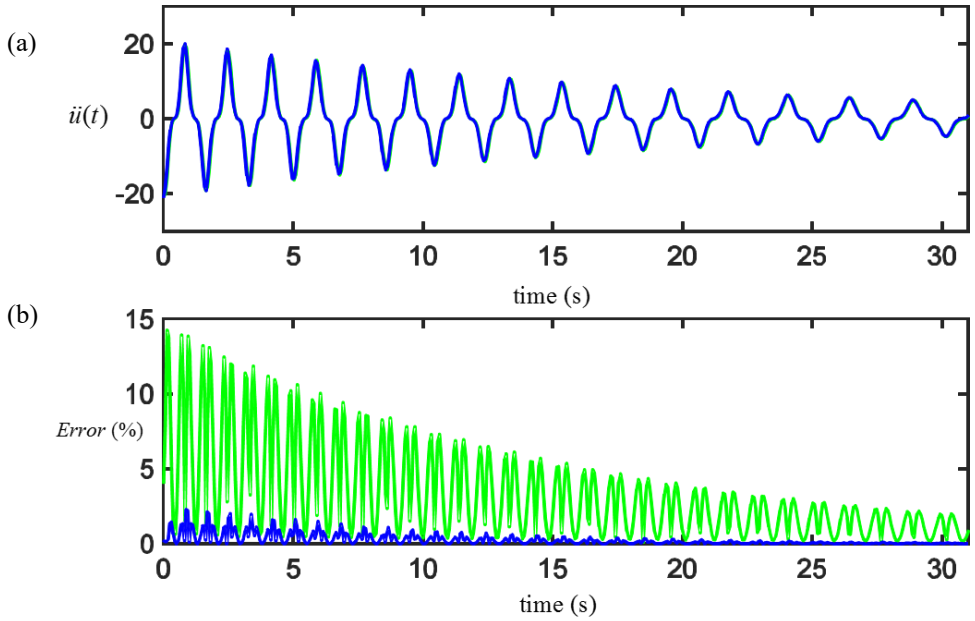

Fig. 2.7 Comparison of applied differentiation methods based on the velocity signal in Fig. 2.6b: (a) computed acceleration signals and (b) corresponding errors of Fig. 2.7a.

After adding the noise defined in Eq. (2.18) to the accurate velocity signal, the result velocity signal is given in Fig. 2.8a. While the backward finite difference can only directly be applied to the result velocity signal, the SG filter method can be used as a filter to compute the filtered velocity signal first then computed the acceleration signal. $n_L = n_R = 5$ and $M = 4$ is used for noise filtering and the same $n_L = 4, n_R = 0$ and $M = 4$ is used for acceleration calculation. Figure 2.8b gives the computed acceleration signal from the finite difference method in green curves while the computed acceleration signal from the SG filter method is given in blue curves. And the corresponding errors are given in Fig. 2.8c with the same color notation. With the pre-applied filtering, the noise tangling has been decreased, and the accuracy of the SG filter is smaller than the applied finite difference method. Therefore, since the SG filter method can be used as a noise filter to deal with measuring noise, easy to adjust to different order of accuracy by changing

n_L, n_R and M and has its efficiency by involving only a few inverse calculations, it will be used for computation of acceleration signals and noise filtering for later numerical and experimental cases.

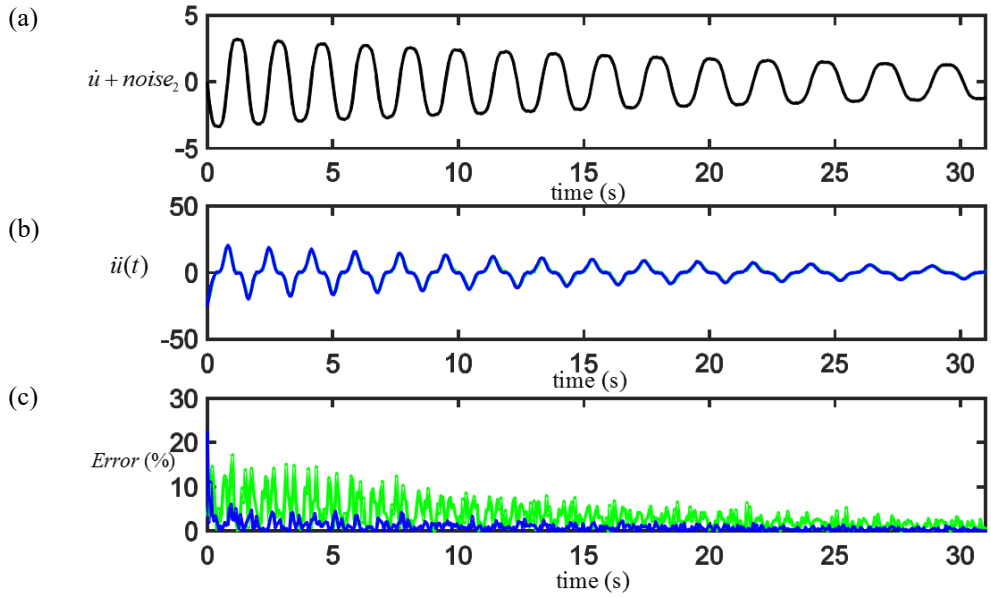

Fig. 2.8 Comparison of applied differentiation methods based on the velocity signal in Fig. 2.6b with added noise: (a) velocity signal from Fig. 2.6b with added noise, (b) computed acceleration signals and (c) corresponding errors of Fig. 2.8b.

2.3 Numerical Integration Methods

2.3.1 Taylor Series Method

Taylor series has been widely used for making the approximation of the function by using information of its derivative as defined below:

$$f(x_{i+1}) = f(x_i) + f'(x_i)h + \frac{f''(x_i)}{2!}h^2 + \frac{f^{(3)}(x_i)}{3!}h^3 + \cdots + \frac{f^{(n)}(x_i)}{n!}h^n + R_n \tag{2.20}$$

where R_n is the remainder term has a magnitude of order $O(h^{n+1})$. To compute displacement by Taylor

series, at most first two derivatives are available as the velocity (the first derivative) and the acceleration (the second derivative). With the velocity signal directly measured from the experiments and the acceleration signal computed by the SG filter method, the displacement can be approximated as:

$$u(t_i) = u(t_{i-1}) + \dot{u}_{i-1}\Delta t + \ddot{u}(t_{i-1})\Delta t^2 / 2 \tag{2.21}$$

where $u(t_{i-1})$ and $\ddot{u}(t_{i-1})$ is the computed displacement and acceleration from the previous time instant respectively, $\dot{u}_{i-1}$ is the measured velocity from the previous time instant and Δt is the time interval of the measured velocity signal. With the accurate velocity and an acceleration signal, Eq. (2.21) can ensure a 3rd order accuracy, and the error depends on the time interval/sampling rate. With only data points of the current and previous time instants involved, it can be applied in signal processing for real-time monitoring. And based on the definition, there is no inverse calculation involved which means this algorithm is quite efficient. However, by using data points from the dynamical signals directly, this method is more of a numerical method rather than an analytical method, it can be easily influenced by existed noise. Meanwhile, the acceleration signal with aggravated noise is involved in the calculation. The accuracy of computed displacement signal will be compromised to case with noise.

2.3.2 Newmark-beta Method

The Newmark-beta method is the most popular algorithm for numerical solutions of dynamic structural problems [40]. It also involves both velocity and acceleration signal in its definition. The numerical solutions of displacement $u(t_j)$ can be approximated by using computed displacement, measured velocity and computed acceleration from the previous/current time instant [41].

$$u(t_j) = u(t_{j-1}) + \dot{u}_j \Delta t + (1-2\beta)\ddot{u}(t_{j-1})\Delta t^2/2 + \beta\ddot{u}(t_j)\Delta t^2 \quad (2.22a)$$

$$\dot{u}(t_j) = \dot{u}_{j-1} + \Delta t(1-\gamma)\ddot{u}(t_{j-1}) + \Delta t\gamma\ddot{u}(t_j) \quad (2.22b)$$

where the algorithm is unconditionally stable and dissipative if the two algorithmic parameters β and γ satisfy $2\beta \geq \gamma > 1/2$ [40]. And $u(t_i), \dot{u}(t_i)$ and $\ddot{u}(t_i)$ represents the computed displacement velocity and acceleration, $\dot{u}_i$ represents data points from measured velocity signal. Although Eq. (2.22b) can be used to re-estimate the velocity data, it will not work as a noise filter because it is based on a numerical calculation and requiring known acceleration signal. Thus, Eq. (2.22b) will not be used for calculation. With no γ involved, the algorithm would be unconditionally stable and dissipative only if $\beta > 1/4$.

Comparing the formula with the Taylor series method, the only difference would be the acceleration term. Instead of only involving $\ddot{u}(t_{j-1})$, both $\ddot{u}(t_{j-1})$ and $\ddot{u}(t_j)$ are used. With extra information from the current time instant t_j, a more accurate acceleration can be achieved. Different choices of β give different weights on those two accelerations. Two common choices would be $\beta = 1/3$ and $\beta = 1/4$. For $\beta = 1/3$, we usually call it as linear acceleration assumption, it gives more weights on acceleration at a current time instant, and definition of displacement is given as:

$$u(t_j) = u(t_{j-1}) + \dot{u}_{j-1}\Delta t + (\ddot{u}(t_{j-1}) + 2\ddot{u}(t_j))\Delta t^2/6 \quad (2.23)$$

$\beta = 1/4$ is known as an average acceleration assumption, the weights of two accelerations are the same, and the displacement definition is given as:

$$u(t_j) = u(t_{j-1}) + \dot{u}_{j-1}\Delta t + (\ddot{u}(t_{j-1}) + \ddot{u}(t_j))\Delta t^2/4 \quad (2.24)$$

Meanwhile, since $\dot{u}_j$ is not involved in all discussed formula, here we derived another definition with all $\dot{u}_{j-1}, \dot{u}_j, \ddot{u}(t_{j-1})$ and $\ddot{u}(t_j)$ involved. A cubic polynomial is used as the velocity function of the observed

time instant t_j :

$$\begin{aligned} \dot{u}_j(\tilde{t}) &= a_0 + a_1\tilde{t} + a_2\tilde{t}^2 + a_3\tilde{t}^3 \\ \Rightarrow \ddot{u}_j(\tilde{t}) &= a_1 + a_2\tilde{t} + a_3\tilde{t}^2 \\ u_j(\tilde{t}) &= u(\tilde{t} - \Delta t) + \int_{-\Delta t}^{\tilde{t}} \dot{u}_j(\tilde{t})d\tilde{t} \end{aligned} \tag{2.25}$$

where time trace has been shifted as $\tilde{t} = t - t_j$ to simplify the equations. Coefficients of velocity function can be solved by four known parameters ($\dot{u}_{j-1}, \dot{u}_j, \ddot{u}(t_{j-1})$ and $\ddot{u}(t_j)$):

$$\left.\begin{aligned} \dot{u}_j &= a_0 \\ \dot{u}_{j-1} &= a_0 - a_1\Delta t + a_2\Delta t^2 - a_3\Delta t^3 \\ \ddot{u}(t_j) &= a_1 \\ \ddot{u}(t_{j-1}) &= a_1 - 2a_2\Delta t + 3a_3\Delta t^2 \end{aligned}\right\} \Rightarrow \begin{cases} a_0 = \dot{u}_j \\ a_1 = \ddot{u}(t_j) \\ a_2 = \left[2\ddot{u}(t_j) + \ddot{u}(t_{j-1}) + \dfrac{3}{\Delta t}\left(\dot{u}_{j-1} - \dot{u}_i\right)\right] \Big/ \Delta t \\ a_3 = \left(\dfrac{2}{\Delta t}\dot{u}_{j-1} + \ddot{u}(t_{j-1}) - \dfrac{2}{\Delta t}\dot{u}_j + \ddot{u}(t_j)\right) \Big/ \Delta t^2 \end{cases} \tag{2.26}$$

Then, the displacement at t_j as $\tilde{t} = 0$ can be determined as:

$$\begin{aligned} u_j(0) &= u_j(-\Delta t) + \int_{-\Delta t}^{\tilde{t}} \dot{u}_j(\tilde{t})d\tilde{t} \\ &= u_j(-\Delta t) + a_0\Delta t - a_1\frac{\Delta t^2}{2} + a_2\frac{\Delta t^3}{3} - a_3\frac{\Delta t^4}{4} \\ &= u_j(-\Delta t) + (\dot{u}_{i+1} + \dot{u}_i)\Delta t + (\ddot{u}_{i+1} - \ddot{u}_i)\Delta t^2/12 \end{aligned} \tag{2.27}$$

Since it has a similar formula with the Newmark-beta method and is developed based on cubic velocity function assumption, here we call this method as cubic Newmark-beta method. Comparing the definition in Eq. (2.27) with Eq. (2.23) and Eq. (2.24), not only we get $\dot{u}_j$ involved in the velocity term, but the operator in the acceleration term also has been changed. With the $\dot{u}_j$ involved, we would get more information of current time instant which can lead to a more accurate approximation. And instead of adding up the accelerations from different time instants in Eq. (2.23) and Eq. (2.24), here we get the difference between the acceleration of two-time instants which may help to reduce the error exists in acceleration data.

However, for all three different definitions of the Newmark-beta method, the accuracy of computed

displacement is depending on velocity and acceleration value directly. It makes this method more of a numerical method, and not able to filter noise. Although the new developed algorithm has a step of determining the velocity signal function in Eq. (2.26), the computed data points back to $\dot{u}_{i+1}$. It cannot be used to re-estimate velocity value or filter noise. Therefore, similarly, although discussed three new formula have their advantage of efficiency and can be applied in signal processing for real-time monitoring, their accuracy would be compromised when it comes to signal with noise.

2.3.3 SG Integration Method

Although the curve fitting method with an analytical algorithm can be used for computing displacement signal by integrating the determined velocity function, it still has the problem of relative inefficient calculation. Meanwhile, although the SG filter is mostly used for filtering high-frequency noise or computing the first derivative of the original signal, it can be developed to work for integration. Based on the SG filter method introduced in section 2.2.3, after time shifting as $\tilde{t} = t - t_j$ for observed time instant t_j, velocity signal function at t_j can be determined as $\dot{u}_j(\tilde{t})$. Then, the relative displacement between the previous and current instant as t_{j-1} and t_j ($-\Delta t$ and 0) can be computed by integrating the $\dot{u}_j(\tilde{t})$ through the period. And the resulting displacement can be solved as:

$$\begin{aligned} u_j(0) &= u_j(-\Delta t) + \int_{-\Delta t}^{0} u_j(\tilde{t})d\tilde{t} = u_j(-\Delta t) + \sum_{k=0}^{M} a_k \frac{(0)^{k+1}}{k+1} - \sum_{k=0}^{M} a_k \frac{(-\Delta t)^{k+1}}{k+1} \\ &= u_j(-\Delta t) + [\frac{\Delta t}{1} \quad -\frac{\Delta t^2}{2} \quad \cdots \quad (-1)^M \frac{\Delta t^{M+1}}{M+1}] \cdot [\tilde{a}] \\ &= u(t_{i-1}) + [\tilde{t}] \cdot [\tilde{C}] \cdot [\dot{u}] \\ [\tilde{t}] &= [\frac{\Delta t}{1} \quad -\frac{\Delta t^2}{2} \quad \cdots \quad (-1)^M \frac{\Delta t^{M+1}}{M+1}] \end{aligned} \tag{2.29}$$

Instead of only asking for first two coefficients a_0 and a_1 in the previous SG filter method, all coefficients a_k are required in the calculation. However, it will not introduce any extra inverse calculation, and the definition of a new vector $\left[\tilde{t}\right]$ is also independent with time instant t_j. Thus, as long as the applied n_L, n_R and M is the same, the used $\left[\tilde{C}\right]$ will be the same. And only $n_L + n_R + 1$ inverse calculations are required in computing the displacement signal through the entire time trace. Moreover, if we apply SG integration method with SG filter method, the determined velocity signal function can be used for both calculation and only $n_L + n_R + 1$ inverse calculations in total are the cost to get both the displacement and acceleration signal.

2.3.4 Methods Comparison

Since all integration methods can only get integrated displacement as relative displacement, to focus on comparing the accuracy of methods selves, here the initial displacement is assumed known. Based on the definition in Eq. (2.21), (2.23), (2.24) and (2.27), the biggest difference between the Tayler series method and three Newmark-beta methods will be the acceleration term. With extra data point $\dot{u}_j$ from the measured signal involved in the definition, the cubic Newmark-beta method can have a better result and will be used as an example of those four methods to compare with SG integration method. The required acceleration signal in its calculation will be computed by the SG filter method to simulate the situation of single measurand (velocity). The accuracy of the cubic Newmark-beta method and SG filter method will be compared based on both linear and nonlinear system with and without simulated noise. While the result based on signals without added noise can indicate the calculation error, the result based on signals with added noise can reflect

the ability of method dealing with measuring noise. In addition, based on the requirement of real-time monitoring in real life, only data points from the past will be used for calculation.

Based on the velocity signals in Fig. 2.1b of the linear system from Eq. (2.13), the displacement signal can be computed by the SG integration method with the same $n_L = 4, n_R = 0$ and $M = 4$ as used in the computation of the acceleration. And with the computed acceleration signal from Fig. 2.2a based on the SG filter method, the displacement signal can be computed by the cubic Newmark-beta method as the green curve in Fig. 2.9a. And the computed displacement signal based on the SG integration method is given in blue curve in Fig. 2.9a. The corresponding error is given in Fig. 2.9b with the same color notation and error is defined in Eq. (2.16).

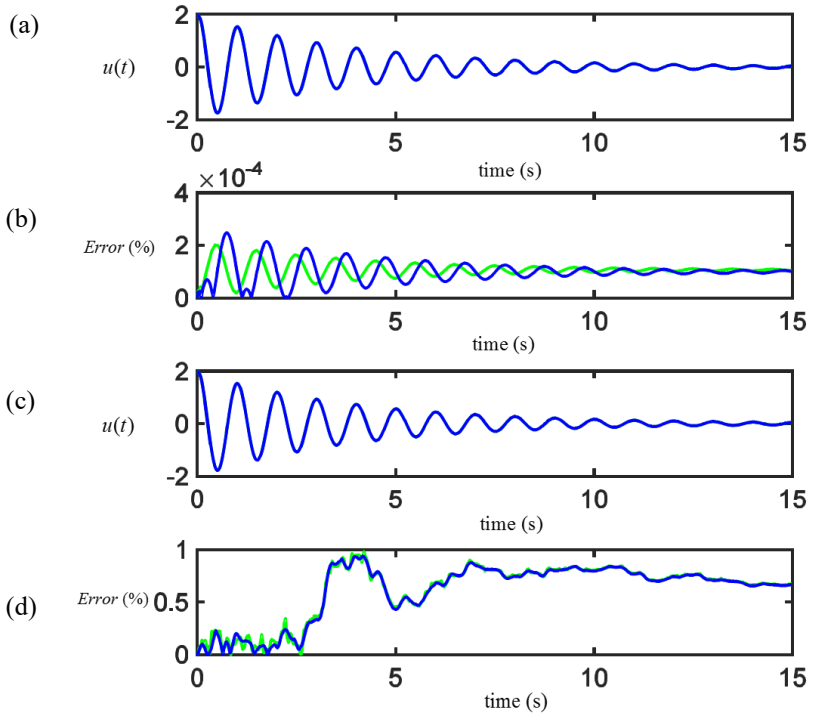

Fig. 2.9 Comparison of applied integration methods based on system from Eq. (2.13): (a) the computed displacement signal based on the velocity signal in Fig. 2.1b, (b) corresponding errors of Fig. 2.9a, (c) computed displacement signal based on the velocity signal in Fig. 2.3b and (d) corresponding errors of Fig. 2.9c.

Notice although the cubic Newmark-beta method is based on the calculated acceleration signal, with relative accurate calculated acceleration signal from the applied SG filter method, the accuracy of computed displacement has not been influenced much. And with $n_L = 4, n_R = 0$ and $M = 4$, the calculated error from the applied SG integration method is even a little bit larger. But, after all, both methods give a relatively accurate result displacement signal that error of both methods is below $3\times10^{-4}\%$. And notice without added noise, computed errors are proportional to the amplitude of the computed displacement signal.

However, when it comes to velocity signal with added noise, in addition to the calculation error, the accumulated noise plays a more important part in the resulting error. To be fair, the same step of noise filtering has been applied to the velocity signal as in Fig. 2.5a. Figure 2.9c gives the compute displacement signal from the cubic Newmark-beta signal and the applied SG integration method in the green and blue curve, respectively. And corresponding errors are presented with the same color notation in Fig. 2.9d. Notice the shape of error in Fig. 2.9d is very different from previously computed errors. Instead of proportional to the amplitude of the computed displacement signal, the computed errors are increasing through the time trace. That is because, with the displacement data from the previous time instant used for the calculation, the existed error will be adding up through the time trace. And the similar moving average from two computed errors are showing the accumulated noise. Meanwhile, the oscillating details are showing the accuracy of two applied methods. As the error of the applied SG integration method gives a less oscillated error, it gives a steadier result.

Considering the nonlinear system in Eq. (2.19), both velocity signal with and without added noise will be used for comparison. Based on accurate velocity data in Fig. 2.6b, Fig. 2.10a gives the result displacement

signals in the green and blue curve from the cubic Newmark-beta method and the SG integration method, respectively. The acceleration signal used in the cubic Newmark-beta method is the blue curve in Fig. 2.7a. The corresponding errors of two computed displacement signals are given in Fig. 2.10b with the same color notation.

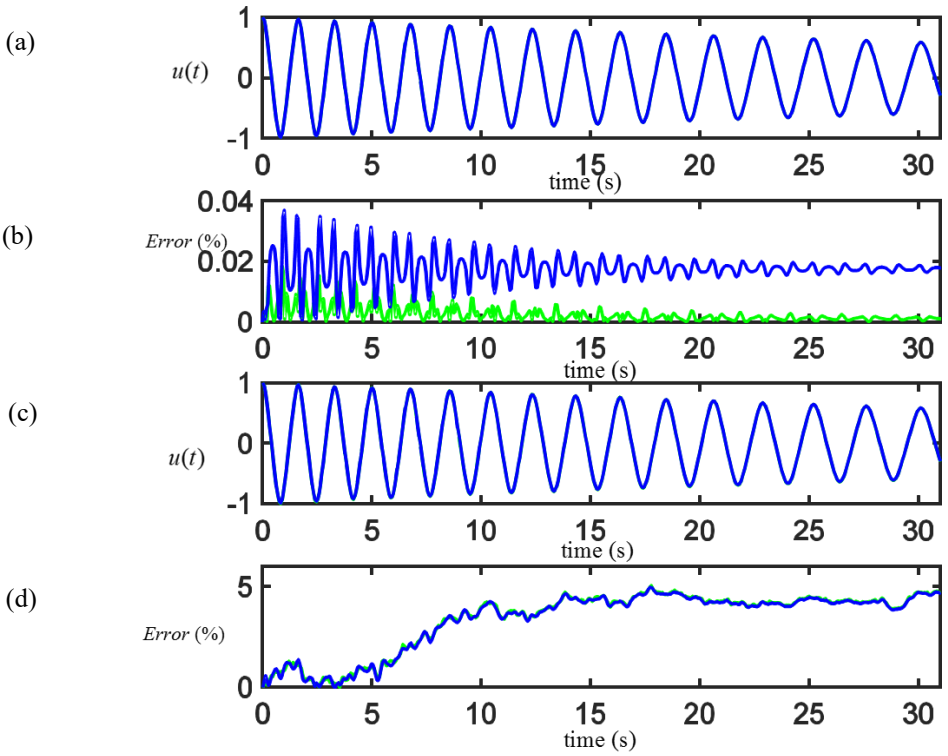

Fig. 2.10 Comparison of applied integration methods based on system from Eq. (2.19): (a) the computed displacement signal based on the velocity signal in Fig. 2.6b, (b) corresponding errors of Fig. 2.10a, (c) computed displacement signal based on the velocity signal in Fig. 2.8a and (d) corresponding errors of Fig. 2.10c.

With relative accurate calculated acceleration signal, the applied cubic Newmark-beta method gives a smaller calculation error than the applied SG integration method with $n_L = 4, n_R = 0$ and $M = 4$. Notice both methods give a relatively accurate result displacement signal that error of both methods is below 0.04%. And without added noise, both calculated errors are proportional to the amplitude of the computed

displacement signal.

Figure 2.10c gives the case with added noise for comparison. Result displacement signal based on the cubic Newmark-beta signal and the SG integration method is given in the green and blue curve, respectively. And corresponding errors are presented with the same color notation in Fig. 2.10d. As in the previous case, noise filtering has been applied before applying the SG integration method. And the accumulated noise shows clearly in both computed errors while the oscillating details are about the same. Therefore, with a relative accurate computed acceleration signal, the cubic Newmark-beta method can have the similar accuracy of the SG integration methods in both cases. However, with adjustable n_L, n_R and M, the SG integration method has more flexible than the cubic Newmark-beta method. And applying it with the SG filter method with the same n_L, n_R and M, the calculation can be simplified even more. Therefore, the SG filter method and the SG integration method will be used together for the displacement and acceleration signal computation in the later numerical case and experimental validation.

2.3.5 Determination of Initial Displacement

Different from numerical differentiation, numerical integration has an extra problem of the integration constant. The integration constant required in computing displacement for each time instant is the displacement of the previous time instant. Since the relative displacement of each time interval will be calculated by integration, the only one integration constant required for the entire time trace is the initial displacement $u(0)$. For the case with unknown initial displacement, a zero initial displacement assumption is usually used, and the resulting displacement can be understood as the relative displacement

$\hat{u}(t)$ $(= u(t) - u(0))$. Then, the initial displacement needs to be determined to get the actual displacement signal.

It can be determined based on the moving average of the relative displacement for many cases. That is because, for the system under free vibration, the actual displacement oscillating around zero and $u(t)$ will approach zero when *t* is large. Therefore, the constant that the relative displacement $\hat{u}(t)$ is approaching will have the same magnitude as initial displacement but with the opposite sign. Then, the determined initial displacement can be used to shift the relative displacement to compute the actual displacement signal. And for the system under steady-state vibration, when *t* is large, transient vibration due to start-up would have mostly damped out. As the actual displacement oscillate around zero, the relative displacement $\hat{u}(t)$ will oscillate around a constant as the vibration amplitude. Then, the determined vibration amplitude can be used to shifting the relative displacement to compute the actual displacement signal. The moving average of the $\hat{u}(t)$ around the end of time trace can be used to compute the actual displacement signal for both cases.

To compute the actual displacement signal, three different methods have been discussed and compared. To simulate the real situation, the relative displacement signal computed based on the velocity signal with added noise will be used for comparison. And the SG integration method will be used for computing the relative displacement signal as discussed in the previous section. Both free-transient vibration and steady state vibration of the linear system from Eq. (2.13) will be discussed.

A) Method 1

The most basic method used to determine the initial displacement by the moving average would be taking an average of local maxima and local minima. However, when it comes to free-transient vibration, each pair of consecutive local maxima and local minima has a different value because of the existed damping. Thus, the average of each pair of consecutive local extrema will deviate from the actual moving average.

Since the local extrema around the end of the time trace have relative small vibration amplitude, it can have a less deviation. And for steady-state vibration, avoid the transient vibration from the start-up, an average of local maxima and local minima can be used to determine the initial displacement and the actual displacement signal.

B) Method 2

In order to avoid the asymmetric of local extrema in free-transient vibration as in Method 1, the actual moving average can be directly determined by data points fall around it. It can be realized by using the corresponding velocity signal. That is because the physical meaning of those data points is that system is at the position of equilibrium. For the system under free vibration (both transient and steady state), at the time instants system across the position of equilibrium, the corresponding velocity will be at its maximum. Then, with data points identified by the time instants that velocity signal is at its local extrema points, the initial displacement/actual moving average can be determined as the average of displacement at those identified data points, and the actual displacement signal can be computed.

C) Method 3

Besides of determine the initial displacement value $u(0)$ and then add it to the entire relative displacement signal, the actual displacement signal can be computed by removing the inaccurate moving average $u^0(t)$ from the $\hat{u}(t)$. And the even existing accumulated noise will be removed along with the inaccurate zero-initial displacement. The basic principle is still that when system is under free transient, or steady state vibration, it should have its displacement signal oscillating around zero. Empirical mode decomposition(EMD) is a data-driven signal decomposition technique that sequentially extracts zero-mean regular/distorted harmonics from a signal [42]. Thus, it can be used here to extract actual

displacement. The local extrema of relative displacement signal will be recognized first. While all local minima are connected using a cubic spline and all local maxima are connected using another cubic spline, the moving average can be determined as their average. Notice the identified moving average can change through the time trace because the accumulated noise is included.

Based on the velocity signal with added noise shown in Fig. 2.3b, the relative displacement signal can be computed by the SG integration method with zero initial displacements as shown in Fig. 2.11a. And same as the case in the previous section, a step of noise filtering has been applied before integration. Discussed three methods have been applied to compute the actual displacement signal. Figure 2.11b gives the computed displacement signals based on method 1, 2 and 3 in red, green and blue curves, respectively. And the corresponding errors are given in Fig. 2.11c with the same color notation.

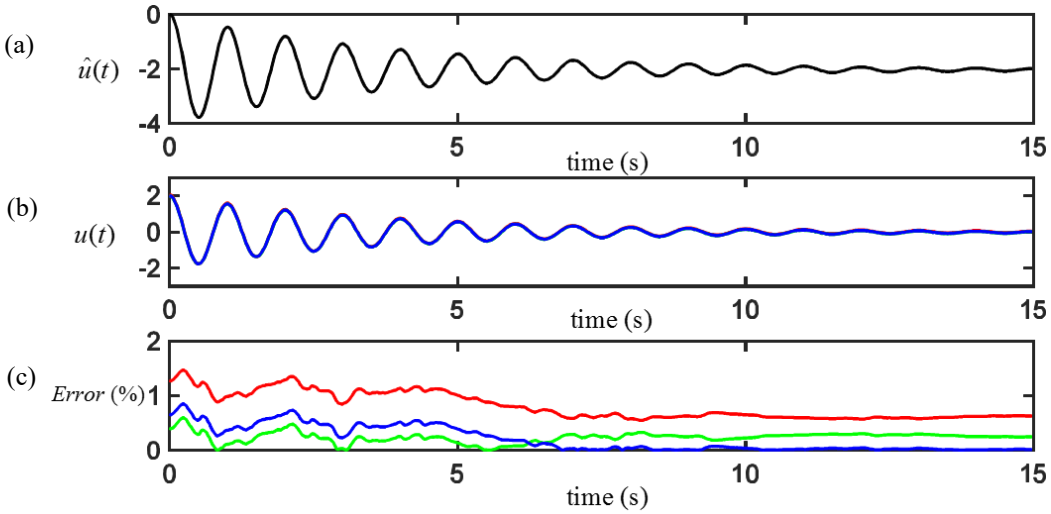

Fig. 2.11 Comparison of three methods for computing the actual displacement signal of the system under free-transient vibration: (a) the computed relative displacement, (b) computed actual displacement signals and (c) corresponding errors of Fig. 2.11b.

For the method 1, considering the asymmetric of local extreme points caused by the existed damping,

only the last pair of local maxima and minima is used to compute the initial displacement. And it is determined as 2.0256. Compare to the actual initial displacement as 2; the relative error is about 1.28%. Meanwhile, based on the Fig. 2.11c, with fewer data points involved, the error of method 1 is larger than the other two through the time trace. For the method 2, since the problem of the asymmetric has been avoided by directly using data points fall around the position of equilibrium, those data points are identified through the entire time trace. The initial displacement is determined as 2.0081 with only 0.405% relative error comparing to the actual initial displacement. And as in Fig. 2.11c, with more data points involved and avoiding the influence from the asymmetric local extrema, the error of method 2 is the smallest at the beginning. However, with a constant amount of shifting through the time trace, the accumulated noise shows as the increasing error. For the method 3, instead of determining the value of the initial displacement, the moving average changing through the time trace has been removed. Therefore, although the computed displacement signal does not have the most accurate result at the beginning, the accumulated noise has been removed, and the error around the end is a lot smaller than the other two methods.

And to excite a steady state vibration, the linear system from Eq. (2.13) is applied to a harmonic input as:

$$2\ddot{u} + 1.0053\dot{u} + 78.9568u = 50\sin(2\pi t) \tag{2.30}$$

where the frequency of exciting force is the same as system's natural frequency, and the system has the same initial condition as before as $u(0) = 2, \dot{u}(0) = 0$. Accurate displacement and velocity signal can be obtained from Runge-Kutta integration with the same sampling rate as before. In order to present the steady state vibration, the transient vibration part due to the start-up is not included. And considering the real situation, the relative displacement signal is computed by the SG integration method with an extra step of noise filtering. The velocity signal with added noise and the computed relative displacement is given in Fig. 2.12a&2.12b, respectively. Figure 2.12c gives the computed displacement signals based on method 1, 2 and 3 in red, green and blue curves, respectively. And the corresponding errors are given in Fig. 2.12d.

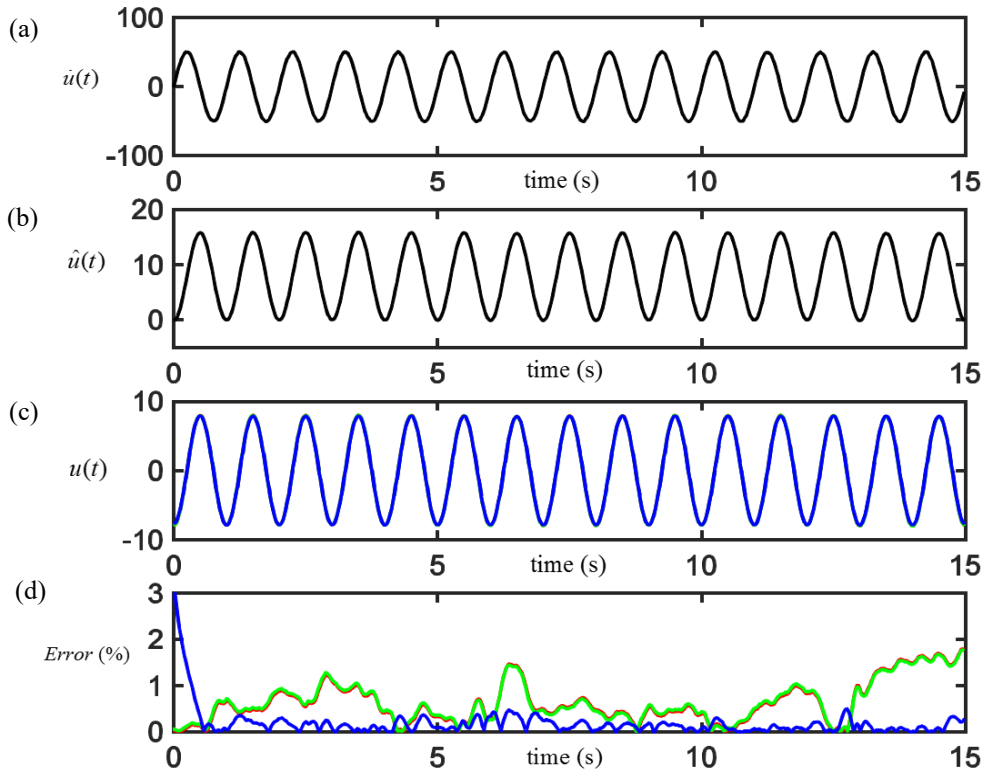

Fig. 2.12 Comparison of three methods for computing the actual displacement signal of the system under steady state vibration: (a) the velocity signal with added noise, (b) the computed relative displacement signal, (c) computed actual displacement signals and (d) corresponding errors of Fig. 2.12c.

For the method 1, without the problem of asymmetric local extrema, local maxima and minima through the entire time trace have been used to determine the amplitude. And it is determined as 7.9137. Compare to the actual amplitude as 8; the relative error is about 1.08%. Meanwhile, based on the Fig. 2.12d, the accuracy of computed displacement signal is the most accurate at the beginning part. However, with the constant shifting applied to the relative displacement signal, the accumulated noise still existed, and the error is much larger after that. Without the problem of the asymmetric local extra, method 1 and 2 gives the similar result. The amplitude is determined as 7.911 by the method 2 with relative error as 1.11%. With constant shifting, method 2 cannot remove the accumulated noise either. For the method 3, instead of determining the value of the initial displacement, the moving average changing through the time trace has been removed. Therefore, although the computed displacement signal has a relatively large error at the beginning, the accumulated noise has been removed, and the error after that is much smaller than the other two methods. Therefore, based on both cases, the EMD can not only use to shifting the relative displacement signal, but also remove the accumulated noise existed in the relative displacement signal. Therefore, when it comes to case with unknown initial displacement and free vibration, EMD will be used to compute the actual displacement signal from the relative displacement signal.

Chapter 3 LEVEL I DAMAGE DETECTION

3.1 Introduction

The system model is often presented in terms of stiffness, mass and damping matrices, which can also be presented in terms of model frequencies, mode shapes, and damping ratios. Hence, extraction of such model parameters from measured dynamical responses is the main task of system identification. There are many ways to extract model parameters out of dynamical data. A system can be represented by an assumed governing equation or by a response function. Many methods work by assuming a governing equation with undetermined parameters and then fitting measured dynamical data to the governing equation to determine the parameter values. These are the so-called parametric identification methods. However, the use of an assumed governing equation may limit the accuracy and capability of system identification, and fitting data into an unmatched assumption may result in misinterpretation. Nonparametric identification methods are to avoid such limits by not assuming the forms of spring and damping functions of a mechanical system. However, the unknown functions often need to be adjusted case by case to obtain better estimations and slightly change in model parameters may not be detected by determined functions. On the other hand, based on the domain of the data being processed for system identification, parametric and nonparametric methods can be divided into direct time-domain methods, indirect time-domain methods, and frequency-domain methods.

Recall the categorization proposed by Rytter[43]:

• Level 1: Determination that damage is present in the structure

• Level 2: Determination of the geometric location of the damage

• Level 3: Quantification of the severity of the damage

• Level 4: Prediction of the remaining service life of the structure.

Level 1 identification is about monitoring the health of an in-situ structure and identify the damage at an early stage. And considering the cost of monitoring/measuring a structure and the influence on the structure's feature, it is better to measure one point or just a few points from the structure. For level 1 identification, the case of measuring one point is considered in this thesis. Therefore, the corresponding numerical model of the structure in level 1 identification will be a single degree-of-freedom (DOF) system. And to identify the damage at an early stage, an instant/quick feedback of certain parameter is required once damage occurs. It not only requires damage detection methods be capable of real-time monitoring but also can detect the small changes of the system. While nonparametric identification methods can be good at identifying the nonlinearity of system, parametric identification methods with determined parameters can give a clear indicate of the occurrence of damage and any small change. The system identification methods studied/developed from my master research will be reviewed in following sections, and the feasible of using them for level 1 damage detection will be discussed and compared based on a numerical case of the damage occurrence.

Once the occurrence of damage is identified, a more comprehensive damage analysis is required. It can start with identify the damage location (level 2 damage detection) and followed by the analysis the severity of the occurred damage (level 3 damage detection) and predicted the remaining useful life of the structure (level 4 damage detection). Structural damage causes changes in structural, physical properties, mainly

stiffness and damping, at damaged locations. And these changes in structural properties, in turn, alter the dynamic response behavior of the structure from its initial pre-damage condition [44]. Therefore, dynamical responses of points located through the entire structure need to be measured. And damage location can be determined by comparing the computed model parameters from the measured responses. With more measured responses, a more precise damage location can be determined. And instead of a single DOF system, a numerical model of a continuous system such as finite element model need to be used for the measured structure.

The severity of the damage can be assessed in many ways. The size of the damage may be one of the focus points; it can be realized by ultrasonic testing [45] or other microscope detection [46]. The value of discussed model parameter from level 2 damage detection can also be used to assessing the severity [47]. Although level 4 damage detection is the ultimate aim of any condition monitoring system, there is not much algorithm was found which attempted the prediction of the remaining service life of a structure. There is a clear challenge to the condition monitoring research community to tackle the so-called level 4 damage detection [5].

3.2 Direct Time-Domain Methods

3.2.1 Least Square Fitting Method

When damage occurs to a system, stiffness and/or damping values of the system will be changed. Accurate estimation of damping and stiffness is always the emphasis on every method for system identification. The main characteristic of direct time-domain methods is to estimate system parameters without transform

dynamical data to the frequency domain. The proposed least square fitting method (LSF) uses a governing equation with undetermined system parameters as the mathematical model of a system. For governing equation of a single-degree-of-freedom (single-DOF) linear dynamic system as:

$$m\ddot{u} + c\dot{u} + ku = f(t) \tag{3.1}$$

The mass m of the system and the applied force $f(t)$ usually are known, and the time-varying displacement, velocity, and acceleration can be obtained by measurement or by integration/differentiation. That leaves k and c to be unknown. Thus, the undetermined system parameters here are k and c. If k and c can be identified from the measured dynamic response, they can be used for health diagnosis. Define error function E_R as in Eq. (3.2), k and c can be solved by least-square fitting.

$$E_R \equiv \sum_{i=j-n}^{j+n} \left[m\ddot{u}(t_i) + c\dot{u}(t_i) + ku(t_i) - f(t_i) \right]^2 \tag{3.2}$$

where it is assumed that the data point at t_j is under estimation, n data points from each side are used for least-squares fitting, and a total of $2n+1$ points are used for estimation. Notice the displacement and acceleration signals as $u(t_i)$ and $\ddot{u}(t_i)$ are assumed computed from the measured velocity signal $\dot{u}_i$. The notation $\dot{u}(t_i) = \dot{u}_i$ is used for the velocity signal from this chapter to have a consistent notation between all three dynamical responses. When only data points from the past in used for calculation as $i = j-n, j-n+1, ..., j$, the LSF can realize real-time monitoring of k and c.

For computed displacement signal $u(t)$, in addition to three methods introduced in section 2.3.5 for determining the unknown initial displacement $u^0 \left(\equiv u(0)\right)$, LSF can also be used for determining the unknown initial displacement. By expressing displacement signal as two parts as initial displacement u^0 and relative displacement $\hat{u}(\equiv u - u^0)$. Unknown initial displacement can be treated as an extra unknown to Eq.

(3.1) and Eq. (3.2), and the number of unknowns increases to three.

$$\begin{aligned} & m\ddot{u} + c\dot{u} + k\hat{u} + ku^0 = f \\ & E_R \equiv \sum_{i=j-n}^{j+n} \left[m\ddot{u}(t_i) + c\dot{u}(t_i) + k\hat{u}(t_i) + ku^0 - f(t_i) \right]^2 \end{aligned} \tag{3.3}$$

where k, c and u^0 are three unknowns that can be estimated by the following least-squares fitting procedure:

$$\begin{aligned} \frac{\partial E_R}{\partial c} &= 0 = \sum_{i=j-n}^{j+n} (m\ddot{u}(t_i) + c\dot{u}(t_i) + k\hat{u}(t_i) + ku^0 - f(t_i))\dot{u}(t_i) \\ \frac{\partial E_R}{\partial k} &= 0 = \sum_{i=j-n}^{j+n} (m\ddot{u}(t_i) + c\dot{u}(t_i) + k\hat{u}(t_i) + ku^0 - f(t_i))\hat{u}(t_i) \\ \frac{\partial E_R}{\partial ku^0} &= 0 = \sum_{i=j-n}^{j+n} (m\ddot{u}(t_i) + c\dot{u}(t_i) + k\hat{u}(t_i) + ku^0 - f(t_i)) \end{aligned} \tag{3.4}$$

As a point-by-point tracking method, solved model parameters will be instantaneous parameters. And for the least-square fitting procedure, with fewer data points involved in the section of the observed point, short-time transient events (e.g., impact loading and sudden change of stiffness due to crack propagation) can be pinpointed on the time axis, and level 1 damage detection can be realized. Although the estimated parameter values may not be accurate because the orthogonality between $\dot{u}, \hat{u}$ and 1 cannot be fully enforced for a short time segment, as long as the occurrence of damage shows clearly in the result, it meets the requirement of the level 1 damage detection. On the other hand, if more data points are involved in the section of the observed point, the estimated parameter values can be more accurate but short-time transient events may not be revealed, and the obtained are the averaged parameter values instead of instantaneous ones. Hence, a relative longer section length can be used when applying LSF for system identification as the accuracy of each model parameters are relatively important. And a relative shorter section length can be used when applying LSF for health monitoring or level 1 damage detection as real-time monitoring, and quick feedback is required. Another shortcoming of this LSF is caused by the one-step parameter estimation process. Because the damping value c is much smaller than other parameter values, the estimated damping value is often

inaccurate.

3.2.2 Force Separation Method

A parametric identification method assumes the forms of stiffness and damping functions with unknown parameters to be determined by processing measured signals. Its accuracy is limited by the forms and number of assumed functions. On the other hand, a nonparametric identification method is proposed to find the forms and parameter values of stiffness and damping forces. The force separation method (FSM) is about to identify a single DOF system by the nonparametric way. Then, a linear/nonlinear single-DOF dynamical system can be represented using a mass *m*, a spring force $F_s(u)$, and a damping force $F_d(\dot{u})$ as:

$$m\ddot{u} + F_d(\dot{u}) + F_s(u) = f(t) \tag{3.5}$$

where mass *m* of a dynamical system often remains unchanged even if the system is damaged, and it is also known in actual applications. The spring force is assumed a function of displacement only and the damping force is assumed a function of velocity only, which is the case for most real-world problems.

The first step of FSM is to separate the two force functions. Then, $F_s(u)$ and $F_d(\dot{u})$ can be determined one by one. However, $F_s(u)$ and $F_d(\dot{u})$ are coupled at most times. Separation of these two force functions can be realized only at some specific times. When $\dot{u} = 0$, $F_d(\dot{u}) = 0$, u is at its extreme value and Eq. (3.5) reduces to Eq. (3.6a). One can obtain the estimation of the spring force function as $F_s(u(t))$ at those discrete time instants by Eq. (3.6b).

$$m\ddot{u}(t_i) + F_s(u(t_i)) = f(t_i) \tag{3.6a}$$

$$F_s(u(t_i)) = f(t_i) - m\ddot{u}(t_i)\Big|_{\dot{u}(t_i)=0} \tag{3.6b}$$

where $f(t_i)$ is assumed known by measurement, $u(t_i)$ and $\ddot{u}(t_i)$ can be calculated from the measured $\dot{u}(t_i) = \dot{u}_i$. The identified spring force at discrete time instants can be fit into a polynomial $F_s(u)$ by the least-squares method, as shown in Eq. (3.7).

$$\begin{aligned} & F_s(u) \approx \sum_{k}^{P} d_k u^k \\ & E_R = \sum_{i=1}^{I} \left(F_s(u) - F_s(u(t_i))\Big|_{\dot{u}(t_i)=0} \right)^2 \\ & \frac{\partial E_R}{\partial d_k} = 0 = \sum_{i=1}^{I} \left(F_s(u) - F_s(u(t_i))\Big|_{\dot{u}(t_i)=0} \right) u(t_i)^k \quad k = 0,1,2,3,\cdots,I \end{aligned} \tag{3.7}$$

where *P* is the order of the assumed spring force polynomial and I is the total number of identified time instants with zero velocity. Based on the function shape presented in the $F_s - u$ coordinate, one can start with an initial guess of *P*. *P* can be adjusted to achieve the best fit between the polynomial assumption and the actual spring force function.

After the spring force function is obtained, all data points can be used to determine the damping force function $F_d(\dot{u})$. The best scenario is to use zero displacement data points because this can avoid inaccuracy from the obtained spring force function. However, it is hard to select those data points precisely. In the meantime, zero acceleration points can be recognized when $\dot{u}$ is at its extreme value. With zero acceleration, noise from the computed acceleration signal can be avoided. With this approach, an estimation function of the damping force $F_d(\dot{u})$ can be reduced from Eq. (3.8a) to Eq. (3.8b).

$$F_d(\dot{u}(t_i)) = f(t_i) - F_s(u(t_i)) - m\ddot{u}(t_i) \tag{3.8a}$$

$$F_d(\dot{u}(t_i)) = f(t_i) - F_s(u(t_i))\Big|_{\ddot{u}(t_i)=0} \tag{3.8b}$$

$$F_d'(\dot{u}(t_i)) = f(t_i) - F_s(u(t_i)) - m\ddot{u}(t_i)\Big|_{\ddot{u}(t_i)\approx 0} \tag{3.8c}$$

If identified time instants in Eq. (3.8b) do have zero acceleration value, it would give a more accurate

estimation than Eq. (3.8a). However, a low sampling rate may cause no data points to existing on the velocity peaks, which leads to non-zero accelerations at the located points with the extreme of $\dot{u}$. Moreover, noise from measured velocity may also lead to non-zero accelerations at located points. Thus, the term $m\ddot{u}(t_i)$ needs to be added back to Eq. (3.8b) (as shown in Eq. (3.8c)) to obtain a more accurate damping force in these circumstances. It ends up with the same form as Eq. (3.8a) but only with a different data point set. Meanwhile, Eq.(3.8a) can be used for all data points and provide a complete estimation than Eq. (3.8c) in these situations. However, the data point set from Eq. (3.8c) can still be used for verification of the result from Eq. (3.8a). With the estimation of the damping force, it can be fitted into a polynomial $F_d(\dot{u})$ by the least-squares method as shown in Eq. (3.9).

$$F_d(\dot{u}) \approx \sum_{k=0}^{Q} \bar{d}_k \dot{u}^k \tag{3.9a}$$

$$E_R = \sum_{i=1}^{II} \left(F_d(\dot{u}) - F_d(\dot{u}(t_i))\big|_{\ddot{u}(t_i)=0} \right)^2 \tag{3.9b}$$

$$\frac{\partial E_R}{\partial \bar{d}_k} = 0 = \sum_{i=1}^{II} \left(F_d(\dot{u}) - F_d(\dot{u}(t_i))\big|_{\ddot{u}(t_i)=0} \right) \dot{u}(t_i)^k = 0, \;\; k = 0,1,2,3 \tag{3.9c}$$

where Q is the order of the assumed damping force polynomial and II is the total number of involved time instants. For measured velocity with noise, differentiation would amplify the noise while integration would accumulate the noise. Estimation of $F_s(u)$ is based on acceleration only while the estimation of $F_d(\dot{u})$ is based on displacement, acceleration and the identified $F_s(u)$. In addition, usually the magnitude of $F_s(u)$ is much larger than that of $F_d(\dot{u})$. Thus, estimation of $F_d(\dot{u})$ would contain more errors than the estimation of $F_s(u)$.

Although various forms of the force function make the FSM better capture existing nonlinearities in the system, it has its own limitation. Notice to well capture a force function, data points need to fall in a wide

range to build a detailed shape of the function. Since only local extrema of displacement are used for separating the spring and damping forces at the first step. Thus, the FSM requires that dynamic data have a wide range of its extrema values. For systems under transient vibration, dynamic data exhibit many different variations in amplitude, and local extrema of displacement would have a wide range. However, when it comes to systems under a steady state vibration that vibrates at a constant amplitude, local extrema of displacement would be constant throughout the time. In this case, there would not be enough points in the $F_s - u$ coordinate to capture the nonlinearity of the spring force function. Therefore, the FSM cannot ensure an accurate identification based on signals of steady-state vibration.

And since FSM requires a relative longer data length to compute the spring/damping force function, the determined spring/damping force is the property of used data length. In other words, the FSM is a section-by-section method. Instead of real-time monitoring, only periodic inspection can be applied with the FSM and the change of system properties may not be revealed timely. Moreover, a short time transient event may not show much difference in the determined spring/damping force that the sensitivity of the FSM to the occurrence of damage is relative low. Meanwhile, the steady state vibration is the common working status for most structures, the application of FSM for level 1 damage detection is limited. Since it does not suit the requirement of level 1 damage detection, it will not be compared in the later numerical analysis.

3.3 Indirect Time-Domain Methods

An indirect time-domain methods process time-domain data (e.g., time-varying frequencies and amplitudes) derived from the displacements measured or computed from the measured velocities to extract a parametric

or nonparametric system model. Eq. (3.1) can be rewritten as:

$$\ddot{u} + 2\zeta\omega\dot{u} + \omega^2 u = \frac{f}{m},\ \omega \equiv \sqrt{\frac{k}{m}},\ \zeta \equiv \frac{c}{2\omega m},\ \omega_d \equiv \omega\sqrt{1-\zeta^2} \tag{3.10}$$

If $f = F_0 \cos\Omega t$, the response $u(t)$ consists a transient part and a steady-state part as:

$$u(t) = Ae^{-\zeta\omega t}\cos(\omega_d t - \theta) + A_0 \cos(\Omega t - \phi) \tag{3.11}$$

Eq. (3.11) shows that the decaying rate of the transient amplitude $Ae^{-\zeta\omega t}$ is directly related to the damping ratio ζ and the undamped natural frequency ω. And the actual, damped natural frequency ω_d of $\cos(\omega_d t - \theta)$ is directly related to ω. If the time-varying values of $\zeta\omega$ and ω_d are separately extracted from $Ae^{-\zeta\omega t}$ and $\cos(\omega_d t - \theta)$, and m is known, ω and ζ and then k and c can be accurately estimated using Eq. (3.10). If m is unknown, it can be determined from the known F_0 and the amplitude A_0 extracted from the steady-state part as:

$$m = \frac{F_0}{A_0\omega^2\sqrt{(1-\Omega^2/\omega^2)^2 + (2\zeta\Omega/\omega)^2}} \tag{3.12}$$

Hence, how to extract the time-varying frequency and amplitude of a displacement response is the key for an indirect time-domain method for system identification. And it is necessary to have a transient part and a steady-state part in order to identify all system parameter values. Because instead of ζ, the vibration amplitude A is directly computed from the given vibration signal, and the ζ is determined based on the changing amplitude from the transient part. On the contract, for level 1 damage detection, realizing the real-time monitoring of one of the model parameters is enough for detecting the occurrence of damage. Therefore, either transient part or steady state part can be enough for level 1 damage detection. Here we present a conjugate-pair decomposition (CPD) method and compare it with the Hilbert-Huang transform (HHT), which

was recently patented by NASA for time-frequency analysis of nonlinear nonstationary signals.

3.3.1 Hilbert-Huang Transform

Hilbert-Huang transform (HHT) combines empirical mode decomposition (EMD) and Hilbert spectral analysis for signal decomposition of a nonlinear and/or nonstationary signal and time-frequency analysis of the decomposed component [42]. EMD, as introduced before, is a data-driven signal decomposition technique that sequentially extracts zero-mean regular/distorted harmonics from a signal, starting from high- to low-frequency components, and it is the first step of HHT [42]. During the sifting process of EMD, a signal $u(t)$ is decomposed into *n* intrinsic mode functions (IMFs) $c_i(t)$ and a residual r_n as [42]:

$$u(t) = \sum_{i=1}^{n} c_i(t) + r_n(t) \tag{3.13}$$

The intrinsic mode functions are usually physically meaningful because their characteristic time scales are physical. In order to extract the first IMF c_1 out of the original signal, extrema of $u(t)$ are first recognized and then all local minima are connected using a cubic spline, and all local maxima are connected using another cubic spline. After the two cubic splines are obtained, their average m_{11} is subtracted from the signal, and the residual is treated as the first estimation of c_1. Treat the residual signal as a new signal and repeat the same process for *K* times until $m_{1K} \approx 0$. Then, the residual is taken as c_1, i.e.,

$$c_1 = u - m_{11} \cdots - m_{1K} \tag{3.14}$$

Note that c_1 is the signal's component that has the shortest characteristic time scale and the highest frequency. Because $m_{11} + \cdots + m_{1K}$ actually represents the signal's low-frequency moving average, the process of identifying extrema explains why IMFs are extracted from high- to low-frequency components.

To obtain a meaningful instantaneous frequency, the extracted IMF must be symmetric with respect to the local zero mean and has the same number of zero crossings and extrema [42]. So the sifting process should eliminate all low-frequency components and make the amplitude envelopes symmetric, that is, $m_{1K} \approx 0$. There is also a numerical way to decide if the sifting process should be ended. A deviation D_v is defined as:

$$\begin{aligned} &D_v \equiv \sqrt{\sum_{i=1}^{N} [c_{1k}(t_i) - c_{1k-1}(t_i)]^2 \Big/ \sum_{i=1}^{N} c_{1k-1}^2(t_i)} \\ &t_i = (i-1)\Delta t,\ T = N\Delta t,\ c_{1k} = u - m_{11} \cdots - m_{1k} \end{aligned} \tag{3.15}$$

where T is the sampled period and N is the total number of samples. One can set a small number to be a limit and stop the sifting process when D_v is smaller than the limit. Or, a maximum number of iterations can be set for stopping the sifting. After the first IMF (c_1) has been obtained, one can treat the residual r_1 $(\equiv u - c_1)$ as the new data and repeat the steps shown in Eq. (3.15) to obtain other $c_i (i = 2, \ldots, n)$ as shown in Eq. (3.16). The whole sifting process can be stopped when the residual $r_n (= r_{n-1} - c_n)$ becomes a monotonic function from which no more IMF can be extracted [42].

$$c_i = r_{i-1} - m_{i1} \cdots - m_{iK},\ \ r_{i-1} \equiv u(t) - c_1 \cdots - c_{i-1} \tag{3.16}$$

For example, the $\dot{w}(t)$ in Fig. 3.1 is the velocity of a point on a vibrating cantilevered beam experimentally measured by a laser vibrometer, where the initial statically deformed beam geometry is close to the beam's third mode shape. The first three natural frequencies of the cantilevered beam are calculated and experimentally verified to be 3.91Hz, 24.22Hz and 67.81 Hz. The measured $\dot{u}(t)$ contains at least the first three modes' vibrations. To have accurate extraction of an individual IMF, an assumed harmonic with the IMF's frequency is added to the signal, then the added harmonic and the IMF are extracted as one IMF, and then subtracting the added harmonic from the extracted IMF yields the actual IMF. The amplitude and

frequency of the added harmonic to extract each of the three IMFs in Fig. 3.1b-d are [0.4m/s, 67.81Hz], [0.8m/s, 24.22Hz], and [0.8m/s, 3.91Hz], respectively. As the way EMD works, the extracted first IMF (c_1) has the highest frequency, and it contains the third mode and other minor higher-frequency modes. Moreover, c_2 and c_3 are the second and first modes, respectively, and r_3 is the residual.

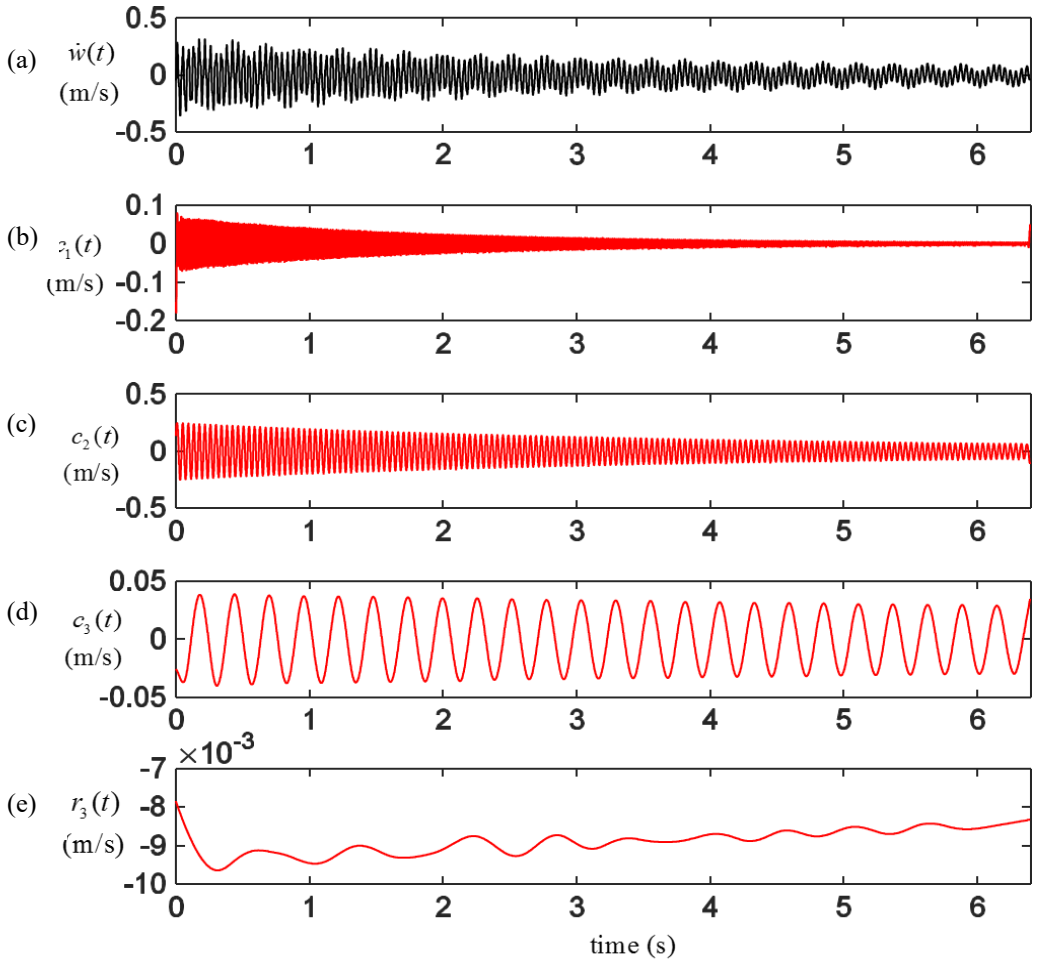

Fig. 3.1 EMD decomposition of a free vibration signal of a cantilevered beam: (a) the measured velocity of a point on the beam, (b) the extracted first IMF, (c) the extracted second IMF, (d) the extracted third IMF, and (e) the residual.

The second step of HHT is to perform Hilbert transform (HT) and compute the time-varying frequency ω_i and amplitude A_i of each c_i [42]. Because the second step is applied to each component separately, one can consider each $c_i(t)$ as a new signal $x(t)$. The HT of $x(t)$ is defined by an integral transform [48]:

$$H[x(t)] = y(t) = \pi^{-1} \int_{-\infty}^{\infty} \frac{x(\tau)}{t-\tau} d\tau \tag{3.17}$$

After $y(t)$ is obtained, $z(t)$ can be defined based on $x(t)$ and $y(t)$ as

$$\begin{aligned} z(t) &\equiv x(t) + jy(t) = a(t)e^{j\varphi(t)} \\ a(t) &= \sqrt{x^2(t) + y^2(t)},\ \varphi(t) = \tan^{-1}\frac{y(t)}{x(t)} \end{aligned} \tag{3.18}$$

where $j = \sqrt{-1}$, $\varphi(t)$ is the instantaneous phase of $x(t)$, and $a(t)$ is the instantaneous amplitude of $x(t)$, which can reflect how the energy of the $x(t)$ varies with time. The controversial instantaneous frequency $\omega(t)$ is defined as the time derivative of the instantaneous phase $\varphi(t)$ [48, 49] as shown in Eq. (3.19). And once the time-varying frequency and amplitude of each IMF are computed, the system's stiffness and damping values can be estimated, and the system's health can be evaluated based on these system parameters.

$$\omega(t) = \frac{d\varphi(t)}{dt} = \frac{y'(t)x(t) - y(t)x'(t)}{x^2(t) + y^2(t)} \tag{3.19}$$

Several shortcomings of HHT have been revealed in the literature [36, 42, 48, 49]. The accuracy of locating local extrema in EMD is affected by the sampling rate. A low sampling rate causes a high-frequency IMF being represented by a small number of data points, and then the located local extrema may deviate from the actual extrema. Moreover, measurement noise can also decrease the accuracy of EMD, and two located adjacent extrema may even jump over several periods. Such inaccurate identification of local extrema will lead to inaccurate upper and lower envelopes, and it may end up with misinterpretation. In other words, HHT is more appropriate for processing signals sampled at a high sampling rate.

The criterion ($m_{1K} \approx 0$) for stopping sifting is also problematic. A meaningful instantaneous frequency can be obtained if the IMF's envelopes are symmetric with respect to a local zero means, but m_{1K} can never

be zero under a finite number of iterations. This leaves errors in the extracted IMFs. Considering the way that EMD extracts IMFs from high to low frequencies, the extracted first IMF may include other high-frequency components and noise. Hence, the first IMF may not be a monocomponent which leads to inaccurate identification.

Hilbert transform can extract accurate time-varying frequencies and amplitudes only for monocomponent signals. And instantaneous frequency from HT analysis of a signal consisting multiple components is meaningless. Hence, EMD becomes an essential tool for pre-processing a structural vibration signal which usually contains several modal vibrations. Because the period of a low-frequency IMF is long and EMD requires several extreme points to extract an IMF, it makes HHT needs to process a long data length in order to extract a low-frequency IMF. Thus, HHT is a section-by-section method that cannot realize a real-time monitoring, but only a periodic inspection and change of system properties may not be identified timely.

Another major shortcoming of HHT is that it seriously suffers from the edge effect. The edge effect, or the Gibbs phenomenon, is caused by Fourier transform and the signal's sampled length being not an integer multiple of the period of each component contained in the signal [48]. Because HT is often and most accurately computed by using discrete Fourier transform for obtaining $y(t)$, the accuracy of HHT seriously suffers from the edge effect introduced by HT. Smooth extension of the signal on both data ends to make $x(0) = x(T)$ or even $\dot{x}(0) = \dot{x}(T)$ is one way of reducing the edge effect, but it can be done only on a case-by-case basis, and it will increase the data length to be processed. Next, we introduce a conjugate-pair decomposition method that requires only a short data length and a low sampling rate and is capable of online tracking.

3.3.2 Conjugate-Pair Decomposition

Conjugate-pair decomposition (CPD) is a three-point method for tracking pointwise instantaneous frequency and amplitude of an arbitrary signal [36]. It sets an assumed form for a signal $u(t)$ as:

$$u(t) = C_0 + e_1 \cos(\omega_1 t) - f_1 \sin(\omega_1 t) \tag{3.20}$$

The assumed form contains three parts. C_0 is a constant to capture the moving average, $e_1 \cos(\omega_1 t)$ captures the central solution without the moving average and $f_1 \sin(\omega_1 t)$ is the Hilbert transform of $e_1 \cos(\omega_1 t)$. To capture the moving average's slope and the signal's discontinuity, one can add an additional term $D_0 \sinh(\omega t)$ to the function. Here ω_1 is assumed to be known. One can get the initial guess of ω_1 by other methods, such as the Teager-Kaiser algorithm(TKA) [50] or short-time Fourier transform.

Use original 4-point TKA as an example. To calculate the pointwise instantaneous frequency (pIF) and pointwise instantaneous amplitude (pIA) of a signal $u(t)$, we assume it to be locally harmonic and hence [36]:

$$\begin{aligned} u &= a\cos\omega t, \qquad \dot{u} = -\omega a \sin\omega t \\ \ddot{u} &= -\omega^2 a\cos\omega t, \dddot{u} = \omega^3 a \sin\omega t \end{aligned} \tag{3.21}$$

Two energy-type functions $\psi(u)$ and $\psi(\dot{u})$ can be derived from Eq. (3.21) as [36]:

$$\psi(u) = \dot{u}^2 - u\ddot{u} = \omega^2 a^2, \psi(\dot{u}) = \ddot{u}^2 - \dot{u}\dddot{u} = \omega^4 a^2 \tag{3.22}$$

Then instantaneous frequency and amplitude can be calculated from:

$$\omega = \sqrt{\psi(\dot{u})/\psi(u)}, a = \psi(u)/\sqrt{\psi(\dot{u})} \tag{3.23}$$

Using finite difference to approximate $\dot{u}$ and $\ddot{u}$ by u, $\psi(u)$ in Eq. (3.22) can be derived to be:

$$
\begin{aligned}
&(\Delta t)^2 \psi(u(t_i)) \\
&= \big(u(t_i) - u(t_{i-1})\big)\big(u(t_{i+1}) - u(t_i)\big) - u(t_i)\big(u(t_{i+1}) - 2u(t_i) + u(t_{i-1})\big) \\
&= u(t_i)^2 - u(t_{i-1})u(t_{i+1}) = a^2 \sin^2(\omega \Delta t)
\end{aligned}
\tag{3.24a}
$$

Replace all u with $\dot{u}$; we can get $(\Delta t)^2 \psi(\dot{u}(t_i)) = \dot{u}(t_i)^2 - \dot{u}(t_{i11})\dot{u}(t_{i+1})$. Using finite difference again to substitute $\dot{u}$ by u, $\psi(\dot{u})$ can be derived to be:

$$
\begin{aligned}
(\Delta t)^4 \psi(\dot{u}(t_i)) &= \big(u(t_i) - u(t_{i-1})\big)^2 - \big(u(t_{i-1}) - u(t_{i-2})\big)\big(u(t_{i+1}) - u(t_i)\big) \\
&= 2a^2 \sin^2(\omega \Delta t)\big[1 - \cos(\omega \Delta t)\big]
\end{aligned}
\tag{3.24b}
$$

Then, instantaneous frequency in finite difference form would be:

$$
\begin{aligned}
\omega &= \frac{1}{\Delta t} \cos^{-1}\left(1 - \frac{(\Delta t)^4 \psi(\dot{u}(t_i))}{2(\Delta t)^2 \psi(u(t_i))}\right) \\
&= \frac{1}{\Delta t} \cos^{-1}\left(1 - \frac{\big(u(t_i) - u(t_{i-1})\big)^2 - \big(u(t_{i-1}) - u(t_{i-2})\big)\big(u(t_{i+1}) - u(t_i)\big)}{2\big(u(t_i)^2 - u(t_{i-1})u(t_{i+1})\big)}\right)
\end{aligned}
\tag{3.25}
$$

where two points from each side of $u(t_i)$ are involved. Thus, the instantaneous frequency of the third point would be computed by Eq. (3.25) as an initial guess for CPD method.

With known frequency ω, C_0, e_1 and f_1 are the three unknowns in Eq. (3.20) need to be determined. Three data points will be enough to set up three algebraic equations for their solutions, and it is the major merit of CPD. After C_0, e_1 and f_1 are determined, amplitude (a) and phase angle (ϕ) of the signal can be determined, and the assumed function can be expressed as:

$$
\begin{aligned}
&a = \sqrt{e_1^2 + f_1^2}, \ \phi = \tan^{-1}\frac{f_1}{e_1}, \ \omega = \frac{d\phi}{dt} \\
&u(t) = C_0 + a\cos(\omega t + \phi)
\end{aligned}
\tag{3.26}
$$

Notice CPD method is a section-by-section method, result a_1 and ω_1 present the situation for the whole section involved in the calculation rather than only the central point. However, the required section length is relatively short as in the LSF; it can be used for real-time monitoring. When the most recent three

data points are used in CPD, the method can predict the following state and enable online tracking. As in the LSF, with more data points used in estimation, the estimated parameter values will be more accurate, but the results will be less sensitive to short-time transient events because the value has been averaged over the section. Only other hand, if only three points are used in sectional estimation since they only cover a short time segment, a_1 and ω_1 can be considered as the instantaneous amplitude and frequency of the central point of the three points. These instantaneous parameter values would be sensitive to short-time transient events and can be used to detect damage-induced transient events. For a nonlinear signal, its amplitude and frequency change with time, and this method can well capture their time-varying values. To well capture the signal's behavior, the time length of three points should cover at least one fourth of the signal's period T [36]. For a signal sampled at a high sampling rate, the data length of $3\Delta t$ may not be longer than $T/4$. Besides of using more successional points, one can also use skipped data points (e.g., t_i, t_{i+3} and t_{i+6}) to increase the data length to cover at least $T/4$. The other way is to use more successional data points to cover at least $T/4$.

To compute amplitude and frequency of certain section, one can pick up the central point t_j as a flag of the section. And response function of the section can be transformed by trigonometric functions to be a function of shifted time $\tilde{t}_i = t_i - t_j$:

$$\begin{aligned} u_j(\tilde{t}) &= C_0 + C_1\cos(\omega\tilde{t}) - D_1\sin(\omega\tilde{t}) \\ C_1 &= a_1\cos(\omega t_j + \phi),\ D_1 = a_1\sin(\omega t_j + \phi) \end{aligned} \tag{3.27}$$

where i ranges from $j-(m-1)/2$ to $j+(m-1)/2$ with $m(\geq 3)$ being the total odd number of data points in the processed section. C_0, C_1 and D_1 can be estimated by least-squares fitting to minimize the

error between the assumed function $u_j(\tilde{t})$ and the actual data u_i using the following equations:

$$\begin{aligned} E_R &\equiv \sum_{i=j-(m-1)/2}^{j+(m-1)/2} \left(u_i - u_j(\tilde{t}_i)\right)^2 \\ \frac{\partial E_R}{\partial C_0} &= 0 = \sum_{i=j-(m-1)/2}^{j+(m-1)/2} \left(u_i - u_j(\tilde{t}_i)\right)\cdot 1 \\ \frac{\partial E_R}{\partial C_1} &= 0 = \sum_{i=j-(m-1)/2}^{j+(m-1)/2} \left(u_i - u_j(\tilde{t}_i)\right)\cdot \cos(\omega_1 \tilde{t}_i) \\ \frac{\partial E_R}{\partial D_1} &= 0 = \sum_{i=j-(m-1)/2}^{j+(m-1)/2} \left(u_i - u_j(\tilde{t}_i)\right)\cdot \sin(\omega_1 \tilde{t}_i) \end{aligned} \tag{3.28}$$

The time-varying amplitude and phase can be estimated using:

$$\tilde{a} = \sqrt{C_1^2 + D_1^2}, \quad \tilde{\theta} = \omega t_n + \phi = \tan^{-1}(D_1 / C_1) \tag{3.29}$$

Except for the first section, one can use the frequency of the last section as an initial guess of the next section, and the frequency of next section will be updated by the finite difference of the phase changes of the two successional sections. If t_j is the central point of the second section, the frequency of the second section ω_2 can be updated by:

$$\omega_2' \approx \frac{\theta(t_j) - \theta(t_j - p\Delta t)}{p\Delta t} \tag{3.30}$$

where $\theta(t_j)$ is phase angle of the second section at the central point, $\theta(t_j - p\Delta t)$ is phase angle of the first section at a central point and ω_2' is the updated frequency. $p\Delta t$ is the length of time between two central points. The backward finite difference is used to average the frequency over $p\Delta t$ in order to reduce the influence of noise in frequency tracking [36]. The frequency updating eliminates the error introduced by the initial guess of the first section's frequency. One way to improve the estimated instantaneous frequency is to use the SG filter on the phase angle of each section to obtain the frequency as its first derivative.

With an appropriate sampling rate, CPD uses only three points to determine a signal's instantaneous

frequency and amplitude, and it is capable of online tracking when only data points from the past are used in Eq. (3.28). However, CPD is more appropriate for treating monocomponent signals. For a signal contains p (>1) independent components, one can assume that:

$$u(\tilde{t}) = C_0 + \sum_{i=1}^{p} \left(C_i \cos \omega_i \tilde{t} - D_i \sin \omega_i \tilde{t} \right) \tag{3.31}$$

Then similar derivations can be obtained by following the same procedure. However, more components in a signal would require more data points and hence a longer window length for least-squares curve fitting to estimate more unknowns. Then the obtained frequency is more an average over the window length, instead of an instantaneous frequency. Moreover, it becomes more difficult to enforce the orthogonality between the many $\cos \bar{\omega}_i t$ and $\sin \bar{\omega}_i t$ functions in order to obtain unique solutions for C_i and D_i. On the other hand, one can use EMD to decompose the signal into *p* IMFs, and then use CPD to perform accurate time-frequency analysis on each IMF. Since EMD often introduces the end effect into each IMF, one can assume the form in Eq. (3.27) for each IMF and then C_0 would capture the end effect as a moving average. Note that an IMF from EMD analysis should have no moving average (i.e., $C_0 = 0$) at points away from the two data ends. Because EMD needs to process the whole data length, this approach will make CPD inappropriate for online tracking of multicomponent signals.

3.4 Health Monitoring and Level I Damage Detection

As discussed in section 3.1, level 1 damage detection is about detecting the occurrence of damage in the early stage and can be understood as the real-time health monitoring. To simulate the working state of a structure, the linear system from Eq. (2.30) is considered. Dynamical data is generated with a length of the 30s and the

occurrence of damage is simulated as a 2% drop in natural frequency at $t = 15s$, then the governing equation has changed to:

$$2\ddot{u} + 0.9852\dot{u} + 75.8301u = 50\sin(2\pi t) \tag{3.32}$$

Accurate displacement and velocity signal can be obtained from Runge-Kutta integration, and acceleration signal can be obtained by governing equation from Eq. (2.30) and Eq. (3.32). Fig. 3.2 gives all three accurate dynamic signals. The occurrence of simulated damage results in a noticeable change in dynamic signal for this case, especially for acceleration signal. Notice for most case, although the change of system parameters alters its dynamic behavior, it may not be noticeable from the amplitude of dynamic signals.

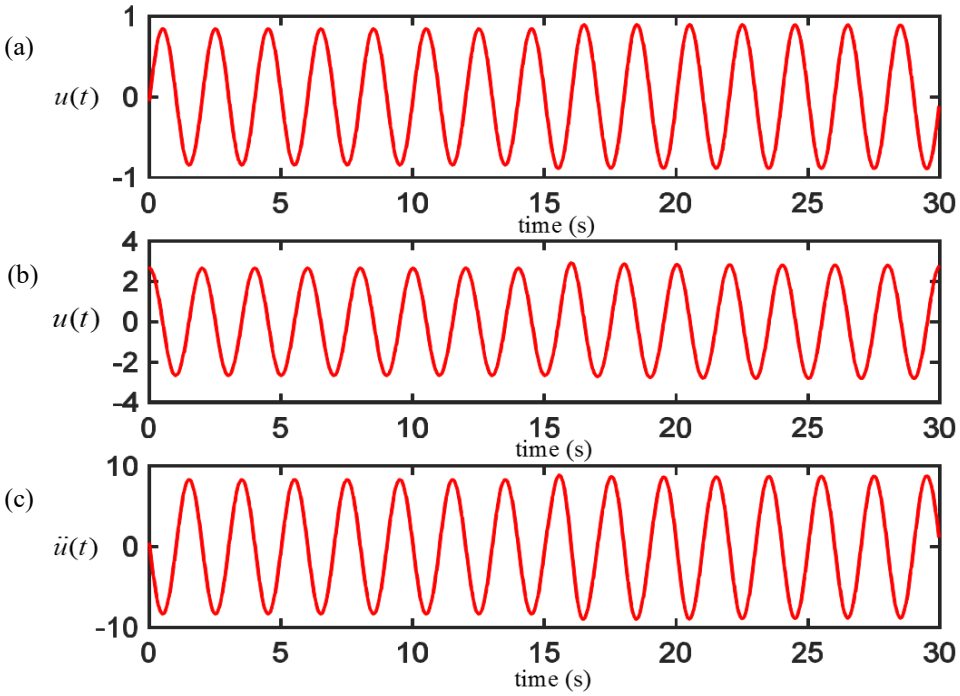

Fig. 3.2 Dynamic signals of a system with the occurrence of damage: (a) accurate displacement signal, (b) accurate velocity signal and (c) accurate acceleration signal.

To simulate the real situation, noise defined in Eq. (2.18) has been added to the velocity signal as the

black curve in Fig. 3.3a. The SG integration method and the SG filter method will be used for computing the displacement and acceleration signal. And as discussed in section 2.2.4, although the step of noise filtering with $n_R \neq 0$ will cause a short delay in real-time monitoring, the accuracy of computed displacement and acceleration can be improved. Therefore, the extra step of noise filtering with $n_L = 6, n_R = 6$ and $M = 3$ is performed to get the filtered velocity as the red dash curve in Fig. 3.3a. Then, the displacement and acceleration signal can be computed with the same n_L, n_R and M as the green curve in Fig. 3.3b and the blue curve in Fig. 3.3c, respectively. The corresponding relative errors based on Eq. (2.16) are given in Fig. 3.3d with the same color notation. Based on the shape of the corresponding errors, one can see the major component of the computed displacement signal is from the accumulated noise and the noise existed in velocity signal has been amplified through the differentiation calculation.

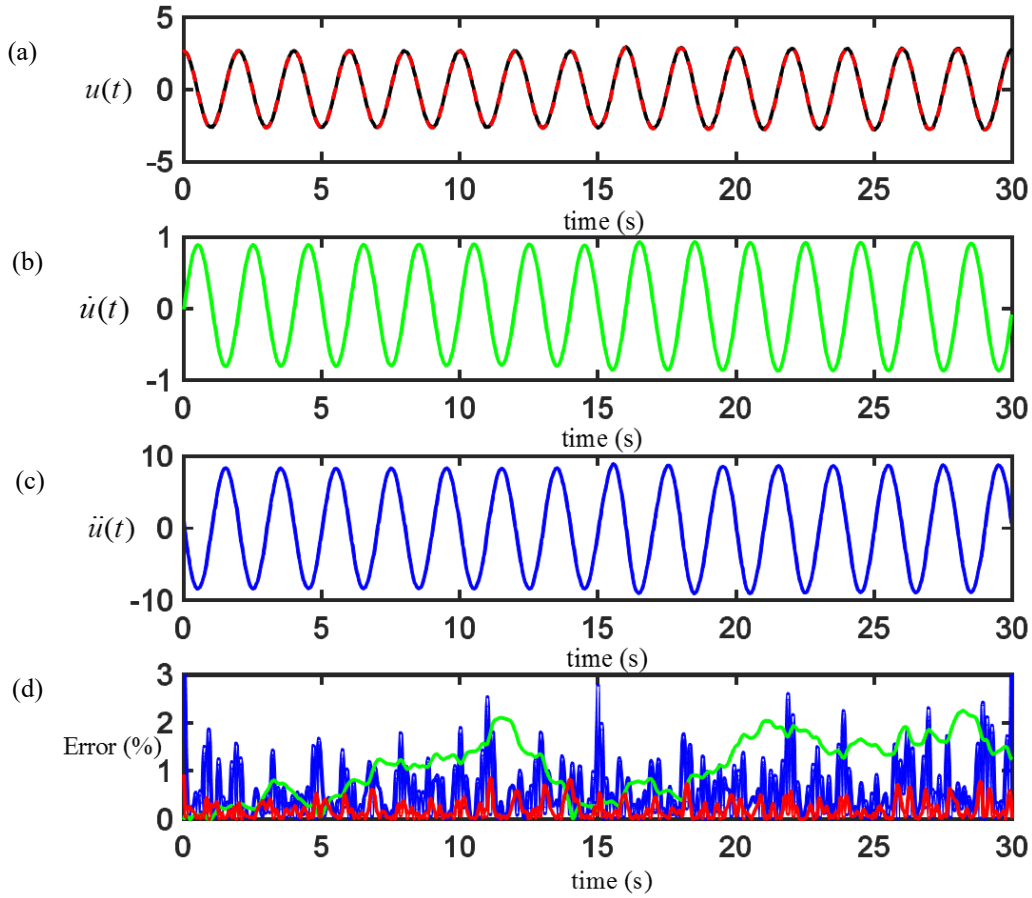

Fig. 3.3 Dynamic signals of the system with the occurrence of damage: (a) Velocity signal with added noise and filtered velocity signal, (b) computed displacement signal, (c) computed acceleration signal and (d) corresponding errors of Figs. 3.3a-c.

3.4.1 Direct Time-Domain Monitoring

As discussed in section 3.2, the FSM is better for nonlinear identification but not health monitoring; only the LFM will be performed and discussed. Since 6 data points after the observed data point have been used in the previous displacement/acceleration computation, at most 6 data points after the observed data point can be used to avoid extra delay of real-time monitoring. On the contract, a number of data points used from the

past are about balance the accuracy of computed model parameters and accuracy of identified time instant. And the definition from Eq. (3.2) of observed time instant t_j can adjust to:

$$E_R \equiv \sum_{i=j-n_L}^{j+n_R} \left[m\ddot{u}(t_i) + c\dot{u}(t_i) + ku(t_i) - f(t_i) \right]^2 \tag{3.33}$$

where n_L represents a number of data points used from the past and n_R represents the number of data points used from after t_j and it is better to control $n_R \leq 6$. With $n_L = 18$ and $n_R = 6$ used in Eq. (3.33), the damping coefficient and stiffness for each time instant through the time trace can be determined as the red curve in Fig. 3.4a and the blue curve in Fig. 3.4b, respectively. The black lines in both figures represent the accurate damping coefficient and stiffness, respectively. The corresponding relative error of computed model parameters is given in Fig. 3.4c with the same color notation.

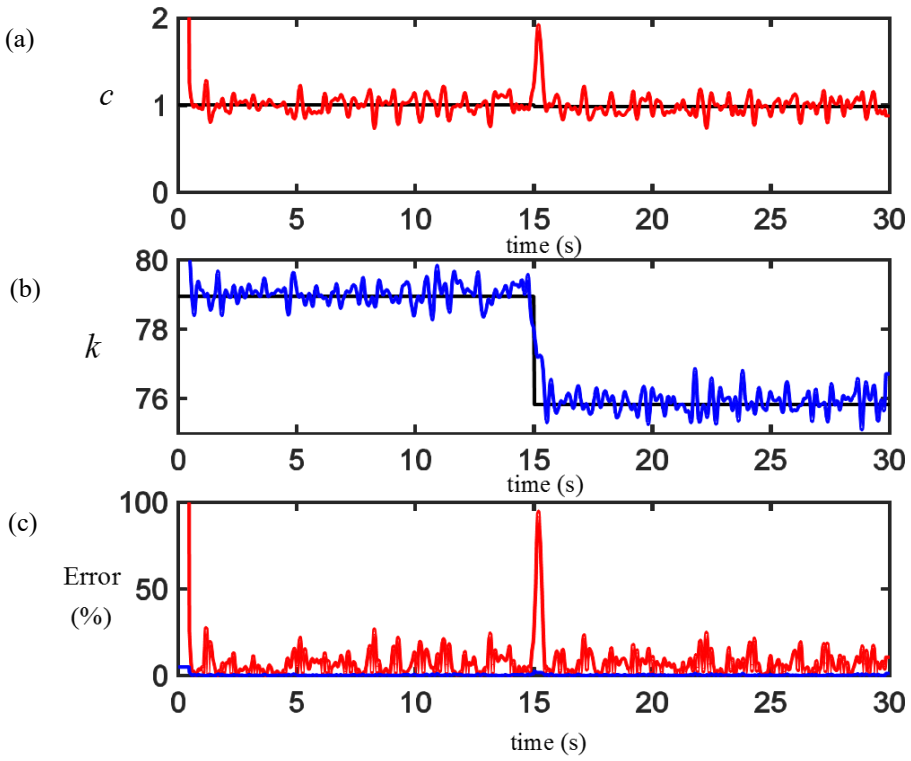

Fig. 3.4 Results of a least-square fitting method based on data in Figs. 3.3a-c: (a) result damping coefficient, (b) result stiffness and (c) corresponding error of Figs. 3.4a&3.4b.

Through LSF, the occurrence of damage simulated by the sudden drop of natural frequency shows clearly as a peak in Fig. 3.4a and as a drop of stiffness in Fig. 3.4b around the time instant $t = 15s$. Since the damping coefficient is calculated by one step inverse calculation with the relative large parameter as stiffness, the error of result damping coefficient is relatively large. And with only 2% drop in natural frequency, the absolute change in damping coefficient is relatively small. Therefore, the difference of damping coefficient before and after the occurrence of damage does not show clearly. However, the existed peak can be used as a good indicator of the occurrence of damage. Meanwhile, with relative large magnitude, the error of computed stiffness is relatively small, and the corresponding drop in stiffness before and after damage shows clearly in Fig. 3.4b. The relative big error existed in both computed parameters at the beginning is caused by inadequate data points from the past for the first few observed data points. Considering the actual measuring noise can be larger, the stiffness with the larger magnitude and smaller error can be used as a good indicator for health monitoring and level 1 damage detection. The computed damping coefficient can be used as an extra reference when measuring noise is relatively small.

3.4.2 Indirect Time-Domain Monitoring

For indirect time domain methods, the identified model parameters are the amplitude and frequency of the given vibration signal. And since changes in structural, physical properties from damage will alter the dynamic response behavior of the structure, the occurrence of damage can be identified by the change of identified vibrating frequency or amplitude. With the same vibrating frequency and similar amplitude behavior existed among all three dynamical signals, the velocity signal as directly measured can have a better

identification without the extra step of the numerical computation. However, the existed noise from measurement can influence the accuracy of identified frequency and amplitude, the filtered velocity as the red curve in Fig. 3.3a will be used for health monitoring.

For the two indirect time domain methods reviewed in previous sections, the HHT method with the first step of the EMD can only give periodic inspection, and the CPD can realize pseudo real-time monitoring with relative short delay. Here the entire length of the sampled velocity signal is used as sampling length for the HHT. And have data points in Eq. (3.28) to cover quarter length as suggest, 10 data points from each side are used for the CPD. Figure 3.5a gives the identified amplitude from the HHT and CPD in the red and blue curve, respectively. And Fig. 3.5b gives the identified frequency of the filtered velocity signal with the same color notation.

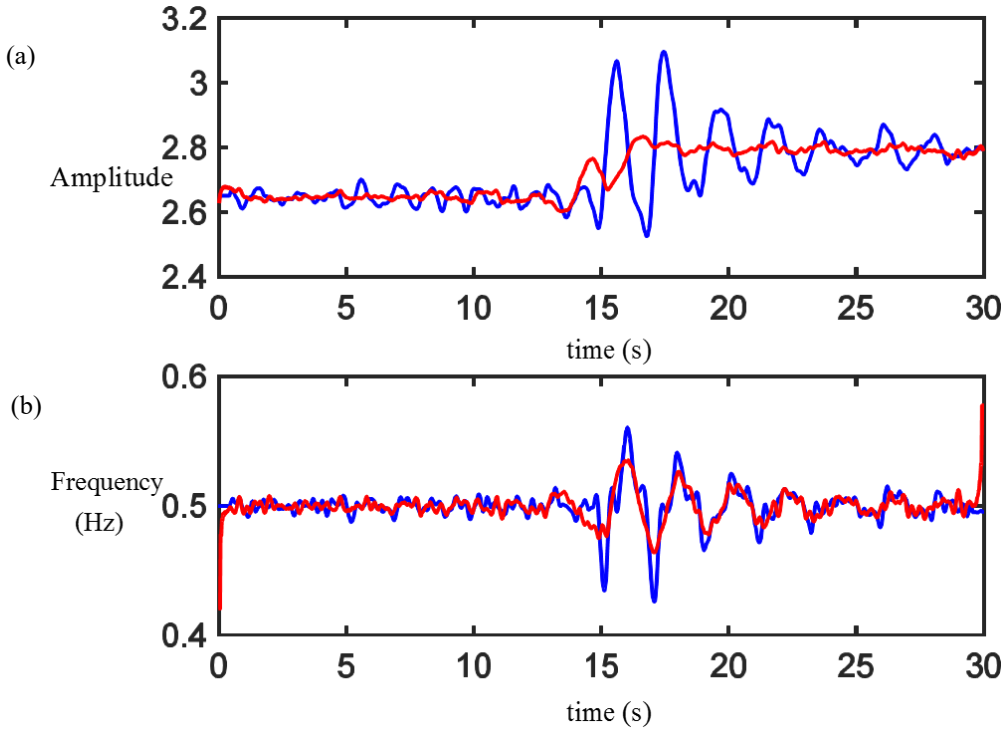

Fig. 3.5 Results of the HHT and CPD based on filtered velocity signal in Fig. 3.3a: (a) identified amplitude and (b) identified frequency.

With the occurrence of damage, the steady state has been a break and a short time transient vibration existed. Correspondingly, the stable identified amplitude and frequency will have disturbances after the occurrence of damage as shown in Fig. 3.5. Although the identified amplitude from the CPD has larger disturbance before and after $t = 15s$ compare to HHT, the local transient event caused by the damage occurrence is also more clearly than in HHT. Therefore, it can be used as a clear indicate of the exaggerated damage. Moreover, with shorter section length in CPD comparing to the length of periodic inspection in HHT, the time instant of the damage occurrence shows more clearly in results from the CPD than HHT. And with extra the edge effect exists in the results of the HHT and the inefficiency caused by periodic inspection, the CPD is the better option for these two methods for health monitoring and level 1 damage detection.

Therefore, parametric identification methods are better than nonparametric identification methods for health monitoring and level 1 damage detection because it can give certain parameter as the indicator. And while section-by-section system identification method can only carry periodic inspection, point-by-point system identification method can give a feedback timely. And among the discussed methods, the LSF and CPD are better for health monitoring and level 1 damage detection.

Chapter 4 NUMERICAL MODEL FOR LEVEL II DAMAGE DETECTION

4.1 Introduction

An early damage detection and remediation is necessary and economy to structure. For example, one of the most important requirements for the proper maintenance of machinery or civil infrastructure systems is the detection of crack-like damage at the early stages of growth [51]. While level 1 damage detection methods can be used to identify the occurrence of damage at an early stage, damage localization (level 2 damage detection) and quantification (level 3 damage detection) are required for damage remediation. Depend on the accuracy of geometric location of damage one want to obtain, dynamic data of more points with certain gridding can be measured from the structure. Thus, the corresponding numerical model of the structure needs to be modified as a continuous system. The finite element model as the most common numerical model of continuous systems will be used as the basic model for further discussion. As the majority of civil and mechanical structure and their main components can be simplified as a beam or plate [10], the beam structure is used as the example in both numerical simulation and experimental validation. And the most basic finite element model of beam structure based on the Euler-Bernoulli theory will be reviewed.

To test and verify damage inspection and health monitoring algorithms before applying them to actual structures, numerical simulation using high-fidelity mathematical models are useful and important for understanding the capabilities of algorithms without expensive and time-consuming physical experiments [52]. Therefore, a numerical model of the damaged structure is necessary. It can be used to predict the

vibration behavior of the damaged structure without the influence from measuring noise. And based on data with/without simulated noise, the accuracy and noise tolerance of newly developed damage detection methods can be verified, respectively.

Usually, the damage will decrease mass and stiffness of the structure and increase damping ratio locally [6]. Reduction in stiffness is associated with a decrease in the natural frequencies and modification of the modes of the structures [53]. As cracks create new surfaces, the damping ratio will increase when damage progresses in the structure [54]. Available conclusions like these have been used for developing a simplified numerical model for the damaged structure. There are a number of approaches to the modeling of cracks in beam structures in the literature, that fall into three main categories; local stiffness reduction, discrete spring models, and complex models in two or three dimensions [55]. An example from each category will be given, and the advantage of disadvantage of each model will be discussed.

4.2 Numerical Model of the Intact Beam

For actual structures in real cases, it is hard to monitor the health of the entire structure by just a few sensors. Instead, most structure or their major components can be monitored part by part as in a simpler shape as beam or plate. Moreover, identifying a specific damage in a beam/plate provides an important benchmark for effectiveness and accuracy of identification techniques [10]. Here the beam structure is used as our prototype for numerical model and experimental validation. Although the beam structure in finite element method has usually been simplified as a one-dimensional (1D) model, it meets the requirement of damage localization (level 2 damage detection). And the identification of damage location in the longitude direction will be the

aim of the level 2 damage detection. Then, detailed analysis of the severity (the depth and the width) of the damage can be carried out by the level 3 damage detection on the identified beam section with less cost. With simplification as a 1D model, fewer measurements are required as only grid of a row is needed in damage localization. It will save not only computation time but also the costs in later experimental validation. Thus, considering the operability and efficiency of locating a damage, the basic 1D beam structure is considered in its numerical model.

Considering a beam structure as shown in Fig. 4.1, the length of the beam structure is L, and dimension of the cross section is $b \times h$.

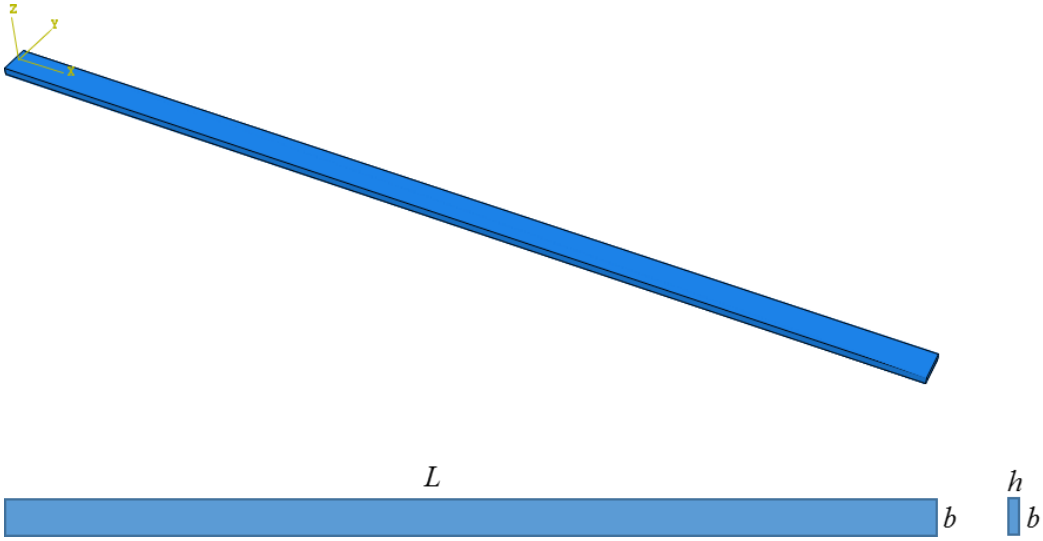

Fig. 4.1 An intact beam structure.

And here are a few assumptions have been applied to the beam structure:

1. The beam is loaded only in the z direction.

2. Deflections of the beam are small in comparison to the characteristic dimensions (L) of the beam.

3. The material of the beam is linearly elastic, isotropic, and homogeneous.

4. The beam is prismatic, and the cross section has an axis of symmetry in the plane of bending.

With these assumptions, the Euler-Bernoulli beam theory can be used to build up the beam's finite element model. It gives 2 degree-of-freedom (DOF) at each node: nodal deflection in the z direction as w and angle of rotation (also known as the angle of slope and angle of inclination) of midline on the node as θ. Grid the beam structure equidistantly into n_E elements; there are $n_N\,(=n_E+1)$ nodes existed. The length of each element can be determined as $l = L/n_E$ and Fig. 4.2 gives a simplified drawing of the beam structure to show the relationship between gridded nodes, elements and the DOF of each element.

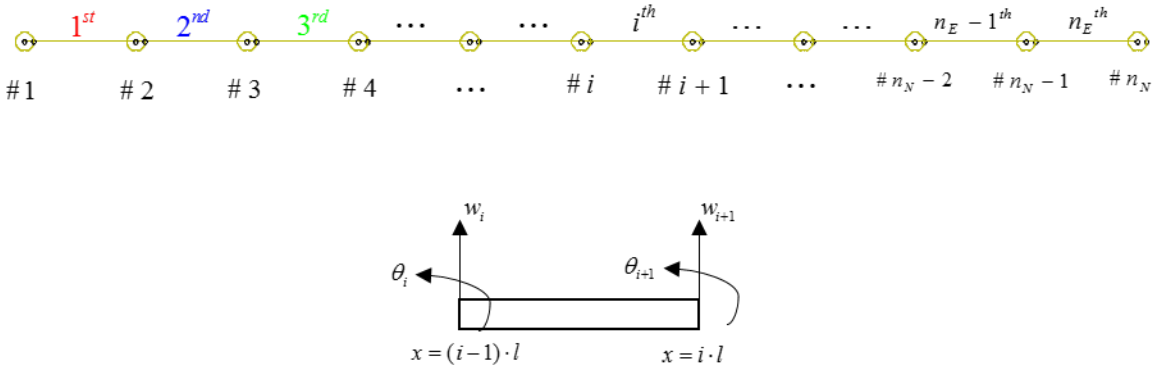

Fig. 4.2 Finite element model of the beam structure from Fig. 4.1.

With 2 DOF at each node, the beam structure can be considered as a linear dynamic system of $n\,(=2n_N)$ DOF governed by:

$$[M][\ddot{D}]+[C][\dot{D}]+[K][D]=[F] \tag{4.1}$$

where $[M],[K]$ and $[C]$ is system's global mass, stiffness, and damping matrix, $[\ddot{D}],[\dot{D}]$ and $[D]$ is a vector of acceleration, velocity and displacement of all DOF and $[F]$ is the forcing vector. While $[M]$ and $[K]$ can be directly assembled by the elemental mass and stiffness matrix as $[m^{(i)}]$ and $[k^{(i)}]$, $[C]$ needs to

be computed from $[M]$ and $[K]$ with the definition of proportional damping or modal damping. Use the i^{th} element as an example; it has 2 nodes as $\#i$ and $\#i+1$ with 4 DOF as w_i, w_{i+1}, θ_i and θ_{i+1}. Since deflection w is much smaller than the length of the beam L in the previous assumption, the angle of rotation θ is relatively small and can be approximated as:

$$\theta \approx \tan\theta = \frac{dw}{dx} \tag{4.2}$$

Then, the shape function of this element can be expressed as a 3rd-order polynomial:

$$w(x,t) = c_0 + c_1 x + c_2 x^2 + c_3 x^3 \tag{4.3}$$

And the angle of rotation can be calculated as:

$$\theta(x,t) = c_1 + 2c_2 x + 3c_3 x^2 \tag{4.4}$$

where the counterclockwise direction of rotation is defined as the positive direction. Then, coefficients c_i can be solved by the four boundary conditions:

$$\begin{bmatrix} w(l(i-1),t) = w_i \\ w'(l(i-1),t) = \theta_i \\ w(li,t) = w_{i+1} \\ w'(li,t) = \theta_{i+1} \end{bmatrix} = \begin{bmatrix} 1 & l(i-1) & l^2(i-1)^2 & l^3(i-1)^3 \\ 0 & 1 & 2l(i-1) & 3l^2(i-1)^2 \\ 1 & li & l^2i^2 & l^3i^3 \\ 0 & 1 & 2li & 3l^2i^2 \end{bmatrix} \begin{bmatrix} c_0 \\ c_1 \\ c_2 \\ c_3 \end{bmatrix}$$
$$\Rightarrow \begin{bmatrix} c_0 \\ c_1 \\ c_2 \\ c_3 \end{bmatrix} = \begin{bmatrix} 1 & l(i-1) & l^2(i-1)^2 & l^3(i-1)^3 \\ 0 & 1 & 2l(i-1) & 3l^2(i-1)^2 \\ 1 & li & l^2i^2 & l^3i^3 \\ 0 & 1 & 2li & 3l^2i^2 \end{bmatrix}^{-1} \begin{bmatrix} w_i \\ \theta_i \\ w_{i+1} \\ \theta_{i+1} \end{bmatrix} \tag{4.5}$$

Shape function can be re-expressed as interpolation function $[N]$ times elemental displacement vector $[d_p]$ as:

$$
\begin{aligned}
w(x,t) &= \begin{bmatrix} 1 & x & x^2 & x^3 \end{bmatrix} \begin{bmatrix} 1 & l(i-1) & l^2(i-1)^2 & l^3(i-1)^3 \\ 0 & 1 & 2l(i-1) & 3l^2(i-1)^2 \\ 1 & li & l^2 i^2 & l^3 i^3 \\ 0 & 1 & 2li & 3l^2 i^2 \end{bmatrix}^{-1} \begin{bmatrix} w_i \\ \theta_i \\ w_{i+1} \\ \theta_{i+1} \end{bmatrix} \\
&= \begin{bmatrix} N \end{bmatrix}^T \begin{bmatrix} d_p \end{bmatrix} = \begin{bmatrix} d_p \end{bmatrix}^T \begin{bmatrix} N \end{bmatrix}
\end{aligned} \tag{4.6}
$$

And the elemental mass and stiffness matrix can be obtained by Rayleigh-Ritz method as [56]:

$$
\begin{aligned}
\begin{bmatrix} m^{(i)} \end{bmatrix} &= \int_{l(i-1)}^{li} \begin{bmatrix} N \end{bmatrix} m \begin{bmatrix} N \end{bmatrix}^T dx = \frac{ml}{420} \begin{bmatrix} 156 & 22l & 54 & -13l \\ 22l & 4l^2 & 13l & -3l^2 \\ 54 & 13l & 156 & -22l \\ -13l & -3l^2 & -22l & 4l^2 \end{bmatrix} \\
\begin{bmatrix} k^{(i)} \end{bmatrix} &= \int_{l(i-1)}^{li} \begin{bmatrix} N'' \end{bmatrix} EI \begin{bmatrix} N'' \end{bmatrix}^T dx = \frac{EI}{l^3} \begin{bmatrix} 12 & 6l & -12 & 6l \\ 6l & 4l^2 & -6l & 2l^2 \\ -12 & -6l & 12 & -6l \\ 6l & 2l^2 & -6l & 4l^2 \end{bmatrix}
\end{aligned} \tag{4.7}
$$

where m is mass per unit length, E is Young's modulus, I is the moment of inertia and EI is known as flexural rigidity. Then, the global mass and stiffness matrix can be assembled by the geometry relationship between each element as shown in Eq. (4.8).

$$
\begin{bmatrix} M \end{bmatrix} = \begin{bmatrix}
m_{11}^{(1)} & m_{12}^{(1)} & m_{13}^{(1)} & m_{14}^{(1)} & 0 & 0 & 0 & 0 & \cdots \\
m_{21}^{(1)} & m_{22}^{(1)} & m_{23}^{(1)} & m_{24}^{(1)} & 0 & 0 & 0 & 0 & \cdots \\
m_{31}^{(1)} & m_{32}^{(1)} & m_{33}^{(1)} + m_{11}^{(2)} & m_{34}^{(1)} + m_{12}^{(2)} & m_{13}^{(2)} & m_{14}^{(2)} & 0 & 0 & \cdots \\
m_{41}^{(1)} & m_{42}^{(1)} & m_{43}^{(1)} + m_{21}^{(2)} & m_{44}^{(1)} + m_{22}^{(2)} & m_{23}^{(2)} & m_{24}^{(2)} & 0 & 0 & \cdots \\
0 & 0 & m_{31}^{(2)} & m_{32}^{(2)} & m_{33}^{(2)} + m_{11}^{(3)} & m_{34}^{(2)} + m_{12}^{(3)} & m_{13}^{(3)} & m_{14}^{(3)} & \cdots \\
0 & 0 & m_{41}^{(2)} & m_{42}^{(2)} & m_{43}^{(2)} + m_{21}^{(3)} & m_{44}^{(2)} + m_{22}^{(3)} & m_{23}^{(3)} & m_{24}^{(3)} & \cdots \\
0 & 0 & 0 & 0 & m_{31}^{(3)} & m_{32}^{(3)} & m_{33}^{(3)} + m_{11}^{(4)} & m_{34}^{(3)} + m_{12}^{(4)} & \cdots \\
0 & 0 & 0 & 0 & m_{41}^{(3)} & m_{42}^{(3)} & m_{43}^{(3)} + m_{21}^{(4)} & m_{44}^{(3)} + m_{22}^{(4)} & \cdots \\
\vdots & \vdots & \vdots & \vdots & \vdots & \vdots & \vdots & \vdots & \ddots
\end{bmatrix} \tag{4.8a}
$$

$$
\begin{bmatrix} K \end{bmatrix} = \begin{bmatrix}
k_{11}^{(1)} & k_{12}^{(1)} & k_{13}^{(1)} & k_{14}^{(1)} & 0 & 0 & 0 & 0 & \cdots \\
k_{21}^{(1)} & k_{22}^{(1)} & k_{23}^{(1)} & k_{24}^{(1)} & 0 & 0 & 0 & 0 & \cdots \\
k_{31}^{(1)} & k_{32}^{(1)} & k_{33}^{(1)} + k_{11}^{(2)} & k_{34}^{(1)} + k_{12}^{(2)} & k_{13}^{(2)} & k_{14}^{(2)} & 0 & 0 & \cdots \\
k_{41}^{(1)} & k_{42}^{(1)} & k_{43}^{(1)} + k_{21}^{(2)} & k_{44}^{(1)} + k_{22}^{(2)} & k_{23}^{(2)} & k_{24}^{(2)} & 0 & 0 & \cdots \\
0 & 0 & k_{31}^{(2)} & k_{32}^{(2)} & k_{33}^{(2)} + k_{11}^{(3)} & k_{34}^{(2)} + k_{12}^{(3)} & k_{13}^{(3)} & k_{14}^{(3)} & \cdots \\
0 & 0 & k_{41}^{(2)} & k_{42}^{(2)} & k_{43}^{(2)} + k_{21}^{(3)} & k_{44}^{(2)} + k_{22}^{(3)} & k_{23}^{(3)} & k_{24}^{(3)} & \cdots \\
0 & 0 & 0 & 0 & k_{31}^{(3)} & k_{32}^{(3)} & k_{33}^{(3)} + k_{11}^{(4)} & k_{34}^{(3)} + k_{12}^{(4)} & \cdots \\
0 & 0 & 0 & 0 & k_{41}^{(3)} & k_{42}^{(3)} & k_{43}^{(3)} + k_{21}^{(4)} & k_{44}^{(3)} + k_{22}^{(4)} & \cdots \\
\vdots & \vdots & \vdots & \vdots & \vdots & \vdots & \vdots & \vdots & \ddots
\end{bmatrix} \tag{4.8b}
$$

To compute the $[C]$ based on Rayleigh damping, the eigenproblem of $[M]$ and $[K]$ can be solved as follows:

$$\left([K]-\omega_i^2[M]\right)[\phi]_i=[0] \tag{4.9}$$

where $[\phi]_i$ (i.e., eigenvectors) is the mode shape of n independent linear normal modes. Then, modal matrix $[\Phi]$ can be constructed with mode shapes $[\phi]_i$ as in Eq. (4.10).

$$[\Phi]=\left[[\phi]_1 \quad \cdots \quad [\phi]_n\right] \tag{4.10}$$

Since system's any free/forced vibration is always a linear combination of these n modal vibrations as [57], the displacement, velocity, and acceleration vectors can be expressed by the modal matrix as:

$$\begin{aligned} &[D]=[\Phi][\eta], \quad [\eta]=\begin{bmatrix}\eta_1(t)\\ \vdots \\ \eta_n(t)\end{bmatrix} \\ &\left[\dot{D}\right]=[\Phi][\dot{\eta}], \quad \left[\ddot{D}\right]=[\Phi][\ddot{\eta}] \end{aligned} \tag{4.11}$$

where $\eta_i(t)$ are the modal coordinates. Replacing the displacement, velocity and acceleration vectors in Eq. (4.1), and time the governing equation with $[\Phi]^T$ as in Eq. (4.12a), the n coupled governing equations can be decoupled into n independent second-order ordinary differential equations(ODEs) as in Eq. (4.12b).

$$[\Phi]^T[M][\Phi][\ddot{\eta}]+[\Phi]^T[C][\Phi][\dot{\eta}]+[\Phi]^T[K][\Phi][\eta]=[\Phi]^T[F] \tag{4.12a}$$

$$\ddot{\eta}+2\zeta_i\omega_i\dot{\eta}_i+\omega_i^2\eta_i=[\phi]_i^T[F], \quad i=1,2,...,n \tag{4.12b}$$

where ζ_i denotes the damping factor for the i^{th} mode. That is because, based on theory from Rayleigh [58], if $[\Phi]$ is mass normalized, linear normal modes $[\phi]_i$ satisfy an orthogonality relationship over $[M]$ and $[K]$ (given by Eq. (4.13)) and then the equations of motion can be decoupled.

$$[\Phi]^T[M][\Phi]=[I],\ [\Phi]^T[K][\Phi]=\begin{bmatrix}\omega_1^2 & & 0\\ & \ddots & \\ 0 & & \omega_n^2\end{bmatrix} \tag{4.13}$$

Based on Eq. (4.12), the $[\Phi]^T[C][\Phi]$ can be determined as in Eq. (4.14) with unknown ζ_i.

$$[\Phi]^T[C][\Phi]=\begin{bmatrix}2\zeta_1\omega_1 & & 0\\ & \ddots & \\ 0 & & 2\zeta_n\omega_n\end{bmatrix} \tag{4.14}$$

On the other hand, the Rayleigh damping (the proportional damping model) expresses the damping matrix as a linear combination of the mass and stiffness matrices as [59]:

$$[C]=\alpha[M]+\beta[K] \tag{4.15}$$

where α and β are selected constants (with appropriate physical dimensions). Then, the modal damping factors in Eq. (4.12b) can be solved as [59]:

$$\begin{bmatrix}2\zeta_1\omega_1 & & 0\\ & \ddots & \\ 0 & & 2\zeta_n\omega_n\end{bmatrix}=\begin{bmatrix}\alpha\omega_1^2+\beta & & 0\\ & \ddots & \\ 0 & & \alpha\omega_n^2+\beta\end{bmatrix} \tag{4.16}$$

$$\zeta_i=\frac{\alpha\omega_i}{2}+\frac{\beta}{2\omega_i}$$

And the $[C]$ can be solved as:

$$[C]=\left([\Phi]^T\right)^{-1}\begin{bmatrix}\alpha\omega_1^2+\beta & & 0\\ & \ddots & \\ 0 & & \alpha\omega_n^2+\beta\end{bmatrix}[\Phi]^{-1} \tag{4.17}$$

With $[M],[K]$ and $[C]$ determined, the finite element model of the beam structure can be used to generate dynamic responses based on different applied force and boundary conditions.

4.3 Numerical Model of Damage

In order to keep the assumptions used in the previous section, a transverse crack with a uniform depth

$h_1 = \alpha h$ through the width of the beam is considered here as shown in Fig. 4.3. The width of the crack is d_1 and located at $x = L_1$ from the left end.

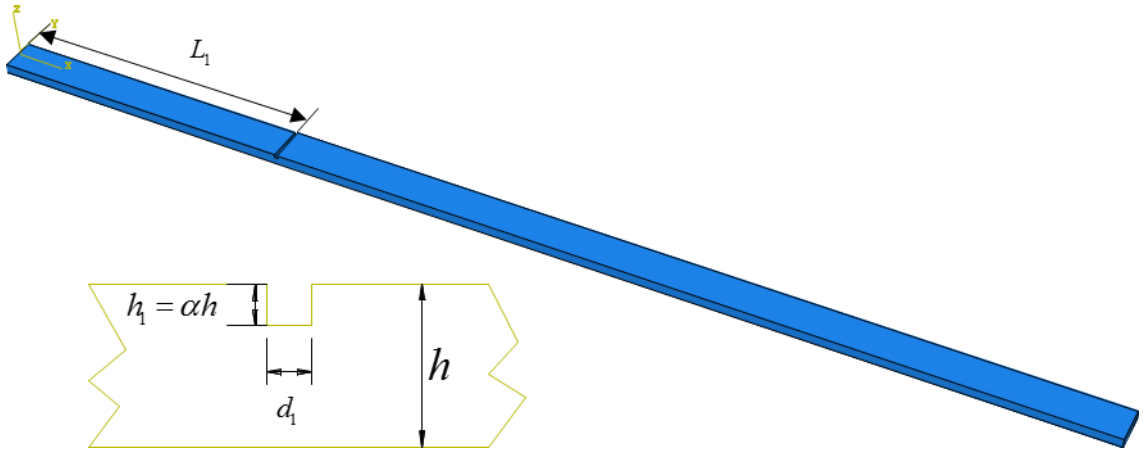

Fig. 4.3 Beam structure with a transverse crack.

4.3.1 Local Stiffness Reduction

The simplest method to simulate the existed damaged beam structure in finite element model is by reducing the stiffness locally [55]. For example, the elemental stiffness matrix of the element with the transverse crack can be simulated as:

$$[k'] = \frac{\alpha_k EI}{l^3}\begin{bmatrix} 12 & 6l & -12 & 6l \\ 6l & 4l^2 & -6l & 2l^2 \\ -12 & -6l & 12 & -6l \\ 6l & 2l^2 & -6l & 4l^2 \end{bmatrix} \tag{4.18}$$

where α_k is the factor describing the influences from damage to stiffness and $[k']$ can be assembled into $[K]$ as other elemental matrixes. For a small crack, the influence of mass can be neglected. Thus, $[M]$ stay the same as a healthy beam structure. Corresponding damping matrix can be computed through the same procedure as before but based on a different $[K]$. And the dynamical responses of a damaged beam structure

can be generated based on Eq. (4.1) with the new $[K]$ and $[C]$. However, the major problem of this kind simulation is that the damage severity cannot be directly matched to the crack depth [55] that the physical meaning of α_k and d_1 are not directly related. And the accuracy of the numerical model is affected by the mesh density. For a relatively small transverse crack, it will only influence the properties within a relatively small range. However, based on Eq. (4.18), the influenced range can only be an integrate multiple of element length. Therefore, with a loose mesh, a relatively small transverse crack cannot be simulated appropriately. Moreover, with the constant α_k, the nonlinear behavior such as the crack is under pressure/tension during the vibration cannot be reflected.

4.3.2 Discrete Spring Model

The second class of methods divides a beam type structure into two parts that are pinned at the crack location, and the crack is simulated by the addition of a rotational spring [55]. An example presents the transverse crack based on a massless rotational spring, and spectral element method has been studied [60]. At the damage location, j^{th} element, previous beam element will be replaced by a new element as shown in Fig. 4.4.

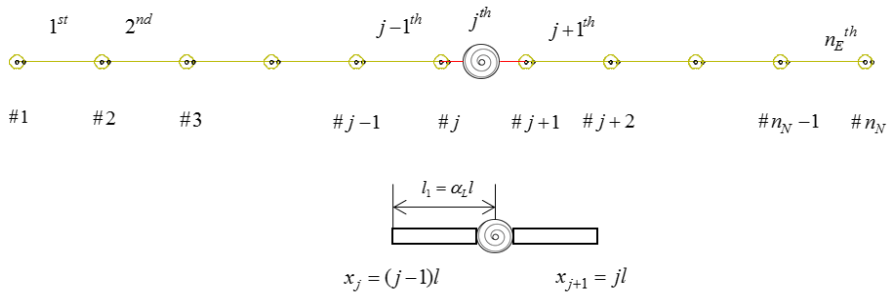

Fig. 4.4 Numerical modal of the damaged beam structure simulated by rotational spring.

where $l_1=\alpha_L l$ .The element in Fig. 4.4 has the same number of nodes and DOF as before. The equivalent spring stiffness for open crack is given by [61]:

$$K = \frac{EI}{6\pi h(1-\nu^2) f(\alpha)} \tag{4.19a}$$

$$\begin{aligned} f(\alpha) = {} & 0.6272\alpha^2 - 1.04533\alpha^3 + 4.5948\alpha^4 - 9.973\alpha^5 + 20.2948\alpha^6 \\ & - 33.0351\alpha^7 + 47.1063\alpha^8 - 40.7556\alpha^9 + 19.6\alpha^{10} \end{aligned} \tag{4.19b}$$

where ν is the Poisson ratio.

For spectral element modeling, the elemental displacements have the following form for the left and right parts of the beam [60]:

$$\begin{aligned} u_1 &= a_1 \sin kx + a_2 \cos kx + a_3 \sinh kx + a_4 \cosh kx \\ u_2 &= a_5 \sin kx + a_6 \cos kx + a_7 \sinh kx + a_8 \cosh kx \end{aligned} \tag{4.20}$$

where $k = \sqrt[4]{\omega^2 m / EI}$ is the wavenumber. And $a_i, (i = 1, 2, \ldots, 8)$ is the coefficients of the element given by boundary conditions as follows:

$$\text{At} \quad x = x_j : \; u_1(x_j) = w_j, \frac{\partial u_1(x_j)}{\partial x} = -\theta_j \tag{4.21}$$

$$\text{At} \quad x = x_j + l_1 = x_d : \begin{array}{l} u_1(x_d) = u_2(x_d), \; K\left(\dfrac{\partial u_2(x_d)}{\partial x} - \dfrac{\partial u_1(x_d)}{\partial x} \right) = EI \dfrac{\partial^2 u_1(x_d)}{\partial x^2} \\ \dfrac{\partial^2 u_1(x_d)}{\partial x^2} = \dfrac{\partial^2 u_2(x_d)}{\partial x^2}, \; \dfrac{\partial^3 u_1(x_d)}{\partial x^3} = \dfrac{\partial^3 u_2(x_d)}{\partial x^3} \end{array} \tag{4.22}$$

$$\text{At} \quad x = x_{j+1} : \; u_2(x_{j+1}) = w_{j+1}, \frac{\partial u_2(x_{j+1})}{\partial x} = -\theta_{j+1} \tag{4.23}$$

It can be written in matrix form as:

$$
\begin{bmatrix} w_j & \theta_j & 0 & 0 & 0 & 0 & w_{j+1} & \theta_{j+1} \end{bmatrix}^T
$$

$$
= \begin{bmatrix}
0 & 1 & 0 & 1 \\
k & 0 & k & 0 \\
\sin kl_1 & \cos kl_1 & \sinh kl_1 & \cosh kl_1 \\
Kk\cos kl_1 - EIk^2 \sin kl_1 & -Kk\sin kl_1 - EIk^2 \cos kl_1 & Kk\cosh kl_1 + EIk^2 \sinh kl_1 & Kk\sinh kl_1 + EIk^2 \cosh kl_1 \\
-k^2 \sin kl_1 & -k^2 \cos kl_1 & k^2 \sinh kl_1 & k^2 \cosh kl_1 \\
-k^3 \cos kl_1 & k^3 \sin kl_1 & k^3 \cosh kl_1 & k^3 \sinh kl_1 \\
0 & 0 & 0 & 0 \\
0 & 0 & 0 & 0
\end{bmatrix}
$$

$$
\begin{bmatrix}
0 & 0 & 0 & 0 \\
0 & 0 & 0 & 0 \\
-\sin kl_1 & -\cos kl_1 & -\sinh kl_1 & -\cosh kl_1 \\
-Kk\cos kl_1 & Kk\sin kl_1 & -Kk\cosh kl_1 & -Kk\sinh kl_1 \\
k^2 \sin kl_1 & k^2 \cos kl_1 & -k^2 \sinh kl_1 & -k^2 \cosh kl_1 \\
k^3 \cos kl_1 & -k^3 \sin kl_1 & -k^3 \cosh kl_1 & -k^3 \sinh kl_1 \\
\sin kl_e & \cos kl_e & \sinh kl_e & \cosh kl_e \\
k\cos kl_e & -k\sin kl_e & k\cosh kl_e & k\sinh kl_e
\end{bmatrix}
\begin{bmatrix} a_1 \\ a_2 \\ a_3 \\ a_4 \\ a_5 \\ a_6 \\ a_7 \\ a_8 \end{bmatrix}
\tag{4.24}
$$

which can be simplified as:

$$
\begin{bmatrix} d_p \end{bmatrix} = \begin{bmatrix} P \end{bmatrix} \cdot \begin{bmatrix} a \end{bmatrix} \tag{4.25}
$$

where $\begin{bmatrix} d_p \end{bmatrix}$ is the displacement vector of all DOFs of the spectral element and $\begin{bmatrix} a \end{bmatrix}$ is the vector of coefficients. Then, the coefficients can be solved as:

$$
\begin{bmatrix} a \end{bmatrix} = \begin{bmatrix} P \end{bmatrix}^{-1} \cdot \begin{bmatrix} d_p \end{bmatrix} \tag{4.26}
$$

On the other hand, nodal forces of the spectral element can be expressed in matrix form as:

$$
\begin{bmatrix} F_1 \\ F_2 \\ F_3 \\ F_4 \end{bmatrix} = EI \begin{bmatrix}
-k^3 & 0 & k^3 & 0 & 0 & 0 & 0 & 0 \\
0 & k^2 & 0 & -k^2 & 0 & 0 & 0 & 0 \\
0 & 0 & 0 & 0 & k^3 \cos kl_e & -k^3 \sin kl_e & -k^3 \cosh kl_e & -k^3 \sinh kl_e \\
0 & 0 & 0 & 0 & -k^2 \sin kl_e & -k^2 \cos kl_e & k^2 \sinh kl_e & k^2 \cosh kl_e
\end{bmatrix}
\begin{bmatrix} a_1 \\ a_2 \\ a_3 \\ a_4 \\ a_5 \\ a_6 \\ a_7 \\ a_8 \end{bmatrix}
\tag{4.27}
$$

which can be simplified as:

$$[F]=[Q]\cdot[a] \tag{4.28}$$

Substitute Eq. (4.26) into Eq. (4.28), one can get the relationship between nodal forces and nodal displacements as:

$$[F]=[Q]\cdot[P]^{-1}\cdot\left[d_p\right]=[z]\cdot\left[d_p\right] \tag{4.29}$$

where $[z]$ is the dynamic stiffness matrix of the spectral element with a crack. Since from the 3rd term to 6th term in $\left[d_p\right]$ are all zeros, right-hand side of Eq. (4.29) can be simplified as:

$$R.H.S.=\begin{bmatrix} z_{11} & z_{12} & z_{17} & z_{18} \\ z_{21} & z_{22} & z_{27} & z_{28} \\ z_{31} & z_{32} & z_{37} & z_{38} \\ z_{41} & z_{42} & z_{47} & z_{48} \end{bmatrix}\begin{bmatrix} w_j \\ \theta_j \\ w_{j+1} \\ \theta_{j+1} \end{bmatrix} \tag{4.30}$$

It can be assembled into the global stiffness matrix as other elemental stiffness matrix and the compatibility of the elemental stiffness matrix is satisfied by constraining each element displacement to match the displacement at the nodes [60]. Then, the stiffness matrix of the beam with crack would change into:

$$[K]=\begin{bmatrix} \ddots & \vdots & \vdots & \vdots & \vdots & \vdots & \vdots & \vdots & \vdots & \iddots \\ \cdots & k_{33}^{(j-2)}+k_{11}^{(j-1)} & k_{34}^{(j-2)}+k_{12}^{(j-1)} & k_{13}^{(j-1)} & k_{14}^{(j-1)} & 0 & 0 & 0 & 0 & \cdots \\ \cdots & k_{43}^{(j-2)}+k_{21}^{(j-1)} & k_{44}^{(j-2)}+k_{22}^{(j-1)} & k_{23}^{(j-1)} & k_{24}^{(j-1)} & 0 & 0 & 0 & 0 & \cdots \\ \cdots & k_{31}^{(j-1)} & k_{32}^{(j-1)} & k_{33}^{(j-1)}+z_{11} & k_{34}^{(j-1)}+z_{12} & z_{17} & z_{18} & 0 & 0 & \cdots \\ \cdots & k_{41}^{(j-1)} & k_{42}^{(j-1)} & k_{43}^{(j-1)}+z_{21} & k_{44}^{(j-1)}+z_{22} & z_{27} & z_{28} & 0 & 0 & \cdots \\ \cdots & 0 & 0 & z_{31} & z_{32} & z_{37}+k_{11}^{(j+1)} & z_{38}+k_{12}^{(j+1)} & k_{13}^{(j+1)} & k_{14}^{(j+1)} & \cdots \\ \cdots & 0 & 0 & z_{41} & z_{42} & z_{47}+k_{21}^{(j+1)} & z_{48}+k_{22}^{(j+1)} & k_{23}^{(j+1)} & k_{24}^{(j+1)} & \cdots \\ \cdots & 0 & 0 & 0 & 0 & k_{31}^{(j+1)} & k_{32}^{(j+1)} & k_{33}^{(j+1)}+k_{11}^{(j+2)} & k_{34}^{(j+1)}+k_{12}^{(j+2)} & \cdots \\ \cdots & 0 & 0 & 0 & 0 & k_{41}^{(j+1)} & k_{42}^{(j+1)} & k_{43}^{(j+1)}+k_{21}^{(j+2)} & k_{44}^{(j+1)}+k_{22}^{(j+2)} & \cdots \\ \iddots & \vdots & \vdots & \vdots & \vdots & \vdots & \vdots & \vdots & \vdots & \ddots \end{bmatrix} \tag{4.31}$$

Then, the dynamic behavior of the damaged beam structure can be generated based on the governing equation from Eq. (4.1). It is an efficient method for estimation both the depth and location of the transverse crack in

beams [60]. However, crack size and location is not involved directly. Moreover, the presence of the transverse crack can introduce a local flexibility that the crack will open and close in time depending on the loading conditions and vibration amplitude [62]. Thus, the spring constant will not remain the same as in this simplified numerical model. A few research has been done to find a better substitution for rotational spring to keep the one-dimensional continuum assumption. Ambartsumyan and Khachatryan [63] developed a different-moduli theory of elasticity, Lenkov and Tolokonnikov [64] studied the axisymmetric strains in materials with different moduli which can be used for presenting a breathing crack. Chondros, Dimarogonasa, and Yao [62] used a bi-linear spring to present the breathing crack. And Ibrahim, Ismail and Martin [65] presented a bond graph technique that models the crack as a torsional spring with two spring constants. However, the accuracy of using spring to present the existed damage cannot be ensured, and those problems can still exist. Alternatively, two or three-dimensional (3D) finite element model can be used for the damaged beam structure [55].

4.3.3 Finite Element Model from ABAQUS

Meshless approaches may also be used to reduce the computational cost of a conventional 2D/3D model in finite element analysis (FEA). But they are more suited to crack propagation studies, and the computational cost of these meshless methods generally exceeds that of conventional FEA [55]. Since 3D approaches produce detailed and accurate models, the behavior of breathing crack can be simulated by the 3D model. And geometry properties of crack would also be involved directly. Computer program ABAQUS can be used to create a 3D model of the beam structure with the transverse crack by using solid 3D elements as shown in

Fig. 4.5. A finer mesh can be used for a better accuracy. However, it has its shortcoming as the 3D solid element from ABAQUS only gives 3 DOF at each node as nodal deflection along x, y, and z-axis. When it comes to damage detection methods require the rotational angle θ, it needs to be computed based on the nodal deflection w. Extra computation error can be introduced into the computed data points especially when it comes to a relatively loose mesh or curvature based methods.

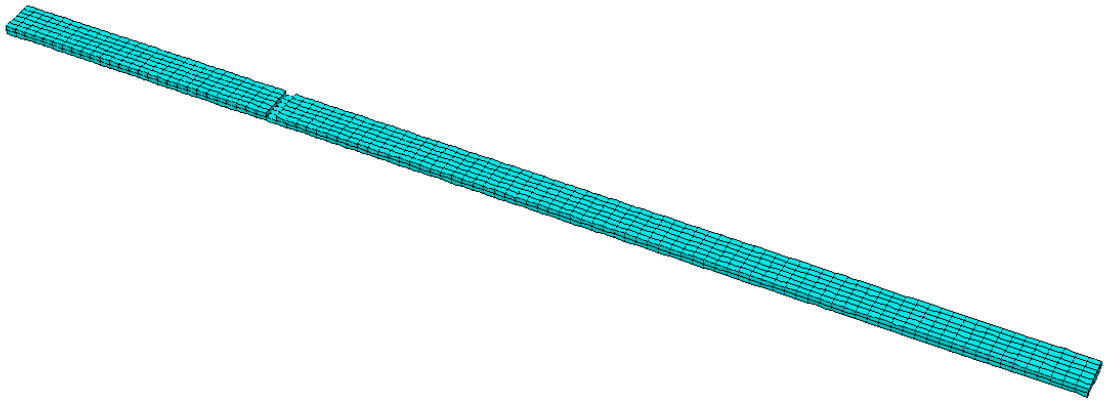

Fig. 4.5 Numerical model of the beam structure with transverse crack from ABAQUS using 3D solid elements.

On the contract, the beam element in ABAQUS gives DOF of both nodal deflection and rotational angle along x, y, and z-axis. And the crack size has been directly involved by assigning a different cross section to the damaged section. Thus, although it may not be able to simulate the behavior of a breathing crack, it can be used to verify the accuracy of the theory used in damage detection methods. And no extra calculation error will be introduced.

In conclusion, with different extends of simplification, models from section 4.3.1 and section 4.3.2 without directly involving the dimension of the crack cannot reflect the existed crack accurately and will not

be used in the later numerical analysis. And although using the 3D solid element from the ABAQUS can present the behavior of breathing crack, the proposed methods in next chapter asks for θ in the calculation that cannot be directly generated from the 3D model. The calculation error of computing θ by $\frac{dw}{dx}$ can cause a problem in the theory verification and it will not be used in the later numerical analysis. It leaves us the finite element model from the ABAQUS based on the beam element. A finer mesh and a quadratic beam element can be used to improve the accuracy of the finite element model. With accurate θ generated from the beam model, the theory of proposed damage detection methods can be verified. And with experimental validation performed in chapter 6, the beam elements from the ABAQUS meets the requirement of numerical analysis. It will be used to build the numerical model of the beam structure with a transverse crack in next chapter. And the actual nonlinear behavior may exist in damaged beam structure will be verified by experimental validation in chapter 6.

Chapter 5 LEVEL II DAMAGE DETECTION (DAMAGE LOCALIZATION)

5.1 Introduction

A method called the stiffness characteristic matrix method (stiffness-CMM) is proposed in section 5.2, and a similar method called the mass characteristic matrix method (mass-CMM) is proposed in section 5.4. It is based on the measured/computed ODS of a vibrating structure that belong to the new category as ODS based damage detection method [5]. Measured signals are only processed in the spatial domain without any sort of transformation, and there is no comparison between responses of the corresponding intact beam structure and the damaged beam structure. Thus, they are both modern signal processing methods, and damage quantification cannot be realized by its inherent limitation.

Signals are processed in the elemental dimension that dynamical signals of two consecutive elements will be used as a pair to calculate the damage index by using a weighting matrix. The damage location will be revealed by the damage index with the largest magnitude. The same algorithm is used for the two methods but only with a different weighting matrix developed from the finite element model of the beam structure. Detailed problems in the algorithm will be discussed and verified by numerical simulations in section 5.3 and 5.4. Involved numerical analysis is based on the finite element from the computer program ABAQUS with quadratic beam element. Corresponding experimental validation will be performed in chapter 6.

5.2 The Stiffness Characteristic Matrix Method

5.2.1 Matrix Setup

Recall Eqs. (4.2-4.6) from section 4.2, with 2 degrees of freedom(DOF) on each node defined by Euler-Bernoulli beam theory, each element has 4 DOFs. Sub notation is needed for later damage localization and has been added to the coefficients and functions as in Eq. (5.1). The nodal deflection of the i^{th} element is approximated by a 3rd order polynomial shape function $w_i(x)$ with interpolation function $\left[N\right]_i$:

$$\begin{aligned} w_i(x,t) &= c_0^i + c_0^i x + c_0^i x^2 + c_0^i x^3 \\ &= \begin{bmatrix} 1 & x & x^2 & x^3 \end{bmatrix} \begin{bmatrix} 1 & l(i-1) & l^2(i-1)^2 & l^3(i-1)^3 \\ 0 & 1 & 2l(i-1) & 3l^2(i-1)^2 \\ 1 & li & l^2 i^2 & l^3 i^3 \\ 0 & 1 & 2li & 3l^2 i^2 \end{bmatrix}^{-1} \begin{bmatrix} w_i \\ \theta_i \\ w_{i+1} \\ \theta_{i+1} \end{bmatrix} \\ &= \left[N\right]_i^T \left[d_p\right]_i = \left[d_p\right]_i^T \left[N\right]_i \end{aligned} \tag{5.1a}$$

$$\left[N\right]_i = \begin{bmatrix} \frac{1}{l^3}(x-il)^2\left(3l+2(x-il)\right) \\ -\frac{1}{l^2}(x-il)^2\left(l+(x-il)\right) \\ \frac{1}{l^3}\left(l+(x-il)\right)^2\left(l-2(x-il)\right) \\ -\frac{1}{l^2}(x-il)\left(l+(x-il)\right)^2 \end{bmatrix} \tag{5.1b}$$

where $x-il = x-x_{i+1}$ and $\left[d_p\right]_i$ is the displacement vector of the i^{th} element including 4 DOF of the corresponding element as $\left[d_p\right]_i^T = \left[w_i, \theta_i, w_{i+1}, \theta_{i+1}\right]$. Equation (5.1b) gives the general form of interpolation functions for the i^{th} element, with x-axis shifted as $\tilde{x} = x - x_{i+1}$, the interpolation functions will be the same for each element. And based on Rayleigh-Ritz method, the mass and stiffness matrix of the i^{th} element can be derived as:

$$\left[m^{(i)}\right]=\int_{l(i-1)}^{li}\left[N\right]_i m_i\left[N\right]_i^T dx=\frac{m_i l}{420}\begin{bmatrix}156 & 22l & 54 & -13l\\ 22l & 4l^2 & 13l & -3l^2\\ 54 & 13l & 156 & -22l\\ -13l & -3l^2 & -22l & 4l^2\end{bmatrix}=m_i\left[m^C\right]$$
$$\left[k^{(i)}\right]=\int_{l(i-1)}^{li}\left[N''\right]_i\left(EI\right)_i\left[N''\right]_i^T dx=\frac{\left(EI\right)_i}{l^3}\begin{bmatrix}12 & 6l & -12 & 6l\\ 6l & 4l^2 & -6l & 2l^2\\ -12 & -6l & 12 & -6l\\ 6l & 2l^2 & -6l & 4l^2\end{bmatrix}=\left(EI\right)_i\left[k^C\right] \quad (5.2)$$

where $\left[m^C\right]$ and $\left[k^C\right]$ is the coefficient matrix of elemental mass and stiffness matrix, m_i and $\left(EI\right)_i$ is the mass and flexural rigidity of the i^{th} element, respectively. After the integration along the x-axis, the computed elemental mass and stiffness matrix are no longer dependent on element number i or node location x_i but only depend on the mass and flexural rigidity as m_i and $\left(EI\right)_i$ (element length is assumed to be constant). Therefore, once the element length is known, the coefficient matries $\left[m^C\right]$ and $\left[k^C\right]$ can be derived and they will be the same for all intact elements.

Recall Eq. (4.8) from section 4.2, if the node #3 is under observed, the two DOFs at the node #3 as w_3 and θ_3 will be the 5th and 6th term in the $\left[D\right],\left[\dot{D}\right]$ and $\left[\ddot{D}\right]$. When it comes to the governing equation, they will couple with the 5th and 6th row in the $\left[M\right]$, $\left[K\right]$ and $\left[C\right]$. On the other hand, since the $\left[M\right]$ and $\left[K\right]$ is assembled from the elemental mass and stiffness matrix by the geometric relationship of each element, terms in the 5th and 6th row are from the elemental matrix of the 2nd and 3rd elements. It can also be understood as the node #3 is shared by the 2nd and 3rd elements. Generally, if the node $\#i\ (i\neq 1, n_N)$ is under observed, the two DOFs at the node $\#i$ as w_i and θ_i will be the $2i-1^{th}$ and $2i^{th}$ terms in the $\left[D\right],\left[\dot{D}\right]$ and $\left[\ddot{D}\right]$. And they will couple with the $2i-1^{th}$ and $2i^{th}$ row in the $\left[M\right]$, $\left[K\right]$ with terms from the elemental matrix of the $i-1^{th}$ and i^{th} elements because the node $\#i$ is shared by the $i-1^{th}$ and i^{th} elements. And the general form of the $2i-1^{th}$ and $2i^{th}$ row in $\left[M\right]$ and $\left[K\right]$ can be determined as:

$$
\begin{aligned}
&M([2i-1 \quad 2i],[2i-3:2i+2]) = \\
&\begin{bmatrix}
m_{i-1}k_{31}^C & m_{i-1}k_{32}^C & \begin{matrix} m_{i-1}k_{33}^C \\ +m_i k_{11}^C \end{matrix} & \begin{matrix} m_{i-1}k_{34}^C \\ +m_i k_{12}^C \end{matrix} & m_i k_{13}^C & m_i k_{14}^C \\
m_{i-1}k_{41}^C & m_{i-1}k_{42}^C & \begin{matrix} m_{i-1}k_{43}^C \\ +m_i k_{21}^C \end{matrix} & \begin{matrix} m_{i-1}k_{44}^C \\ +m_i k_{22}^C \end{matrix} & m_i k_{23}^C & m_i k_{24}^C
\end{bmatrix} \\
&M([2i-1 \quad 2i],[1:2i-4,\ 2i+3:end]) = 0
\end{aligned}
\tag{5.3a}
$$

$$
\begin{aligned}
&K([2i-1 \quad 2i],[2i-3:2i+2]) = \\
&\begin{bmatrix}
(EI)_{i-1}k_{31}^C & (EI)_{i-1}k_{32}^C & \begin{matrix} (EI)_{i-1}k_{33}^C \\ +(EI)_i k_{11}^C \end{matrix} & \begin{matrix} (EI)_{i-1}k_{34}^C \\ +(EI)_i k_{12}^C \end{matrix} & (EI)_i k_{13}^C & (EI)_i k_{14}^C \\
(EI)_{i-1}k_{41}^C & (EI)_{i-1}k_{42}^C & \begin{matrix} (EI)_{i-1}k_{43}^C \\ +(EI)_i k_{21}^C \end{matrix} & \begin{matrix} (EI)_{i-1}k_{44}^C \\ +(EI)_i k_{22}^C \end{matrix} & (EI)_i k_{23}^C & (EI)_i k_{24}^C
\end{bmatrix} \\
&K([2i-1 \quad 2i],[1:2i-4,\ 2i+3:end]) = 0
\end{aligned}
\tag{5.3b}
$$

where the m_{ij}^C and k_{ij}^C are constants from the coefficient matrix $\left[m^C\right]$ and $\left[k^C\right]$ defined in Eq. (5.2). Considering the Eq. (5.3b), as the stiffness matrix is coupled with a vector of displacement as $[K]_{2n_N \times 2n_N}[D]_{2n_N \times 1}$ ($n_N = number\ of\ nodes$) in the governing equation, the nonzero terms from the Eq. (5.3b) is coupled with $[D]$ as:

$$
\begin{aligned}
\left([K][D]\right)_{2i-1} &= (EI)_{i-1}\left(k_{31}^C w_{i-1} + k_{32}^C \theta_{i-1} + k_{33}^C w_i + k_{34}^C \theta_i\right) + (EI)_i\left(k_{11}^C w_i + k_{12}^C \theta_i + k_{13}^C w_{i+1} + k_{14}^C \theta_{i+1}\right) \\
&= (EI)_{i-1}\left[k^C(3,:)\right][d]_{i-1} + (EI)_i\left[k^C(1,:)\right][d]_i \\
\left([K][D]\right)_{2i} &= (EI)_{i-1}\left(k_{41}^C w_{i-1} + k_{42}^C \theta_{i-1} + k_{43}^C w_i + k_4^C \theta_i\right) + (EI)_i\left(k_{21}^C w_i + k_{22}^C \theta_i + k_{23}^C w_{i+1} + k_{24}^C \theta_{i+1}\right) \\
&= (EI)_{i-1}\left[k^C(4,:)\right][d]_{i-1} + (EI)_i\left[k^C(2,:)\right][d]_i
\end{aligned}
\tag{5.4}
$$

Then, Eq. (5.4) can be rearranged as:

$$
\begin{bmatrix} \left([K][D]\right)_{2i-1} \\ \left([K][D]\right)_{2i} \end{bmatrix} = \begin{bmatrix} \left[k^C(3,:)\right][d]_{i-1} & \left[k^C(1,:)\right][d]_i \\ \left[k^C(4,:)\right][d]_{i-1} & \left[k^C(2,:)\right][d]_i \end{bmatrix} \begin{bmatrix} (EI)_{i-1} \\ (EI)_i \end{bmatrix}
\tag{5.5}
$$

And $[K]_{2n_N \times 2n_N}[D]_{2n_N \times 1}$ can be rearranged as:

$$[K]_{2n_N\times 2n_N}[D]_{2n_N\times 1}=\left[\tilde{K}\right]_{2n_N\times n_E}[EI]_{n_E\times 1}$$

$$\left[\tilde{K}\right]=\begin{bmatrix}
\left[k^C(1,:)\right][d]_1 & & & & & & \\
\left[k^C(2,:)\right][d]_1 & & & & & & \\
\left[k^C(3,:)\right][d]_1 & \left[k^C(1,:)\right][d]_2 & & & & & \\
\left[k^C(4,:)\right][d]_1 & \left[k^C(2,:)\right][d]_2 & & & & & \\
 & \left[k^C(3,:)\right][d]_2 & \left[k^C(1,:)\right][d]_3 & & & & \\
 & \left[k^C(4,:)\right][d]_2 & \left[k^C(2,:)\right][d]_3 & & & & \\
 & & \left[k^C(3,:)\right][d]_3 & \left[k^C(1,:)\right][d]_4 & & & \\
 & & \left[k^C(4,:)\right][d]_3 & \left[k^C(2,:)\right][d]_4 & & & \\
 & & & \ddots & & & \\
 & & & & & \left[k^C(3,:)\right][d]_{n_E} & \\
 & & & & & \left[k^C(4,:)\right][d]_{n_E} &
\end{bmatrix} \tag{5.6}$$

$$[EI]^T=\begin{bmatrix}(EI)_1 & (EI)_2 & (EI)_3 & \cdots & (EI)_{n_E}\end{bmatrix}$$

For the observed node $\#i$ shared by the $i-1^{th}$ and i^{th} elements, a 2×2 matrix is formed by the nonzero terms in the $i-1^{th}$ and i^{th} row from the rearranged $\left[\tilde{K}\right]$ as:

$$[A]_i=\begin{bmatrix}\left[k^C(3,:)\right][d]_{i-1} & \left[k^C(1,:)\right][d]_i\\ \left[k^C(4,:)\right][d]_{i-1} & \left[k^C(2,:)\right][d]_i\end{bmatrix} \tag{5.7}$$

where the $[A]_i$ is defined as the stiffness characteristic matrix of the observed node $\#i$. Since the $i-1^{th}$ and i^{th} row of the $\left[\tilde{K}\right]$ is coupled with the term $(EI)_{i-1}$ and $(EI)_i$ from the $[EI]$, and the characteristic matrix can also be understood as stiffness characteristic matrix of the $i-1^{th}$ and i^{th} elements.

Considering an intact beam structure with general boundary points/lines only at two ends, the operational deflection shapes (ODSs) and spatial derivatives of ODSs is continuous [66]. And when the ODSs is in form of 3rd order polynomial, the shape function that also in form of 3rd order polynomial will be the same for each element through the entire beam structure. An example of beam structure with 3rd order polynomial ODSs is given as following.

Considering a cantilever beam only with applied force on the right end (as shown in Fig. 5.1), it will have a constant shear force function along the x-axis as:

$$F_s(x) = \bar{F} \tag{5.8}$$

And the integrated moment function can be derived as:

$$M(x) = \bar{F}x + M_0 = \bar{F}x - \bar{F}L \tag{5.9}$$

where M_0 is the integration constant as the reaction moment at the fixed end. Then, the integrated rotational angle function can be derived as:

$$\Theta(x) = \frac{\bar{F}x^2}{2EI} - \frac{\bar{F}Lx}{EI} \tag{5.10}$$

where the integration constant is zero because the fixed end has a zero deflection and rotation. Then, the static deflection of the beam can be derived as a continuous 3rd-polynomial as in Eq. (5.11a). Considering the cantilever beam under the free vibration with applied force on the free end as its initial condition, the vibration signal of the entire structure will be both function of location and time as Eq. (5.11b). Then, with the $W(x,0)$ in form of 3rd-order polynomial, the shape function of each element $w_i(x,t)$ will be the same as the $W(x,t)$ through the structure.

$$W_S(x) = \frac{1}{6}\frac{\bar{F}}{EI}x^3 - \frac{1}{2}\frac{\bar{F}L}{EI}x^2 = W(x,0) \tag{5.11a}$$

$$\begin{aligned} W(x,t) &= W(x,0)T(t) \\ T(t) &= e^{-\zeta\omega t} \end{aligned} \tag{5.11b}$$

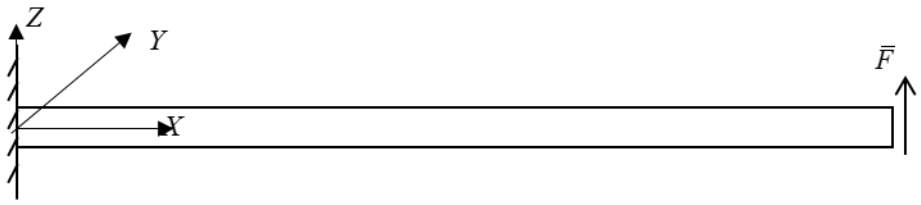

Fig. 5.1 A cantilever beam under an applied force at the free end.

And for general cases with ODSs in form of a continuous 3rd order polynomial as in Eq. (5.12a), the rotational angle function and DOFs of the observed $i-1^{th}$, i^{th} elements (before/after the node $\#i$) can be calculated as in Eq. (5.12b).

$$W(x) = c_0 + c_1 x + c_2 x^2 + c_3 x^3 \quad x = \{x_i = (i-1)l\} \tag{5.12a}$$

$$\begin{aligned}
&\Theta(x) = \frac{dW(x)}{dx} = c_1 + 2c_2 x + 3c_3 x^2 \\
&w_{i-1} = c_0 + c_1(i-2)l + c_2(i-2)^2 l^2 + c_3(i-2)^3 l^3 \\
&w_i = c_0 + c_1(i-1)l + c_2(i-1)^2 l^2 + c_3(i-1)^3 l^3 \\
&w_{i+1} = c_0 + c_1 il + c_2 i^2 l^2 + c_3 i^3 l^3 \\
&\theta_{i-1} = c_1 + 2c_2(i-2)l + 3c_3(i-2)^2 l^2 \\
&\theta_i = c_1 + 2c_2(i-1)l + 3c_3(i-1)^2 l^2 \\
&\theta_{i+1} = c_1 + 2c_2 il + 3c_3 i^2 l^2
\end{aligned} \tag{5.12b}$$

where the independent variable *x* has been transformed to node number i. Substitute Eq. (5.12b) back into Eq. (5.7), the determinant of $[A]$ can be calculated as:

$$\begin{aligned}
&A_{11}^i = -6c_3,\ A_{12}^i = 6c_3 \\
&A_{21}^i = 2c_2 + 6ic_3 l,\ A_{22}^i = -2c_2 - 6ic_3 l \\
&d_i \triangleq \det([A]_i) = A_{11}^i A_{22}^i - A_{12}^i A_{21}^i = 0
\end{aligned} \tag{5.13}$$

Notice the zero-determinant existed and it is not depending on the coefficient of the 3rd order polynomial ODSs. And when the d_i is nonzero, one (or more) of following three situations may exist.

First, discontinuity can exist in ODSs from the node $\#i-1$ and $\#i+1$. For an intact beam structure with general boundary points/lines only at two ends, ODSs and spatial derivatives of ODSs is continuous [66]. However, existed damage will introduce extra boundary points/lines to the structure [66] and create a discontinuity in ODSs at damage location. Considering the discontinuity existed on either the $i-1^{th}$ element or the i^{th} element, the shape function $w_i(x)$ and $w_{i+1}(x)$ will be different as in terms of different

coefficient sets:

$$\begin{aligned} w_{i-1}(x) &= c_0 + c_1 x + c_2 x^2 + c_3 x^3 \\ w_i(x) &= c_0' + c_1' x + c_2' x^2 + c_3' x^3 \end{aligned} \tag{5.14a}$$

If the damage does not fall on the shared node $\#i$ ($x_i = (i-1)l$) at which the nodal deflection and rotational angle are continuous:

$$\begin{aligned} w_i &= w_{i-1}((i-1)l) = c_0 + c_1(i-1)l + c_2(i-1)^2 l^2 + c_3(i-1)^3 l^3 \\ &= w_i((i-1)l) = c_0' + c_1'(i-1)l + c_2'(i-1)^2 l^2 + c_3'(i-1)^3 l^3 \\ \theta_i &= \theta_{i-1}((i-1)l) = c_1 + 2c_2(i-1)l + 3c_3(i-1)^2 l^2 \\ &= \theta_i((i-1)l) = c_1' + 2c_2'(i-1)l + 3c_3'(i-1)^2 l^2 \end{aligned} \tag{5.14b}$$

The determinant will still be nonzero:

$$\begin{aligned} &A_{11}^i = -6c_3,\ A_{12}^i = 6c_3' \\ &A_{21}^i = 2c_2 + 6ic_3 l,\ A_{22}^i = -2c_2' - 6ic_3' l \\ &d_i = A_{11}^i A_{22}^i - A_{12}^i A_{21}^i \neq 0 \end{aligned} \tag{5.14c}$$

On the other hand, notice that without extra boundary lines exist on the beam section before and after damage location, the ODSs in each section is still continuous. Therefore, if the damage existed on the j^{th} element, the discontinuous would only exist between shape functions of the $j-1^{th}\&j^{th}$ elements and the $j^{th}\&j+1^{th}$ elements and two nonzeroes will exist as the d_j and d_{j+1} (corresponding to the node $\#j$ and $\#j+1$ as node before and after actual damage location). Then, the determinant of the characteristic matrix can be used as a damage index that when two consecutive nonzeroes existed as d_j and d_{j+1}, damage location can be determined as on the j^{th} element.

However, the measuring noise can also result in multiple discontinuities in the ODSs and give nonzero d_i. Therefore, nonzero d_i caused by measuring error can be identified as a false damage location. Section 5.4 gives the discussion about the problem of measuring noise by adding simulated noise. A mass

characteristic matrix method (mass-CMM) that is more robust with noise will be derived in section 5.4.2.

Second, if only nodal deflection signals are available, rotational angle signals need to be computed as the first derivative of deflection to x-axis. The differentiation methods applied in the calculation can contain calculation error and give the computed rotational angle signals deviated from the actual $\Theta(x)$. Then, d_i can be nonzero for intact structure. Moreover, the single measurand in this thesis is assumed as the velocity signal. The calculation error and accumulated noise from the integration step to nodal deflection can also result in a nonzero d_i. Meanwhile, as discussed in chapter 2, considering the efficiency, the SG integration method will be used to computing nodal deflection and the SG filter method will be used to computing rotational angle signal. Therefore, with certain choice of n_L, n_R and M, the general form of computed data point can be derived, and the nonzero d_i caused by calculation error can be derived. In order to simplify the situation, the step of computing nodal deflection signals from velocity signals is not included. Section 5.3.1 uses two sets of n_L, n_R and M as examples, derived the general form of damage index. It proves that with the same n_L, n_R and M, even there existed calculation error makes the d_i nonzero, the nonzero d_i will be continuous through the x-axis for intact structure. The nonzero d_i caused by the calculation error can be understood as a baseline b_i, and the d_j with extra nonzero magnitude caused from the existed damage can be identified as the deviated data point from the formed baseline. With the deviation calculated as the filtered damage index $\hat{d}_i = d_i - b_i$, the damage index still can be used for damage localization.

Third, the ODSs can be in other forms rather than 3rd order polynomial that shape function of each element through the structure can be different. For example, for cantilever beam under pressure p over the whole plate, the ODSs will be a 4th order polynomial as:

$$W(x) = -\frac{px^2}{24EI}\left(x^2 - 4Lx + 6L^2\right) \tag{5.15}$$

And for a beam subjected to a harmonic excitation at a frequency Ω, its ODSs of a uniform segment without any loading or damage points will have the following form [67, 68]:

$$W(x) = a_1 \cos\beta x + b_1 \sin\beta x + a_2 \cosh\beta x + b_2 \sinh\beta x \tag{5.16}$$

where β can be calculated from $\beta^4 = m\Omega^2 / EI$, Ω is the exciting frequency in rad/s and coefficients a_1, a_2, b_1 and b_2 can be determined by boundary conditions. With different shape functions (different coefficient sets) for two consecutive intact elements, the damage index will be nonzero as proved in Eq. (5.14). However, for an intact structure with a continuous ODSs and corresponding continuous $\Theta(x)$, the nonzero damage index caused by changing shape functions will still be continuous along the x-axis and result in a continuous baseline. As in the previous case, instead of detect damage location by identifying nonzero d_i form all zero values, d_i still can be used as a damage index that identifying the location by the deviated d_i from the formed baseline. A detailed discussion will be given in Section 5.3.2.

5.2.2 Method Verification

Before further discussion, the stiffness-CMM can be verified firstly with accurate dynamical data from the numerical simulation. And as discussed in section 4.3, the beam section in ABAQUS with quadratic beam elements will be used in the numerical simulation. Meshing the beam structure while providing 6 DOF on each node, accurate w and θ can be generated. Figure 5.2 gives the designed case for our first verification. For the cantilever beam with a transverse crack, w and θ of each node will be generated under a free transient response to the applied force at the free end.

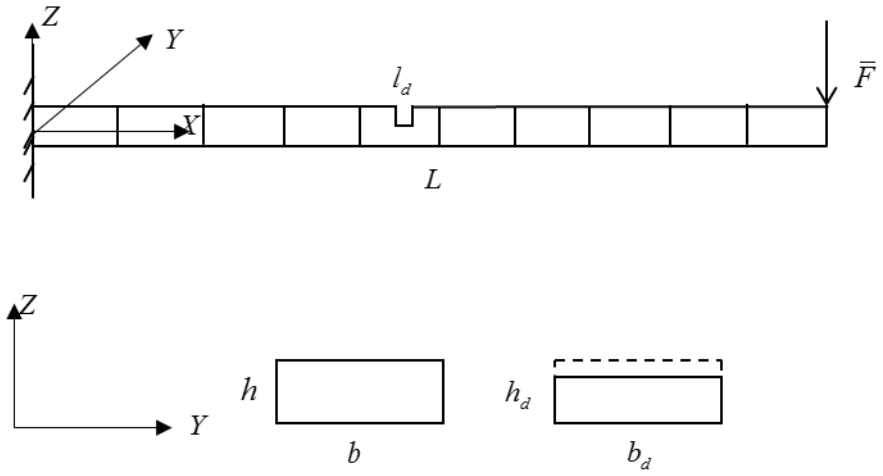

Fig. 5.2 Cantilever beam with a transverse crack and an applied force on the free end.

where $L = 0.6m$ is the length of the beam, $b = 0.02m$ and $h = 0.005m$ is the size of the cross section for healthy section, $b_d = b$ and $h_d = 0.75h$ is the size of the cross section for damaged section. Damage location is chosen as $L_1 = 0.27L$ with crack width as $l_d = L/400$. The concentrated force on the free end is applied along negative z direction with the amplitude as:

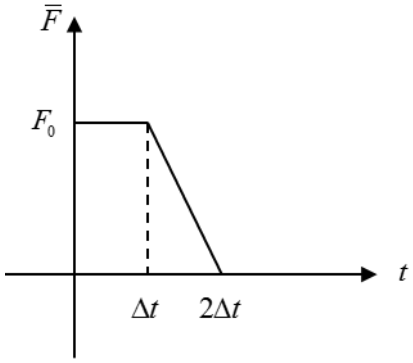

Fig. 5.3 Amplitude of applied force

where $\Delta t = 0.0001s$ (sampling rate as 10000Hz) that about 80 data points will exist in each period for the 1st mode vibration. A total 5000 steps of data as $t = 0 \sim 0.5s$ has been calculated. Since system's any

free/forced vibration is always a linear combination of these n modal vibrations [57], the free transient vibration can be generated as superposition different mode vibrations. With the applied force on the free end, the deformed geometry is close to its first mode shape, and the beam's free transient vibration would mainly consist of the 1st mode vibration. Thus, a simplification has been applied as generating the free transient response by modal dynamics with only the 1st mode involved.

Modal damping of the 1st mode is defined as ζ=0.03. In order to get a more accurate response from the finite element model, 400 elements mesh is used along the longitude direction to have the element length match the crack width. For $L_1 = 0.27L$ as $x_d = 0.162\,m$, the numerical beam model from the ABAQUS is shown in Fig. 5.4.

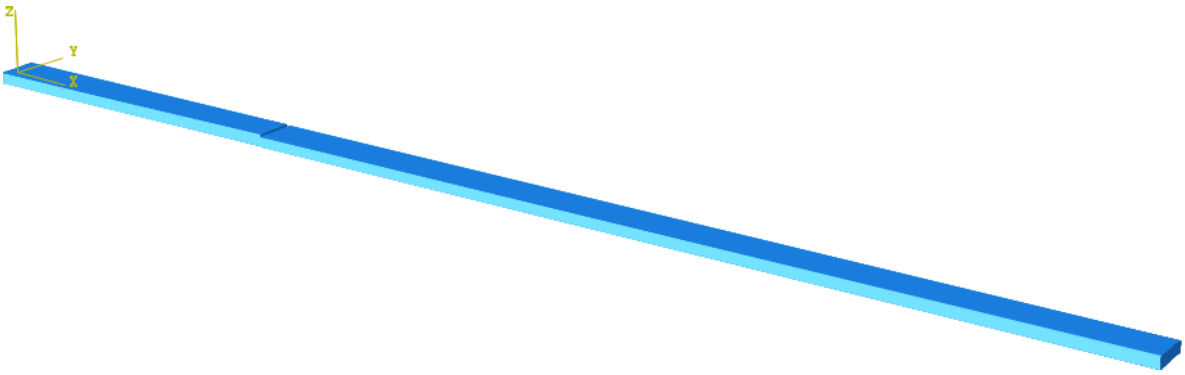

Fig. 5.4 The numerical beam model from the ABAQUS.

w and θ of every 5 elements are output to simulate the situation of 81 measured points. Since d_i can be calculated for each node at each time constant, the average of calculated d_i at each node over the entire time trace will be used as the result damage index as $\bar{d}_i$. Figure 5.5 gives the result damage index in red line with dots, and the black dash line in Fig. 5.5 indicates the actual damage location. Two consecutive $\bar{d}_i$ with evident nonzero value and opposite signs as the $\bar{d}_{22}$ and $\bar{d}_{23}$ can be easily identified by the red line in Fig.

5.5. While $\bar{d}_{22}=1.86\times10^{-7}$ and $\bar{d}_{23}=-1.99\times10^{-7}$, the magnitude of $\bar{d}_i$ of rest points are below 2×10^{-9}. The nonzero value of rest $\bar{d}_i$ is caused by the applied simplification that using modal dynamics analysis with only 1st mode involved for the free transient response where the ODSs of 1st mode vibration is in terms of trigonometric functions instead of a 3rd order polynomial. However, with the discontinuity existed in ODSs caused by the existed damage, the relative small nonzero d_i caused by the simplification is not obvious from the result damage index from Fig. 5.5. Baseline computation and filtering are not needed. And damage location can be identified as between nodes $\#22$ and $\#23$ as between $x_{22}=0.1575\,m$ and $x_{23}=0.165\,m$. The identified damage location is marked as the gray area in Fig. 5.5 and it matches with the actual damage location as in the black dash line.

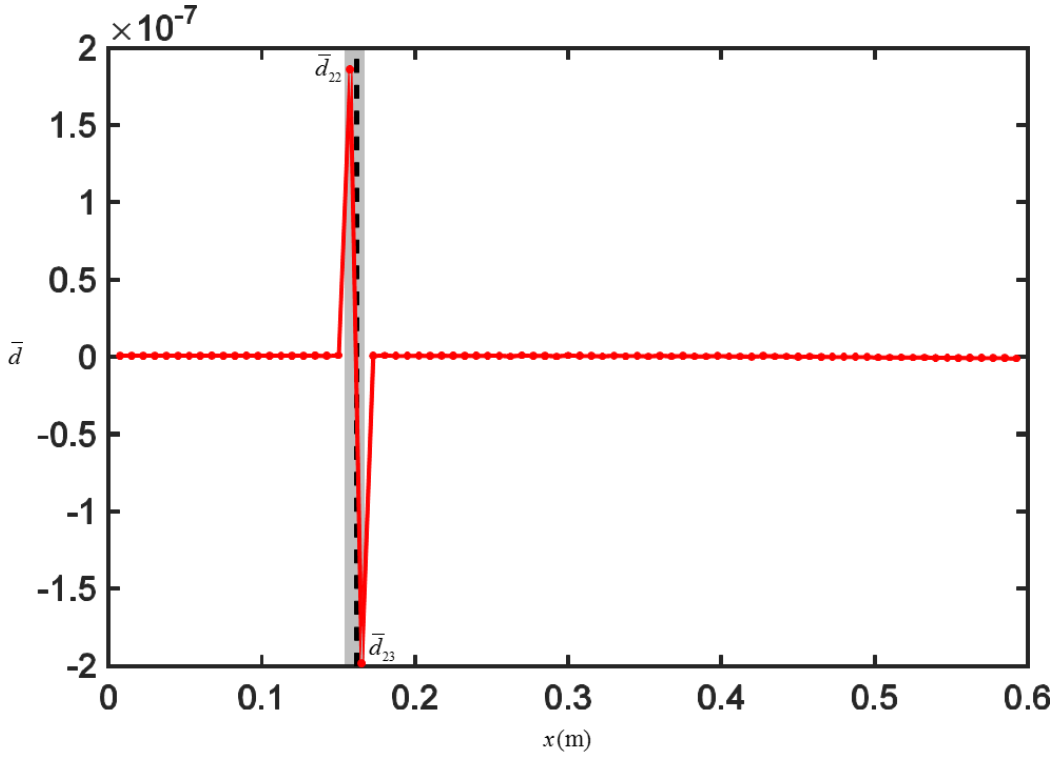

Fig. 5.5 Result damage indexes based on damage beam model from Fig. 5.4

Notice that, the identified nonzero as $\bar{d}_{22}$ and $\bar{d}_{23}$ have opposite signs. That is because with different flexural rigidity $(EI)_j$ at damage location, even if the existed damage is relatively small and no extra applied force or moment existed to Eq. (5.8) and Eq. (5.9), the integrated rotational angle function and ODSs will still be different before and after actual damage location. And with no extra boundary condition existed for those two beam sections, the ODSs of two sections can be continuous and as defined in Eq. (5.17).

$$W_1(x)=\sum_{k=0}^{3}\bar{c}_k x^k \quad x \le x_j < x_d \tag{5.17a}$$

$$W_2(x)=\sum_{k=0}^{3}\bar{c}'_k x^k \quad x \ge x_{j+1} > x_d \tag{5.17b}$$

where $W_1(x)$ is the ODSs of the beam section before the damage location x_d (on the j^{th} element) and $W_2(x)$ is the ODSs of the beam section after the damage location x_d. Then, shape functions of the elements before or after the j^{th} element will be the same as $W_1(x)$ or $W_2(x)$, respectively. If the damage does not locate on the node $\#j$ and $\#j+1$, the w and θ at these two nodes still can be calculated by its corresponding ODSs function as the nodes around the damage location:

$$w_{j-1}=W_1(x_{j-1}),\ w_j=W_1(x_j),\ w_{j+1}=W_2(x_{j+1}),\ w_{j+2}=W_2(x_{j+2}) \tag{5.18a}$$

$$\theta_{j-1}=W_1'(x_{j-1}),\ \theta_j=W_1'(x_j),\ \theta_{j+1}=W_2'(x_{j+1}),\ \theta_{j+2}=W_2'(x_{j+2}) \tag{5.18b}$$

Then, the damage index of nodes $\#j$ and $\#j+1$ can be calculated out as d_j shown in Eq. (5.19) and d_{j+1} shown in (5.20), respectively.

$$
\begin{aligned}
A_{11}{}^{j} &= -6\bar{c}_3 \\
A_{12}{}^{j} &= 12(\bar{c}_0 - \bar{c}_0')/l^3 + (12j-6)(\bar{c}_1 - \bar{c}_1')/l^2 + (12j^2 - 12j)(\bar{c}_2 - \bar{c}_2')/l \\
&\quad + (12j^3 - 18j^2)(\bar{c}_3 - \bar{c}_3') + 6\bar{c}_3 \\
&= C_1 + 6\bar{c}_3 \\
A_{21}{}^{j} &= 2\bar{c}_2 + (6j-6)\bar{c}_3 l \\
A_{22}{}^{j} &= 6(\bar{c}_0 - \bar{c}_0')/l^2 + (6j-2)(\bar{c}_1 - \bar{c}_1')/l + (6j^2 - 4j)(\bar{c}_2 - \bar{c}_2') \\
&\quad + (6j^3 - 6j^2)(\bar{c}_3 - \bar{c}_3')l - 2\bar{c}_2 + (-6j+6)\bar{c}_3 l \\
&= C_2 - 2\bar{c}_2 + (-6j+6)\bar{c}_3 l \\
d_j &= A_{11}{}^{j} A_{22}{}^{j} - A_{12}{}^{j} A_{21}{}^{j} \\
&= -6\bar{c}_3 (C_2 - 2\bar{c}_2 + (-6j+6)\bar{c}_3 l) - (C_1 + 6\bar{c}_3)(2\bar{c}_2 + (6j-6)\bar{c}_3 l) \\
&= -6\bar{c}_3 C_2 - C_1 (2\bar{c}_2 + (6j-6)\bar{c}_3 l)
\end{aligned}
\tag{5.19}
$$

$$
\begin{aligned}
A_{11}{}^{j+1} &= 12(\bar{c}_0' - \bar{c}_0)/l^3 + (12j-6)(\bar{c}_1' - \bar{c}_1)/l^2 + (12j^2 - 12j)(\bar{c}_2' - \bar{c}_2)/l \\
&\quad + (12j^3 - 18j^2)(\bar{c}_3' - c_3) - 6\bar{c}_3 \\
&= -C_1 - 6\bar{c}_3 \\
A_{12}{}^{j+1} &= 6\bar{c}_3' \\
A_{21}{}^{j+1} &= 6(\bar{c}_0 - \bar{c}_0')/l^2 + (6j-4)(\bar{c}_1 - \bar{c}_1')/l + (6j^2 - 8j)(\bar{c}_2 - \bar{c}_2') \\
&\quad + (6j^3 - 12j^2)(\bar{c}_3 - \bar{c}_3')l + 2\bar{c}_2 + 6j\bar{c}_3 l \\
&= C_3 + 2\bar{c}_2 + 6j\bar{c}_3 l \\
A_{22}{}^{j+1} &= -2\bar{c}_2' - 6j\bar{c}_3' l \\
d_{j+1} &= A_{11}{}^{j+1} A_{22}{}^{j+1} - A_{12}{}^{j+1} A_{21}{}^{j+1} \\
&= (-C_1 - 6\bar{c}_3)(-2\bar{c}_2' - 6j\bar{c}_3' l) - 6b_3 (C_3 + 2\bar{c}_2 + 6j\bar{c}_3 l) \\
&= C_1 (2\bar{c}_2' + 6j\bar{c}_3' l) - 6\bar{c}_3' C_3
\end{aligned}
\tag{5.20}
$$

where C_1, C_2 and C_3 are defined to simplify the result as color denoted. And a relation $C_2 + C_3 = C_1 l$ existed between C_1, C_2 and C_3. Then, d_j can be rearranged as in Eq. (5.21a) while d_{j+1} can be rearranged as in Eq. (5.21b).

$$
d_j = 6\bar{c}_3 C_3 - C_1 (2\bar{c}_2 + 6j\bar{c}_3 l) \tag{5.21a}
$$

$$
d_{j+1} = -6\bar{c}_3' C_3 + C_1 (2\bar{c}_2' + 6j\bar{c}_3' l) \tag{5.21b}
$$

With different ODSs before and after the damage location, coefficients $\bar{c}_k$ and $\bar{c}_k'$ will have different

values that term C_1, C_3 will be nonzero. Then, d_j and d_{j+1} will be nonzero and damage location can be identified as the element between the two consecutive nodes both have nonzero damage index. With the small deflection assumption used in Euler-Bernoulli beam theory, the discontinuous existed between $W_1(x)$ and $W_2(x)$ will only result in coefficients $\overline{c}_k$ and $\overline{c}'_k$ with different but close values. Thus, the magnitude of d_j and d_{j+1} will have a relatively small difference and opposite signs as in Fig. 5.5. Therefore, theoretically, the damage index of the nodes before and after the actual damage location will not only be both nonzero but also with opposite signs.

5.3 Discussion

5.3.1 Computation of the Rotational Angle

Although rotational angle θ is not easily to be measured directly from experiment, it can be calculated as the first derivative of deflection function as defined in Eq. (4.2). With discrete nodal deflection data, the calculated rotational angle may not be accurate and can result in a nonzero damage index for two intact elements. With the SG filter method with the same n_L, n_R and *M* used for all data points, the nonzero damage index can be continuous along the x-axis of a structure with the continuous ODSs. Then, the continuous nonzero value from the calculation error from a baseline and damage location can be detected by the deviated d_i. Notice, the chosen n_L, n_R may not be applicable for the first/last few data points because of lacking enough points from one side. And the corresponding result nonzero d_i can have a deviation from the baseline too.

With the different n_L, n_R and *M*, the calculation error existed in the computed rotational angle θ'

will be different and the number of nonzero/deviated $\boldsymbol{d}_i$ around the damage location would be different. Since the shape function in the Euler-Bernoulli beam theory is in the form of the 3rd-order polynomial, $M = 3$ will be a fair choice to get a more accurate θ'. And for n_L and n_R, with the same n_L and n_R, general form of $\boldsymbol{d}_i$ can be derived. Recall the SG filter method from section 2.2.3; the rotational angle θ'_i can be calculated as:

$$\begin{aligned} \theta'_i &= \left[\tilde{C}(2,:)\right]\cdot[w]_i \\ [w]_i &= \begin{bmatrix} w_{i-n_L} & w_{i-n_L+1} & \cdots & w_i & \cdots & w_{i+n_R-1} & w_{i+n_R} \end{bmatrix}^T \end{aligned} \tag{5.22}$$

where $\left[\tilde{C}\right]$ only depend on n_L, n_R and M and is calculated as:

$$\begin{aligned} \left[\tilde{C}\right] &= \left(\left[\tilde{A}\right]^T\cdot\left[\tilde{A}\right]\right)^{-1}\cdot\left[\tilde{A}\right]^T \\ \left[\tilde{A}\right] &= \begin{bmatrix} (-n_L l)^0 & (-n_L l)^1 & \cdots & (-n_L l)^M \\ (-n_L l+l)^0 & (-n_L l+l)^1 & \cdots & (-n_L l+l)^M \\ \vdots & \vdots & \vdots & \vdots \\ 0^0 & 0^1 & \cdots & 0^M \\ \vdots & \vdots & \vdots & \vdots \\ (n_R l-l)^0 & (n_R l-l)^1 & \cdots & (n_R l-l)^M \\ (n_R l)^0 & (n_R l)^1 & \cdots & (n_R l)^M \end{bmatrix} \end{aligned} \tag{5.23}$$

The case with $n_L = 0, n_R = 1$, $M = 3$ and $n_L = 2, n_R = 2$, $M = 3$ will be used for comparison. And to eliminate other factors and only show the nonzero value of $\boldsymbol{d}_i$ caused by the applied differentiation method, case of an intact structure with a continuous ODSs (as in Eq. (5.12a)) will be discussed too.

First, the general form of θ'_i using $n_L = 0, n_R = 1$ can be derived from Eq. (5.24a) and general form of θ'_i using $n_L = 2, n_R = 2$ can be derived as in Eq. (5.24b).

$$\theta'_i = \left[\tilde{C}(2,:)\right]\cdot\begin{bmatrix} w_i & w_{i+1} \end{bmatrix}^T = \frac{w_{i+1}-w_i}{l} \tag{5.24a}$$

$$\begin{aligned} \theta'_i &= \left[\tilde{C}(2,:)\right]\cdot\begin{bmatrix} w_{i-2} & w_{i-1} & w_i & w_{i+1} & w_{i+2} \end{bmatrix}^T \\ &= \frac{w_{i-2}-8w_{i-1}+8w_{i+1}-w_{i+2}}{12l} \end{aligned} \tag{5.24b}$$

As from Eq. (5.24a), with $n_L = 0, n_R = 1, M = 3$, the SG filter method works the same as 1st order forward finite difference. And as from Eq. (5.24b), with $n_L = 2, n_R = 2, M = 3$, the SG filter method works as a 2nd order central difference. Then, the general form of θ_i' with $n_L = 0, n_R = 1, M = 3$ can be derived in terms of coefficients from ODSs as in Eq. (5.25a) and the general formula of θ_i' with $n_L = 2, n_R = 2$, $M = 3$ can be derived in terms of coefficients from ODSs as in Eq. (5.25b).

$$\theta_i' = c_1 + (2i-1)c_2 l + \left(3i^2 - 3i + 1\right)c_3 l^2 \tag{5.25a}$$

$$\begin{aligned} \theta_i' &= c_1 + (2i-2)c_2 l + \left(3i^2 - 6i + 3\right)c_3 l^2 \\ &= c_1 + 2(i-1)c_2 l + 3\left(i-1\right)^2 c_3 l^2 = \theta_i \end{aligned} \tag{5.25b}$$

Notice that with $n_L = 2, n_R = 2$, $M = 3$, the computed rotational angle θ_i' match with the accurate rotational angle θ_i. With the accurate nodal deflection signals and continuous ODSs, the θ_i' at nodes will be accurate with no calculation error introduced. Therefore, based on the θ_i' computed with $n_L = 2, n_R = 2$, $M = 3$, the damage index of two intact elements will stay zero, in this case, no baseline will be formed. However, with $n_L = 2, n_R = 2$ used for computation, the discontinuity existed in ODSs will be spread and cause more than two nonzeroes d_i around damage location.

Consider the same model from the previous case. The ODSs of beam section before and after damage location is defined as Eq. (5.17a) and Eq. (5.17b), and the damage located on the j^{th} element (not fall on the node). Then, the nonzero damage index can be determined as in Table 5.1.

Table 5.1 Nodal deflection, rotational angle and damage index of nodes around damage location with $n_L = 2, n_R = 2$, $M = 3$ used for rotational angle calculation.

Element #	Node #	x	w_i	θ_i	θ_i'	d_i
⋮	⋮	⋮	⋮	⋮	⋮	⋮
$j-3^{th}$	$\#\, j-3$	$jl-4l$	$W_1(jl-4l)$	$W_1'(jl-4l)$	$f(W_1)$	$d_{j-3}=0$
$j-2^{th}$	$\#\, j-2$	$jl-3l$	$W_1(jl-3l)$	$W_1'(jl-3l)$	$f(W_1)$	$d_{j-2}\neq 0$
$j-1^{th}$	$\#\, j-1$	$jl-2l$	$W_1(jl-2l)$	$W_1'(jl-2l)$	$f(W_1,W_2)$	$d_{j-1}\neq 0$
j^{th}	$\#\, j$	$jl-l$	$W_1(jl-l)$	$W_1'(jl-l)$	$f(W_1,W_2)$	$d_j\neq 0$
$j+1^{th}$	$\#\, j+1$	jl	$W_2(jl)$	$W_2'(jl)$	$f(W_1,W_2)$	$d_{j+1}\neq 0$
$j+2^{th}$	$\#\, j+2$	$jl+l$	$W_2(jl+l)$	$W_2'(jl+l)$	$f(W_1,W_2)$	$d_{j+2}\neq 0$
$j+3^{th}$	$\#\, j+3$	$jl+2l$	$W_2(jl+2l)$	$W_2'(jl+2l)$	$f(W_2)$	$d_{j+3}\neq 0$
⋮	$\#\, j+4$	$jl+3l$	$W_2(jl+3l)$	$W_2'(jl+3l)$	$f(W_2)$	$d_{j+4}=0$
	⋮	⋮	⋮	⋮	⋮	⋮

While the nodal deflections w_i of nodes before and after actual damage location fit the function

$W_1(x)$ or $W_2(x)$ as listed in the 4th column from

Element #	Node #	x	w_i	θ_i	θ_i'	d_i
$\vdots$	$\vdots$	$\vdots$	$\vdots$	$\vdots$	$\vdots$	$\vdots$
$j-3^{th}$	$\#\, j-3$	$jl-4l$	$W_1(jl-4l)$	$W_1'(jl-4l)$	$f(W_1)$	$d_{j-3}=0$
$j-2^{th}$	$\#\, j-2$	$jl-3l$	$W_1(jl-3l)$	$W_1'(jl-3l)$	$f(W_1)$	$d_{j-2}\neq 0$
$j-1^{th}$	$\#\, j-1$	$jl-2l$	$W_1(jl-2l)$	$W_1'(jl-2l)$	$f(W_1,W_2)$	$d_{j-1}\neq 0$
j^{th}	$\#\, j$	$jl-l$	$W_1(jl-l)$	$W_1'(jl-l)$	$f(W_1,W_2)$	$d_j\neq 0$
$j+1^{th}$	$\#\, j+1$	jl	$W_2(jl)$	$W_2'(jl)$	$f(W_1,W_2)$	$d_{j+1}\neq 0$
$j+2^{th}$	$\#\, j+2$	$jl+l$	$W_2(jl+l)$	$W_2'(jl+l)$	$f(W_1,W_2)$	$d_{j+2}\neq 0$
	$\#\, j+3$	$jl+2l$	$W_2(jl+2l)$	$W_2'(jl+2l)$	$f(W_2)$	$d_{j+3}\neq 0$

$j+3^{th}$						
	$\#\, j+4$	$jl+3l$	$W_2(jl+3l)$	$W_2'(jl+3l)$	$f(W_2)$	$d_{j+4}=0$
$\vdots$	$\vdots$	$\vdots$	$\vdots$	$\vdots$	$\vdots$	$\vdots$

Table 5.1, the actual rotational angle θ_i of nodes before and after damage location fit the function $W_1'(x)$ or $W_2'(x)$ as listed in the 5th column from

Element #	Node #	x	w_i	θ_i	θ_i'	d_i
	$\vdots$	$\vdots$	$\vdots$	$\vdots$	$\vdots$	$\vdots$
$\vdots$	$\#\, j-3$	$jl-4l$	$W_1(jl-4l)$	$W_1'(jl-4l)$	$f(W_1)$	$d_{j-3}=0$
$j-3^{th}$	$\#\, j-2$	$jl-3l$	$W_1(jl-3l)$	$W_1'(jl-3l)$	$f(W_1)$	$d_{j-2}\neq 0$
$j-2^{th}$	$\#\, j-1$	$jl-2l$	$W_1(jl-2l)$	$W_1'(jl-2l)$	$f(W_1,W_2)$	$d_{j-1}\neq 0$
$j-1^{th}$	$\#\, j$	$jl-l$	$W_1(jl-l)$	$W_1'(jl-l)$	$f(W_1,W_2)$	$d_j\neq 0$
j^{th}	$\#\, j+1$	jl	$W_2(jl)$		$f(W_1,W_2)$	$d_{j+1}\neq 0$

$j+1^{th}$				$W_2'(jl)$		
	$\#\, j+2$	$jl+l$	$W_2(jl+l)$	$W_2'(jl+l)$	$f(W_1,W_2)$	$d_{j+2}\neq 0$
$j+2^{th}$						
	$\#\, j+3$	$jl+2l$	$W_2(jl+2l)$	$W_2'(jl+2l)$	$f(W_2)$	$d_{j+3}\neq 0$
$j+3^{th}$						
	$\#\, j+4$	$jl+3l$	$W_2(jl+3l)$	$W_2'(jl+3l)$	$f(W_2)$	$d_{j+4}=0$
$\vdots$						
	$\vdots$	$\vdots$	$\vdots$	$\vdots$	$\vdots$	$\vdots$

Table 5.1. However, with the applied differentiation method, while most θ_i' are calculated based on w_i from one of the $W_1(x)$ and $W_2(x)$, some θ_i' (marked in red) are calculated based on w_i from both ODSs as listed in the 6th column in

Element #	Node #	x	w_i	θ_i	θ_i'	d_i
	$\vdots$	$\vdots$	$\vdots$	$\vdots$	$\vdots$	$\vdots$
$\vdots$						
	$\#\, j-3$	$jl-4l$	$W_1(jl-4l)$	$W_1'(jl-4l)$	$f(W_1)$	$d_{j-3}=0$
$j-3^{th}$						
	$\#\, j-2$	$jl-3l$	$W_1(jl-3l)$	$W_1'(jl-3l)$	$f(W_1)$	$d_{j-2}\neq 0$
$j-2^{th}$						

$j-1^{th}$	$\#\, j-1$	$jl-2l$	$W_1(jl-2l)$	$W_1'(jl-2l)$	$f(W_1,W_2)$	$d_{j-1}\neq 0$
j^{th}	$\#\, j$	$jl-l$	$W_1(jl-l)$	$W_1'(jl-l)$	$f(W_1,W_2)$	$d_j\neq 0$
$j+1^{th}$	$\#\, j+1$	jl	$W_2(jl)$	$W_2'(jl)$	$f(W_1,W_2)$	$d_{j+1}\neq 0$
$j+2^{th}$	$\#\, j+2$	$jl+l$	$W_2(jl+l)$	$W_2'(jl+l)$	$f(W_1,W_2)$	$d_{j+2}\neq 0$
$j+3^{th}$	$\#\, j+3$	$jl+2l$	$W_2(jl+2l)$	$W_2'(jl+2l)$	$f(W_2)$	$d_{j+3}\neq 0$
$\vdots$	$\#\, j+4$	$jl+3l$	$W_2(jl+3l)$	$W_2'(jl+3l)$	$f(W_2)$	$d_{j+4}=0$
	$\vdots$	$\vdots$	$\vdots$	$\vdots$	$\vdots$	$\vdots$

Table 5.1. For the calculated rotational angle based on the two different ODSs functions, extra calculation error will be introduced from the difference between $W_1(x)$ and $W_2(x)$ and damage index d_i calculated based on those rotational angles will result in a nonzero value as marked in red in the 7th column from

Table 5.1. Therefore, although $n_L = 2, n_R = 2, M = 3$ can give accurate rotational angle for most nodes,

Element #	Node #	x	w_i	θ_i	θ_i'	d_i
$\vdots$	$\vdots$	$\vdots$	$\vdots$	$\vdots$	$\vdots$	$\vdots$
$j-3^{th}$	$\#\, j-3$	$jl-4l$	$W_1(jl-4l)$	$W_1'(jl-4l)$	$f(W_1)$	$d_{j-3}=0$
$j-2^{th}$	$\#\, j-2$	$jl-3l$	$W_1(jl-3l)$	$W_1'(jl-3l)$	$f(W_1)$	$d_{j-2}\neq 0$
$j-1^{th}$	$\#\, j-1$	$jl-2l$	$W_1(jl-2l)$	$W_1'(jl-2l)$	$f(W_1,W_2)$	$d_{j-1}\neq 0$
j^{th}	$\#\, j$	$jl-l$	$W_1(jl-l)$	$W_1'(jl-l)$	$f(W_1,W_2)$	$d_j\neq 0$
$j+1^{th}$	$\#\, j+1$	jl	$W_2(jl)$	$W_2'(jl)$	$f(W_1,W_2)$	$d_{j+1}\neq 0$
$j+2^{th}$	$\#\, j+2$	$jl+l$	$W_2(jl+l)$	$W_2'(jl+l)$	$f(W_1,W_2)$	$d_{j+2}\neq 0$
$j+3^{th}$	$\#\, j+3$	$jl+2l$	$W_2(jl+2l)$	$W_2'(jl+2l)$	$f(W_2)$	$d_{j+3}\neq 0$
$\vdots$	$\#\, j+4$	$jl+3l$	$W_2(jl+3l)$	$W_2'(jl+3l)$	$f(W_2)$	$d_{j+4}=0$
	$\vdots$	$\vdots$	$\vdots$	$\vdots$	$\vdots$	$\vdots$

it will spread the existed discontinuity by introducing error to the rotational angle of nodes around damage

location. The number of deviated damage indexes has increased to 6. However, since the existed discontinuity between $W_1(x)$ and $W_2(x)$ in w_i will give extra nonzero magnitude to d_j and d_{j+1}, either d_j or d_{j+1} will result in a larger magnitude than other nonzero damage indexes. And damage location still can be identified within a short range. Without knowing which of d_j and d_{j+1} have the largest magnitude, damage location can be identified as elements before and after the nonzero damage index with the largest magnitude to cover the both cases.

Use the same numerical model from the Section 5.2.2, Fig. 5.6 gives the result damage index in a red curve with dots and damage location is marked by the black dash line. As derived in Eq. (5.25b), with rotational angle accurately calculated by SG filter method with $n_L = 2, n_R = 2, M = 3$, damage index of intact beam section stays zero as in Fig. 5.6. And the discontinuous existed in ODSs has resulted into 6 nonzero result damage index. The gray area is identified damage location as elements before and after the result damage index $\bar{d}_{22}$ with the largest magnitude. The damage location has been identified accurately within a slightly extended range.

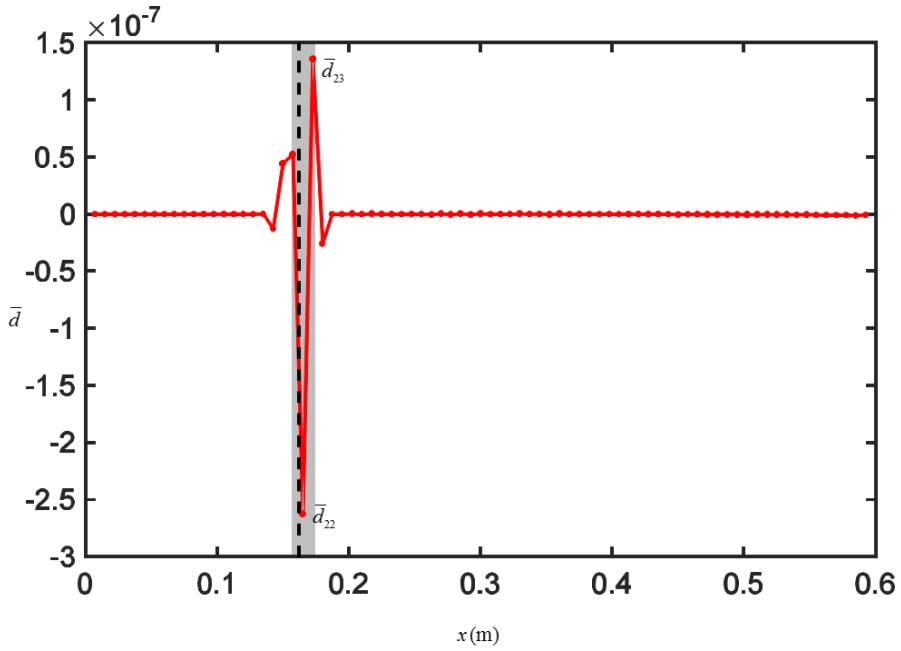

Fig. 5.6 Result damage indexes based on damage beam model from Fig. 5.4 with $n_L = 2$, $n_R = 2$ and $M = 3$ used for θ calculation

However, with $n_L = 0, n_R = 1, M = 3$, the θ_i' can only ensure the accuracy of the term coupling with the coefficient c_1 from the ODSs as in Eq. (5.25a). Then, the damage index will be nonzero for the considered intact structure, and the general form of damage index d_i can be derived as:

$$\begin{aligned} A_{11} &= -12c_2/l + (36 - 36i)c_3 \\ A_{12} &= 12c_2/l + 36ic_3 \\ A_{21} &= 8c_2 + (24i - 24)c_3 l \\ A_{22} &= 4c_2 + 12ic_3 l \end{aligned} \tag{5.26a}$$

$$d_i = -144c_2^2/l + 432c_2c_3(1-2i) + 1296c_3^2 l(i - i^2) \tag{5.26b}$$

where d_i depends on node number i and the ODSs function (c_k). For intact structure that gives the same shape function for each element as $w_i(x) = W(x)$, the d_i only depends on node number i and is continuous through the beam structure. Therefore, a continuous baseline is formed as $B(i)$ and can be

expressed as in Eq. (5.27).

$$B(i) = -144c_2^{\,2}/l + 432c_2c_3(1-2i) + 1296c_3^{\,2}l(i-i^2) \tag{5.27}$$

where $i = 2,3,\ldots(n_N - 2)$. Since the d_i is corresponding to the observed node $\#i$ as a shared node for two consecutive elements, the d_i can only be calculated for $i = 2,3,\ldots(n_N - 1)$. Moreover, since there is no point on the right of the last node, the calculated θ_{n_N} will have a different accuracy (calculation error) with others, and the calculated d_{n_N-1} will not match with the general form of d_i in Eq. (5.26b). With the formed continuous baseline, the discontinuity of ODSs from damage can be identified by the damage index deviated from the formed baseline. A filtered damage index can be calculated as $\hat{d}_i = \bar{d}_i - b_i$ to give a more obvious indication of the existed deviation. And baseline value b_i can be computed either from a reference baseline or approximated baseline as following.

The reference baseline is the baseline of the corresponding intact structure with same properties as the damaged structure. However, the ODSs coefficients in Eq. (5.27) are usually unknown in a real situation, the reference baseline cannot be directly determined by Eq. (5.27) as a function. Responses of the intact structure are required to determine the reference baseline (b_i^r) that a real intact structure or an accurate numerical model of the intact structure is required. Meanwhile, notice the reference baseline based on the corresponding intact beam structure will not exactly match with the actual baseline of the damaged structure. That is because, for a damaged beam structure, two different ODSs existed as before and after damage location. Based on different coefficients from two ODSs and Eq. (5.27), the actual baseline function of a damaged beam structure will be a piecewise function as:

$$B(i)=\begin{cases}B_1(i) & i<j\\ B_2(i) & i>j+1\end{cases} \tag{5.28}$$

Even the existed crack only influence the ODSs of beam section after damage location; the b_i^r can only match with $B_1(i)$ as for the section before damage. With the difference existed between $B_2(i)$ and b_i^r, all damage index will have a relatively small deviation from b_i^r and result in nonzero $\hat{d}_i$.

The approximated baseline function is computed directly from the damage index of the damaged beam structure by curve fitting. The curve fitting is applied to $\bar{d}_i$ point by point with certain window length. However, the accuracy of approximated baseline is influenced by the used window length. Different window length will be used for comparison. The reference baseline and the approximated baseline will also be compared.

Consider the same model from the previous case. The ODSs of beam section before and after damage location is defined as Eq. (5.17a) and Eq. (5.17b) and the damage is located on the j^{th} element. With $n_L=0, n_R=1, M=3$ used for differentiation, the discontinuity existed in ODSs would also be spread and cause more than two deviated d_i around damage location. The deviated d_i can be determined by Table 5.2.

Table 5.2 Displacement, rotational angle and damage index of nodes around damage location with $n_L=0, n_R=1$,

$M = 3$ used for rotational angle calculation.

Element #	Node #	x	w_i	θ_i	θ_i'	d_i	$\hat{d}_i$
⋮	⋮	⋮	⋮	⋮	⋮	⋮	⋮
$j-2^{th}$	$\#\, j-2$	$jl-3l$	$W_1(jl-3l)$	$W_1'(jl-3l)$	$f(W_1)$	$d_{j-2} = B_1(j-2)$	$\hat{d}_{j-2} = 0$
$j-1^{th}$	$\#\, j-1$	$jl-2l$	$W_1(jl-2l)$	$W_1'(jl-2l)$	$f(W_1)$	$d_{j-1} \neq B_1(j-1)$ $\neq B_2(j-1)$	$\hat{d}_{j-1} \neq 0$
j^{th}	$\#\, j$	$jl-l$	$W_1(jl-l)$	$W_1'(jl-l)$	$f(W_1, W_2)$	$d_j \neq B_1(j) \neq B_2(j)$	$\hat{d}_j \neq 0$
$j+1^{th}$	$\#\, j+1$	jl	$W_2(jl)$	$W_2'(jl)$	$f(W_2)$	$d_{j+1} \neq B_1(j+1)$ $\neq B_2(j+1)$	$\hat{d}_{j+1} \neq 0$
$j+2^{th}$	$\#\, j+2$	$jl+l$	$W_2(jl+l)$	$W_2'(jl+l)$	$f(W_2)$	$d_{j+2} = B_2(j+2)$	$\hat{d}_{j+2} = 0$
⋮	$\#\, j+3$	$jl+2l$	$W_2(jl+2l)$	$W_2'(jl+2l)$	$f(W_2)$	$d_{j+3} = B_2(j+3)$	$\hat{d}_{j+3} = 0$
	⋮	⋮	⋮	⋮	⋮	⋮	⋮

Here only one calculated rotational angle as θ_j' is based on the two different ODSs functions that will result in extra calculation error as marked in red in the 6th column from Table 5.2. It will give extra nonzero magnitude to d_{j-1}, d_j or d_{j+1}. While the existed discontinues in ODSs will give extra nonzero magnitude to d_j and d_{j+1}, d_j or d_{j+1} will still result in the largest deviation from the actual baseline.

Damage location can be identified as on elements before and after the filtered damage index with the largest magnitude.

Use the same numerical model from the previous case, Fig. 5.7a gives the result damage index in the red curve with red dots and damage location in black dash line. With rotational angle inaccurately calculated by the SG filter method with $n_L = 0, n_R = 1, M = 3$, a continuous baseline is formed. The magenta dash line in Fig. 5.7a is the reference baseline b_i^r computed based on an intact structure with the same physical property and dimension. And Fig. 5.7b gives the filtered damage index $\hat{d}^r = \overline{d}_i - b_i^r$ in magenta curve and dots and damage location in black dash line. As discussed, for the beam section after damage location, there exists a difference between the ODSs of the intact and damaged structure, then the reference baseline and the actual baseline will be different. Using the reference baseline function will result in nonzero $\hat{d}^r$ for the intact section. However, with the discontinues in ODSs, the filtered damage index still give the largest magnitude at damage location, and the damage location can be identified accurately by using the reference baseline for this case.

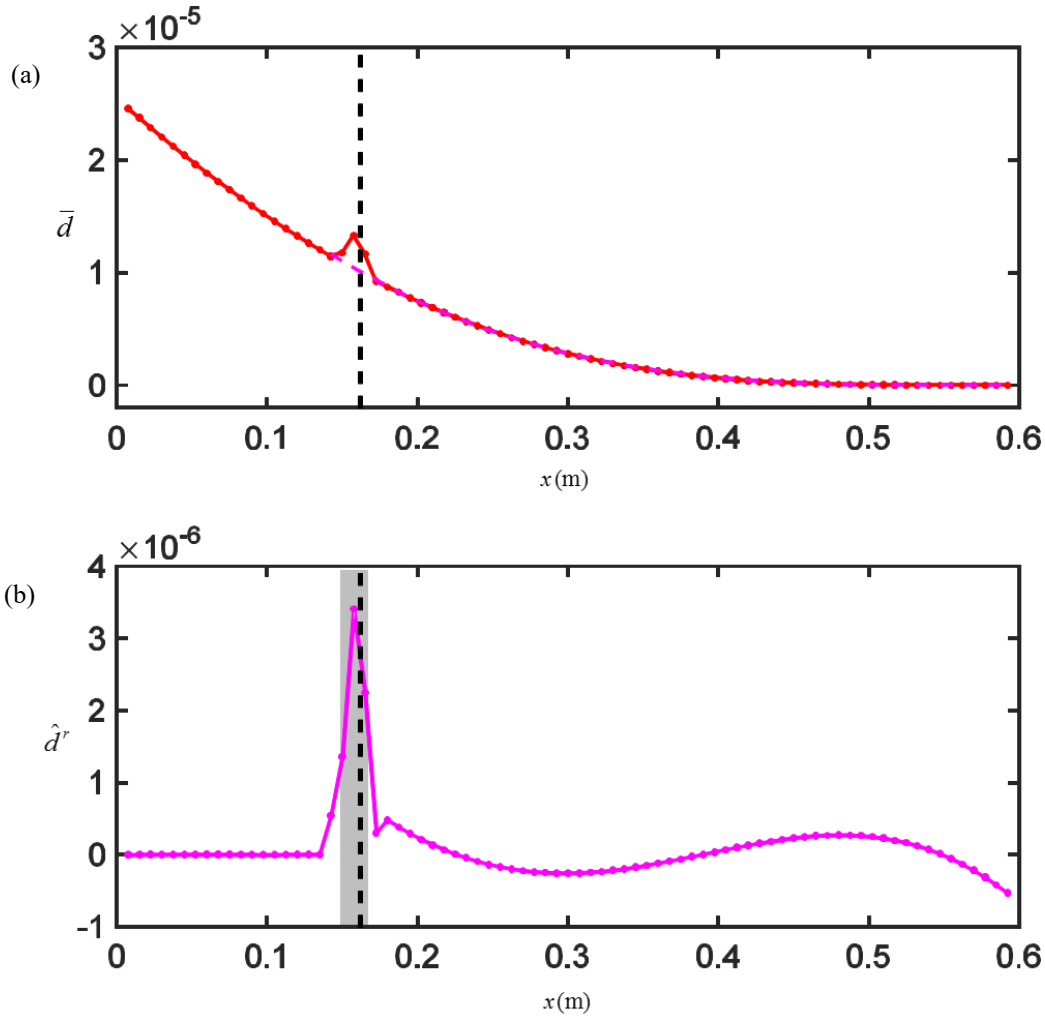

Fig. 5.7 (a) Result damage index of damaged beam model from Fig. 5.4 with rotational angle calculated with $n_L = 0, n_R = 1, M = 3$ and reference baseline computed by corresponding intact beam model, (b) filtered damage index based on reference baseline.

When it comes to computing the approximated baseline, different window length used in curve fitting will give a different baseline value and a different filtered damage index. With a cubic polynomial assumption, Fig. 5.8a gives computed baseline based on window length of 10 elements, 20 elements, 40 elements and 78 elements (since d_i can only be calculated for $i = 2,3,...,n_N - 1$) as b_i^{10a}, b_i^{20a}, b_i^{40a} and b_i^{78a} in blue, green, cyan and brown dash curves, respectively. The red curve with dots is the calculated damage index, and the

black dash line indicates the damage location. Figure 5.8b gives the filtered damage index based on b_i^{10a}, b_i^{20a}, b_i^{40a} and b_i^{78a} in blue, green, cyan and brown dash curves with dots, respectively.

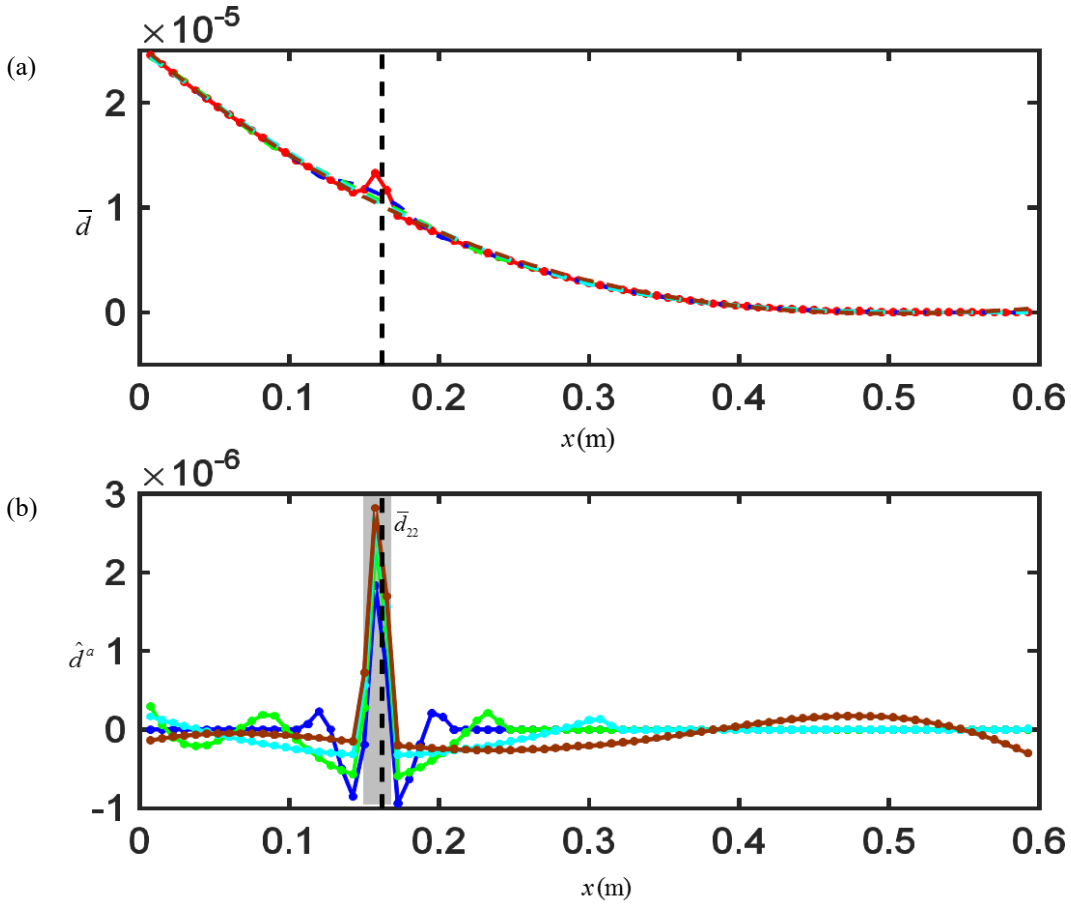

Fig. 5.8 (a) Result damage index of damaged beam model from Fig. 5.4 with rotational angle calculated with $n_L = 0, n_R = 1, M = 3$ and approximated baselines computed by curve fitting with different window length, (b) filtered damage index based on different approximated baselines.

From Fig. 5.8a one can see that with a relative shorter window length such 10 elements, the deviation existed in result damage index will be captured more obviously in approximated baseline. Therefore, the filtered damage index will have a relative small nonzero value at damage location. However, the shorter window length also has less b_i influenced by the existed deviation and result in smaller $\hat{d}_i^a$ around damage location as the blue curve in Fig. 5.8b. On the contract, with a relatively long section length as 78 elements,

the existed deviation will not be captured locally in the approximated baseline, so the filtered damage index has a relative large magnitude at damage location. Meanwhile, more nonzero $\hat{d}_i^a$ exist. For all four window length used here, filtered damage index gives the largest magnitude at the damage location, and the damage location can accurately be identified as the marked gray area.

In addition to the reason that deviated damage index is influencing the accuracy of the approximated baseline, the situation that the actual baseline is a picewise function also leads to an inaccurate computation of approximated baseline. If the result damage index can be divided into two different sets and fitted as a piecewise function, a more accurate approximated baseline can be achieved. When the deviation existed in result damage index is recognizable, an initial guess of damage location can be defined as $\{S_d\}$. Then, result damage index before and after the damage location can be divided into two sets as $\{S_1\}$ and $\{S_2\}$ and can be used to compute two approximated baseline separately. Notice that the extension of the baseline from sections before and after damage location can be used as the baseline of the damage section $\{S_d\}$. Fig. 5.9a gives result damage index in red curve and dots and damage location by the black dash line. The existed deviation is recognizable from Fig. 5.9a and the initial guess of damage can be defined as $\{S_d\} = \{\#20, \#21, ..., \#24\}$ as the marked gray area in Fig. 5.9a. Then, rest of result damage index can be divided into two sets as $\{S_1\} = \{\#2, \#3, ..., \#19\}$ and $\{S_2\} = \{\#25, \#26, ..., \#80\}$. Approximated baseline of nodes in those two sets can be computed based on curve fitting separately. The green dash line in Fig. 5.9a is the approximated baseline based on the set $\{S_1\}$ and has been extended to cover the $\{S_d\}$, the blue dash line in Fig. 5.9a is the approximated baseline based on set $\{S_2\}$ and has also been extended to cover the $\{S_d\}$. The curve fitting of nodes in each set was performed with the window length same as the set length. The

approximated baseline of the set $\{S_d\}$ is calculated as the average of the baseline value given by the extension of the baseline from the set $\{S_1\}$ and $\{S_2\}$ as in Eq. (5.29). Then, filtered damage index can be calculated as $\hat{d}_i^a = \bar{d}_i - b_i^a$ as the blue curve with dots in Figure 5.9b. The black dash line indicates the damage location.

$$b_i^a = \begin{cases} B_{a1}(i) & i \in \{S_1\} \\ \left(B_{a1}(i) + B_{a2}(i)\right)/2 & i \in \{S_d\} \\ B_{a2}(i) & i \in \{S_2\} \end{cases} \tag{5.29}$$

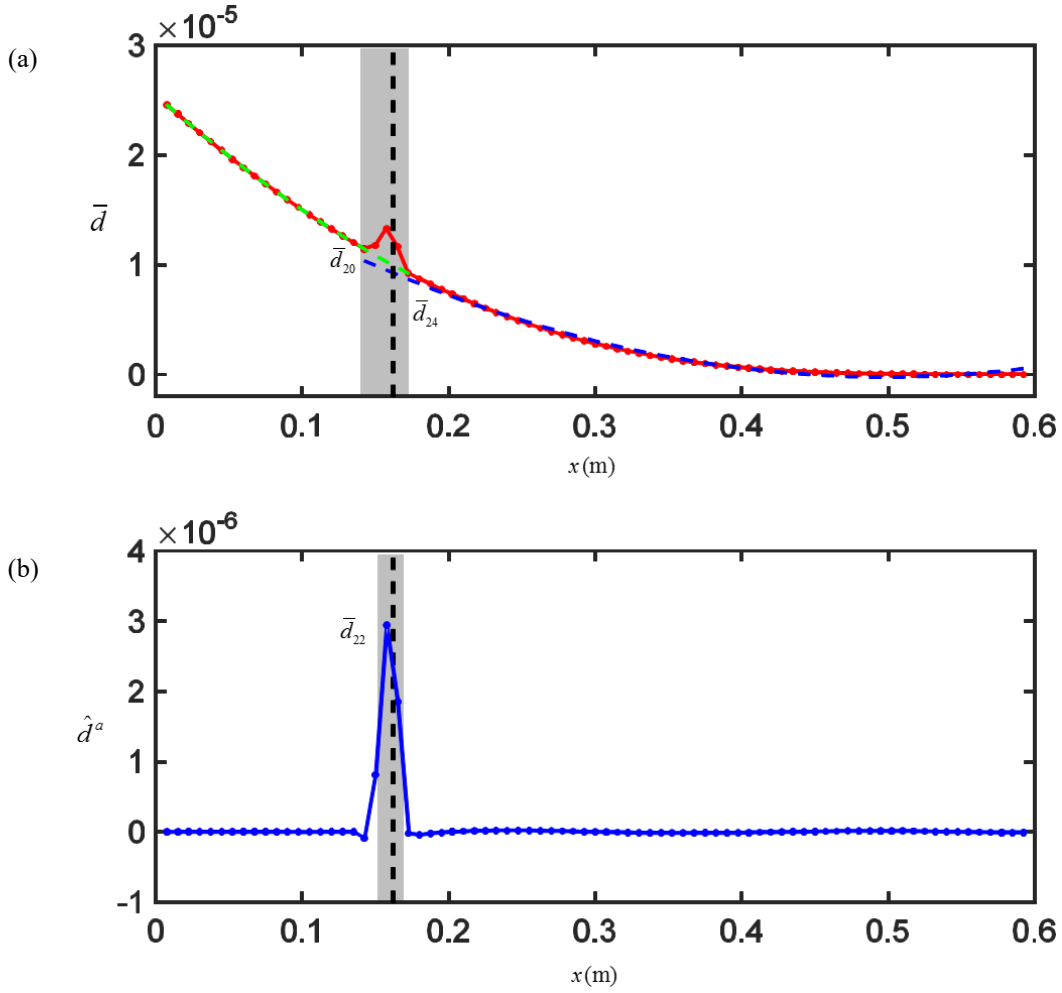

Fig. 5.9 (a)Result damage index of damaged beam model from Fig. 5.4 with rotational angle calculated with $n_L = 0$, $n_R = 1$, $M = 3$ and approximated baselines computed by the set $\{S_1\}$ and $\{S_2\}$ and (b) filtered damage index.

With the approximated baseline computed as a piecewise function, a more accurate baseline has been achieved. The filtered damage index of intact beam section has a relatively smaller value than previous cases, and damage location shows more clearly. The gray area is identified damage location, and it matches with the actual damage location. However, with measuring noise and nonlinear behavior existed, the deviation may not be recognizable from the result damage index. Approximated baseline can be computed directly from curve fitting without dividing sets. And since the reference baseline requires an intact structure or the numerical model of an intact structure which may not be available or accurate, it is not practically for experimental validation. Therefore, the approximated baseline will be used to compute the baseline and the filtered damage index in later cases.

5.3.2 Application on Steady-State Vibration

Since the case that a cantilever beam with an applied force on the free end gives the ODSs in the form of 3^{rd} order polynomial that match with the form of the shape function from the Euler-Bernoulli beam theory, it will give the same shape function for each element with continuous ODSs and damage index will be all zero for intact structure. However, there exists a lot more cases with ODSs that are not in the form of a 3^{rd} order polynomial. For example, when a distribution pressure is applied to the surface of the cantilever beam, the deflection would be in a 4^{th} order polynomial as in Eq. (5.15). And more commonly, all the steady state vibration are exited by harmonic input would give the ODSs as a pseudo-trigonometric function as in Eq. (5.16). Therefore, having a continuous ODSs that are not in 3^{rd} order polynomial is a common situation and needs to be discussed.

Meanwhile, considering the operability, for measurements that can only measure dynamical signal point by point, a designed free-transient vibration as a cantilever beam with applied force needs to be repeated at least n_N times to get all the nodes measured. It requires the repeated experiments has high consistent to simulate the measured responses as the responses to the same excitation. Although an applied force can be relatively easier to realized and controlled, the consistency between each measured response still cannot be ensured. And the applied distributed pressure is hard to realize in the experiment. Therefore, the steady state vibration with consistent behavior is better for experimental validation. And it is also more widely used [66, 67] for damage detection.

With a harmonic input, once the structure reached the steady state vibration, responses measured point by point would be relatively more consistent along the x-axis and the time trace. And it is practically easier to do in experimental validation without a lot of repeated experiments. Therefore, the feasibility of applying the stiffness-CMM to responses from steady state needs to be discussed before experimental validation. Recall Eq. (5.16) as the ODSs of an intact beam structure subjected to a harmonic excitation frequency ω. It is continuous, and its first three derivative functions are also continuous as: 1st derivative as rotational angle function $\Theta(x) = W'(x)$, 2nd derivative as moment function $M(x) = \frac{1}{EI}W''(x)$ and 3rd derivative as shear force function $F_s(x) = \frac{1}{EI}W'''(x)$. With continuous displacement and rotational angle along the x-axis in this case, although the calculated damage index of the intact structure will be nonzero, it forms a continuous baseline. However, it is relative hard to derive the general form of shape function from the ODSs with trigonometric function term existed. Therefore, instead of the general formula of damage index, a numerical model of an intact structure will be used to explain and confirm the existed relationship of the continuous ODSs to

continuous baseline.

Consider an intact beam structure with the same dimension and physical property as the beam from Fig. 5.4, the first six natural frequency can be calculated by its finite element model.

Table 5.3 Natural frequency and designed exciting frequency of an intact beam structure

Natural frequency	f_1	f_2	f_3	f_4	f_5	f_6
Intact structure (Hz)	11.449	71.726	200.73	393.04	649.07	968.39
Case #	1	2	3	4	5	6
Exciting Frequency(Hz)	15	80	220	450	700	1200

The first row in

Table 5.3 gives the first six natural frequencies based on numerical beam model from the ABAQUS. Although the ODSs is more sensitive to damage because it is the actual response of all modes combined, the used exciting frequency away from certain natural frequency can cost mixed mode vibration, irregular ODSs and difficult to detect damage location [3]. Therefore, it is better to use the exciting frequency close to certain natural frequency. Here the exciting frequencies are chosen higher than the first six natural frequencies to have a vibration close to the first six mode vibration. The designed exciting frequencies are given in the 4th row in

Table 5.3. A simplification of first 10 mode vibration instead of the response of all modes are used in

the numerical model. Then, ODSs of the 1st, 2nd, 3rd, 4th, 5th and 6th case can be collected by the displacement responses given by ABAQUS. Figure 5.10 gives the normalized ODSs of the 1st, 2nd, 3rd, 4th, 5th and 6th case by the red, green, blue, magenta, yellow and brown curve, respectively.

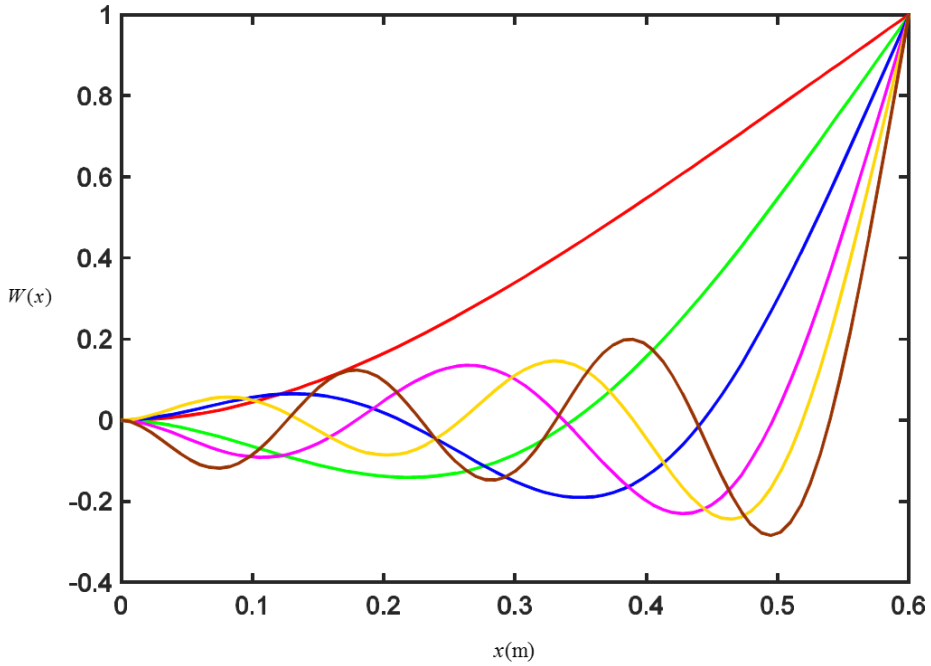

Fig. 5.10 ODSs of an intact beam structure with exciting frequency listed in the 4th row of Table 5.3.

To simulate the real situation, the rotational angle will be calculated based on the displacement. Although the designed two sets of n_L, n_R and M have been compared and discussed in the section 5.3.1, that is only based on the assumption of ODSs is a 3rd order polynomial. With the ODSs as a 3rd order polynomial, its first derivative can be accurately calculated by 2nd order central differentiation. However, when it comes to steady state vibration with trigonometric function term existed in its the ODSs, the actual rotational angle as the Eq. (5.30) cannot be calculated accurately by a simple linear combination of

displacement.

$$\Theta(x) = -\beta p_1 \sin \beta x + \beta q_1 \cos \beta x + \beta p_2 \sinh \beta x + \beta q_2 \cosh \beta x \tag{5.30}$$

On the other hand, $n_L = 0, n_R = 1, M = 3$ or $n_L = 1, n_R = 0, M = 3$ with relative fewer points involved in the calculation would introduce less coupling from different shape function of different elements. $M = 3$ is still used here since the shape function is still in the form of a 3rd order polynomial. Based on ODSs give in Fig. 5.10, rotational angle signal calculated with $n_L = 0, n_R = 1$ and $M = 3$ are given in Fig. 5.11. The value of each case has been normalized to have a maximum as 1. The red, green, blue, magenta, yellow and brown curve present the rotational angle of the 1st, 2nd, 3rd, 4th, 5th and 6th case, respectively.

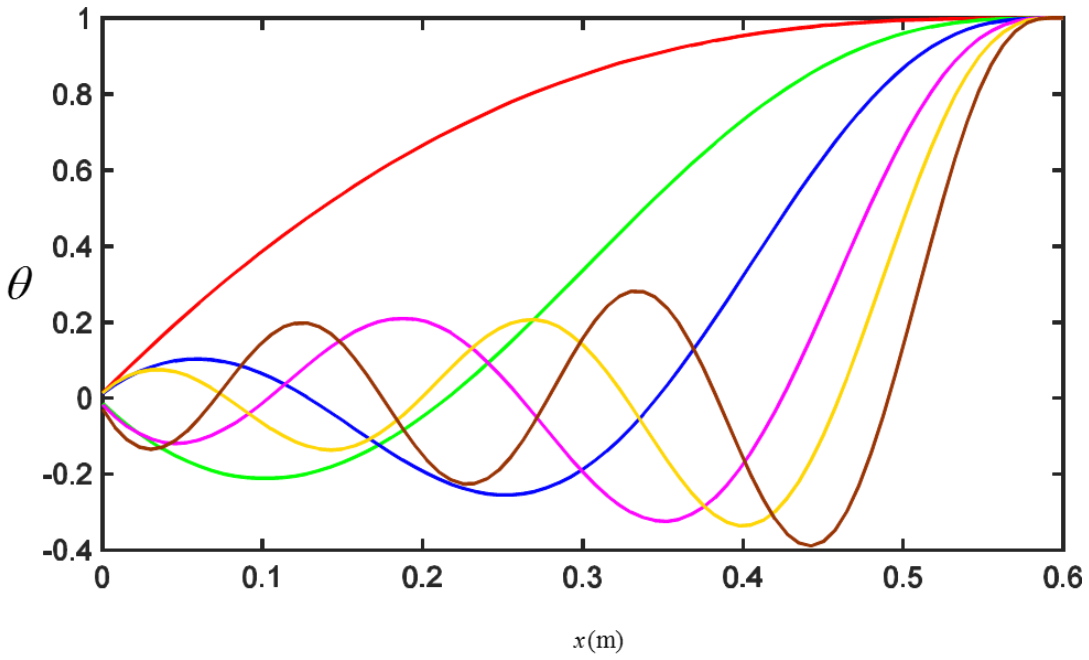

Fig. 5.11 Rotational angle of six mode vibration at certain time instant with exciting frequency from Table 5.3.

Then, damage index (reference baseline) of six mode vibrations can be calculated. Figure 5.12 gives result damage index of these six cases. And the value of each case has been normalized to have a maximum value as 1. The red, green, blue, magenta, yellow and brown curve present the resulting damage index of the 1st, 2nd, 3rd, 4th, 5th and 6th case, respectively.

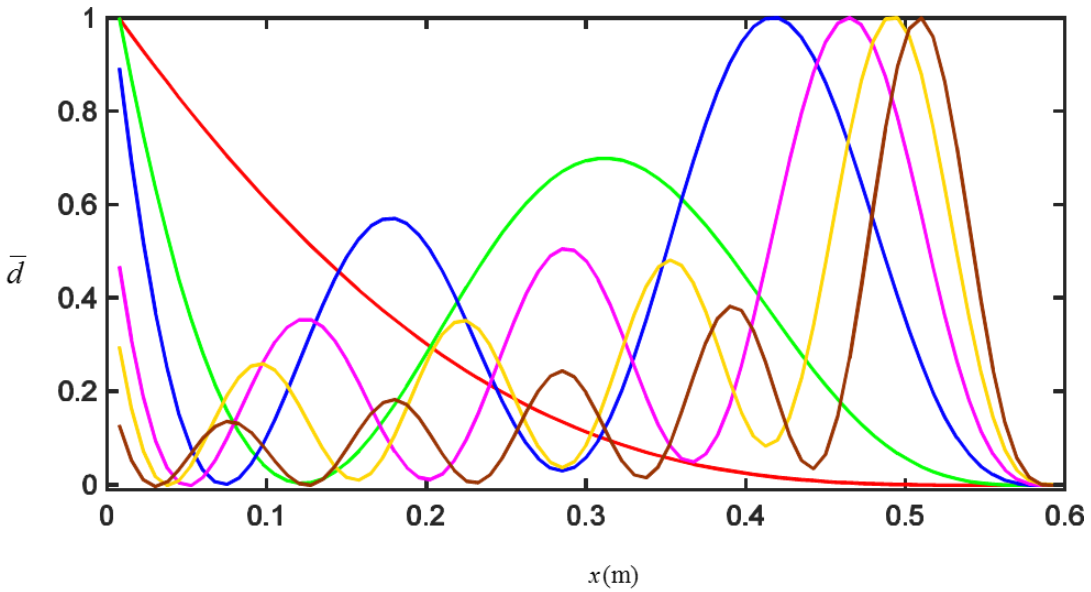

Fig. 5.12 Result damage index of six mode vibration with exciting frequency from Table 5.3.

As shown in Fig. 5.12, the resulting damage index is continuous through the beams structure in all six cases. Therefore, although a continuous ODSs not in the form of 3rd order polynomial will result in nonzero damage index, the result damage index is continuous through the beams structure and can be understood as a baseline. Then, damage location can be identified by the deviated damage index from the formed baseline. And filtered damage index will be computed with the approximated baseline as $\hat{d}_i^a = \bar{d}_i - b_i^a$. With the pseudo-trigonometric function shape existed in the baseline, window length used for different mode shape would be different to get the best fit. And if deviation caused by damage is recognizable in result damage

index, a more accurate baseline function can be computed by dividing result damage index into different sets and do the curve fitting separately.

Based on the numerical model of the beam with transverse crack as shown in Fig. 5.4, the first six natural frequency can be calculated as the second row in Table 5.4. First six natural frequency of the corresponding intact beam has been listed in the first row in Table 5.4. Then, the natural frequency change ratio can be calculated as the third row in Table 5.4. According to natural frequency change ratio, the 1st mode would be the most sensitive mode to this specific damage [10].

Natural frequency	f_1	f_2	f_3	f_4	f_5	f_6
Intact structure (Hz)	11.449	71.726	200.73	393.04	649.07	968.39
Crack at L_1 (Hz)	11.418	71.723	200.33	392.42	649.06	967.09
$(f_H - f_D)/f_H$	2.7×10^{-3}	4.2×10^{-5}	2.0×10^{-3}	1.5×10^{-3}	1.5×10^{-5}	1.3×10^{-3}

Table 5.4 First six natural frequency of heathy/damaged beam model from ABAQUS.

Using harmonic force input with the same exciting frequency from the 4th row of

Table 5.3, beam with transverse crack can be excited to steady state vibration with its ODSs close to the 1st, 2nd, 3rd, 4th, 5th and 6th mode shape. Based on displacement signals generated from the numerical model in ABAQUS, rotational angle can be calculated by the SG filter method with $n_L = 0, n_R = 1$ and $M = 3$. And result damage index can be calculated by applying the stiffness-CMM to displacement and calculated rotational angle signals. Fig. 5.13a, 5.14a, 5.15a, 5.16a, 5.17a, 5.18a, gives corresponding result damage

index of six cases in a red curve with dots, respectively. Damage location has been marked by the black dash line. Approximated baseline for each case has been computed with different window length. A general rule is used here to determine the window length used in computing approximated baseline. Counting the existed local extreme points along with the first/last points as p, then window length of $\frac{n_E}{p}$ is used with the same number of points from each side. In other words, $n_L = n_R = \frac{n_E}{2p}$ and $M = 3$ is used. Based on the shape of the result damage index, used window length for 1st, 2nd, 3rd, 4th, 5th and 6th case is 40 elements, 16 elements, 12 elements, 10 elements, 8 elements, 6 elements, respectively. And the approximated baseline is given as

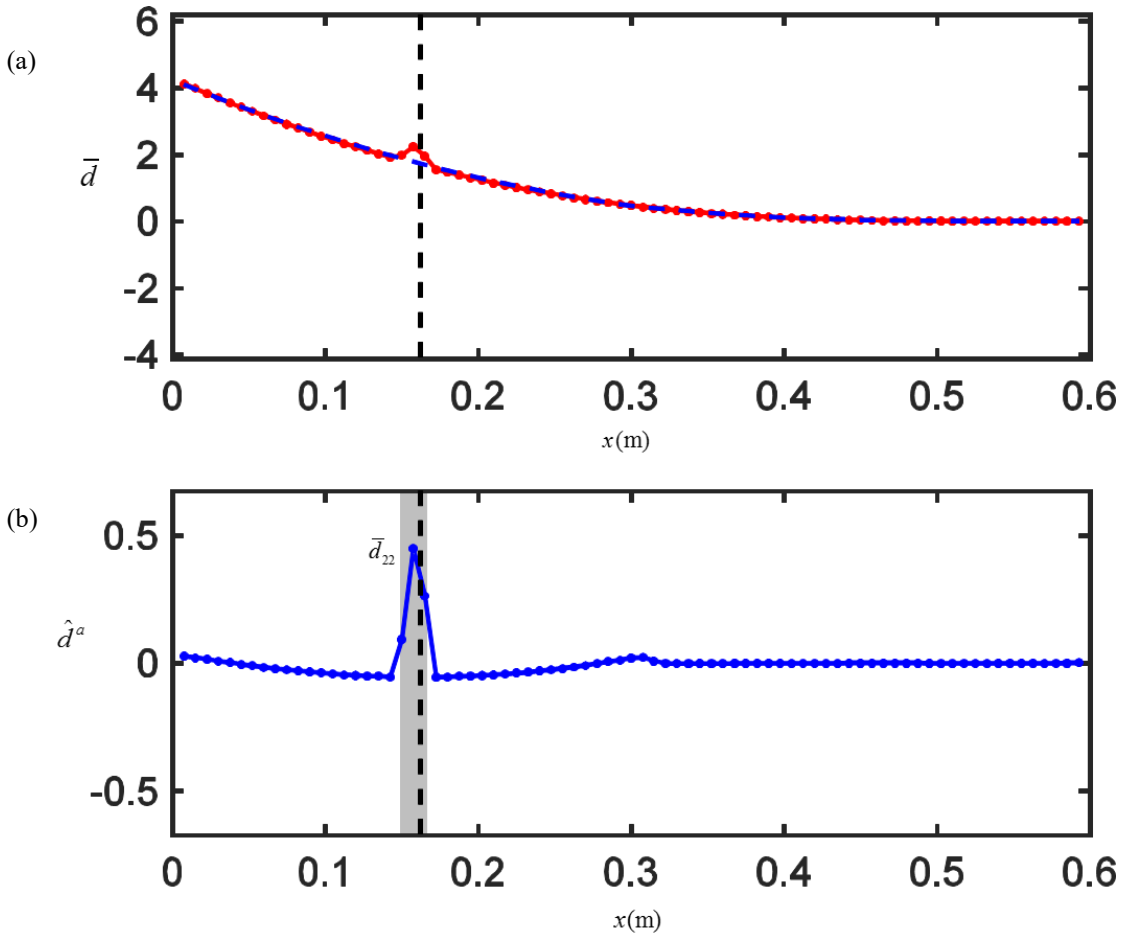

the blue dash curve in Fig. 5.13a, 5.14a, 5.15a, 5.16a, 5.17a, 5.18a, respectively. The filtered damage index calculated as $\hat{d}_i^a = \bar{d}_i - b_i^a$ is given in blue curve with dots in Fig. 5.13b, 5.14b, 5.15b, 5.16b, 5.17b, 5.18b,

respectively.

Fig. 5.13 (a) Damage index of the 1st case with an exciting frequency of $f_1 = 15Hz$, (b) corresponding filtered damage index based on approximated baseline.

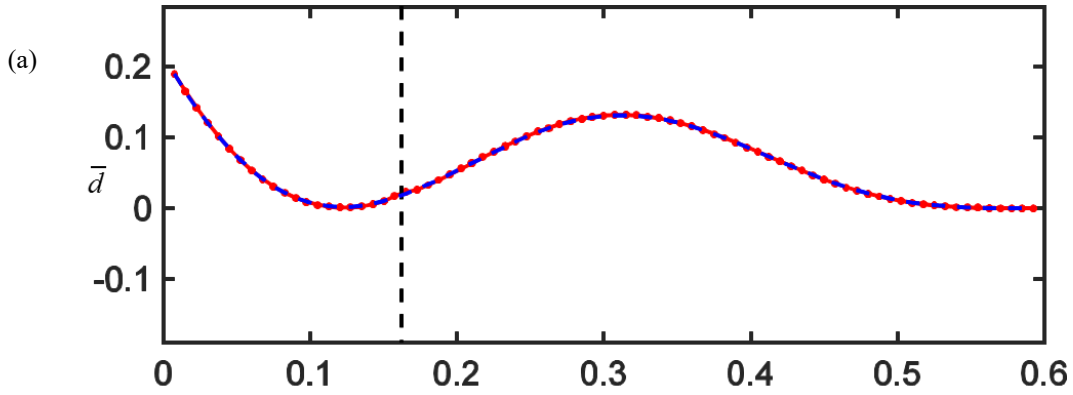

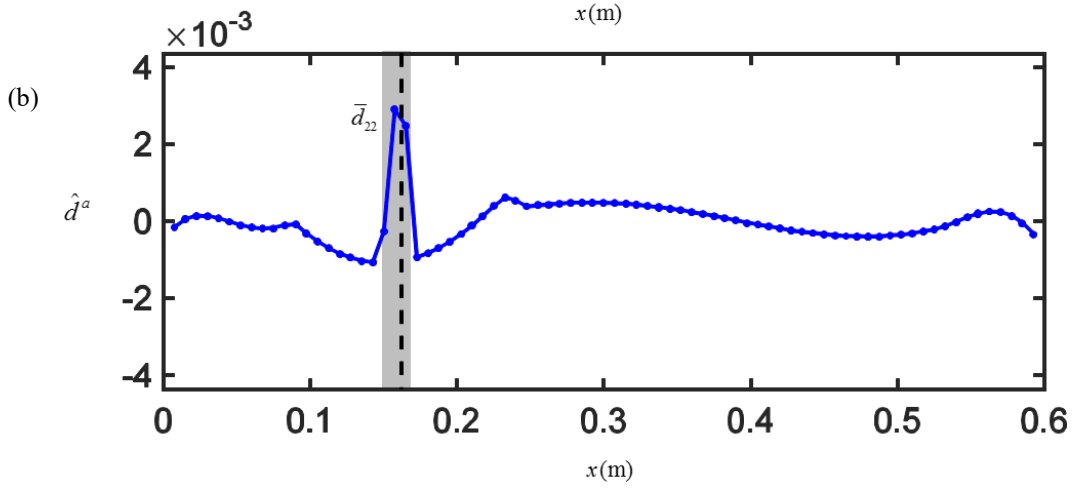

Fig. 5.14 (a) Damage index of the 2nd case with an exciting frequency of $f_2 = 80Hz$, (b) corresponding filtered damage index based on approximated baseline.

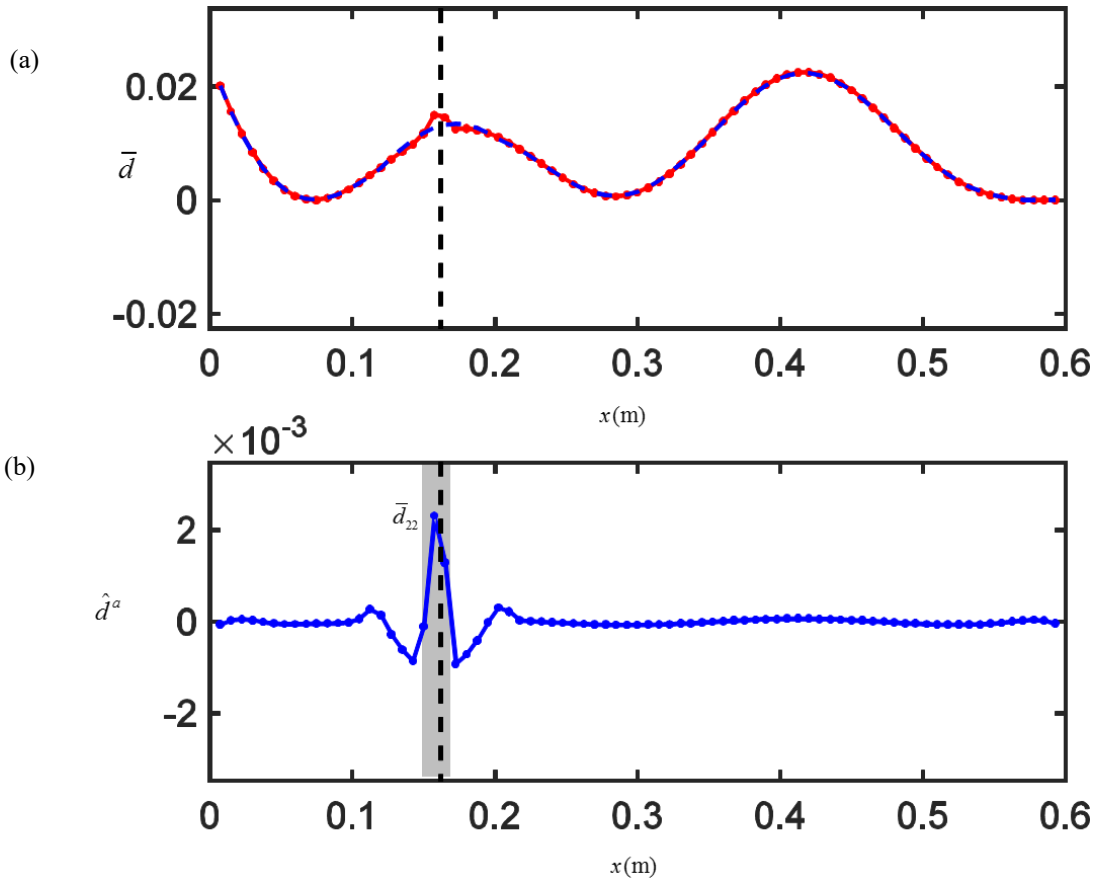

Fig. 5.15(a) Damage index of the 3rd case with an exciting frequency of $f_3 = 220Hz$, (b) corresponding filtered damage index based on approximated baseline.

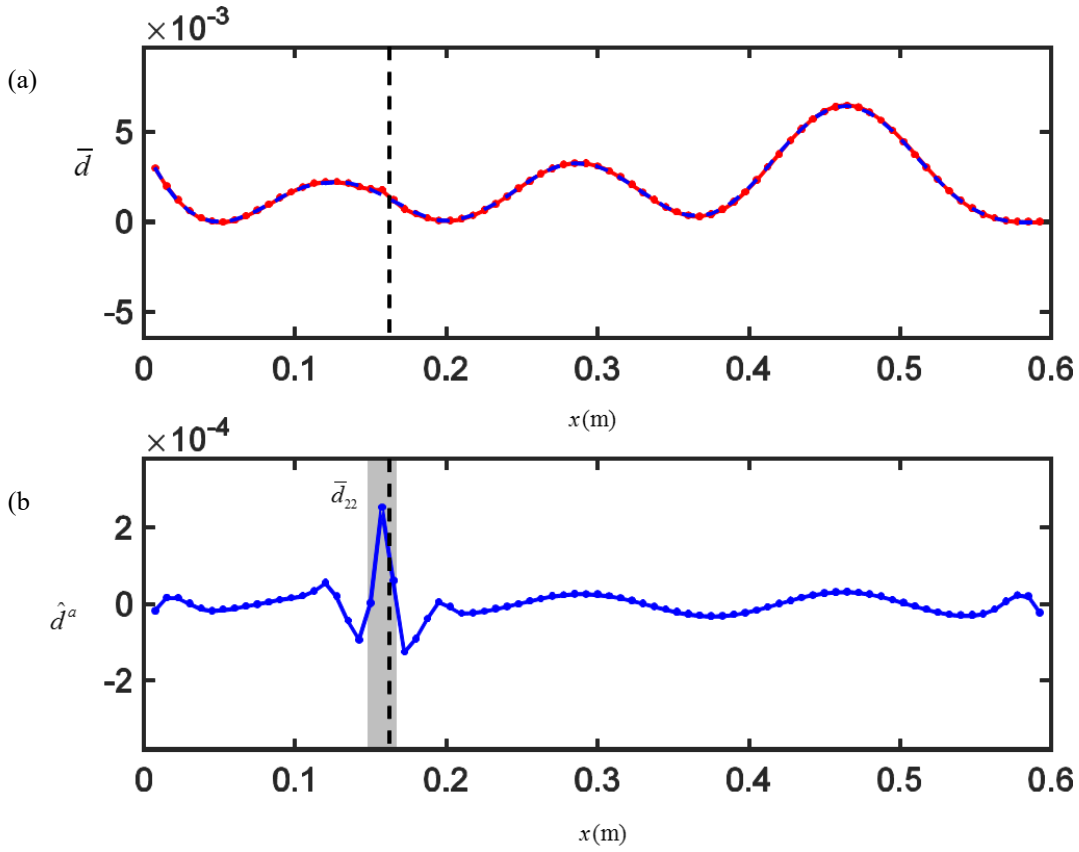

Fig. 5.16(a) Damage index of the 4th case with an exciting frequency of $f_4 = 450Hz$, (b) corresponding filtered damage index based on approximated baseline

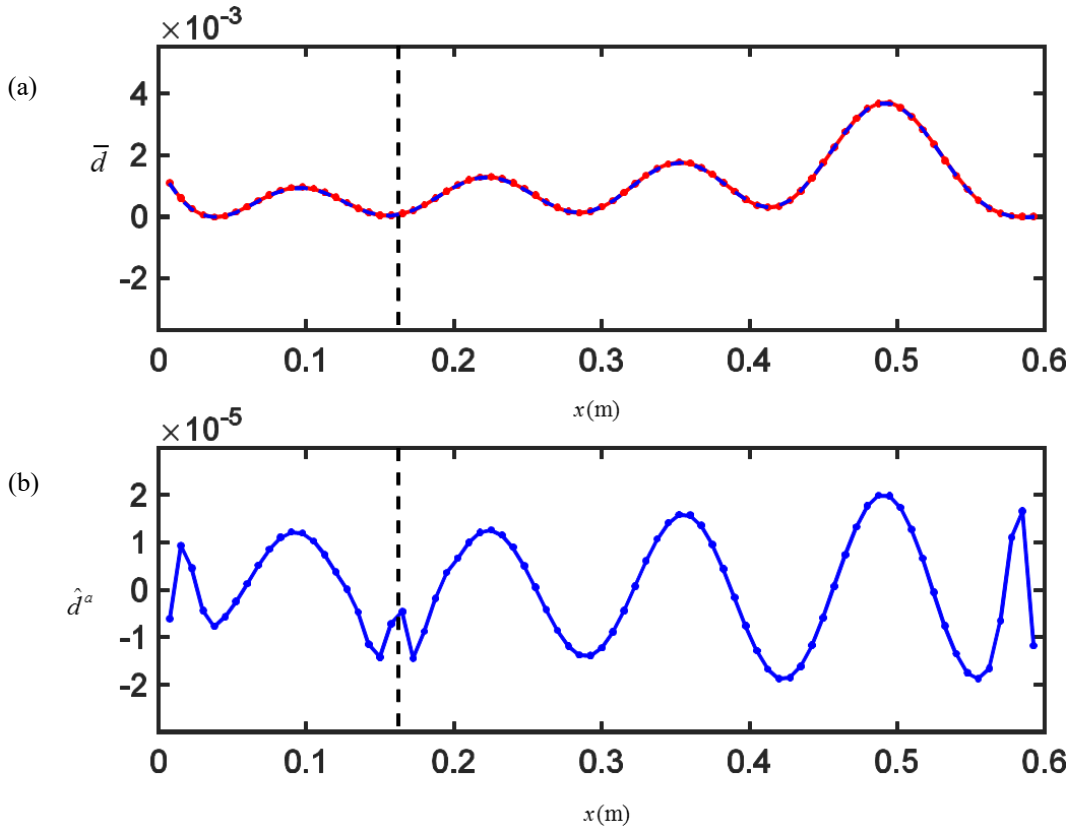

Fig. 5.17(a) Damage index of the 5th case with an exciting frequency of $f_5 = 700Hz$, (b) corresponding filtered damage index based on approximated baseline.

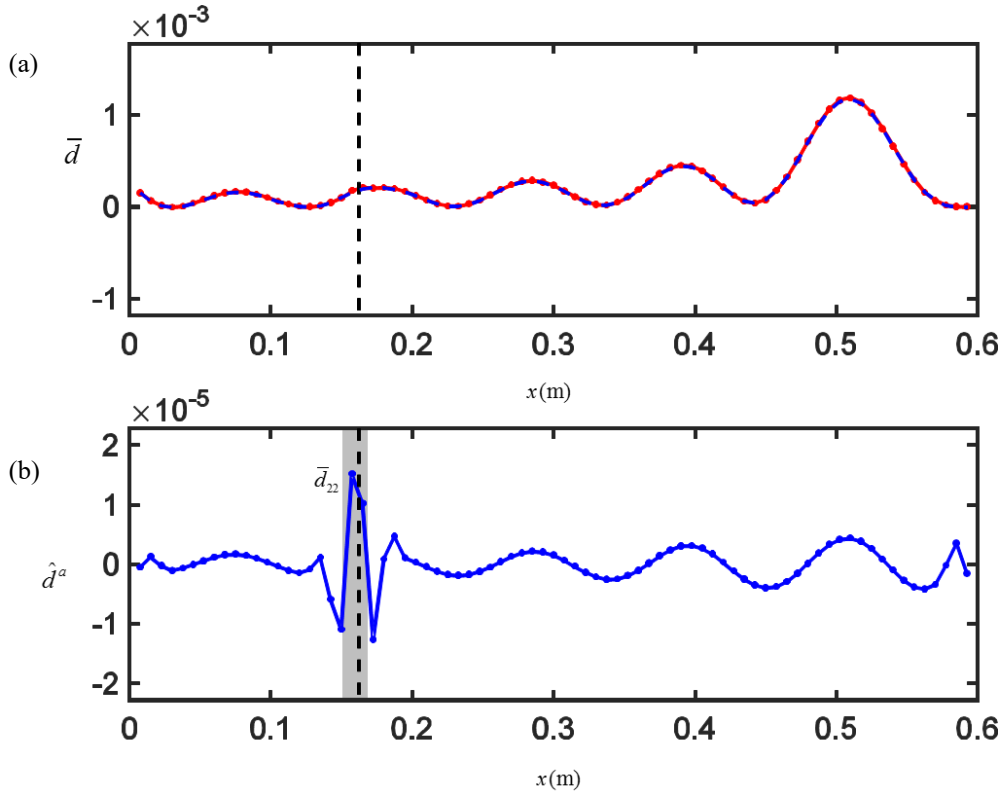

Fig. 5.18(a) Damage index of the 6th case with an exciting frequency of $f_6 = 1200Hz$, (b) corresponding filtered damage index based on approximated baseline.

Based on Fig. 5.13b, 5.14b, 5.15b, 5.16b and 5.18b, $\hat{d}_{22}$ gives the largest magnitude among the filtered damage index. Therefore, damage location can be identified accurately as on elements before and after $\hat{d}_{22}$ for these cases. And among these cases, the 1st and 3rd case with relative large natural frequency change ratio has a relative obvious deviated damage index from the formed baseline as in Fig. 5.13a&5.15a. An initial guess of damage location can be defined as in set $\{S_d\}$, and a more accurate baseline can be computed by dividing result damage index into two sets as $\{S_1\}$ and $\{S_2\}$ as before and after the defined set $\{S_d\}$.

For the 5th case with relative small natural frequency change ratio, although baseline filtering has been applied to result in damage index once, the filtered damage index still has an obvious baseline. It can be caused by the relative longer window length, or the calculation error existed between approximated baseline (polynomial curve fitting) and actual baseline (trigonometric function). And although neither $\hat{d}_{22}$ or $\hat{d}_{23}$ has the largest magnitude, the existed damage still can be recognized by the obvious deviation at damage location from the baseline of the filtered damage index. The reason 5th case is relative insensitive to existed damage is that based on the ODSs of 5th case from Fig. 5.10, the responses around the damage location have relative small vibration amplitude. Therefore, the discontinuous existed between those responses can only result in relative small nonzero value for damage index and relative small deviation for $\bar{d}_{22}$ and $\bar{d}_{23}$ from the actual baseline.

5.4 Noise Simulation and the Mass Characteristic Matrix Method

5.4.1 Noise simulation

When it comes to measured responses from the experiment with measuring noise existed, measuring noise and measuring error from interference signal can create a discontinuity in ODSs and be identified as a false damage location. Therefore, mode vibration with relative small natural frequency change ratio may not give an identified damage location. On the contract, mode vibration with relative large natural frequency change ratio can be more robust to give the accurate damage location with existed measuring error. Other research [9] also points out the most important factor for identifying damage location would be the selection of the modes used in the analysis. Therefore, based on calculated natural frequency change ratio given in Table 5.4,

with exciting frequency around the 1st and 3rd mode natural frequency, the ODSs will give a more robust behavior with measuring noise, and vibration that mainly consist of 2nd and 5th mode vibration would be easily influenced by measuring noise.

In order to simulate noise in the measurement, a vector of random numbers is generated by each component drawn from a standard normal distribution as discussed in section 2.2.4. The standard deviation of noise is proportional to the magnitude of displacement of each point at each time instant. Consider the case with exciting frequency as $f_1 = 15Hz$, noise with the standard deviation of $\sigma = 0.01u_i(t)$ at each time instant is added to each displacement signal. Figure 5.19 gives a few ODSs from the displacement signals with added noise.

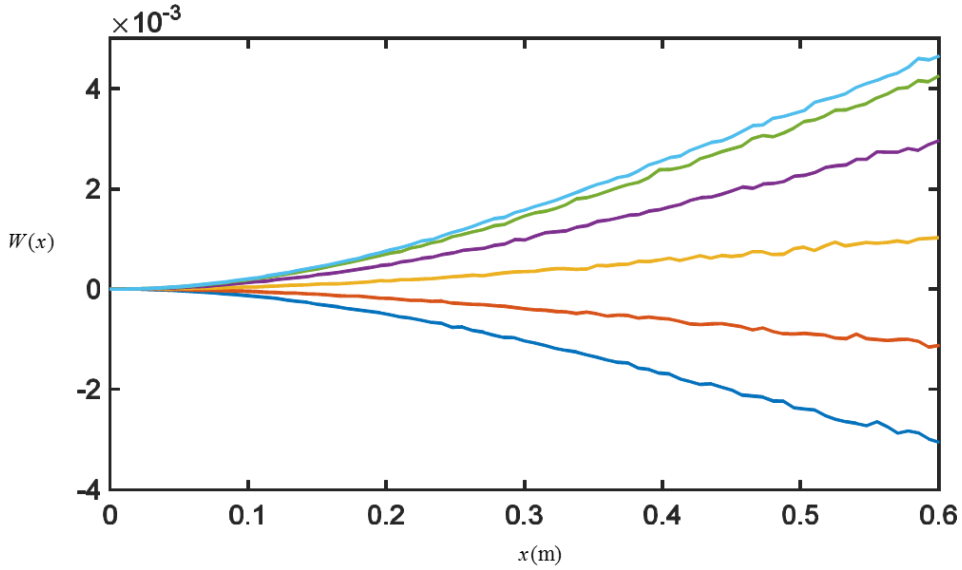

Fig. 5.19 ODSs from displacement signals with added noise.

With a standard deviation of noise proportional to the magnitude of displacement, beam section close to the free end with a relatively large vibration amplitude will have added noise in larger magnitude. It will

result in a larger error in displacement along the z-axis. With the same element length along the x-axis, the larger error along the z-axis will result in a larger error in its first derivative (rotational angle) and give a more obvious discontinuity in ODSs. Moreover, the discontinuity caused by noise can be larger than the discontinuity from existed damage. Then, the actual damage location cannot be identified accurately.

When computing the rotational angle, getting fewer displacement signals and their added noise coupled together can have a less accumulated error. Thus, only one displacement from the left/right of the observed node will be used. For 1st mode vibration with increasing vibration amplitude along the x-axis, the node from left always have a smaller amplitude, and smaller added noise, displacement of the node from left is used for rotational angle calculation. In other words, the finite difference will be performed by SG filter with $n_L = 1, n_R = 0$ and $M = 3$ to compute the rotational angle signals of each node. Figure 5.20a gives displacement signals of node #1, #11, ..., #81 and Fig. 5.20b gives computed rotational angle signal of the node #1, #11, ..., #81.

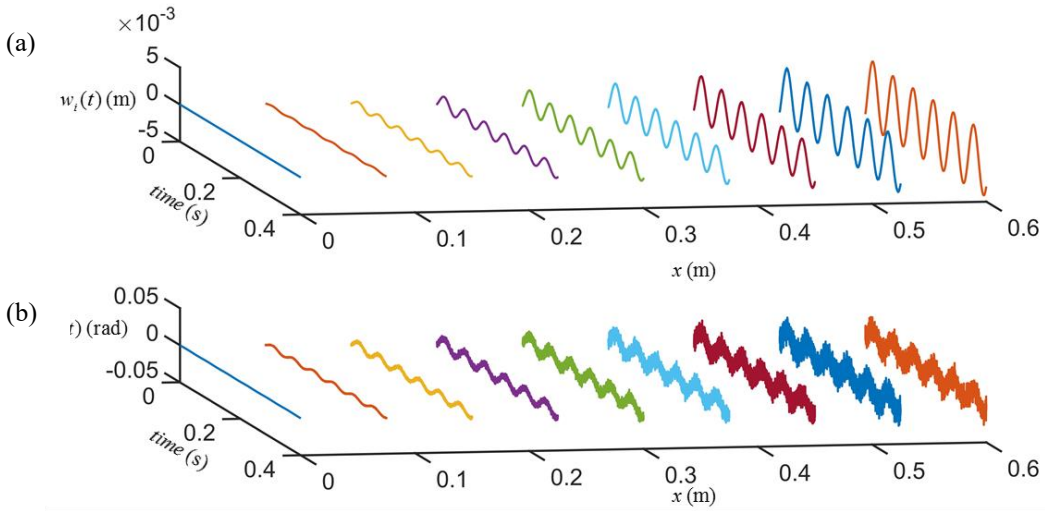

Fig. 5.20 (a) Displacement signal with added noise of node #1, #11, ..., #81 for beam structure from Fig. 5.4 with an exciting frequency of $f_1 = 15Hz$ and (b) corresponding rotational angle signals.

Although added noise cannot be recognized by displacement signal in Fig. 5.20a, the existed noise amplified by differentiation shows clearly in rotational angle signal as in Fig. 5.20b. Moreover, rotational angle signals of beam section close to the free end have a relative larger noise. Applying stiffness-CMM to the displacement signals and computed rotational angle signals, result damage index can be computed as the average of calculated damage index at each time constant. Based on the general rule of window length given in section 5.3.2, window length used for computing approximated baseline is 40 elements. Figure 5.21a gives the result damage index in the red curve with dots and computed approximated baseline in blue dash line and

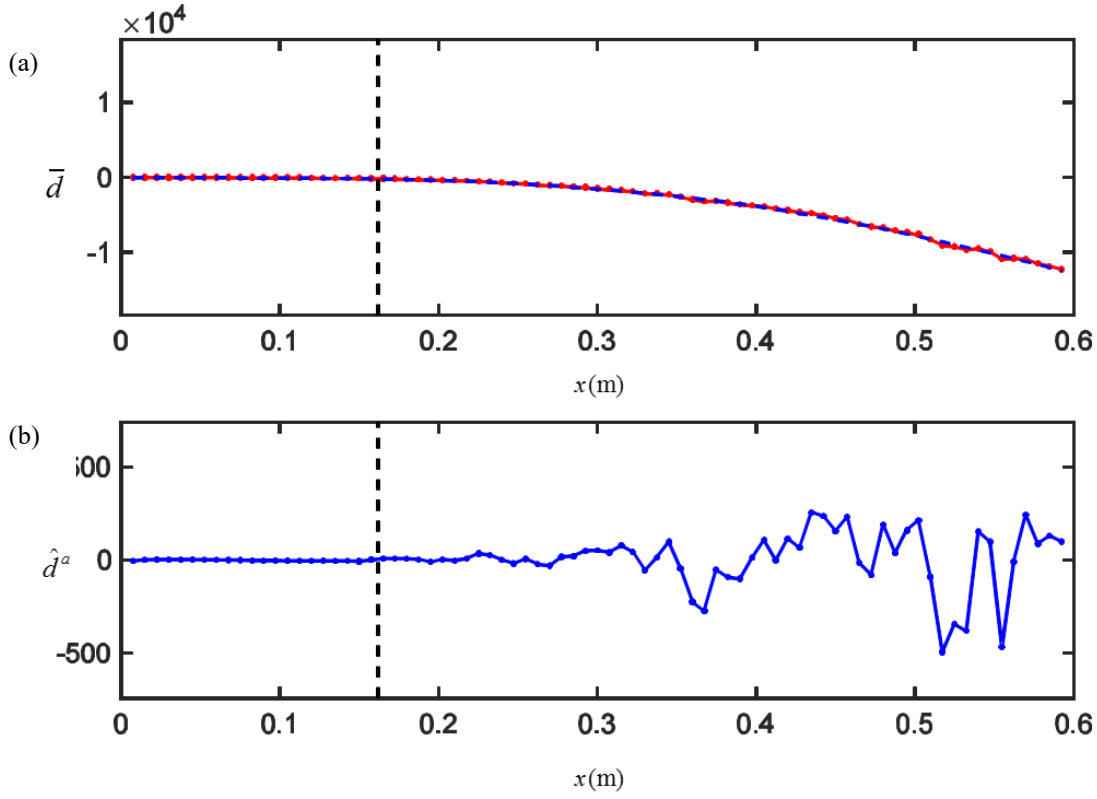

Fig. 5.21b gives the filtered damage index calculated as $\hat{d}_i^a = \bar{d}_i - b_i^a$ in blue curve with dots. The black dash line in both figures indicates the actual damage location.

Fig. 5.21 (a) Damage index of the case with an exciting frequency of $f_1 = 15Hz$ and added noise, (b) corresponding filtered damage index based on approximated baseline.

As expected, the relative large discontinuity caused by noise at beam section close to the free end is larger than discontinuity from the actual damage, and the actual damage location cannot be identified in this case. Although a relative deviation can be calculated as $\hat{d}_i' = \frac{\bar{d}_i - b_i^a}{b_i^a}$ to eliminate the influence from the amplitude, with the nearly zero baseline value for beam section close to the fixed end, the problem of singularity existed, and the calculated relative deviation cannot reflect the actual situation. Figure. 5.22 gives the calculated relative deviation $\hat{d}_i'$. A false damage location will be identified because of the existed singularity, and actual damage location still cannot be identified.

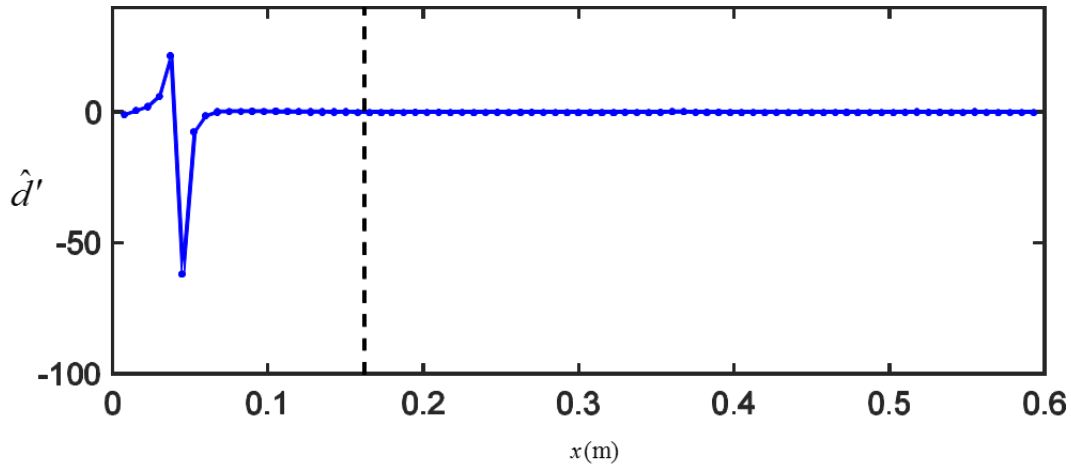

Fig. 5.22 Relative deviation of result damage index from the approximated baseline.

For the case with $f_3 = 220Hz$, noise with the same standard deviation of $\sigma = 0.01u_i(t)$ at each time instant is added to each displacement signal. Figure 5.23 gives a few ODSs from the displacement signals with added noise.

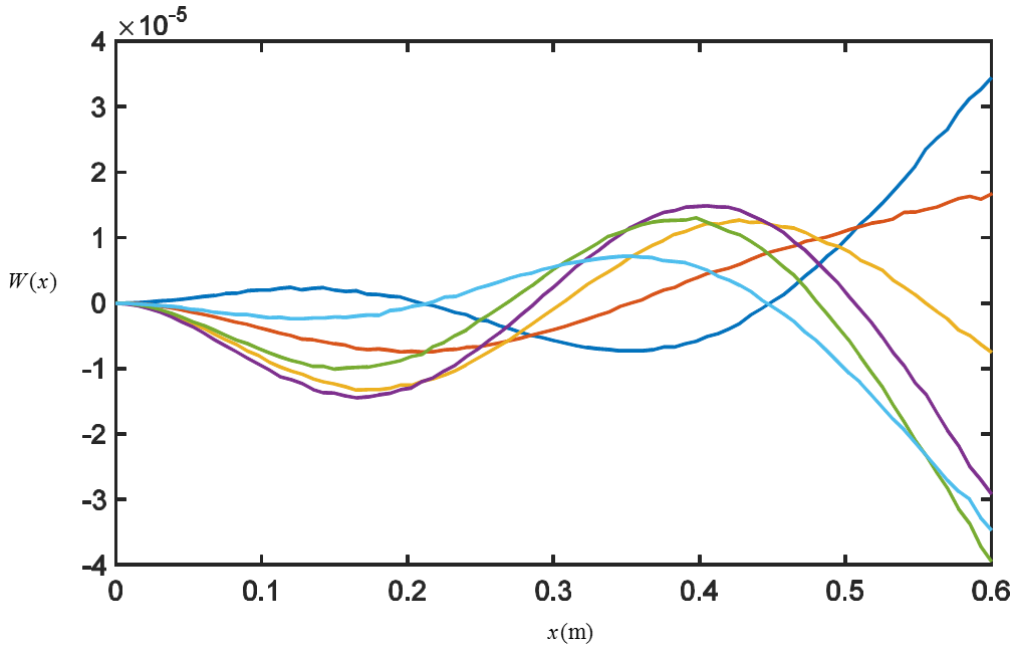

Fig. 5.23 ODSs from displacement signals with added noise.

With a standard deviation of noise proportional to the magnitude of displacement, beam section with a relatively large vibration amplitude still results in a larger error along the z direction. And a larger error will be introduced to the rotational angle of those nodes, and a clearer discontinuity will exist in ODSs at those locations. Use the same finite difference performed by SG filter with $n_L = 1, n_R = 0$ and $M = 3$, rotational angle signals of each node can be computed. Figure 5.24a gives displacement signals of node #1, #11, ..., #81 and Fig. 5.24b gives computed rotational angle signal of the node #1, #11, ..., #81.

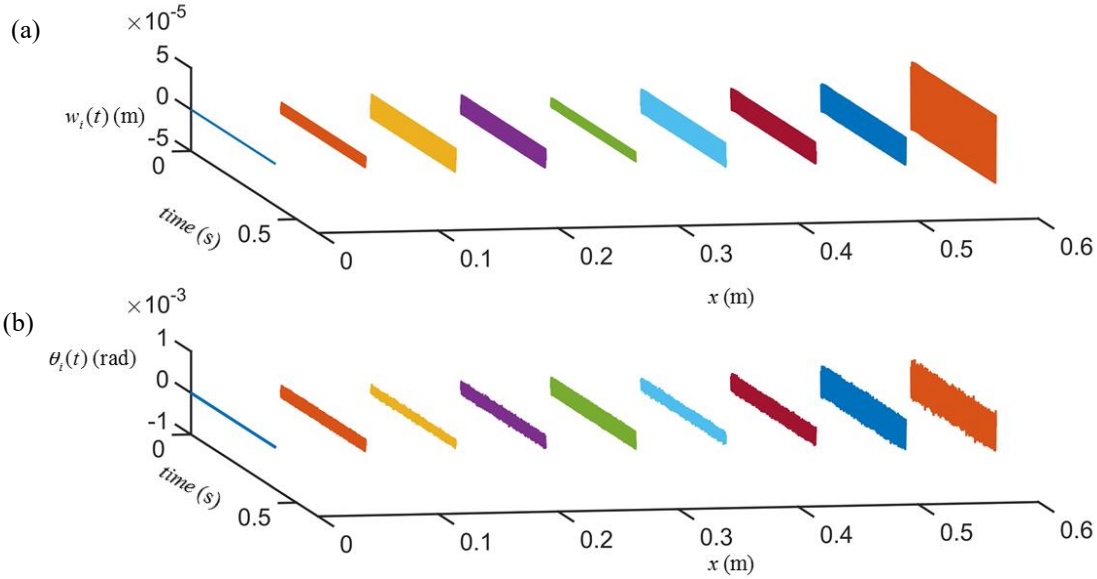

Fig. 5.24 (a) Displacement signal with added noise of node #1, #11, ..., #81 for beam structure from Fig. 5.4 with an exciting frequency of $f_3 = 220Hz$ and (b) corresponding rotational angle signals.

Although added noise cannot be recognized by displacement signal from Fig. 5.24a, the existed noise has been amplified by differentiation and shows clearly in rotational angle signals as the inconsistent amplitude shown in Fig. 5.24b. Applying the stiffness-CMM to the displacement signals and computed rotational angle signals, result damage index can be computed as the average of calculated damage index at each time constant. Based on the general rule of window length given in section 5.3.2, window length used for computing approximated baseline is 12 elements. Figure 5.25a gives the result damage index in the red curve with dots and computed approximated baseline in blue dash line and Fig. 5.25b gives the filtered damage index calculated as $\hat{d}_i^a = \bar{d}_i - b_i^a$ in blue curve with dots. The black dash line in both figures indicates the actual damage location.

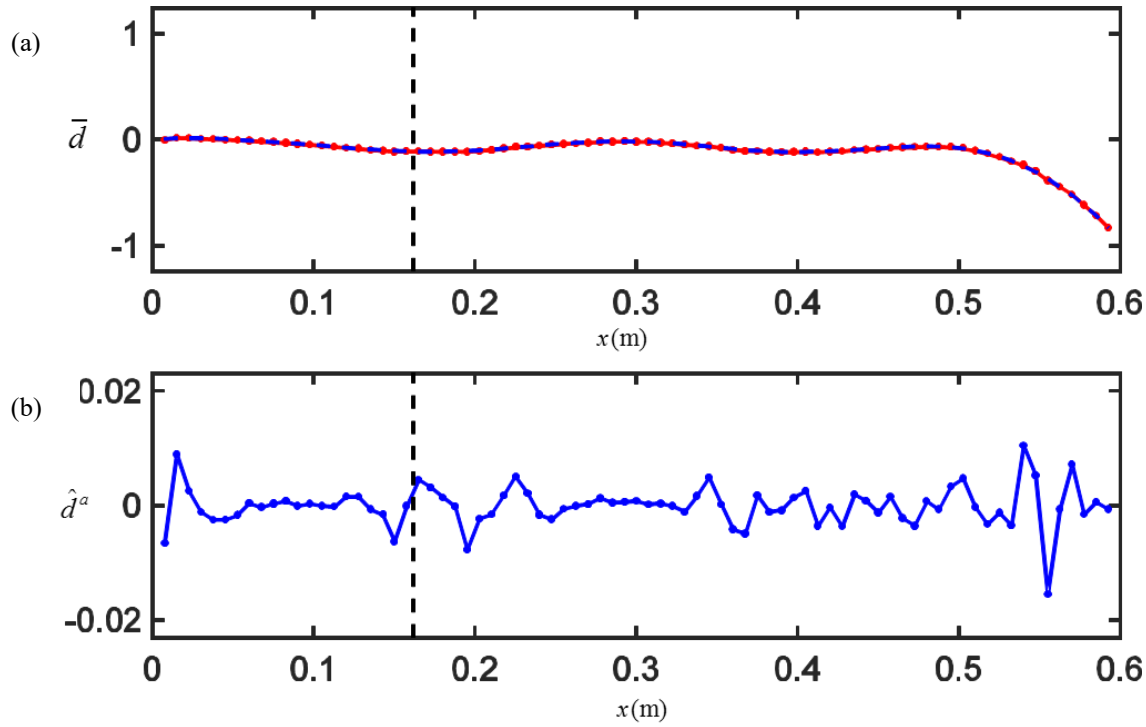

Fig. 5.25 (a) Damage index of the case with an exciting frequency of $f_3 = 220Hz$ and added noise, (b) corresponding filtered damage index based on approximated baseline.

Although the filtered damage index gives a relative large nonzero value at damage location, there existed larger $\hat{d}_i$ at two ends. Meanwhile, it results in multiple peaks and valleys around the actual location. There is no evidence shows the peak at the actual damage location is the right one. Damage location still cannot be recognized accurately.

Since the transverse crack is only simulated by a different cross section by the beam model from the ABAQUS, when it comes to a real beam structural with damage, a nonlinear behavior can exist at damage location such as a breathing crack. And it can result in a larger deviation/nonzero value at damage location. And there is a simplification of only using first 10 mode vibration instead of a real response; the real ODSs can be more sensitive to existed damage. On the other hand, the added noise here is only a simulation of

measuring noise, and the actual measuring noise can be either larger or smaller. Therefore, the although the stiffness-CMM does not give an accurate damage localization in both cases with added noise, it needs to be validate by real experimental data. Meanwhile, the stiffness-CMM can be confirmed as relative sensitive to noise and require a relatively high accuracy for measured data.

The reason of the stiffness-CMM being sensitive to measuring noise is the coefficient matrix $\left[k^C\right]$ used in the characteristic matrix is derived with the 2nd derivative of interpolation functions $[N]_i$. With the 2nd derivative, some information of interpolation functions $[N]_i$ (some coefficients of the shape function) has been lost during differentiation that the computed $\left[k^C\right]$ doesn't contain all information of $[N]_i$. Meanwhile, the displacement vector of the i^{th} element coupled with $\left[k^C\right]$ in CMM is directly related to interpolation functions $[N]_i$ as:

$$w_i(x) = [N]_i^T \left[d_p\right]_i \tag{5.31}$$

Therefore, use $\left[k^C\right]$ as a weighting matrix while lacking information of $[N]_i$ to test the continuity of ODSs can be relatively sensitive to any kind of existed discontinuity from ODSs.

5.4.2 The Mass-CMM

Meanwhile, the mass coefficient matrix $\left[m^C\right]$ from Eq. (5.2) is derived directly from the interpolation functions $[N]_i$, it can be used as a weighting matrix with as well. With all information of $[N]_i$ preserved in the coefficient matrix, it can be more robust to measuring noise. Moreover, for the case of proportional damping, each modal vector of a system will be orthogonal to all other modal vectors of that system when weighted by the mass, stiffness or damping matrix as in Eq. (4.12), theoretically. And in practice, normally

the mass matrix is considered to be the most accurate [12]. Therefore, the mass characteristic matrix method (mass-CMM) is proposed here with the same algorithm as in the stiffness-CMM but with a different weighting matrix as $\left[m^C \right]$. Like Eq. (5.7), the mass characteristic matrix can be derived as:

$$\left[A\right]'_i = \begin{bmatrix} \left[m^C(3,:) \right]\left[d_p \right]_{i-1} & \left[m^C(1,:) \right]\left[d_p \right]_i \\ \left[m^C(4,:) \right]\left[d_p \right]_{i-1} & \left[m^C(2,:) \right]\left[d_p \right]_i \end{bmatrix} \tag{5.32}$$

And the damage index of mass-CMM can be calculated as:

$$q_i = \det(\left[A\right]'_i) = A_{11}^{\prime(i)} A_{22}^{\prime(i)} - A_{12}^{\prime(i)} A_{21}^{\prime(i)} \tag{5.33}$$

In order to confirm its stability, the case of 3rd mode vibration with added noise will be used. Applying mass-CMM to the same displacement signals and computed rotational angle signals, result damage index $\bar{q}_i$ can be computed as the average of calculated damage index q_i through the time trace. Use the same window length as 12-elements for computing approximated baseline. Figure 5.26a gives the result damage index $\bar{q}_i$ in red curve with dots and computed approximated baseline in blue dash line and Fig. 5.26b gives the filtered damage index calculated as $\hat{q}_i = \bar{q}_i - b_i^a$ in blue curve with dots.

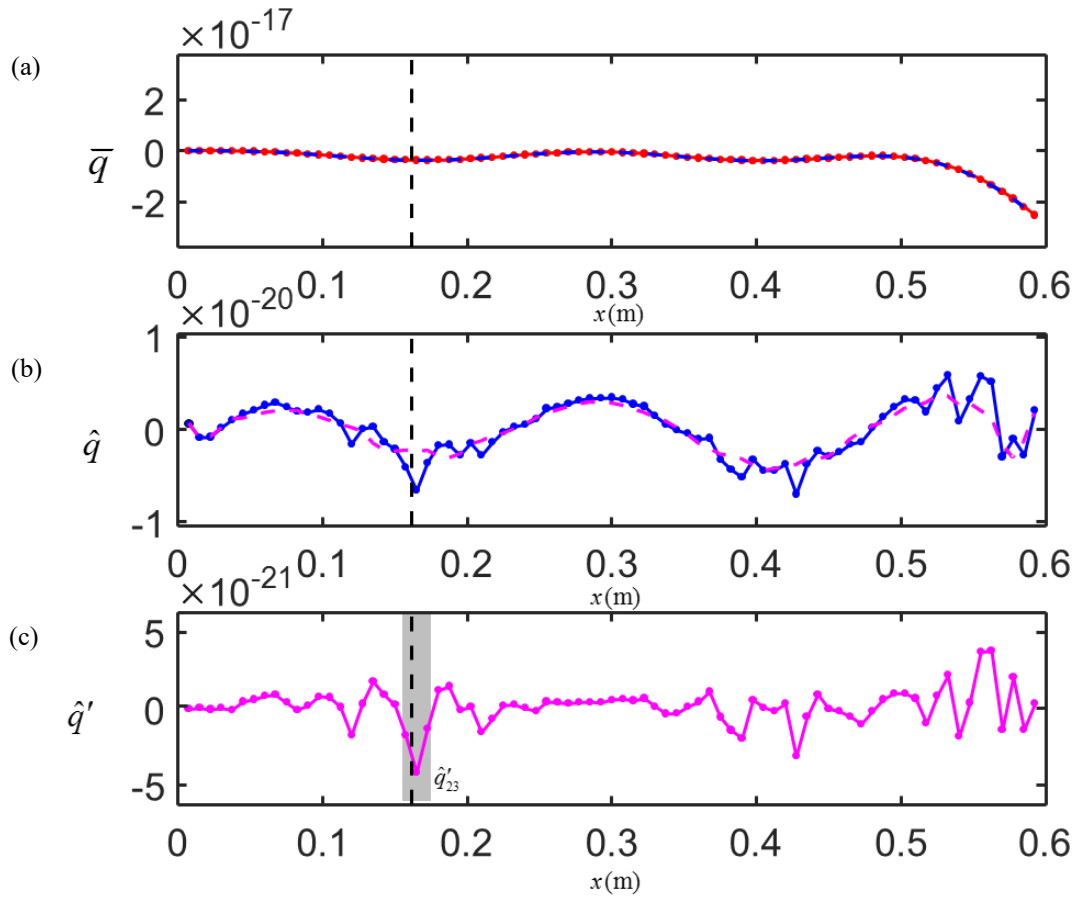

Fig. 5.26 (a) Applying the mass-CMM to case with an exciting frequency of $f_3 = 220Hz$ and added noise, (b) once filtered damage index based on approximated baseline and (c) twice filtered damage index based on approximated baseline.

However, there still have a baseline left in the filtered damage index $\hat{q}$ as shown in Fig. 5.26b, another baseline filtering needs to be applied. Notice that the filtered damage index has a different shape at two ends. That is because, when computing the approximated baseline from $\bar{q}$, for points at two ends, same window length can only be realized by using more points from one side. Therefore, the computed baseline has a different accuracy at two ends and the computed $\hat{q}$ has a different shape at two ends. The same problem can also be noticed by Fig. 5.16b, 5.17b and 5.18b. With different shape at two ends, the baseline computation of

$\hat{q}$ is applied with half window length for those points at two ends. Then, the twice filtered damage index $\hat{q}'$ can be computed and given in magenta curve and dots in Fig. 5.26c while the approximated baseline of $\hat{q}$ is given in magenta dash line in Fig. 5.26b. The black dash line in all three figures indicates the actual damage location. $\hat{q}'$ gives the largest magnitude to $\hat{q}'_{23}$ at the damage location and damage location can be identified accurately for this case. It a shorter window length is applied to filter the baseline by one step, the deviation caused by existed damage can be captured locally into the approximation baseline, and damage location cannot be revealed accurately. Therefore, while the mass-CMM is more robust to existed noise based on numerical analysis, it requires two step baseline filtering to filter out the existed baseline and preserve the deviation caused by existed damage. And again, since the numerical simulation of transverse crack and noise cannot reflect the real situation, experimental validation is necessary.

Chapter 6 EXPERIMENTAL VALIDATION

6.1 Introduction

The beam model used in chapter 5 from ABAQUS can only present the existed transverse crack by its different cross section dimension. When it comes to crack with nonlinear behavior such as a breathing crack, it is not enough for simulation. The real ODSs consist response of all modes, but only limited mode vibration is included in previous numerical model. The magnitude of the simulated noise used in section 5.3.3 is chosen without any theoretical basis, it cannot reflect the real situation of measuring noise. And the velocity responses are the actual measured responses, and displacement signal integrated from velocity signal could introduce more error and has not been simulated in chapter 5. Therefore, experimental verifications are needed to validate the stiffness characteristic matrix method (stiffness-CMM) and the mass characteristic matrix method (mass-CMM) proposed in Chapters 5.

As from Chapter 5, CMMs can be applied to both free transient vibration with applied force or steady state vibration with harmonic input. Mode vibration with larger natural frequency change ratio can be more sensitive to existed damage. And the mass-CMM can be more robust to existed noise than the stiffness-CMM. Therefore, although all performed experiments will be introduced in Section 6.2.1, cases with more consistency (steady-state vibration) and its major vibration with a larger natural frequency change ratio will be used for verification. Without the actual intact structure, numerical model of the corresponding intact structure will be used to predict the actual natural frequency change ratio. The mass-CMM will be applied to all discussed cases and approximated baseline will be used for baseline filtering. Meanwhile, the stiffness-

CMM will be applied to cases with relative small measuring noise and a new counting damage index d^C will be used to interpolate the result and decrease the influence from measuring noise/error.

6.2 Experiment Setup and Signal processing

6.2.1 Experiment Setup

A horizontal cantilevered beam is considered. And here we use a Polytec PI PSV-200 scanning laser vibrometer for measuring velocities along the *z*-axis of equally spaced points on the beam structure when the beam is subjected to a certain excitation. A retro-reflective tape is put on the beam to have strong backscattered laser light and obtained more accurate velocity values.

For free transient vibration, since the laser vibrometer can only measure the response point by point, to capture the same time trace from the beginning for each point, the transient experiment needs to be repeated for each point's measuring. Consider the repeatability and the consistency of the applied excitation of the free transient vibration; two set-ups have been designed for the free transient vibration. For the steady state vibration, once the steady state has been reached, the responses of points will be consistent along the x-axis and the time trace, then the experiments don't need to be repeated for each point.

Figure 6.1 gives the first set-up used for free transient vibration. A pendulum is controlled by a holding magnet to fall from a certain height and impact the beam around the free end. And the holding magnet is connected to a circuit that the switch is manual controlled. It is designed to simulate the situation of an applied force on the free end and to obtain a 3rd order polynomial deflection. With the falling height controlled by the holding magnet, the experiment can be repeated multiple times for all points.

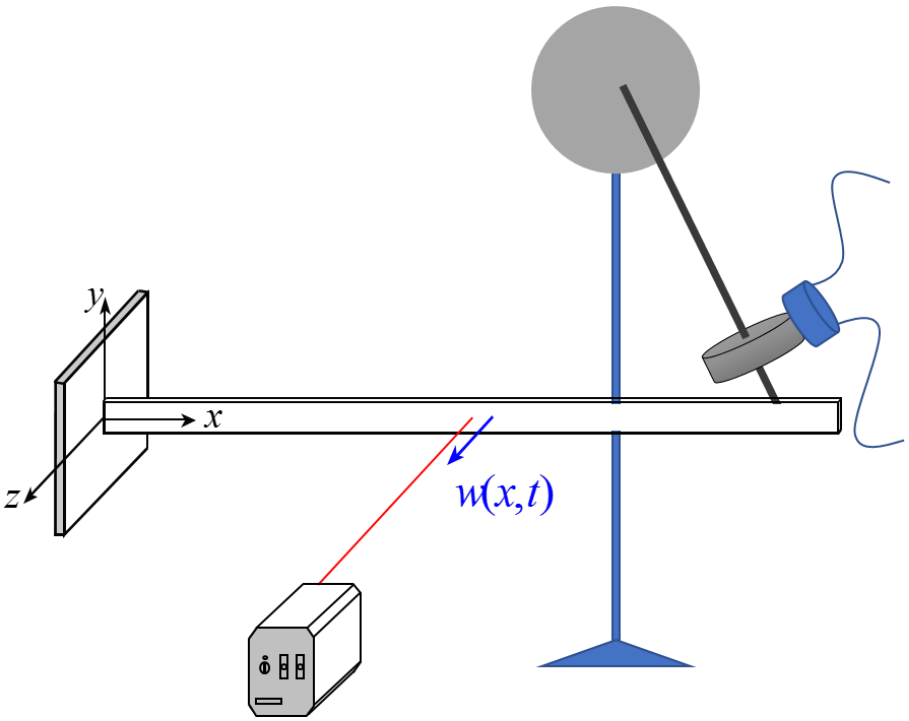

Fig. 6.1 Setup of a horizontal cantilevered steel beam for free transient vibration.

Figure 6.2 gives the second set-up used for free transient vibration, and it is also the set-up used for steady-state vibration. A QuickPack QP10N PZT patch is integrated into the beam structure close to the fixed end. The excitation of the free transient vibration is designed as giving a square wave function to the PZT patch by the input voltage from the HP-33120A function generator. The input voltage has been amplified by the PCB-790 power amplifier as shown in Fig. 6.2. It is designed to simulate the situation of an applied force near the fixed end. With the deformation of the PZT patch caused by the input voltage, the experiment can be repeated multiple times for all measured points for their transient vibration. And without a nonlinear behavior as the impact from the first set-up, more consistent responses can be excited. To use the set-up from Fig. 6.2 for steady-state vibration, a harmonic voltage as $180\sin\omega_i t$ volts is applied to the PZT patch. The

excitation frequency ω_i is close or at one of the beam's natural frequencies predetermined by FFT analysis of the beam's response to a chirp excitation.

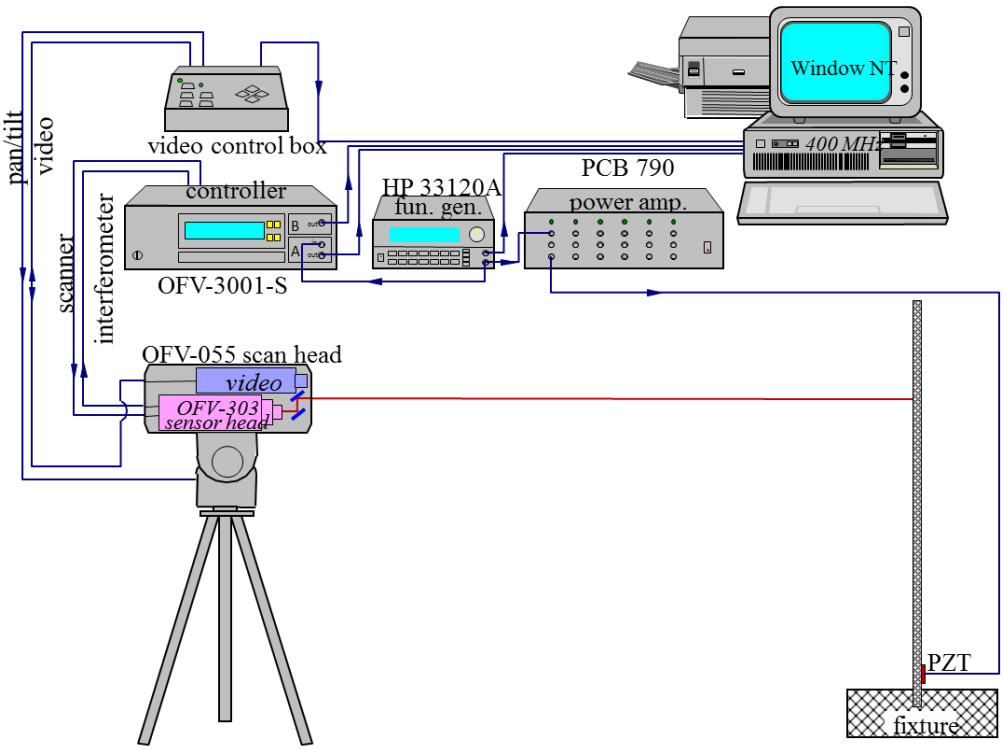

Fig. 6.2 Setup of a horizontal cantilevered steel beam for free transient vibration and steady-state vibration.

6.2.2 Specimen Information and Case Information

There are three specimens have been used for the experiments. But since the specimen is clamped each time randomly and cannot be measured precisely with the fixed end, the actual length used in each experiment is unknown. Meanwhile, the length of the crack to the free end is easily to measure, and the measured point number before and after damage location is known. Therefore, the accuracy of identified damage location can still be confirmed. All used specimens are made of the same aluminum alloy material with cross section size of $25.4\text{mm}\times 6.35\text{mm}\ (=b\times h)$. The material properties are known as: Young's modulus $E=60\text{GPa}$

(estimated from the experimental data), Poisson's ratio ν=0.33 and mass density ρ=2710kg/m^3. A through-the-width open crack is created to each specimen to simulate a fatigue crack. And Table 6.1 gives the difference of the used three specimens.

Table 6.1 Specimen information

Specimen number	Approximated Length (mm)	Crack width (mm)	Crack depth (mm)	Crack location to the free end (mm)	The PZT patch
#1	598	1	1	279.5	With
#2	598	1	1	279.5	Without
#3	590	0.3	0.5	305	With

Experiments are performed with different mesh and sampling rate. Table 6.2 lists the information of all performed experiments. The intact surface on the opposite side of the damaged surface is measured in all experiments. In order to avoid the influence of the deformation of the PZT patch from the input voltage, no point is measured for the beam section with the patch on the opposite side. For steady state vibration, since the excitation frequency is chosen as a little higher than one of the beam's natural frequencies that the ODSs will consist the corresponding mode vibration as its major vibration. The 4th column gives the existed major mode vibration for applicable case.

Table 6.2 Experiments' information

Date of experiment	Case number	Used Specimen	Free transient vibration/ Steady state vibration	Damage location (Point number)	Number of measured points	Exciting frequency(Hz)/ Applied excitation	Sampling rate (Hz)
11/22/2016	1	#3	1st mode	[15,16]	40	12	12800
12/13/2016	2A	#1	6th mode	[39,40]	83	1210	256000
	2B	#1	7th mode	[39,40]	83	1714	256000
	2C	#1	8th mode	[39,40]	83	2278	256000
1/10/2017	3A	#3	8th mode	[37,38]	91	2250	51200
	3B	#3	9th mode	[37,38]	91	2870	51200
	3C	#3	10th mode	[37,38]	91	3600	51200
1/15/2017	4	#2	Transient	[46,47]	91	Hammer	12800
1/20/2017	5A	#1	Transient	[41,42]	91	Impulse	12800
	5B	#1	Transient	[41,42]	91	Impulse	12800
	5C	#1	1st mode	[41,42]	91	17	12800
	5D	#1	2nd mode	[41,42]	91	100	51200
	5E	#1	8th mode	[41,42]	91	2400	512000
	5F	#1	9th mode	[41,42]	91	3100	512000
2/12/2017	6A	#1	3rd mode	[41,42]	91	300	256000
	6B	#1	4th mode	[41,42]	91	550	128000
	6C	#1	5th mode	[41,42]	91	890	512000
	6D	#1	6th mode	[41,42]	91	1350	512000
	6E	#1	7th mode	[41,42]	91	1900	512000

Although the measured length may not be precise, the numerical model corresponding intact structure with measured length can still be used to predict the natural frequency change ratio of the used specimen. And since the specimen #1 and #2 only have the difference as with/without integrated PZT patch, the same numerical model will be used for these two specimens. Table 6.3&6.4 gives the predicted natural frequency

of the intact structure and the corresponding natural frequency change ratio of those listed major modes vibration of the specimen #1(#2) and #3, respectively. The 5th natural frequency of the specimen #1(#2) cannot be identified in the FFT analysis using the laser vibrometer. And the FFT is not performed on the specimen #3, so here we use the numerical model to predict the natural frequency of the damaged structure too. Notice there can exist certain mode vibration with a larger natural frequency change ratio but has not been performed.

Table 6.3 Predicted natural frequency, natural frequency change ratio of the specimen #1(#2).

Natural frequency	f_1	f_2	f_3	f_4	f_5	f_6	f_7	f_8	f_9
f_H (Hz)	14.302	89.575	250.58	490.38	809.21	1206.2	1680.5	2230.9	2856.1
f_D (Hz)	14.1	90	251	488	-	1198	1682	2224	2860
$\frac{(f_H - f_D)}{f_H}$	0.014	0.0047	0.0017	0.0048	-	0.0068	0.0009	0.0031	0.0014

Table 6.4 Predicted natural frequency, natural frequency change ratio of the specimen #3.

Natural frequency	f_1	f_8	f_9	f_{10}
f_H (Hz)	14.692	2291.1	2932.9	3650.0
f_D (Hz)	14.689	2289.7	2932.5	3648.0
$\frac{(f_H - f_D)}{f_H}$	2.04 $\times 10^{-4}$	6.11 $\times 10^{-4}$	1.36 $\times 10^{-4}$	5.48 $\times 10^{-4}$

6.2.3 Signal Processing

Since both the stiffness-CMM and the mass-CMM are based on the measured ODSs, the accuracy of displacement signal and computed rotational signal would give a directly influence on the result. For free transient experiments performed by repeated experiments, although the falling position of the hammer or the square wave function applied on the PZT patch is fixed, the consistency of responses through the x-axis is relatively poor. That is because the falling of the hammer is artificially controlled by switch off the current to the electronic magnet. Complete consistency is not ensured. And for the excitation from the PZT patch, the repeated experiment may cause a problem of overheat on the PZT patch and give a different deflection to the same applied square wave function. Therefore, the obvious discontinuity existed in the ODSs from inconsistent responses along the x-axis can lead to a false damage location. Fig. 6.3a and 6.3b gives the computed ODSs of certain time instant of the case 4 and case 5A as an example, respectively. On the other hand, the steady state vibration is excited by a harmonic input, so the computed ODSs is relative more consistent as shown in later discussed cases.

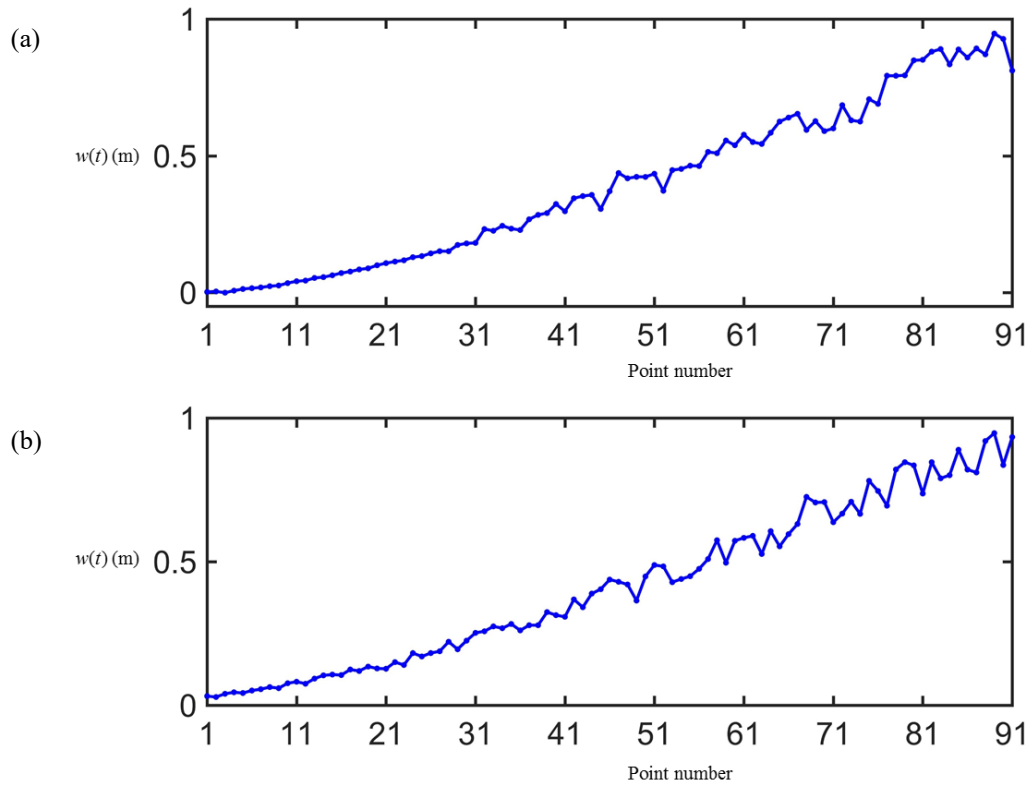

Fig. 6.3 Computed ODSs of certain time instant of case 4 and case 5A: (a) ODSs of the case 4 and (b) ODSs of the case 5A.

For measuring noise existed for all experiments, it can be accumulated through the integration and exist in computed displacement signals. Through differentiation, accumulated noise from the displacement signals can be amplified. Based on the numerical simulation from the section 5.3.2, the case with relative larger natural frequency change ratio can result in a larger deviation at damage location and be more robust to existed measuring noise. Therefore, cases with its major mode vibration have a larger predicted natural frequency change ratio will be discussed. Based on Table 6.3&6.4, cases 2A, 2C, 3A, 3C, 5D, 5E, 6B and 6D will be discussed. And a general procedure will be used to compute displacement signals and rotational angle

signals as shown in Fig. 6.4.

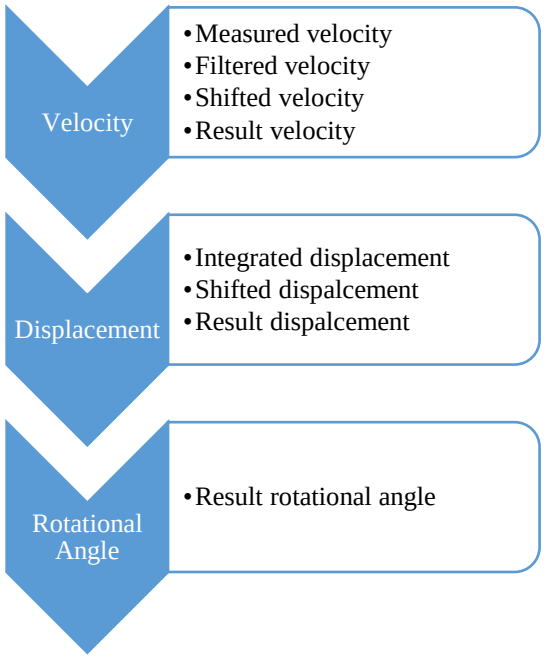

Fig. 6.4 Basic steps of signal processing

1) With known exciting frequency of each case, bandpass filter based on the fast Fourier transform(FFT) will be applied to the measured velocity through the computer program ORIGIN. Applied band pass is chosen as an extended range around the corresponding exciting frequency; then the filtered velocity signals $\dot{w}_i'(t)$ can be computed.

2) With certain measuring range used in each case, points with relatively small amplitude will have relative larger measuring error and can even have an inaccurate moving average. Therefore, the empirical mode decomposition(EMD) from section 2.3.5 will be used to get rid of the inaccurate moving average and the shifted velocity signals $\dot{w}_i''(t)$ can be computed.

3) Since the applied FFT filter is based on Fourier transform which suffered from the edge effect,

filtered velocity signals would contain a relative larger error at two ends. And like the FFT filter, coded EMD is also based on Fourier transform and can leave the edge effect on shifted signals. Therefore, the first and last few periods of $\dot{w}_i''(t)$ can have a relative larger error. On the other hand, since the damage index from both the stiffness-CMM and mass-CMM methods is computed at each time instant and the result damage index is only the average of computed damage index along the time trace, the stiffness-CMM and mass-CMM have relatively low demand on the length of time trace. Therefore, the first/last few periods of data can be avoided to get a more accurate identification. After cutting off the first/last few periods of $\dot{w}_i''(t)$ and the result velocity signal $\bar{\dot{w}}_i(t)$ can be constructed by aligning certain local maximum/minimum of the shortened $\dot{w}_i''(t)$ (based on the ODSs). Time trace has been shifted to start with $t = 0s$.

4) Integrate the result velocity signals $\bar{\dot{w}}_i(t)$ with zero initial displacement assumption by SG integration method; the integrated displacement signals $\hat{w}_i(t)$ can be computed.

5) Since the resulting velocity signals are constructed by aligning shortened velocity based on its local maximum/minimum, the zero initial displacement assumption used in integration is correct. However, the error existed in result velocity signals can be accumulated through integration and result in an inaccurate moving average in integrated displacement signal. Therefore, EMD needs to be applied to get rid of the inaccurate moving average, and the shifted displacement signals $w_i'(t)$ can be computed.

6) Again, since the EMD is coded based on Fourier transform, it can leave the edge effect on the first/last few periods of the $w_i'(t)$. After cut off the first/last few periods of $w_i'(t)$ to avoid the edge

effect, the resulting displacement signal $w_i(t)$ can be constructed by aligning certain local maximum/minimum of the shortened $w_i'(t)$ based on the ODSs.

7) Differentiate the resulting displacement signal $w_i(t)$ by SG filter method; result rotational angle signals $\theta_i(t)$ can be computed.

Although some of measuring noise and calculation error can be eliminated by the general procedure, those large noises from other interference signals can still exist and will result in abnormal transient events around certain time instants. On the other hand, the signal of points located near the 'nodes' of the major mode vibration can have a relatively large error. That is because, for mode vibration, the 'nodes' will have zero vibration amplitude. Therefore, with superimpose of other mode vibration, points located close to the 'nodes' of the major mode vibration will have relative small vibration amplitude. With the fixed measuring range from the laser, the existed measuring noise from the machine can be close to or even larger than actual vibration signal. It is hard to filter out the accurate vibration signal from the measured signal and the information of those points can be buried under the measuring noise. Then, the accuracy of filtered signal cannot be ensured, inconsistent amplitude or abnormal transient events can exist in its result displacement signal. And the information of those points has been damaged.

With error amplified through the differentiation to the rotational angle, the inaccurate nonlinear behavior existed in damaged signals can result in a false damage location. It is better to reconstruct those displacement signals to eliminate the influence. Based on the reference signal, the inaccurate displacement signal can be reconstructed as:

$$w_{r_i}(t) = \frac{\bar{w}_{r_i}(0)}{\bar{w}_{r_i+\Delta_i}(0)} w_{r_i+\Delta_i}(t) \tag{6.1}$$

where the r_i belong to the set $\{r\}$ as points need to be reconstructed, the Δ_i belong to the set $\{\Delta\}$ as the distance between the reconstructed point and its reference point, $\bar{w}(0)$ is result of curve fitting the initial ODSs ($w(0)$) along the x-axis. Based on the initial ODSs, the curve fitting will be applied point by point with the same window length. And the general rule used for choosing the reference point is 'next to the reconstructed point' and 'with a larger amplitude than reconstructed point' (for case of inaccurate signals caused by their location close to the 'nodes'). Notice although the reconstruction based on curve fitting of initial ODSs cannot ensure the accuracy of reconstructed signals and may even spread the error from the reference signal, it still can generally decrease the influence from inaccurate displacement signals and result in a more accurate damage location. That is because, for corrected signals located near the 'nodes', with the relative small vibration amplitude, the accuracy of those signals will not give a big difference in the ODSs. The mode vibration is relatively insensitive to the behavior of those points [3], and the result of damage identification will not be influenced much. And for corrected signals with interference signals, the influence of the error of reconstruction will be much smaller than existed transient events.

Table 6.5 gives the location of the 'nodes' for involved mode vibration. Notice the measured range does not cover the entire beam structure so that not all 'nodes' will fall into measured range. Only the 'nodes' fall in the measured range are given in Table 6.5. The 'node' located between two measured points is expressed as $[i, i+1]$ and the 'node' almost coincide with certain measured points is expressed as i .

Table 6.5 Location of 'nodes' of cases will be discussed.

Case number	Major mode vibration	Node location
2A	6th mode vibration	[8,9], [26,27], 45, 63, [79,80]
2C	8th mode vibration	[2,3], 16, [29,30], [42,43], 56, 69, 81
3A	8th mode vibration	15, [28,29], 42, [55,56], [69,70], [83,84], [96, 97]
3C	10th mode vibration	[11,12], [22,23],33, [43,44], 54, 65, 76,87, [97,98]
5D	2nd mode vibration	70
5E	8th mode vibration	[4,5], 19, 33, [46,47], [60,61], [74,75], 87
6B	4th mode vibration	27, [55,56], [81,82]
6D	6th mode vibration	13, [31,32], 50, [68,69], 85

6.2.4 Result Interpolation

With inaccurate displacement signals correct by reconstruction, a more accurate rotational angle signal can be computed. Then damage identification methods can be applied. First, the mass-CMM can be applied to compute damage index q_i at each time instant, and the result damage index $\bar{q}_i$ can be computed as its average. Then, the filtered damage index $\hat{q}_i$ can be calculated by subtracting the approximated baseline where the baseline is computed based on curve fitting. Multiple times of baseline subtraction can be applied

until nearly no baseline left and damage location can be identified as elements before and after point with the largest magnitude of filtered damage index.

As discussed in chapter 5, the stiffness-CMM is relative sensitive to measuring noise, only cases with relative small measuring noise will be used to verify the stiffness-CMM. And a new counting damage index d^C will be used to interpolate the computed damage index $d_i(t_k)$. Instead of taking an average of computed damage index first and then filtering the baseline, existed baseline for each time instant will be filtered at each time instant t_k as $\hat{d}_i(t_k) = d_i(t_k) - b_i(t_k)$. Then, damage location at each time instant t_k can be identified as the elements before and after point with the largest magnitude of $\hat{d}(t_k)$. Counting damage location through the time trace, in other words, counting the number of times each element has been identified as damage location through the time trace, the d^C can be used to locate the actual damage and decrease the influence from measuring noise. Notice d_i^C is corresponding to element number as $i = 1, 2, ..., n_E$. For the existed damage on the j^{th} element, it can result in either $\hat{d}_j(t_k)$ or $\hat{d}_{j+1}(t_k)$ with the largest magnitude. Then, one count will be added to either the $j-1^{th}$ and j^{th} elements or the j^{th} and $j+1^{th}$ elements. With calculation error and measuring noise exist, either $j-1^{th}$, j^{th} or $j+1^{th}$ can result in the largest d^C. Therefore, damage location will be identified as an element with the largest d^C and the element before and after it to include the actual damage location.

The reason of the d^C can decrease the influence from measuring noise is explained as follows. For time instants around the ODSs with relative large deformation, the difference existed between the displacement of each point is relatively large. Points with larger displacement can have a relative larger error in displacement and result in a false damage location. Moreover, with a relatively large error in displacement,

the filtered damage index at the false damage location can be relatively large. And for other time instants that the displacement of each point is relative close, measuring noise will give the same influence along the x-axis and existed damage can be revealed. By counting the identified damage location, the magnitude of the filtered damage index at the identified damage location will not influence the final result and always count as 1. And results of each time instant can be interpolated more evenly.

6.3 Experiments of Specimen #1

6.3.1 ODSs Close to the 6th Mode Shape

6.3.1.1 Case 2A

Case 2A is performed with an exciting frequency of $f_6 = 1210Hz$ to have the 6th mode vibration as its major vibration. With the sampling rate of 256000Hz, about 211 measured time instants fall in each period. The crack is located at the 39th element among the measured 83 points. Figure 6.5 gives the measured velocity $\dot{w}(t)$, the x-axis is the axis of time, and the y-axis gives the point number, and the z-axis is the axis of measured velocity.

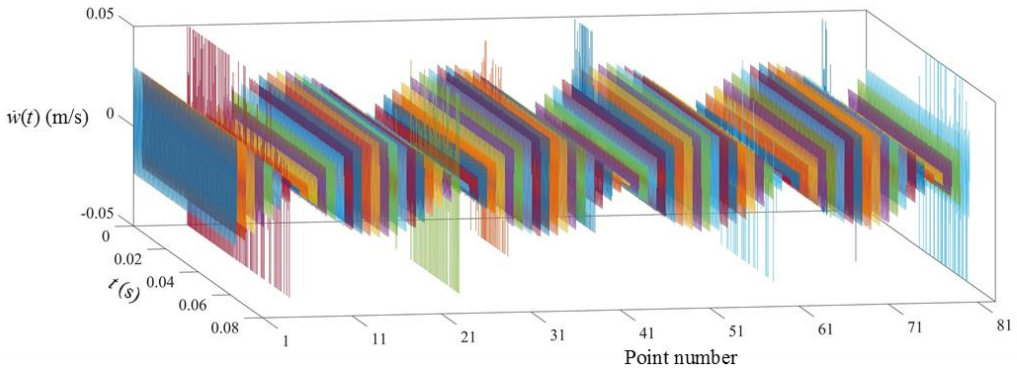

Fig. 6.5 Measured velocity signals of case 2A.

From Fig. 6.5 one can see that most of the measured signals with relative large noise are located close to the 'nodes'. However, there also existed measured signals located away from the 'nodes' contains relative large error such as $\dot{w}_7(t)$ and $\dot{w}_{83}(t)$. Reconstruction may need to be applied to the resulting displacement signal of those locations. Apply a band pass filter with the range of 600-1800Hz to measured velocity; filtered velocity signals $\dot{w}'(t)$ can be computed as shown in Fig. 6.6.

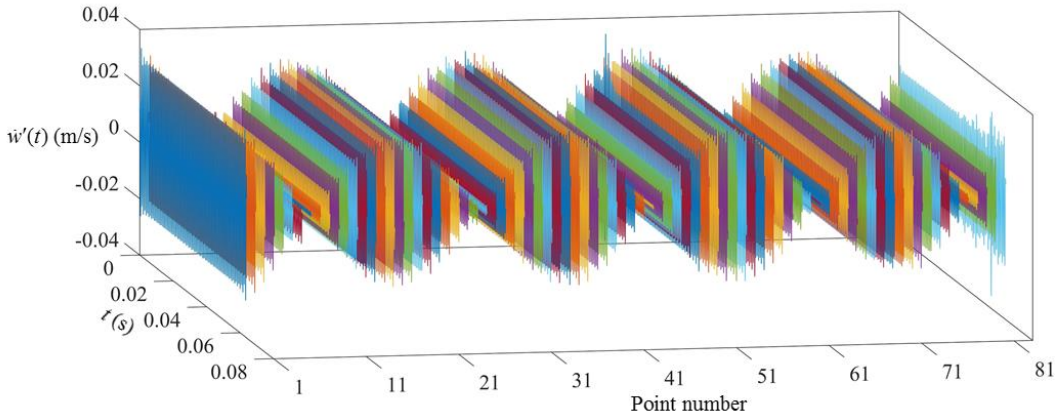

Fig. 6.6 Filtered velocity signals of case 2A.

With the applied band pass filter, the existed big measuring noise has been decreased, and the existed disturbance of amplitude for each response through the time trace is in relative small range. The edge effect can be noticed clearly as the existed disturbance in amplitude at two ends for each filtered velocity signal. Figure 6.7 gives the shifted velocity signals $\dot{w}''(t)$ by applying the EMD to remove nonzero moving average.

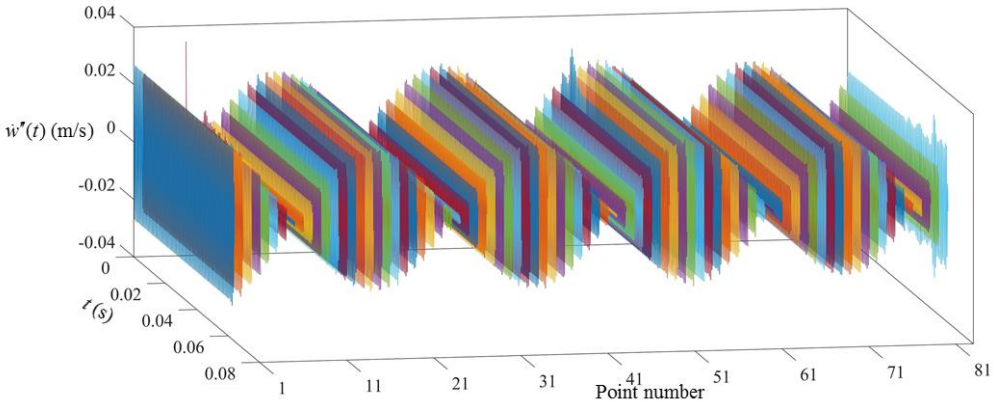

Fig. 6.7 Shifted velocity signals of case 2A.

Although the existed edge effect at two ends has been decreased by the nonzero moving average, it is better to follow the general procedure to cut off the first/last few periods and avoid the left edge effect. Then, the result velocity signals $\bar{\dot{w}}(t)$ can be constructed by aligning shortened velocity signals by its local maximum/minimum based on its ODSs, and it is given in Fig. 6.8.

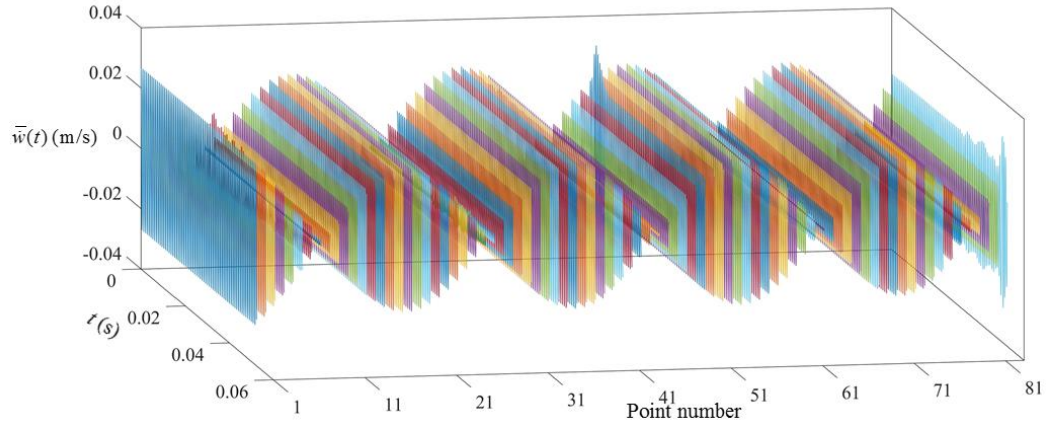

Fig. 6.8 Result velocity signals of the case 2A.

Based on the result velocity signals in Fig. 6.8, the integrated displacement signals can be computed by SG integration method. With about 211 measured time instants fall in each period, relatively accurate

integrated displacement signals $\hat{w}(t)$ can be computed. Figure 6.9 gives the integrated displacement signal $\hat{w}(t)$ with $n_L = 1, n_R = 1$ and $M = 2$ used in the applied SG integration method.

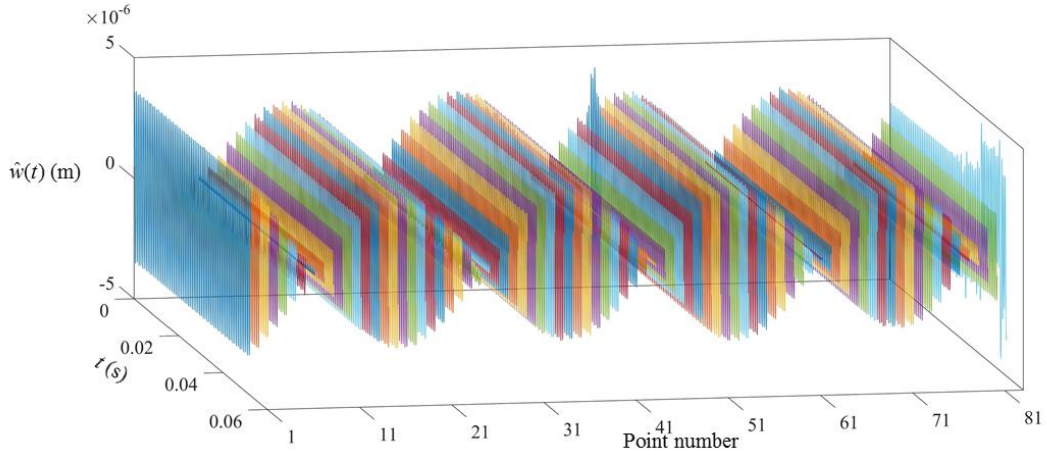

Fig. 6.9 Integrated displacement signals of the case 2A.

Follow the general procedure, EMD has been applied to remove nonzero moving average. Then, shifted displacement signals $w'(t)$ can be computed as shown in Fig. 6.10. And the first and last few periods will be cut off to avoid the edge effect from applied EMD, and result displacement signals $w(t)$ can be constructed by aligning its local maximum/minimum based on the ODSs as shown in Fig. 6.11.

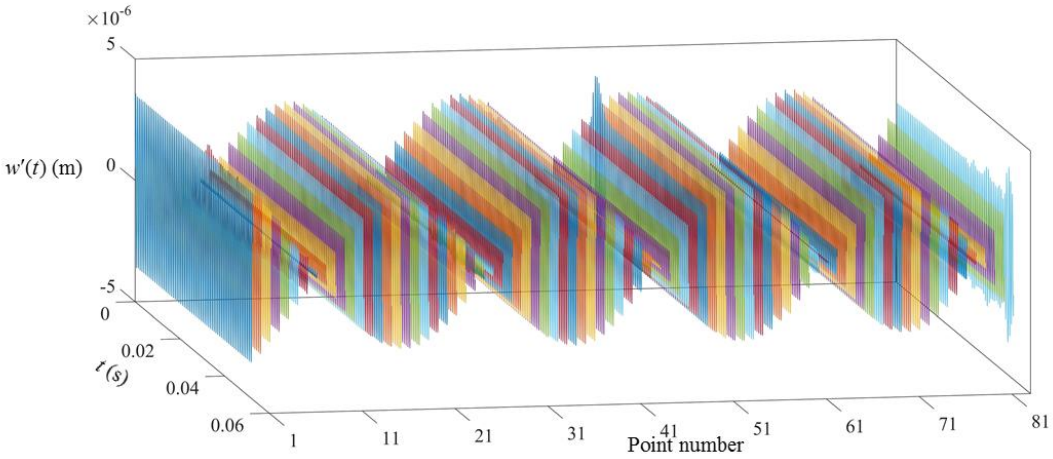

Fig. 6.10 Shifted displacement signals of the case 2A.

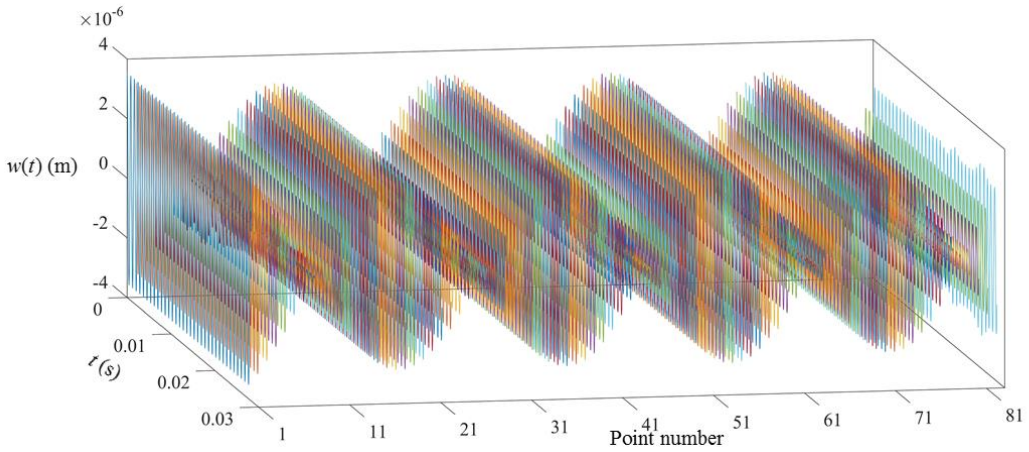

Fig. 6.11 Result displacement signals of the case 2A.

Figure 6.12 gives the initial ODSs in red curve and dots, and the blue dash curve presents the curve fitting of the ODSs with a window length of 12 elements. Red circles marked the points need to be reconstructed, and blue circles marked the corresponding reference points. With the 'nodes' of mode shape located at: [8,9], [26,27], 45, 63, [79,80], points need to be reconstructed is decided as: $\{r\} = \{7, 26, 62, 63, 83\}$. And the used reference point can be located by $\{\Delta\} = \{-1, -1, -1, 1, -1\}$. The abnormal transient events existed in $w_7(t), w_{83}(t)$ is caused by the existed large noise from other interference signals as shown originally in Fig. 6.5. The abnormal transient events existed in $w_{26}(t), w_{62}(t)$ and decreasing amplitude existed in $w_{63}(t)$ is caused by inaccurate filtered velocity signals by the relative large measuring noise (comparing to actual vibration signal) from the measured velocities. Figure 6.13 gives the displacement signals of the set $\{r\}$ before and after reconstruction in red curves and blue curves, respectively.

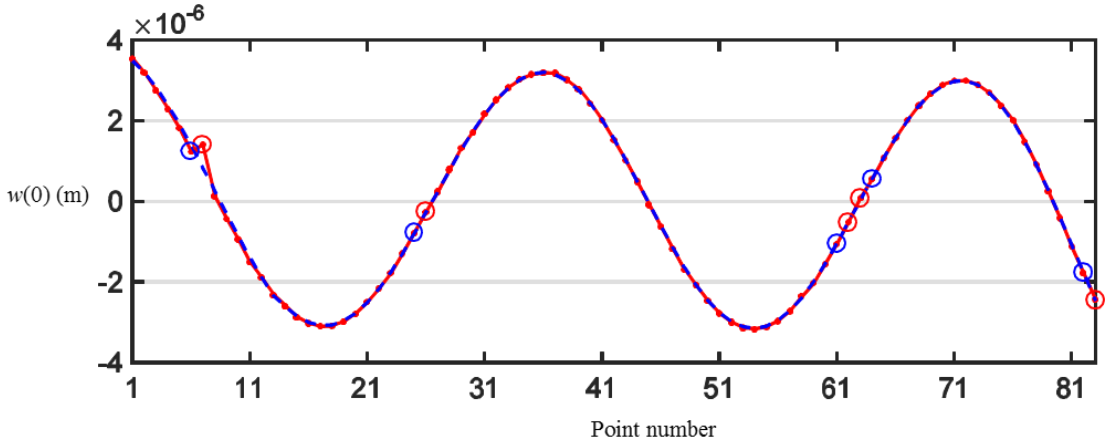

Fig. 6.12 The initial ODSs of result displacement signals.

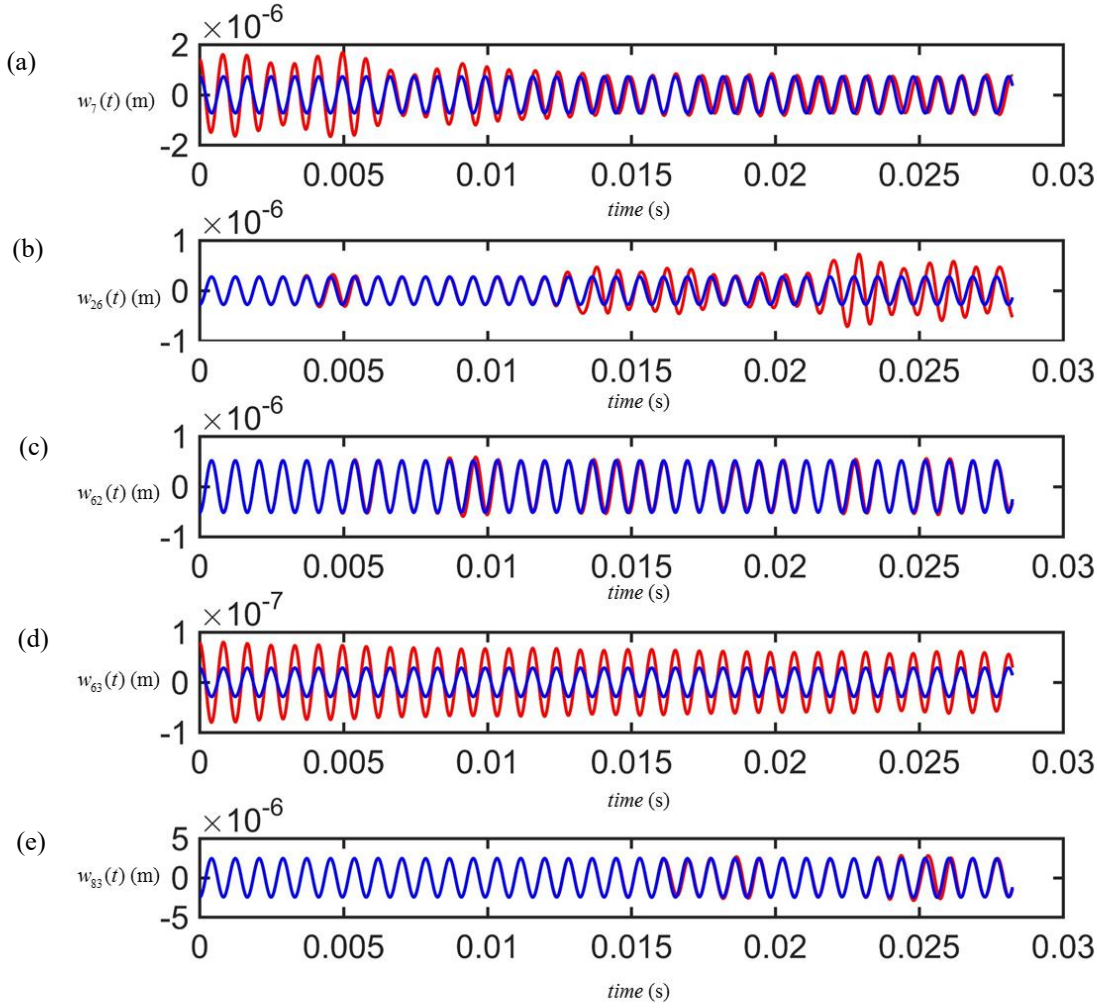

Fig. 6.13 Reconstructed displacement signals of case 2A.

With reconstruction, existed transient events for $w_7(t), w_{26}(t), w_{62}(t), w_{83}(t)$ having been fixed and $w_{63}(t)$ has a more consistent vibration amplitude. Then, rotational angle signals can be computed based on the result displacement signals with reconstructed signals. The finite difference method with fewer signals coupled together is used here for differentiation and Fig. 6.14 gives the result rotational angle signals $\theta(t)$.

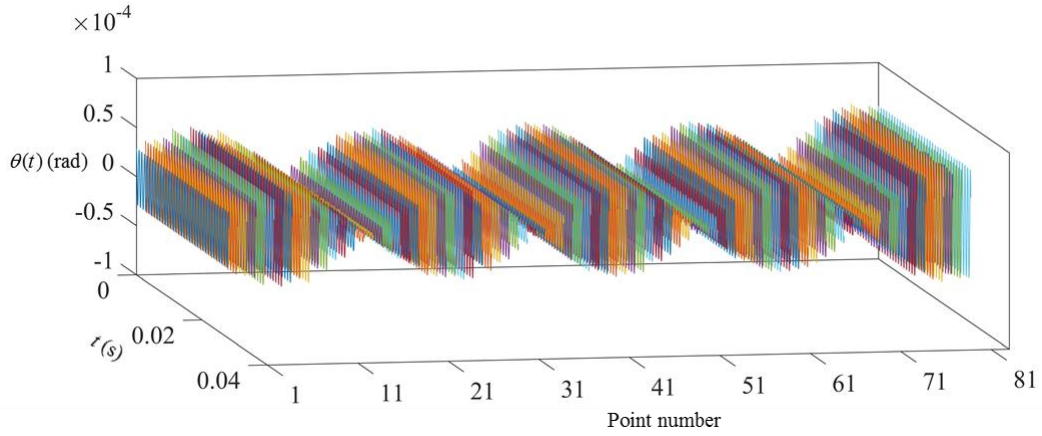

Fig. 6.14 Result rotational angle signals of case 2A.

Then the mass-CMM can be applied to compute the damage index at each time instant, and result damage index can be calculated as its average. Figure 6.15a gives the result damage index $\bar{q}_i$ in red curve with dots and the approximated baseline in blue dash curve. A window length of 14 elements is used for baseline computation. Figure 6.15b gives the filtered damage index $\hat{q}_i$ in blue lines and dots. However, there still existed obvious baseline left in $\hat{q}_i$, and deviation existed on damage location is not clear. Then, a second-time baseline filtering needs to be applied. The computed approximated baseline is given in magenta dash curve. The same window length as 14 elements is used for most points while half window length is used for the first/last 7 points as discussed in section 5.4.2. Figure 6.15c gives the twice filtered damage index $\hat{q}_i'$ in

magenta lines and dots. While the damage location is identified as elements before and after $\hat{q}'_{39}$ and marked by the grey area, the actual damage location (the 39th element) as marked by black dash lines is included in the identified damage range. The mass-CMM gives the accurate damage localization for this case.

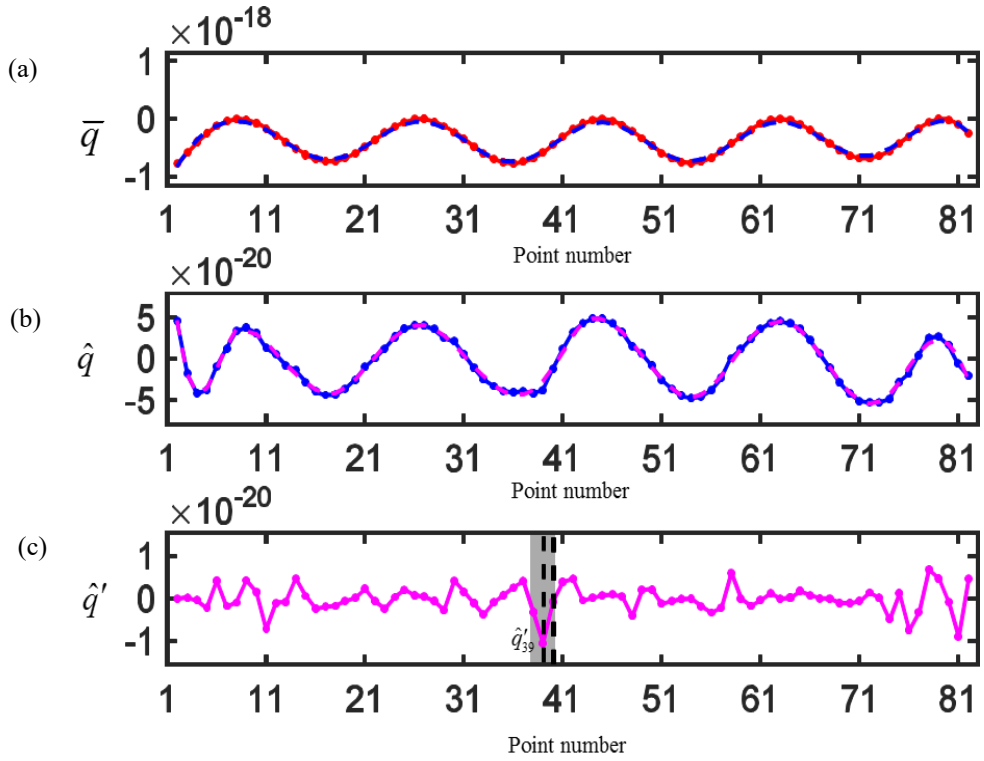

Fig. 6.15 (a) Result damage index $\bar{q}_i$ of case 2A using coefficient matrix from the elemental mass matrix, (b) corresponding filtered damage index $\hat{q}_i$ and (c) corresponding twice filtered damage index $\hat{q}'_i$.

6.3.1.2 Case 6D

With the same specimen and exciting frequency close to the same natural frequency, the case 6D will be used for comparison. The crack is located at the 41st element among the measured 91 points. The used exciting frequency is higher than case 2A as $f_6 = 1350Hz$. With the sampling rate of 512000Hz, about 379 measured time instants fall in each period. Since the experiments are performed at different time, the fixed end can be clamped with difference tightness. And with the different deviation between exciting frequency and natural

frequency, a more/less steady state vibration can be excited. Based on the measured velocity signals shown in Fig. 6.16a, much larger measuring noise existed in case 6D. The bandpass filter applied to the measured velocity signals is 1000-1600Hz and Fig. 6.16b gives the filtered velocity signals.

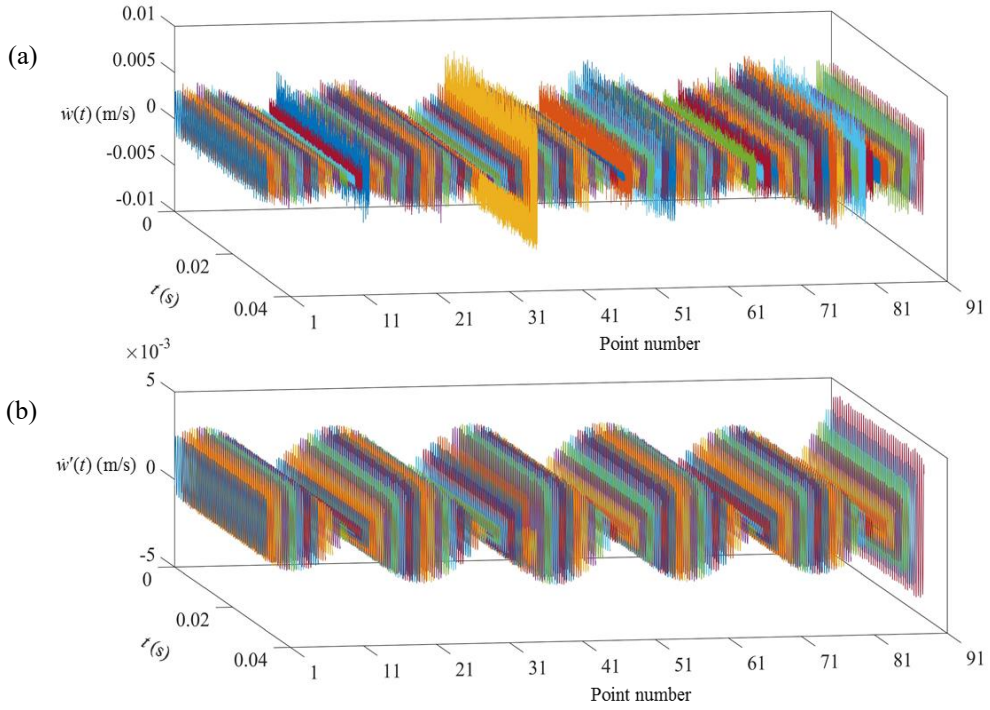

Fig. 6.16 (a) Measured velocity signals of the case 6D and (b) filtered velocity signals of the case 6D.

Based on the measured velocities shown in Fig. 6.16a, other than points located close to the 'nodes', there also exists a few points located away from the 'nodes' but contain a large measuring error (such as $\dot{w}_{15}(t)$, $\dot{w}_{38}(t)$). And displacement signals of those points may need to be reconstructed after the general procedure. EMD has been applied to the filtered velocity signals and first/last few periods of shifted velocity signals have been eliminated to avoid the edge effect. Then, the result velocity signals $\bar{\dot{w}}_i(t)$ can be constructed by aligning signals with their local maximum/minimum based on the ODSs as shown in Fig. 6.17a. Integrate the result velocity signals, apply the EMD to remove the nonzero moving average, shorten

the shifted displacement signals and aligning by their local maximum/minimum based on the ODSs, the result displacement signals can be computed as shown in Fig. 6.17b.

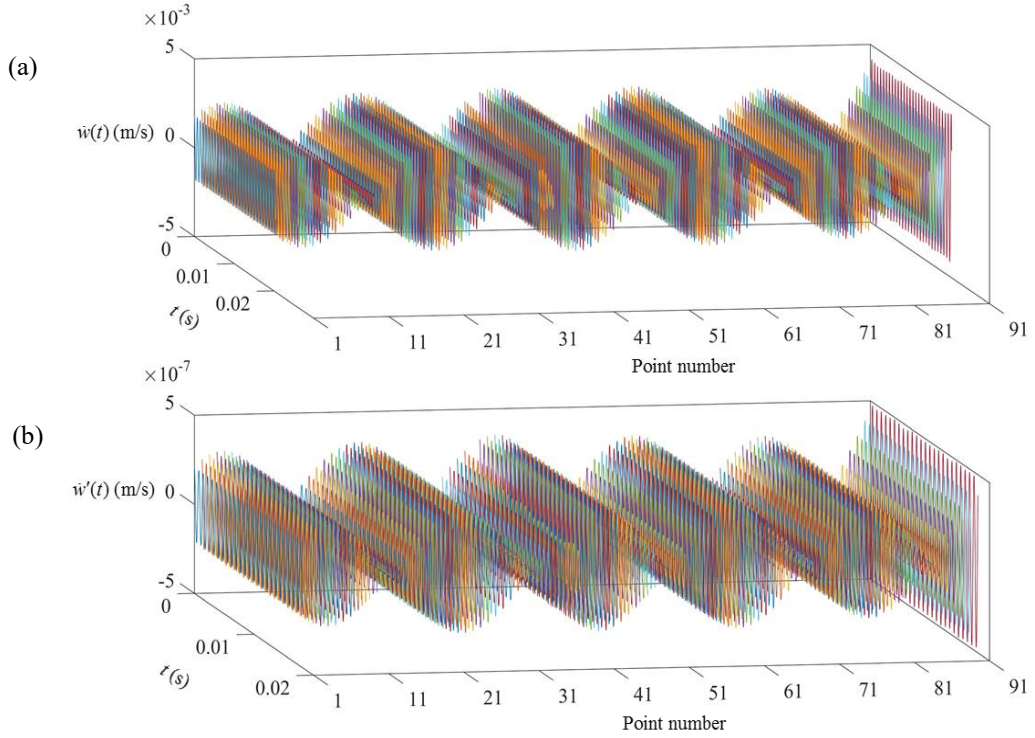

Fig. 6.17 (a) Result velocity signals of the case 6D and (b) result displacement signals of the case 6D.

Figure 6.18 gives the initial ODSs in red curve and dots, and the blue dash curve presents the curve fitting of the ODSs with a window length of 12 elements. Red circles marked the points need to be reconstructed, and blue circles marked the corresponding reference points. With the 'nodes' of mode shape located at: 13, [31,32], 50, [68,69], 85, points that need to be reconstructed is decided as: $\{r\} = \{38, 50, 85\}$. And the used reference point can be located by $\{\Delta\} = \{1, 1, 1\}$. The changing amplitude existed in $w_{38}(t)$ is caused by the inaccurate filtered velocity signal which caused by the relative larger noise existed in measured velocity. The abnormal transient events existed in $w_{50}(t), w_{85}(t)$ is caused by inaccurate filtered velocity

signal which caused by the relative large measuring noise (comparing to actual vibration signal) from the measured velocities. Figure 6.19 gives the displacement signals of the set $\{r\}$ before and after reconstruction in red curves and blue curves, respectively.

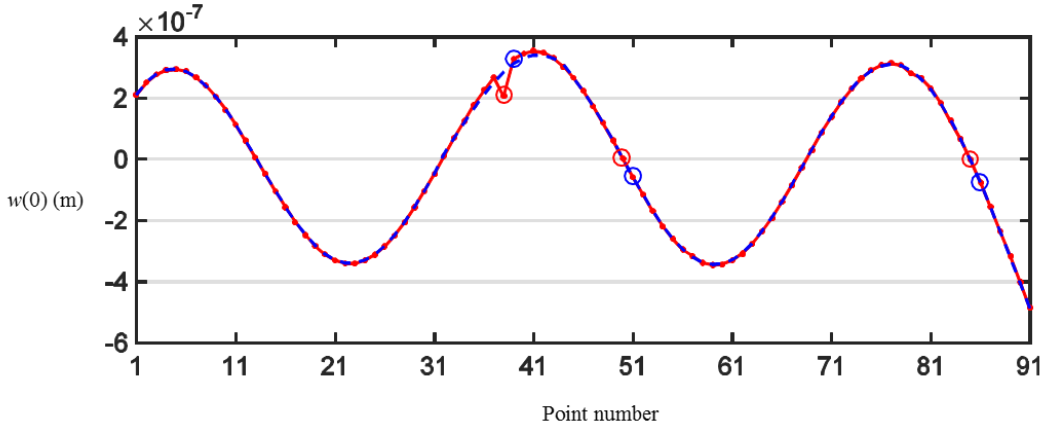

Fig. 6.18 The initial ODSs of result displacement signals.

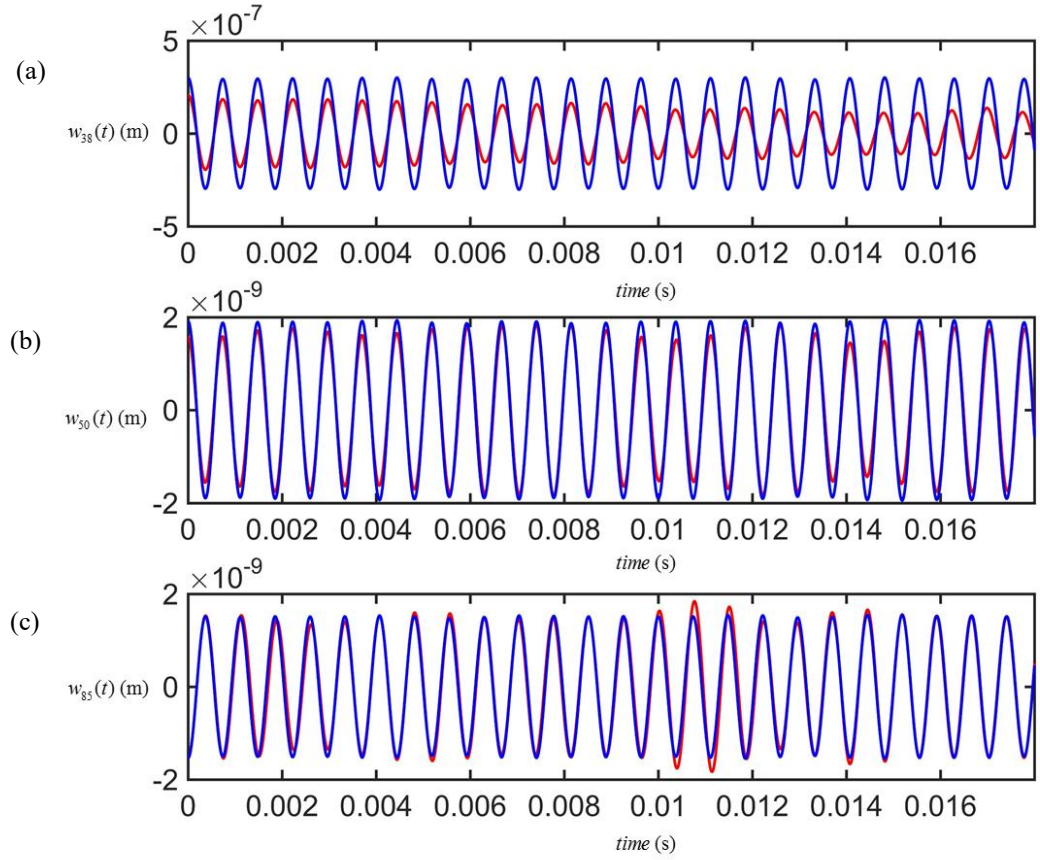

Fig. 6.19 Reconstructed displacement signals of case 6D.

The existed transient events, and changing amplitude has been corrected by reconstruction. Then, rotational angle signals can be computed by finite difference method based on the result displacement signals with a few reconstructions. Figure 6.20 gives the result rotational angle signals $\theta(t)$ computed based on finite difference method.

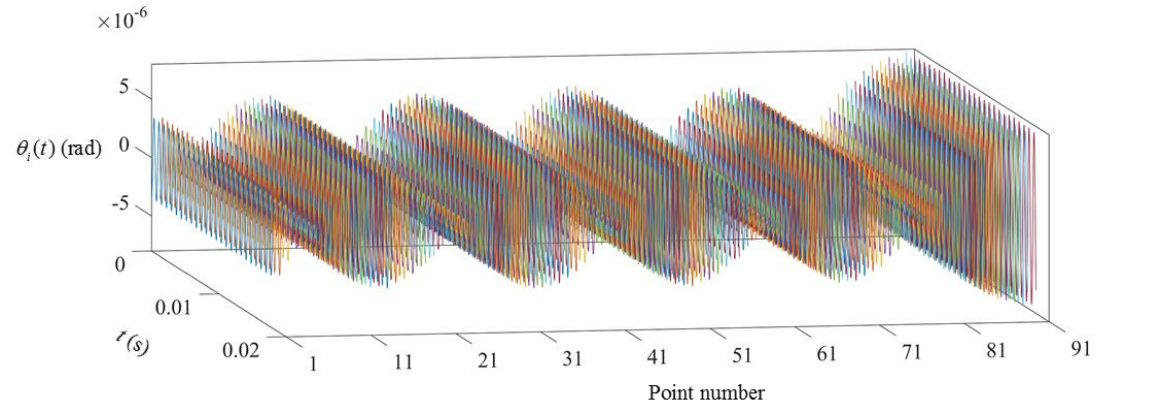

Fig. 6.20 Result rotational angle signals of case 6D.

Then the mass-CMM can be applied to compute the damage index at each time instant, and result damage index can be calculated as its average. Figure 6.21a gives the result damage index $\overline{q}_i$ in red curve with dots and the approximated baseline in blue dash curve. A window length of 14 elements is used for baseline computation. Figure 6.21b gives the filtered damage index $\hat{q}_i$ in blue lines and dots. With baseline exists in $\hat{q}_i$, a second-time baseline filtering has applied. The computed approximated baseline is given in magenta dash curve. While the same window length as 14 elements is used for most points, half window length is used for the first/last 7 points. Figure 6.21c gives the twice filtered damage index $\hat{q}_i'$ in magenta lines and dots. While the damage location is identified as elements before and after $\hat{q}_{42}'$ and marked by the grey area, the actual damage location (the 41st element) as marked by black dash lines is included in the identified damage range. The mass-CMM gives the accurate damage localization for this case.

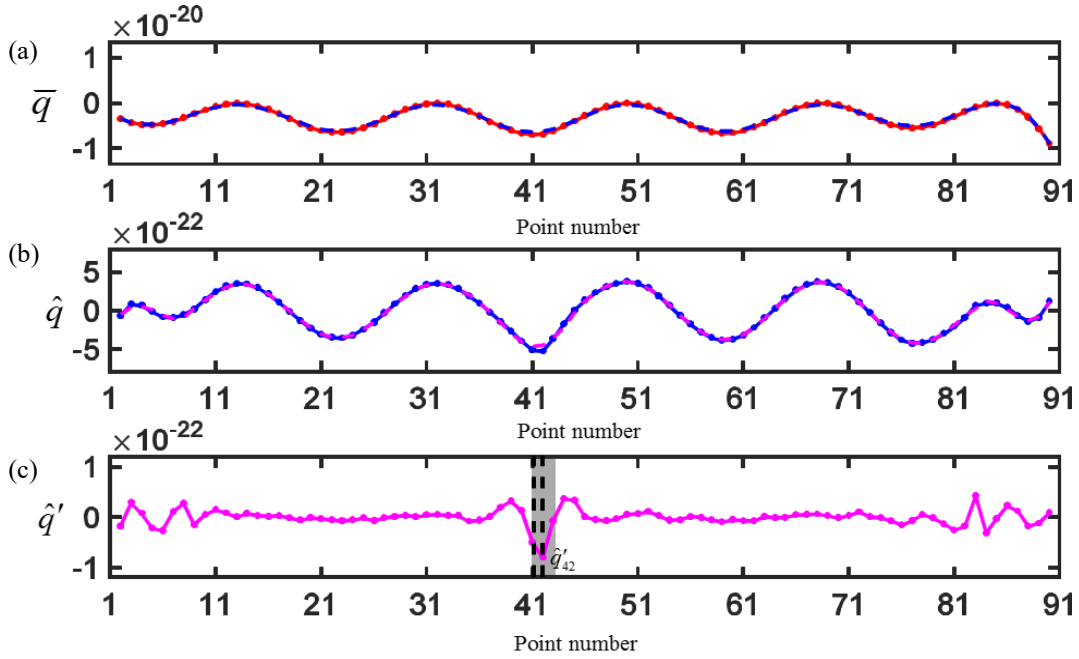

Fig. 6.21 (a) Result damage index $\bar{q}_i$ of case 6D, (b) corresponding filtered damage index $\hat{q}_i$ and (c) corresponding twice filtered damage index $\hat{q}_i'$.

Since only 3 points need to be reconstructed in the case 6D compare to the case 2A. It indicates the result displacement signals of the case 6D contains less measuring noise and error. Therefore, the stiffness-CMM will also be applied to method verification. Filtered damage index $\hat{d}(t_k)$ can be computed from the damage index $d_i(t_k)$ at each time instant t_k, and the counting damage index d^C will be computed based on filtered damage index. While Fig. 6.22a gives the d^C in bars, Fig. 6.22b gives the filtered damage index $\hat{d}_i = \bar{d}_i - b_i$ (take average first and then filter the baseline) in red curves and dots for comparison. While the identified damage location marked by the grey area in both Fig. 6.22a&b, the actual damage location (the 41th element) is marked by black dash lines in Fig. 6.22a&b. As we can see, while the calculation error gives an false damage location as elements before and after $\hat{d}_2$, the counting damage index gives the accurate

identified damage location as elements before and after d_{42}^{C}. The counting damage index d^{C} can eliminate the influence from the calculation error and gives a more accurate identified damage location for the applied stiffness-CMM.

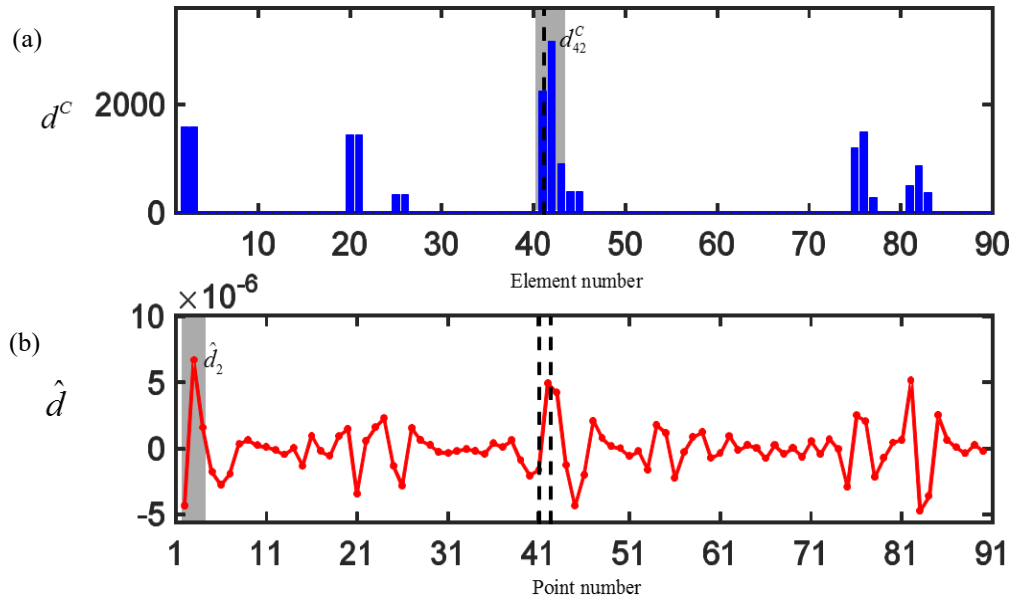

Fig. 6.22 (a) Counting damage index of the case 6D and (b) filtered damage index of the case 6D.

6.3.2 ODSs Close to the 8th Mode Shape

6.3.2.1 Case 2C

Case 2C is performed with an exciting frequency of $f_8 = 2278Hz$ to have the 8th mode vibration as its major vibration. With the sampling rate of 256000Hz, about 112 measured time instants fall in each period. Same grid is used for measuring as in the case 2A. Figure 6.23a gives the measured velocity, and Fig. 6.23b gives the filtered velocity signals with applied band pass filter in the range of 1300-3300Hz.

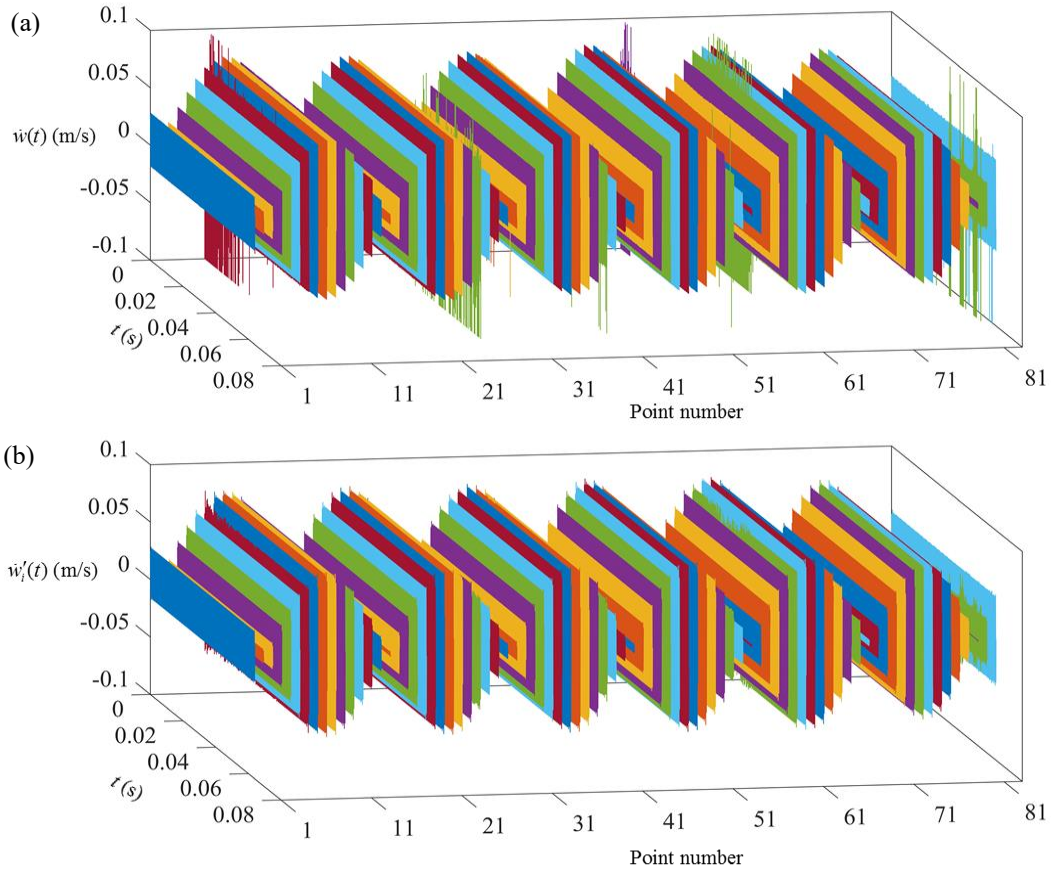

Fig. 6.23 (a) Measured velocity signals of the case 6D and (b) filtered velocity signals of the case 6D.

Based on Fig. 6.23a, there exist several points located away from the 'nodes' but with relative large measuring noise and may need to be reconstructed after the general procedure. Apply the EMD to remove the nonzero moving average, shorten the shifted velocity signal to avoid the edge effect, the result velocity signals $\bar{\dot{w}}_i(t)$ can be constructed by aligning signals with their local maximum/minimum based on the ODSs as shown in Fig. 6.24a. Integrate the result velocity signals, apply the EMD to remove the nonzero moving average, shorten the shifted displacement signals and aligning by their local maximum/minimum based on the ODSs, the result displacement signals $w_i(t)$ can be computed as shown in Fig. 6.24b.

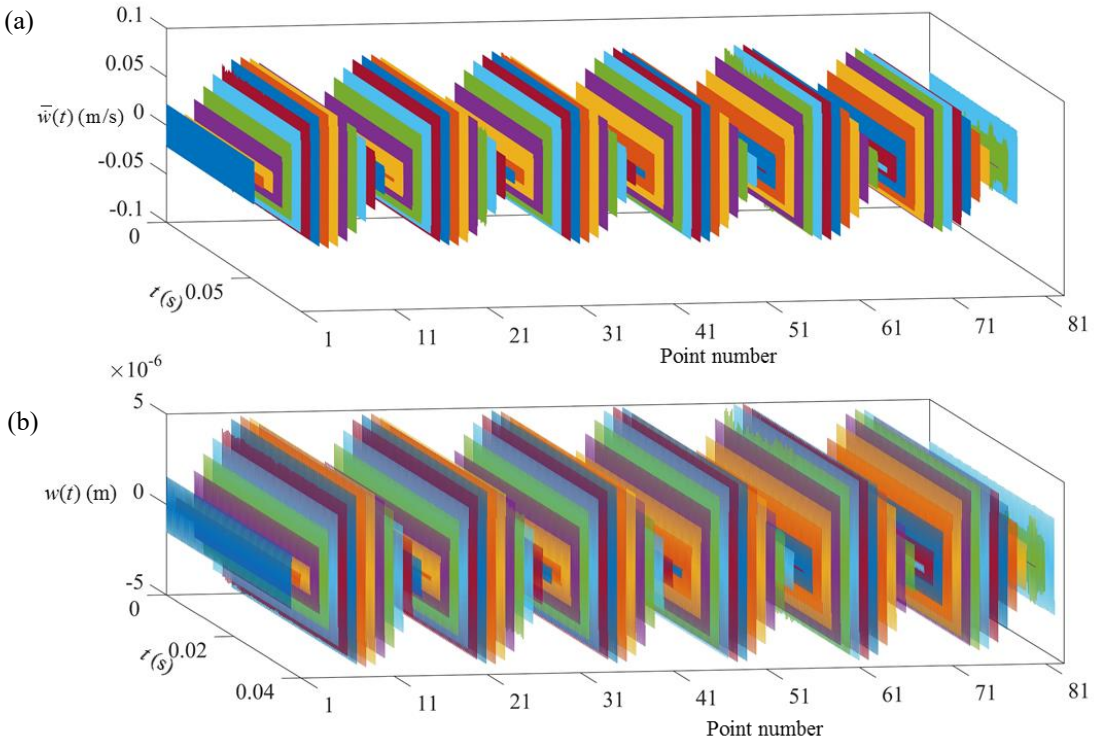

Fig. 6.24 (a) Result velocity signals of the case 2C and (b) result displacement signals of the case 2C.

Figure 6.25 gives the initial ODSs in red curve and dots, and the blue dash curve presents the curve fitting of the ODSs with a window length of 8 elements. Red circles marked the points need to be reconstructed, and blue circles marked the corresponding reference points. With the 'nodes' of mode shape located at: [2,3], 16, [29,30], [42,43], 56, 69, 81, points need to be reconstructed is decided as: $\{r\} = \{56, 61, 81, 82\}$. And the used reference point can be located by $\{\Delta\} = \{-1, 1, -1, 1\}$. The abnormal transient events existed in $w_{61}(t), w_{82}(t)$ is caused by the relative larger noise caused by other interference signals as shown in Fig. 6.23a. The changing amplitude existed in $w_{56}(t), w_{81}(t)$ is caused by inaccurate filtered velocity signal which caused by the relative large measuring noise (comparing to actual vibration

signal) from the measured velocities. Figure 6.26 gives the displacement signals of the set $\{r\}$ before and after reconstruction in red curves and blue curves, respectively.

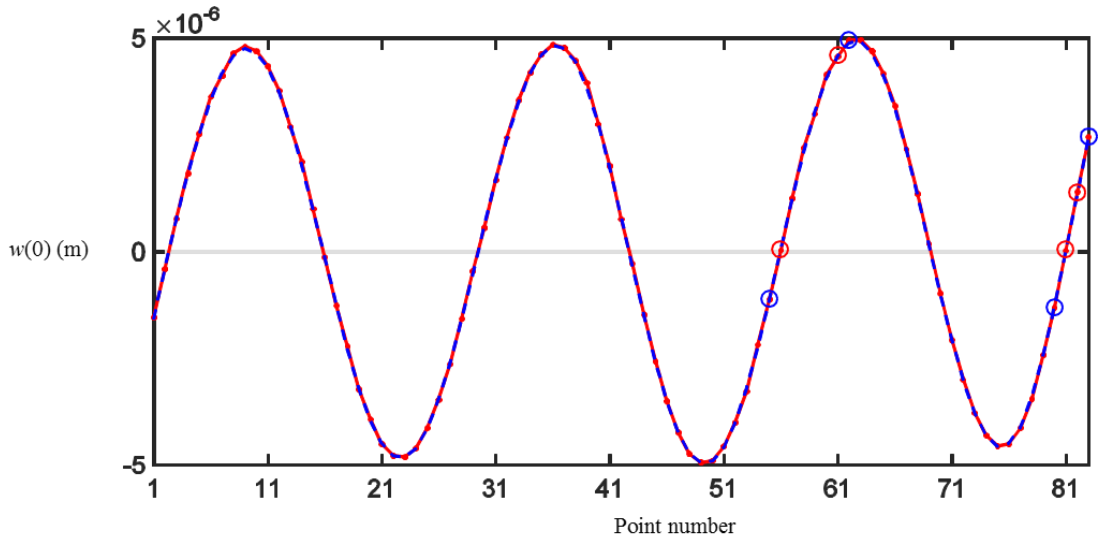

Fig. 6.25 The initial ODSs of result displacement signals.

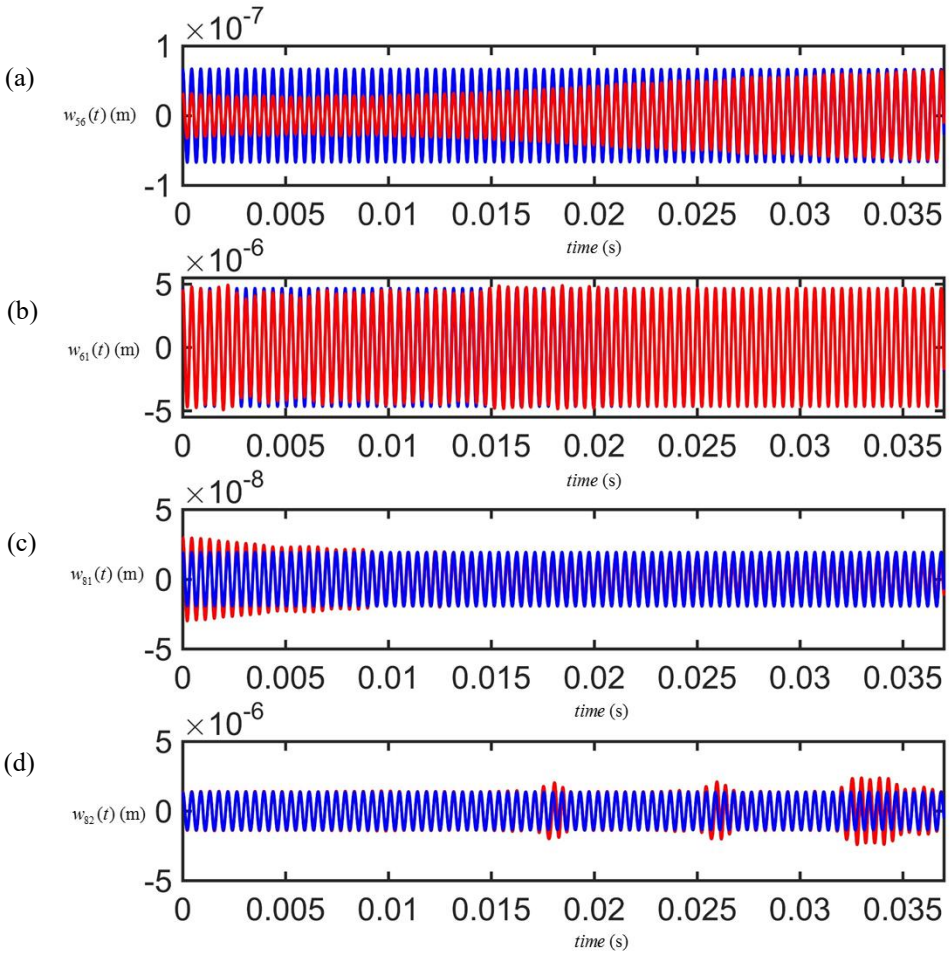

Fig. 6.26 Reconstructed displacement signals of case 2C.

Although the nonlinear behavior of signal $w_{61}(t)$ is relatively small, with the relative large vibration amplitude, it can be easily noticed as a discontinuous in ODSs at point 61. On the contract, although the nonlinear behavior of signal $w_{56}(t)$ is relatively large, with the relative small vibration amplitude, it cannot be noticed directly in ODSs. Through the reconstructions, existed changing the amplitude and abnormal transient events have been corrected. Then, rotational angle signals can be computed by finite difference method based on the result displacement signals with a few points reconstructed. And Fig. 6.27 gives the

result rotational angle signals.

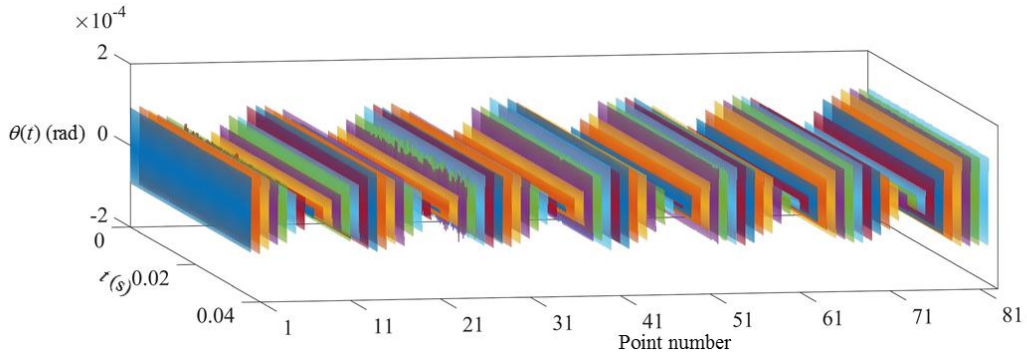

Fig. 6.27 Result rotational angle signals of case 2C.

Then the mass-CMM can be applied to compute the damage index at each time instant, and result damage index can be calculated as its average. Figure 6.28a gives the result damage index $\bar{q}_i$ in red curve with dots and the approximated baseline in blue dash curve. A window length of 12 elements is used for baseline computation. Figure 6.28b gives the filtered damage index $\hat{q}_i$ in blue lines and dots. With baseline exists in $\hat{q}_i$, a second-time baseline filtering has applied. The computed approximated baseline is given in magenta dash curve. While the same window length as 12 elements is used for most points, half window length is used for the first/last 6 points. While the damage location is identified as elements before and after $\hat{q}'_{39}$ and marked by the grey area, the actual damage location (the 39th element) as marked by black dash lines is included in the identified damage range. The mass-CMM gives the accurate damage localization for this case.

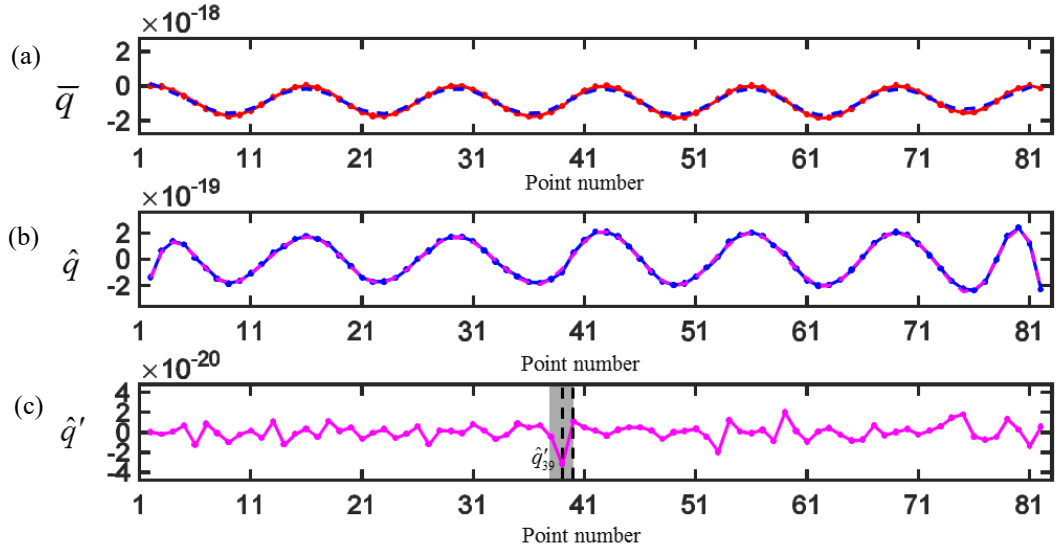

Fig. 6.28 (a) Result damage index $\bar{q}_i$ of case 2C, (b) corresponding filtered damage index $\hat{q}_i$ and (c) corresponding twice filtered damage index $\hat{q}'_i$.

6.3.2.2 Case 5E

With the same specimen and exciting frequency close to the same natural frequency, the case 5E will be used for comparison. The same grid is used for measuring as in case 6D. The crack is located at the 41st element among the measured 91 points. The used exciting frequency is higher than case 2C as $f_8 = 2400Hz$. With the sampling rate of 512000Hz, about 213 measured time instants fall in each period. Based on the measured velocity signals shown in Fig. 6.29a, measured signals are relative consistent along the time trace and fewer points have large measuring error. The bandpass filter applied to the measured velocity signals is 1400-3400Hz and Fig. 6.29b gives the filtered velocity signals.

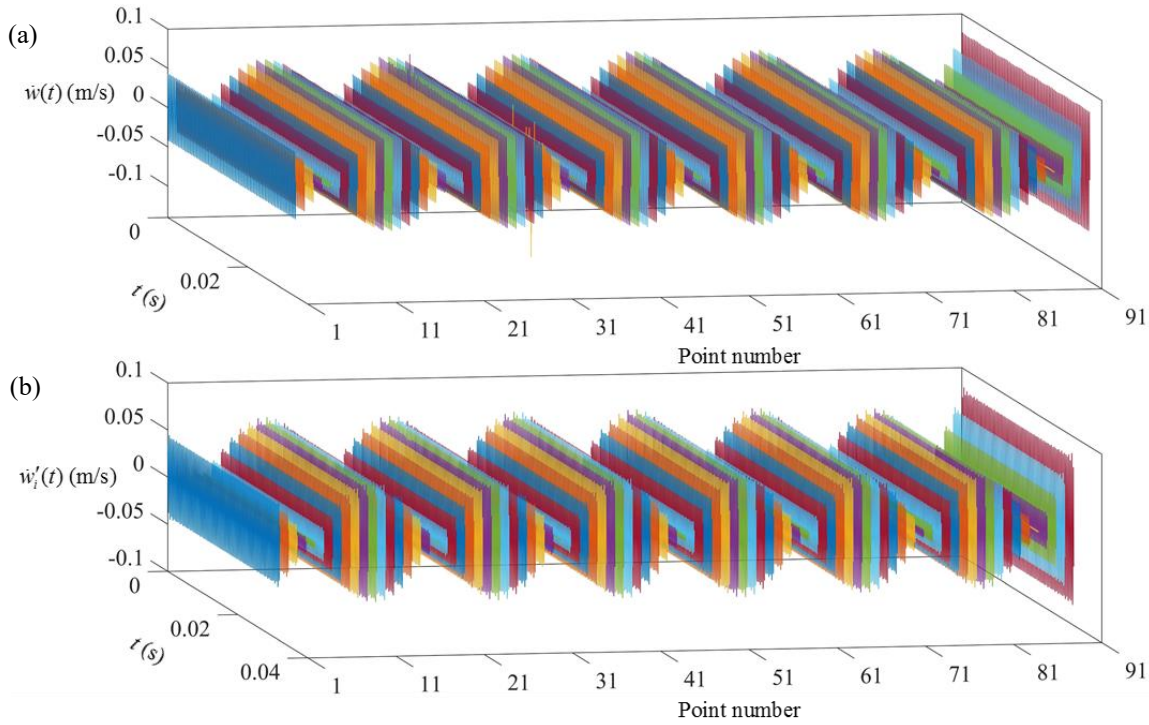

Fig. 6.29 (a) Measured velocity signals of the case 5E and (b) filtered velocity signals of the case 5E.

Based on the measured velocities shown in Fig. 6.29a, other than points located close to the 'nodes', there also exists points away from the 'nodes' contain a large measuring error (such as $\dot{w}_{25}(t), \dot{w}_{30}(t)$). And the signals of these points may need to be reconstructed after the general procedure. EMD has been applied to the filtered velocity signals and first/last few periods of shifted velocity signals have been eliminated to avoid the edge effect. Then, the result velocity signals $\bar{\dot{w}}_i(t)$ can be constructed by aligning signals with their local maximum/minimum based on the ODSs as shown in Fig. 6.30a. Integrate the result velocity signals, apply the EMD to remove the nonzero moving average, shorten the shifted displacement signals and aligning by their local maximum/minimum based on the ODSs, the result displacement signals can be computed as shown in Fig. 6.30b.

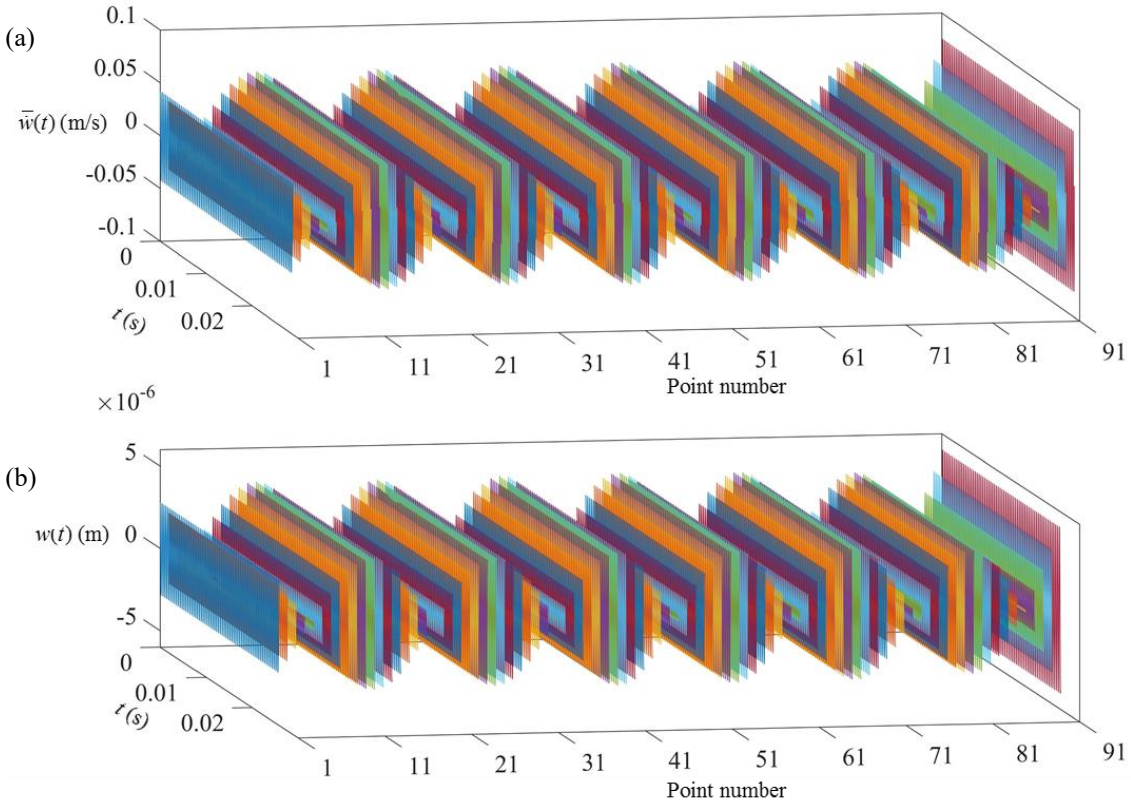

Fig. 6.30 (a) Result velocity signals of the case 5E and (b) result displacement signals of the case 5E.

Figure 6.31 gives the initial ODSs in red curve and dots, and the blue dash curve presents the curve fitting of the ODSs with a window length of 8 elements. Red circles marked the points need to be reconstructed, and blue circles marked the corresponding reference points. With the 'nodes' of mode shape located at: [4,5], 19, 33, [46,47], [60,61], [74,75], 87, points need to be reconstructed is decided as: $\{r\} = \{19, 33, 87\}$. And the used reference point can be located by $\{\Delta\} = \{1, 1, 1\}$. Large noise existed in $\dot{w}_{25}(t)$ and $\dot{w}_{30}(t)$ has been corrected by the general procedure, and signals of those two points do not need to be reconstructed. The inaccurate and inconsistent amplitude existed in $w_{19}(t), w_{33}(t)$ and $w_{87}(t)$ is caused by the inaccurate filtered velocity signal which caused by the relative large measuring noise

(comparing to actual vibration signal) from the measured velocities. Figure 6.32 gives the displacement signals of the set $\{r\}$ before and after reconstruction in red curves and blue curves, respectively.

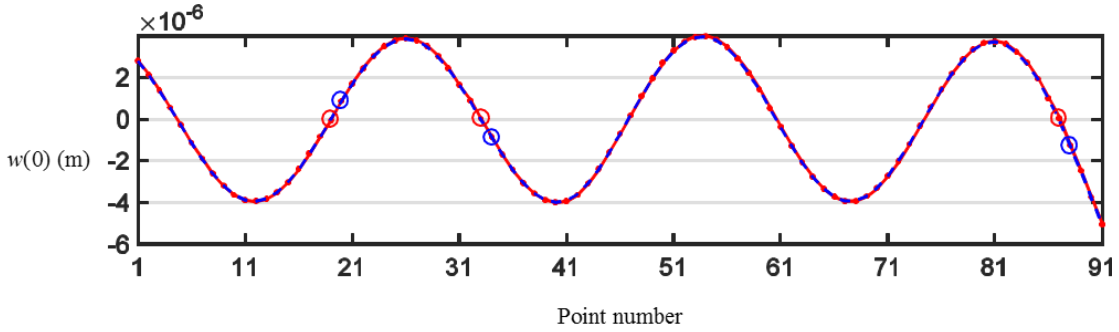

Fig. 6.31 The initial ODSs of result displacement signals.

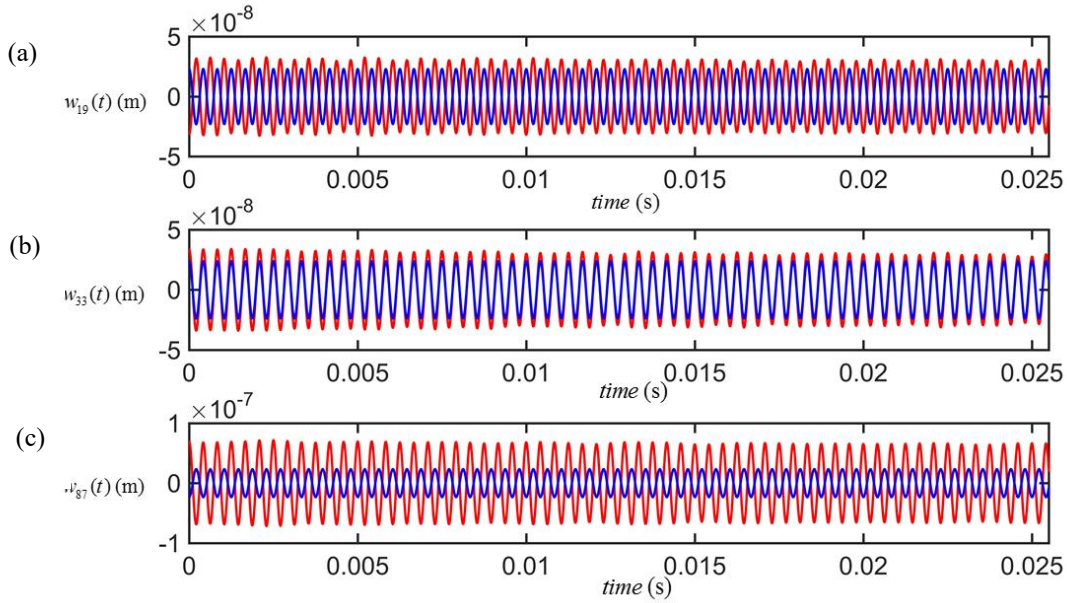

Fig. 6.32 Reconstructed displacement signals of case 5E.

With point 19, 33, 87 located nearly coincide with the 'nodes' as shown in Fig. 6.31, the amplitude of displacement response is relative inconsistent along the time trace. Moreover, based on Eq. (6.1), the reconstructed and result displacement signal of point 19,87 has opposite signs. However, with relatively small

amplitude, the relatively large change is shown in Fig. 6.32 will not give much influence on the ODSs, and the mode vibration is relatively insensitive to these signals. Rotational angle signals can be computed by finite difference method based on the result displacement signals with a few reconstructions. Figure 6.33 gives the result rotational angle signals $\theta(t)$ computed based on finite difference method.

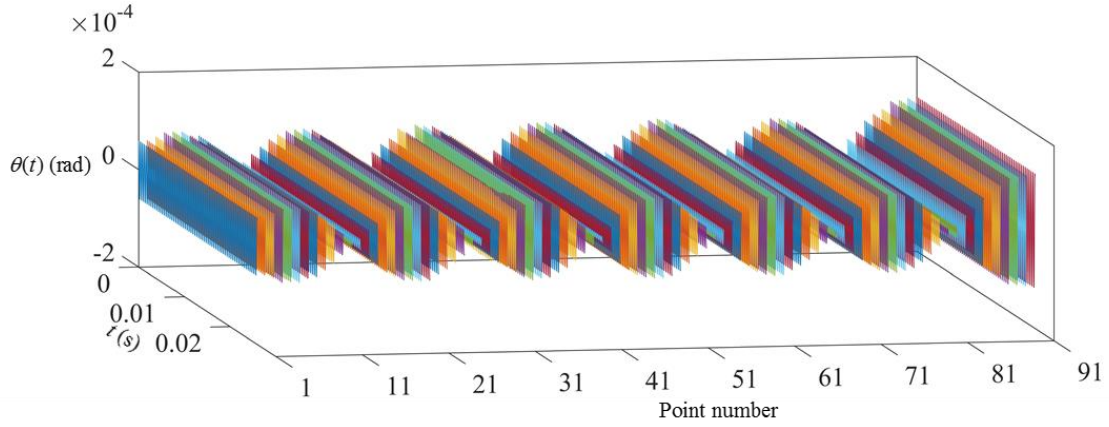

Fig. 6.33 Result rotational angle signals of case 5E.

Then the mass-CMM can be applied to compute the damage index at each time instant, and result damage index can be calculated as its average. Figure 6.34a gives the result damage index $\bar{q}_i$ in red curve with dots and the approximated baseline in blue dash curve. A window length of 10 elements is used for baseline computation. Figure 6.34b gives the filtered damage index $\hat{q}_i$ in blue lines and dots. With baseline exists in $\hat{q}_i$, a second-time baseline filtering has applied. The computed approximated baseline is given in magenta dash curve. While the same window length as 10 elements is used for most points, half window length is used for the first/last 5 points. Figure 6.34c gives the twice filtered damage index $\hat{q}_i'$ in magenta lines and dots. While the damage location is identified as elements before and after $\hat{q}_{42}'$ and marked by the grey area, the actual damage location (the 41st element) as marked by black dash lines is included in the identified

damage range. The mass-CMM gives the accurate damage localization for this case.

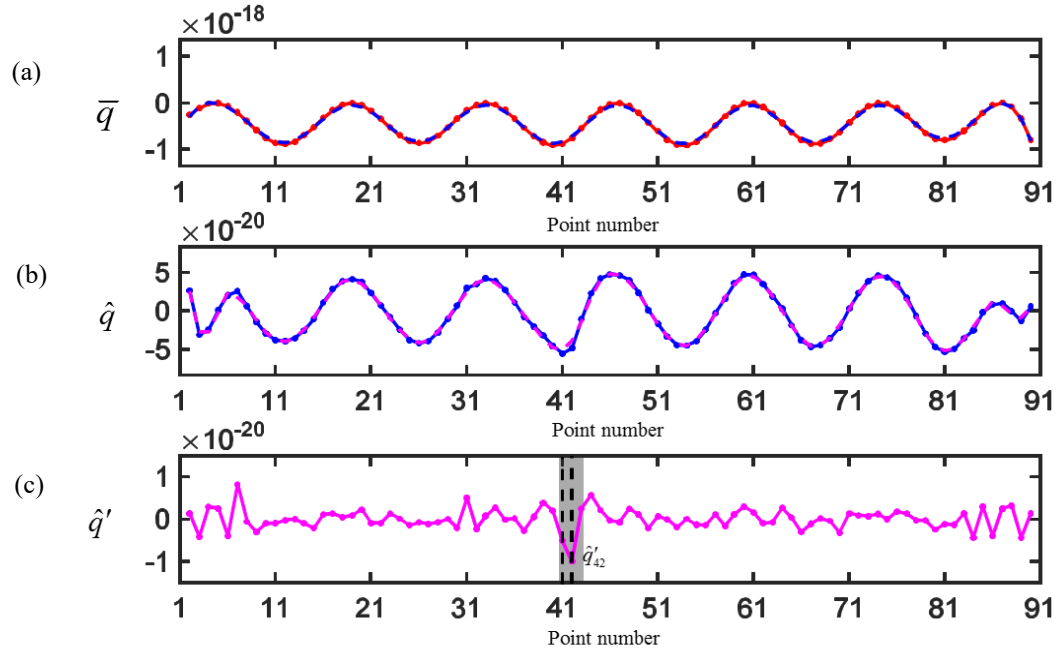

Fig. 6.34 (a) Result damage index $\bar{q}_i$ of case 5E using coefficient matrix from the elemental mass matrix, (b) corresponding filtered damage index $\hat{q}_i$ and (c) corresponding twice filtered damage index $\hat{q}'_i$.

Since only 3 points need to be reconstructed in the case 5E compare to the case 2C and all caused by locating close to the 'nodes'. It indicates the result displacement signals of the case 5E contains less measuring noise and error. Therefore, the stiffness-CMM will also be applied to method verification. Filtered damage index $\hat{d}(t_k)$ can be computed from the damage index $d_i(t_k)$ at each time instant t_k, and the counting damage index d^C will be computed based on filtered damage index. While Fig. 6.35a gives the d^C in bars, Fig. 6.35b gives the filtered damage index $\hat{d}_i = \overline{d}_i - b_i$ (take average first and then filter the baseline) in red curves and dots for comparison. While the identified damage location marked by the grey area in both Fig. 6.35a&b, the actual damage location (the 41th element) is marked by black dash lines in Fig. 6.35a&b. For this case, both filtered damage index and counting damage index gives the accurate identified damage location as the elements before and after d^C_{41} (d^C_{42}) in Fig. 6.35a and elements before and after $\hat{d}_{42}$ in Fig. 6.35b. With relative small measuring error, the stiffness-CMM can give an accurate damage location by both the filtered damage index and the counting damage index.

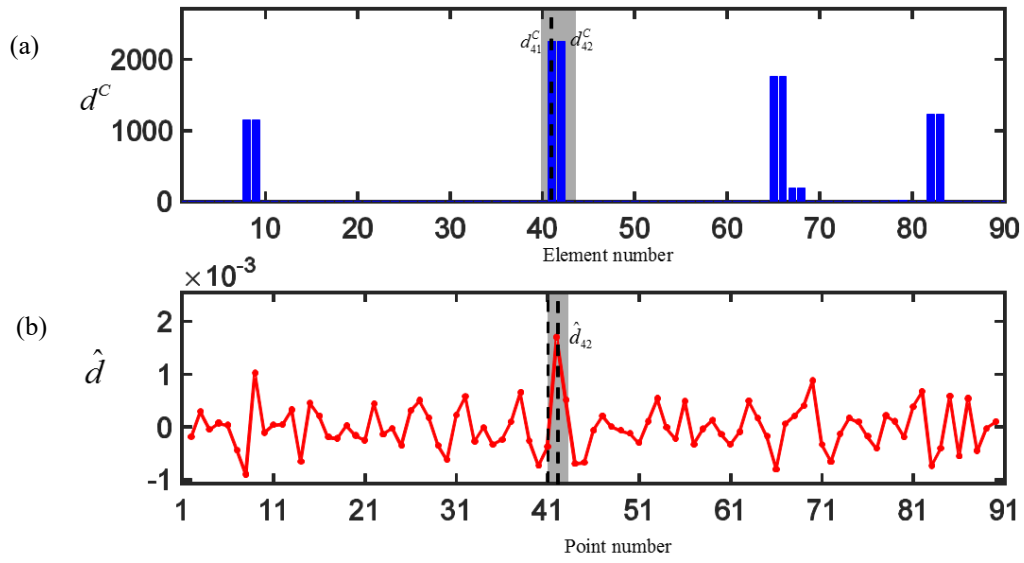

Fig. 6.35 (a) Counting damage index of the case 5E and (b) filtered damage index of the case 5E.

6.3.3 ODSs Close to the 2nd Mode Shape (Case 5D)

Although there are no multiple experiments can be used to double-confirm the rest mode vibrations, the performed experiments still can be used to testify the sensitivity of mode vibration according to predicted natural frequency change ratio. With the largest predicted natural frequency change ratio, experimental data of case 5D having the 2nd mode vibration as its major vibration is discussed here. The used exciting frequency is in the case 5D as $f_2 = 100Hz$. With the sampling rate of 51200Hz, about 512 measured time instants fall in each period. The crack is located at the 41st element among the measured 91 points. Based on the measured velocity signals shown in Fig. 6.36a, measured signals are relative consistent along the time trace, and there is no obvious damage from other interference signals. The bandpass filter applied to the measured velocity signals is 50-150Hz and Fig. 6.36b gives the filtered velocity signals.

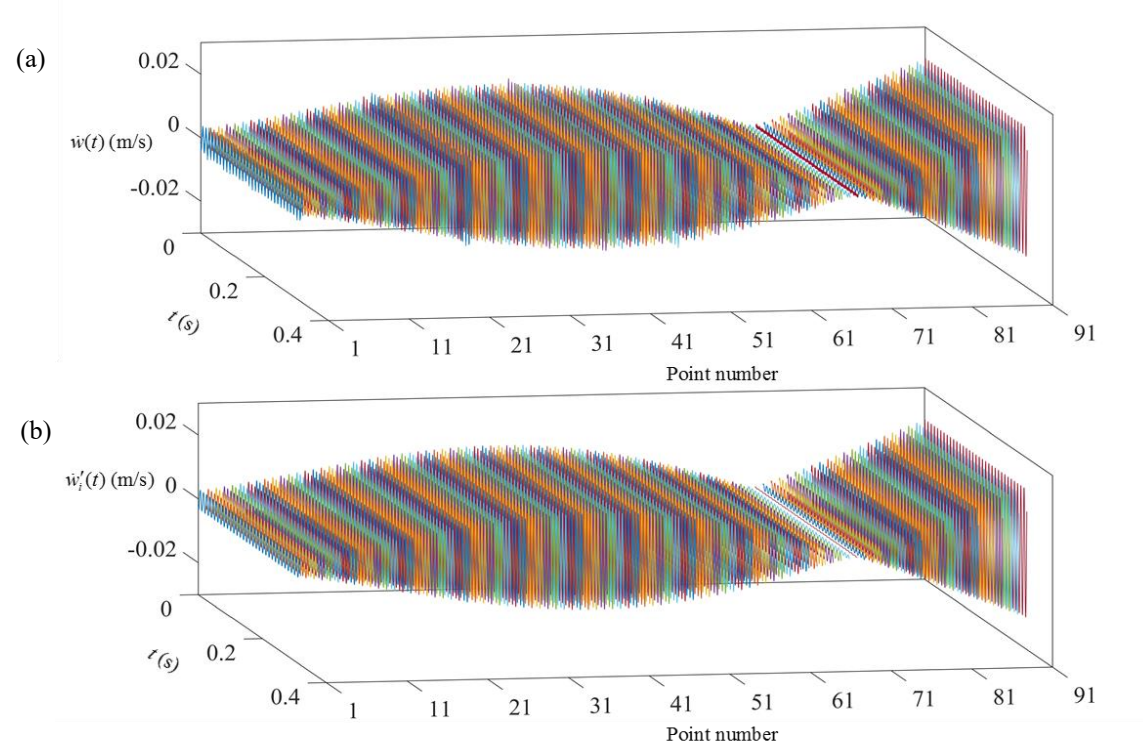

Fig. 6.36 (a) Measured velocity signals of the case 5D and (b) filtered velocity signals of the case 5D.

Without any obvious damage from other interference signals, the only signal may need to be reconstructed would be $w_{70}(t)$ since it is located at the 'node'. EMD has been applied to the filtered velocity signals and first/last few periods of shifted velocity signals have been eliminated to avoid the edge effect. Then, the result velocity signals $\bar{\dot{w}}_i(t)$ can be constructed by aligning signals with their local maximum/minimum based on the ODSs as shown in Fig. 6.37a. Integrate the result velocity signals, apply the EMD to remove the nonzero moving average, shorten the shifted displacement signals and aligning by their local maximum/minimum based on the ODSs, the result displacement signals can be computed as shown in Fig. 6.37b.

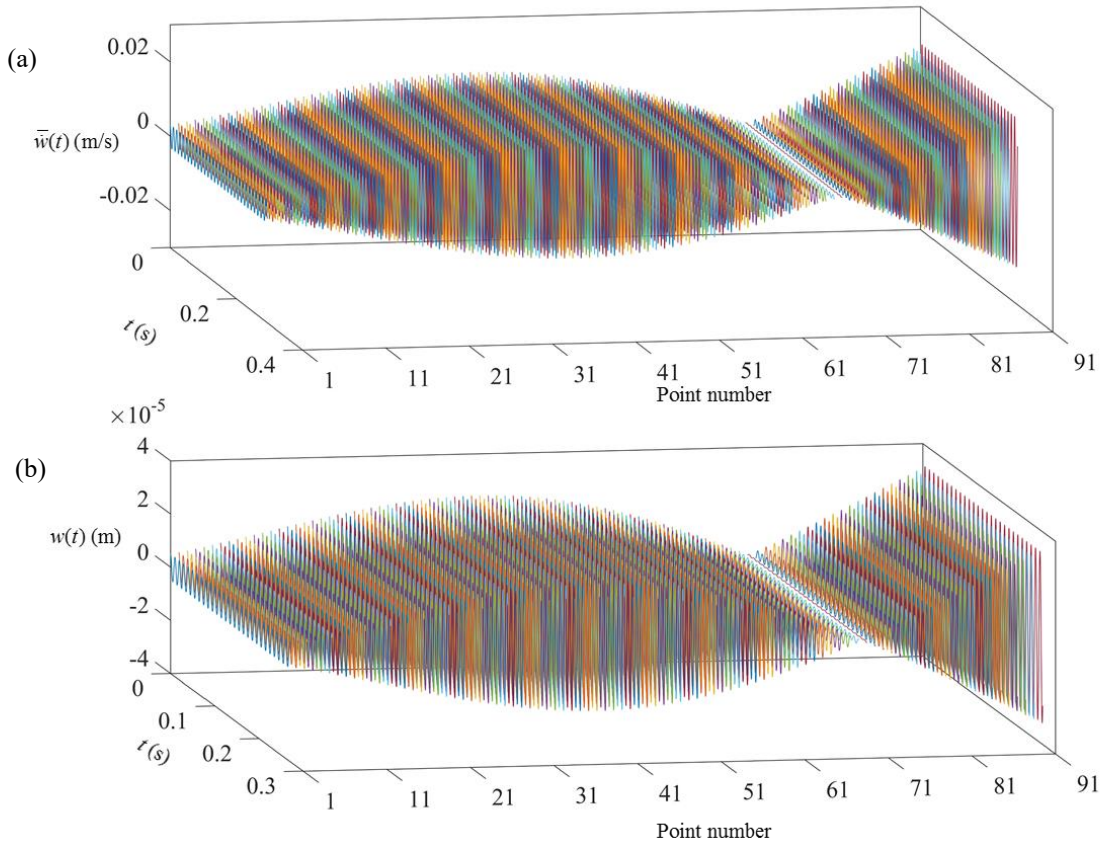

Fig. 6.37 (a) Result velocity signals of the case 5D and (b) result displacement signals of the case 5D.

Figure 6.38a gives the initial ODSs in red curve and dots, and the blue dash curve presents the curve fitting of the ODSs with a window length of 24 elements. Red circles marked the points need to be reconstructed, and blue circles marked the corresponding reference points. With the 'nodes' of mode shape located at: 70, points that need to be reconstructed is decided as: $\{r\} = \{70\}$. And the used reference point can be located by $\{\Delta\} = \{1\}$. The abnormal transient events existed in $w_{70}(t)$ is caused by inaccurate filtered velocity signal which caused by the relative large measuring noise (comparing to actual vibration signal) from the measured velocities. Figure 6.38b gives the displacement signals of set $\{r\}$ before and after reconstruction in red curves and blue curves, respectively.

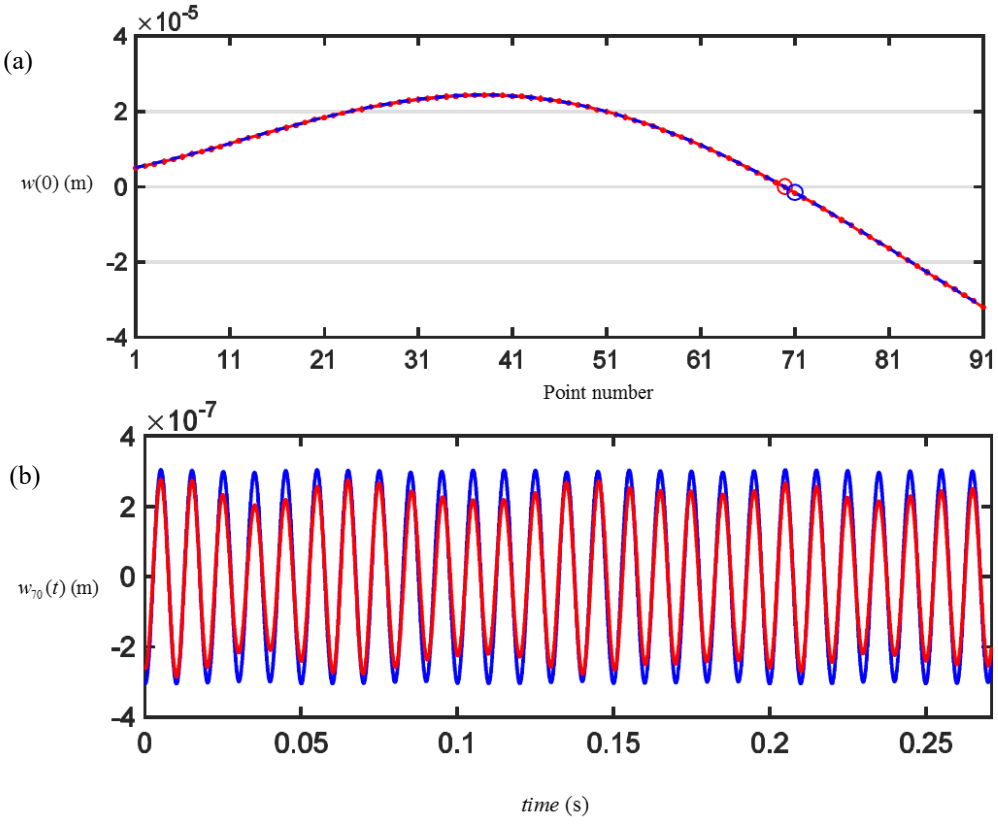

Fig. 6.38 (a) The initial ODSs of result displacement signals and (b) reconstructed displacement signals of case 5D.

The existed abnormal transient events have been corrected by reconstruction. Then, rotational angle signals can be computed by finite difference method based on the result displacement signals with a few reconstructions. Figure 6.39 gives the result rotational angle signals $\theta(t)$ computed based on finite difference method.

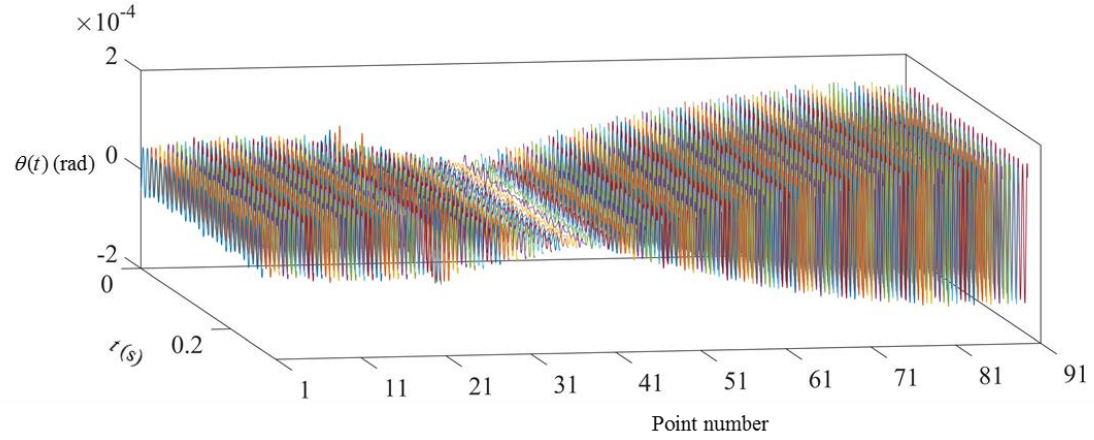

Fig. 6.39 Result rotational angle signals of case 5D.

Then the mass-CMM can be applied to compute the damage index at each time instant, and result damage index can be calculated as its average. Figure 6.40a gives the result damage index $\bar{q}_i$ in red curve with dots and the approximated baseline in blue dash curve. A window length of 30 elements is used for baseline computation. Figure 6.40b gives the filtered damage index $\hat{q}_i$ in blue lines and dots. With baseline exists in $\hat{q}_i$, a second-time baseline filtering has applied. The computed approximated baseline is given in magenta dash curve. While the same window length as 30 elements is used for most points, half window length is used for the first/last 15 points. Figure 6.40c gives the twice filtered damage index $\hat{q}_i'$ in magenta lines and dots. While the damage location is identified as elements before and after $\hat{q}_{42}'$ and marked by the grey area, the actual damage location (the 41st element) as marked by black dash lines is included in the identified

damage range. The mass-CMM gives the accurate damage localization for this case.

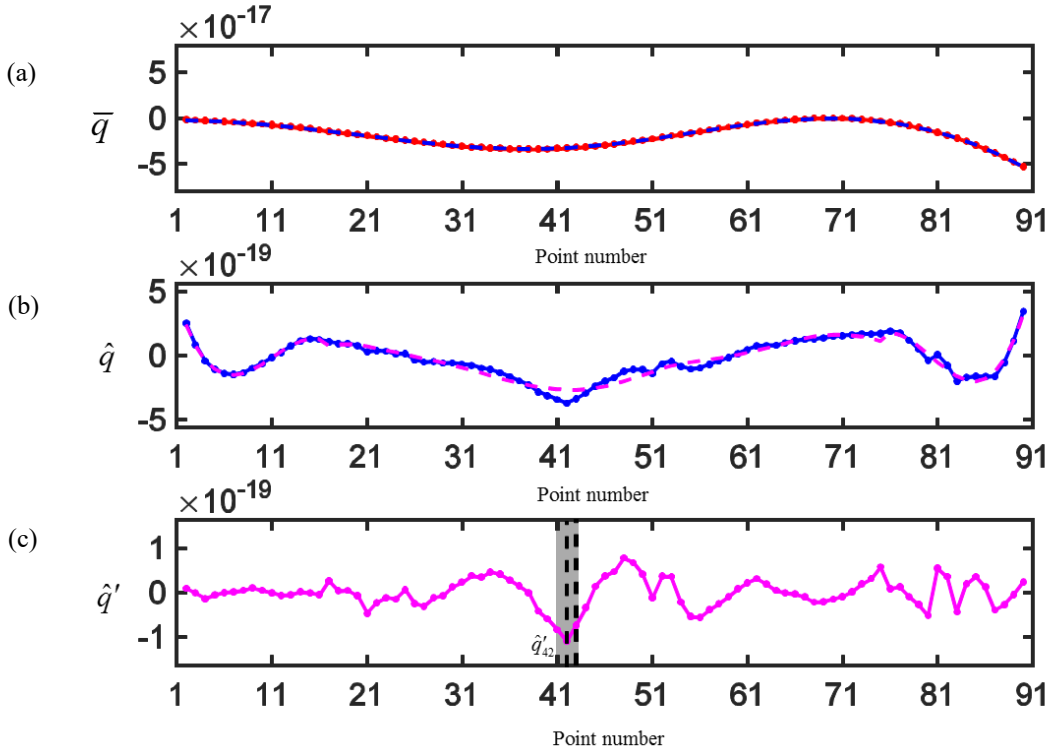

Fig. 6.40 (a) Result damage index $\bar{q}_i$ of case 5D using coefficient matrix from the elemental mass matrix, (b) corresponding filtered damage index $\hat{q}_i$ and (c) corresponding twice filtered damage index $\hat{q}'_i$.

6.3.4 ODSs Close to the 4th Mode Shape (Case 6B)

With the relative large predicted natural frequency change ratio, experimental data of case 6B having the 4th mode vibration as its major vibration is discussed here. The used exciting frequency is in the case 6B as $f_4 = 550Hz$. With the sampling rate of 128000Hz, about 232 measured time instants fall in each period. The crack is located at the 41st element among the measured 91 points. Based on the measured velocity signals shown in Fig. 6.41a, measured signals are relative consistent along the time trace, and there is no obvious damage from other interference signals. The bandpass filter applied to the measured velocity signals is 250-

850Hz. Figure 6.41b gives the filtered velocity signals, and the edge effect from FFT filter shows clearly as the existed disturbance at two ends of amplitude in each signal.

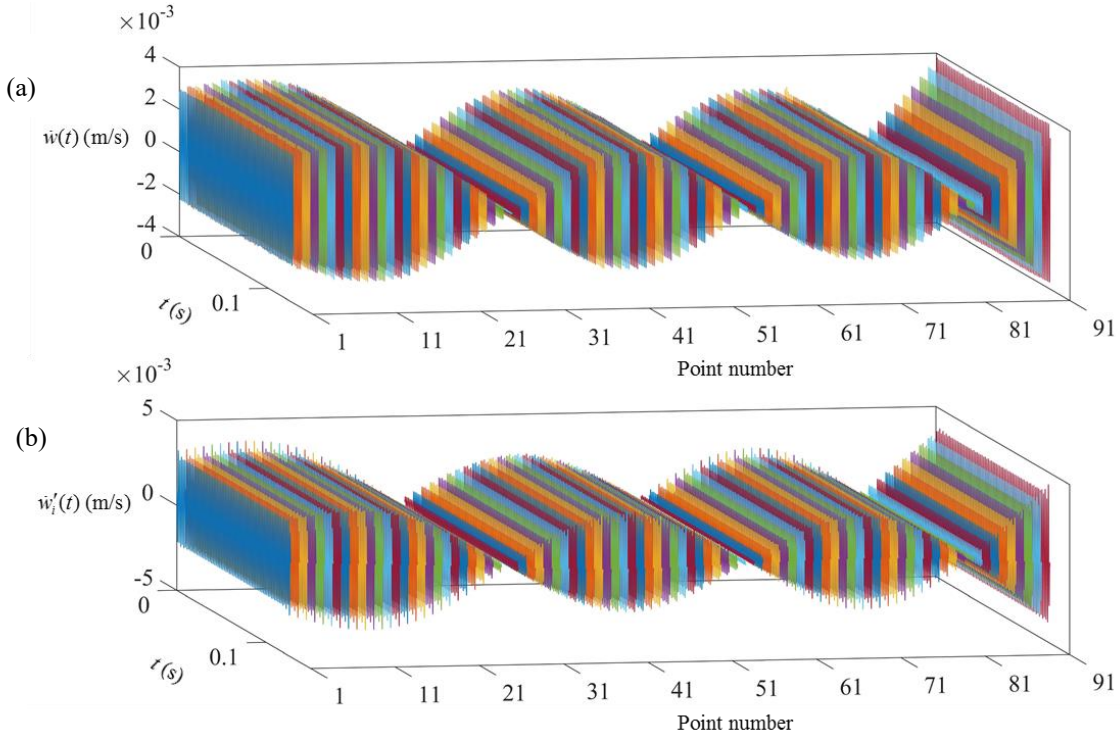

Fig. 6.41 (a) Measured velocity signals of the case 6B and (b) filtered velocity signals of the case 6B.

Without any obvious damage from other interference signals, only signals located around the 'nodes' may need to be reconstructed. EMD has been applied to the filtered velocity signals and first/last few periods of shifted velocity signals have been eliminated to avoid the edge effect. Then, the result velocity signals $\bar{\dot{w}}_i(t)$ can be constructed by aligning signals with their local maximum/minimum based on the ODSs as shown in Fig. 6.42a. Integrate the result velocity signals, apply the EMD to remove the nonzero moving average, shorten the shifted displacement signals and aligning by their local maximum/minimum based on the ODSs, the result displacement signals can be computed as shown in Fig. 6.42b.

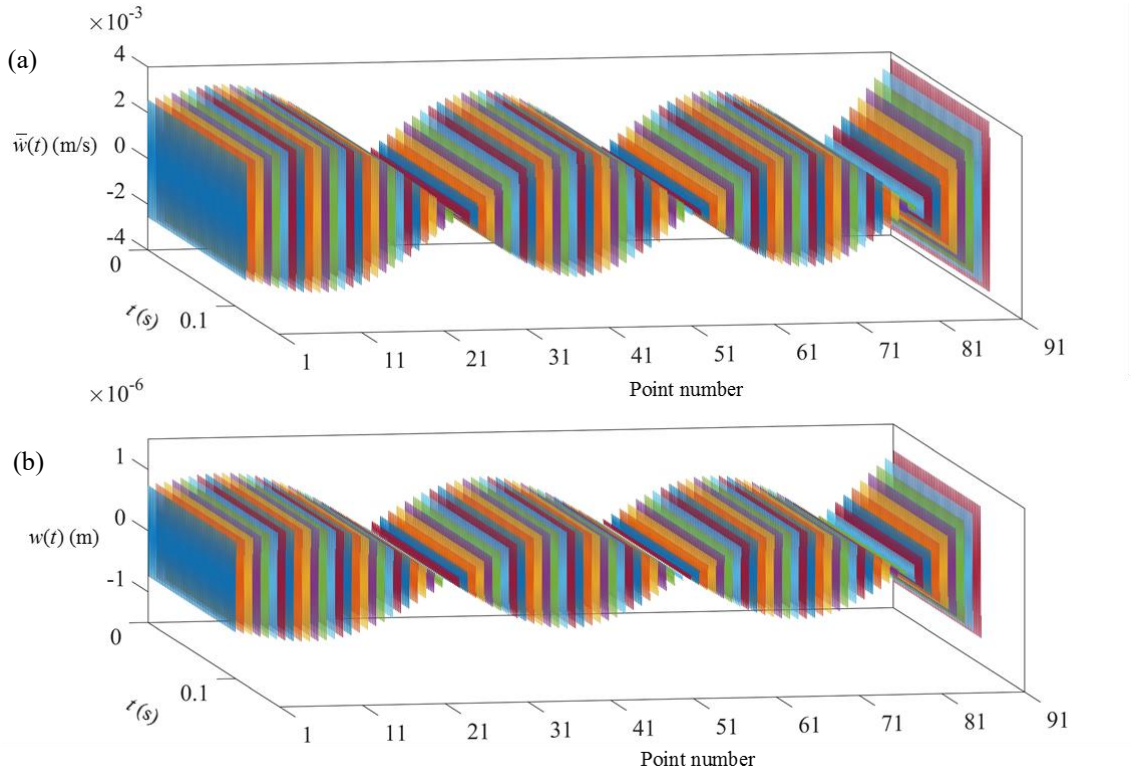

Fig. 6.42 (a) Result velocity signals of the case 6B and (b) result displacement signals of the case 6B.

Figure 6.43a gives the initial ODSs in red curve and dots, and the blue dash curve presents the curve fitting of the ODSs with a window length of 16 elements. Red circles marked the points need to be reconstructed, and blue circles marked the corresponding reference points. With the 'nodes' of mode shape located at: 27, [55,56], [81,82], points that need to be reconstructed is decided as: $\{r\} = \{27\}$. And the used reference point can be located by $\{\Delta\} = \{-1\}$. The abnormal transient events existed in $w_{27}(t)$ is caused by inaccurate filtered velocity signal which caused by the relative large measuring noise (comparing to actual vibration signal) from the measured velocities. Figure 6.43b gives the displacement signals of the set $\{r\}$ before and after reconstruction in red curves and blue curves, respectively.

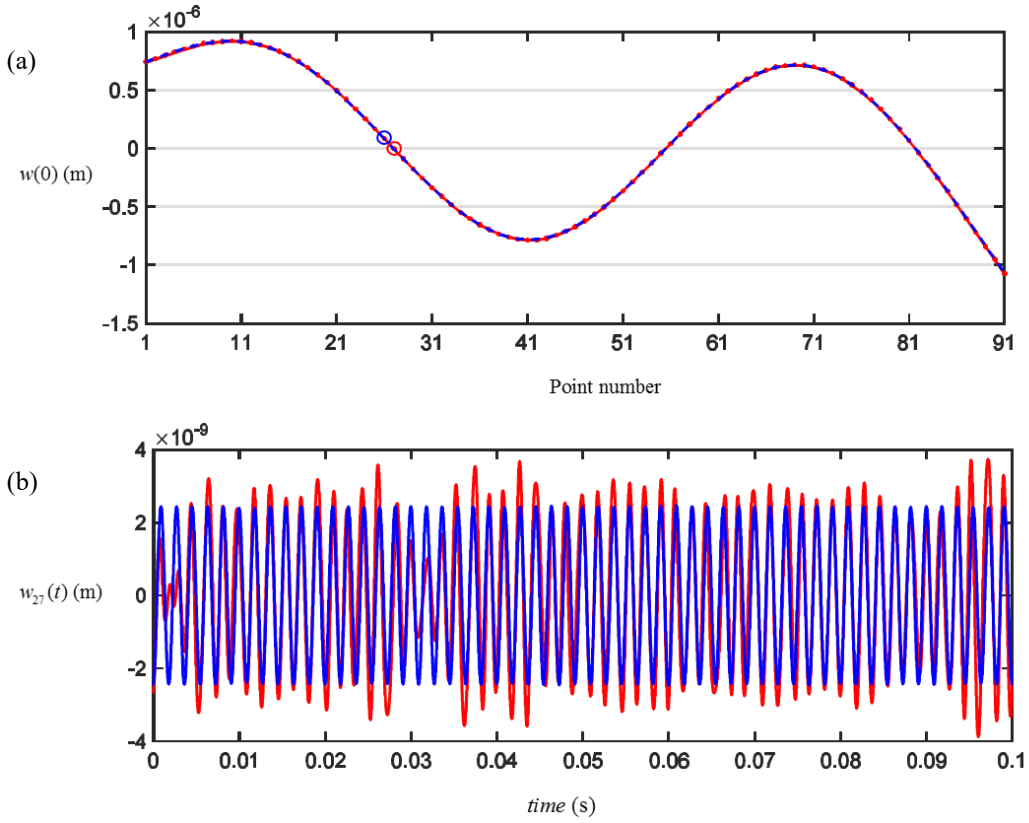

Fig. 6.43 (a) The initial ODSs of result displacement signals and (b) reconstructed displacement signals of case 6B.

With point 27 located nearly coincide with the 'nodes' as shown in Fig. 6.43a, the existed abnormal transient events have been corrected by reconstruction. Then, rotational angle signals can be computed by finite difference method based on the result displacement signals with a few reconstructions. Figure 6.44 gives the result rotational angle signals $\theta(t)$ computed based on finite difference method.

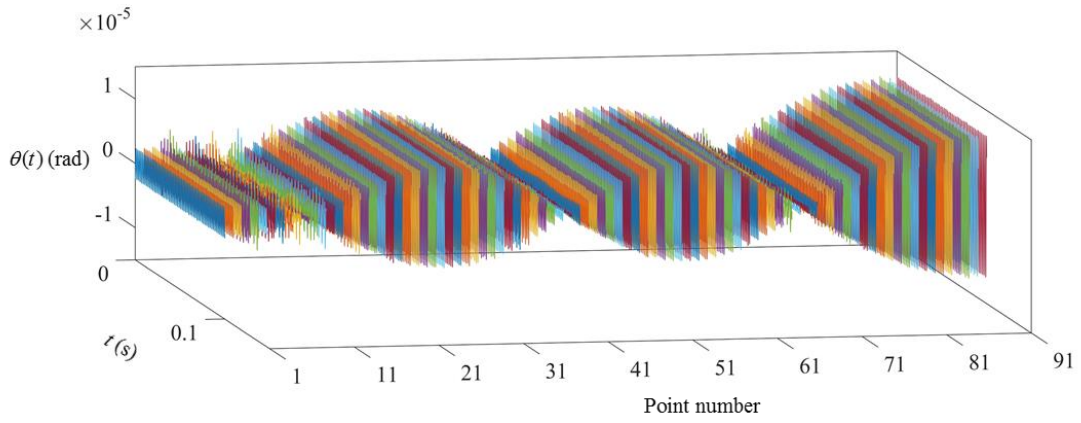

Fig. 6.44 Result rotational angle signals of case 6B.

Then the mass-CMM can be applied to compute the damage index at each time instant, and result damage index can be calculated as its average. Figure 6.45a gives the result damage index $\bar{q}_i$ in red curve with dots and the approximated baseline in blue dash curve. A window length of 16 elements is used for baseline computation. Figure 6.45b gives the filtered damage index $\hat{q}_i$ in blue lines and dots. With baseline exists in $\hat{q}_i$, a second-time baseline filtering has applied. The computed approximated baseline is given in magenta dash curve. While the same window length as 16 elements is used for most points, half window length is used for the first/last 8 points. Figure 6.45c gives the twice filtered damage index $\hat{q}_i'$ in magenta lines and dots. While the damage location is identified as elements before and after $\hat{q}_{42}'$ and marked by the grey area, the actual damage location (the 41st element) as marked by black dash lines is included in the identified damage range. The mass-CMM gives the accurate damage localization for this case.

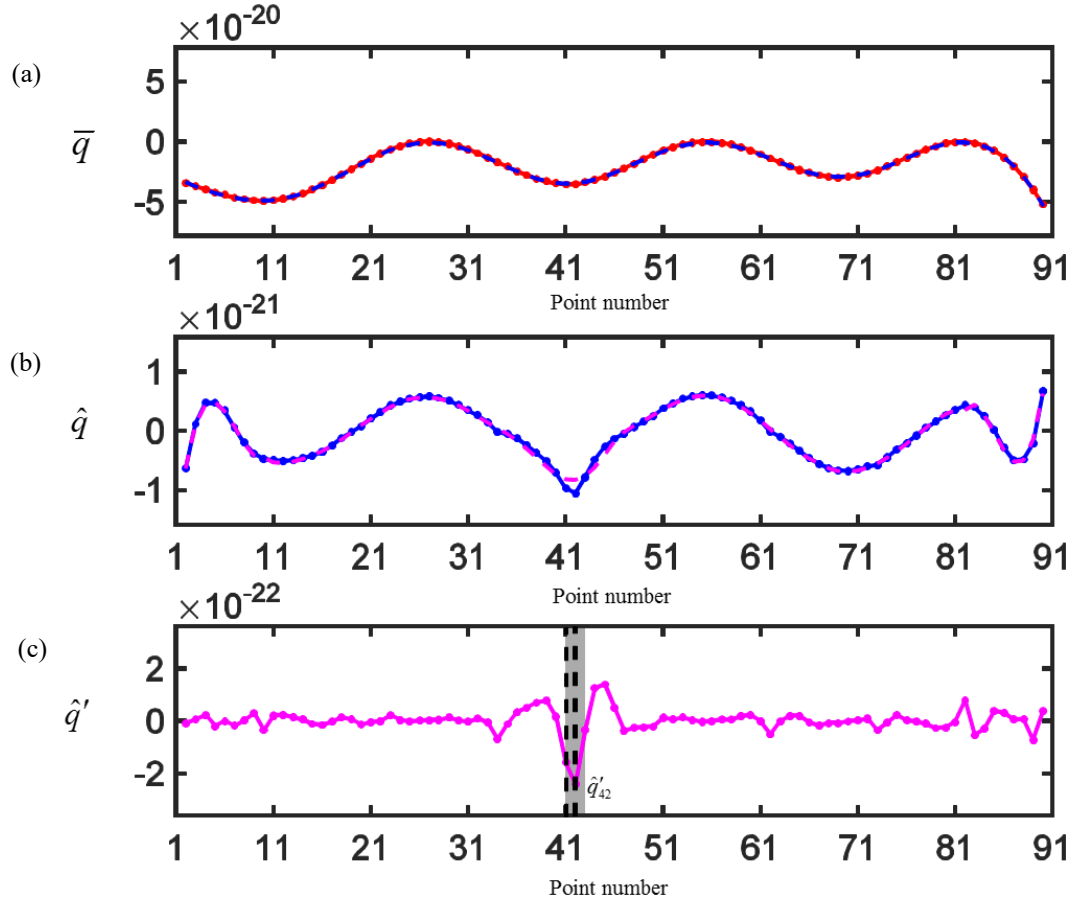

Fig. 6.45 (a) Result damage index $\bar{q}_i$ of case 6B using coefficient matrix from the elemental mass matrix, (b) corresponding filtered damage index $\hat{q}_i$ and (c) corresponding twice filtered damage index $\hat{q}'_i$.

With three 'nodes' existed in the case 6B, only one of them need to be reconstructed. It indicates the result displacement signals of the case 6B contains less measuring noise and error. Therefore, the stiffness-CMM will also be applied to method verification. Filtered damage index $\hat{d}(t_k)$ can be computed from the damage index $d_i(t_k)$ at each time instant t_k, and the counting damage index d^C will be computed based on filtered damage index. While Fig. 6.46a gives the d^C in bars, Fig. 6.46b gives the filtered damage index $\hat{d}_i = \bar{d}_i - b_i$ (take average first and then filter the baseline) in red curves and dots for comparison. While the

identified damage location marked by the grey area in both Fig. 6.46a&b, the actual damage location (the 41th element) is marked by black dash lines in Fig. 6.46a&b. As we can see, while the calculation error gives an false damage location as elements before and after $\hat{d}_{88}$, the counting damage index gives the accurate identified damage location as elements before and after d_{42}^{C}. The counting damage index d^{C} can eliminate the influence from the calculation error and gives a more accurate identified damage location for the applied stiffness-CMM.

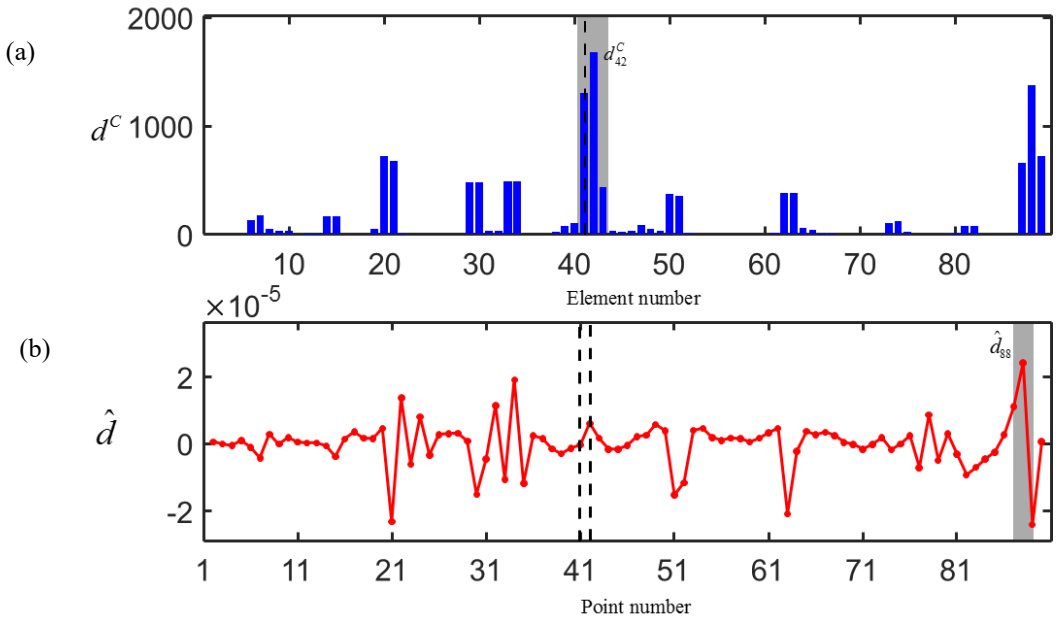

Fig. 6.46 (a) Counting damage index of the case 6B and (b) filtered damage index of the case 6B.

6.4 Experiments of Specimen #3

6.4.1 ODSs Close to the 8th Mode Shape (case 3A)

Different from previous cases, a relatively low sampling rate is used for case 3A to 3C. The used exciting frequency is in the case 3A as $f_8 = 2250Hz$. With the sampling rate of 51200Hz, only about 22 measured time instants fall in each period. The crack is located at the 37th element among the measured 91 points. Measured velocity signals are given in Fig. 6.47a. With the bandpass filter applied to the measured velocity signals as 1250-3250Hz, Figure 6.47b gives the filtered velocity signals.

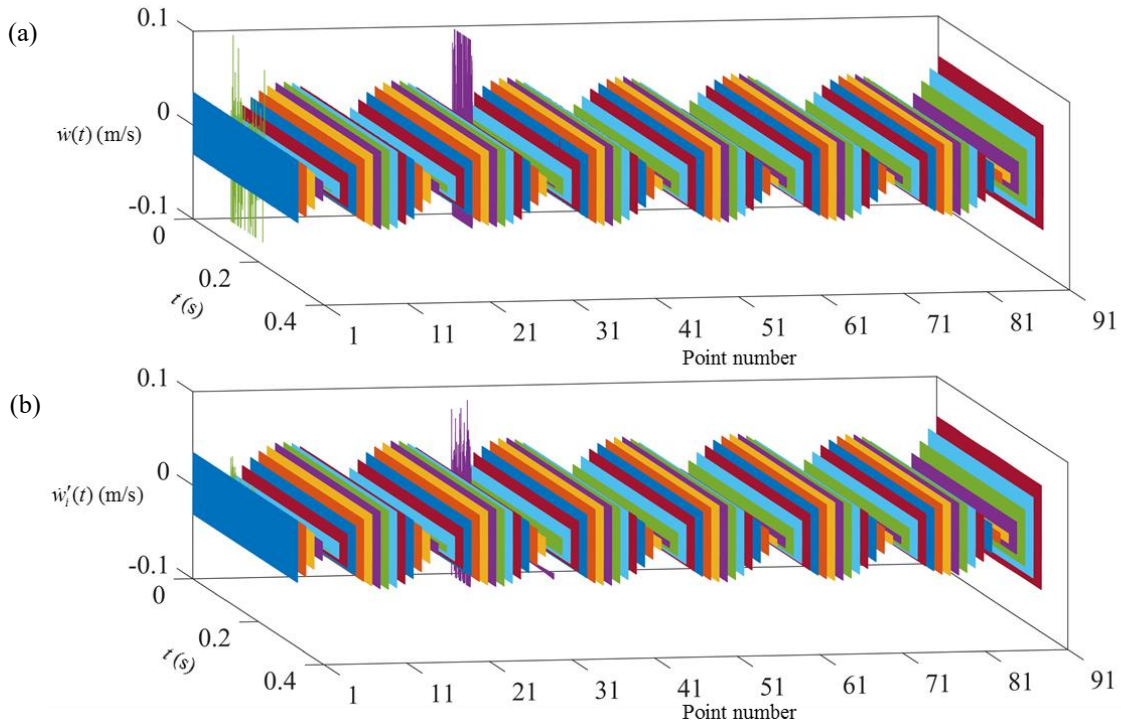

Fig. 6.47 (a) Measured velocity signals of the case 3A and (b) filtered velocity signals of the case 3A.

Based on the measured velocity signals shown in Fig. 6.47a, most measured signals are relative

consistent along the time trace except two points have relative large measuring noise as $\dot{w}_5(t), \dot{w}_{32}(t)$. That is because with relative small vibration amplitude at that two locations, during the experiment, the laser vibrometer treated the existed vibration as noise and stopped measuring at that point until new trigger applied. Therefore, we waved in front of the camera to trigger the laser start to measure again, and the big noise is from the motion of waving. As shown in Fig. 6.47b, even with applied filter, the damaged signal still has an obvious nonlinear behavior around certain time instant. A reconstruction may be necessary for later step. EMD has been applied to the filtered velocity signals and first/last few periods of shifted velocity signals have been eliminated to avoid the edge effect. Then, the result velocity signals $\bar{\dot{w}}_i(t)$ can be constructed by aligning signals with their local maximum/minimum based on the ODSs as shown in Fig. 6.48a. Integrate the result velocity signals, apply the EMD to remove the nonzero moving average, shorten the shifted displacement signals and aligning by their local maximum/minimum based on the ODSs, the result

displacement signals can be computed as shown in Fig. 6.48b.

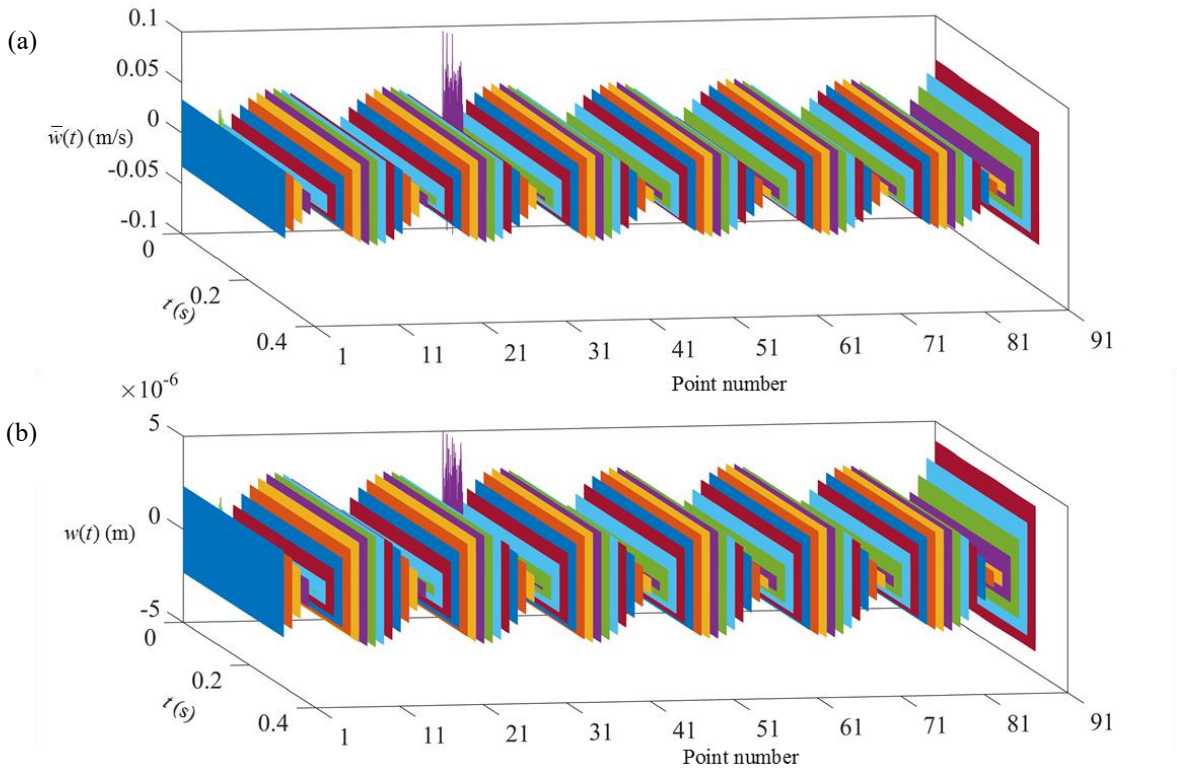

Fig. 6.48 (a) Result velocity signals of the case 3A and (b) result displacement signals of the case 3A.

Figure 6.49 gives the initial ODSs in red curve and dots, and the blue dash curve presents the curve fitting of the ODSs with a window length of 8 elements. Red circles marked the points need to be reconstructed, and blue circles marked the corresponding reference points. With the 'nodes' of mode shape located at: 5, [18,19], 32, [45,46], [59,60], [73,74], [86, 87], points need to be reconstructed is decided as: $\{r\} = \{5, 32\}$. And the used reference point can be located by $\{\Delta\} = \{1, -1\}$. The abnormal transient events existed in . $w_5(t), w_{32}(t)$. is caused by hand motion captured by the laser vibrometer. Figure 6.50 gives the displacement signals of the set $\{r\}$ before and after reconstruction in red curves and blue curves, respectively.

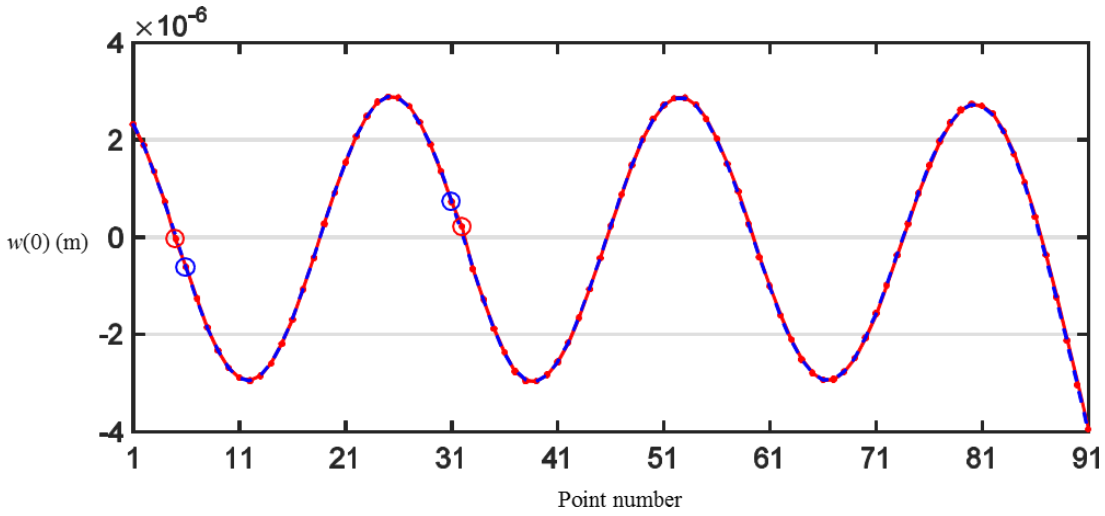

Fig. 6.49 The initial ODSs of result displacement signals.

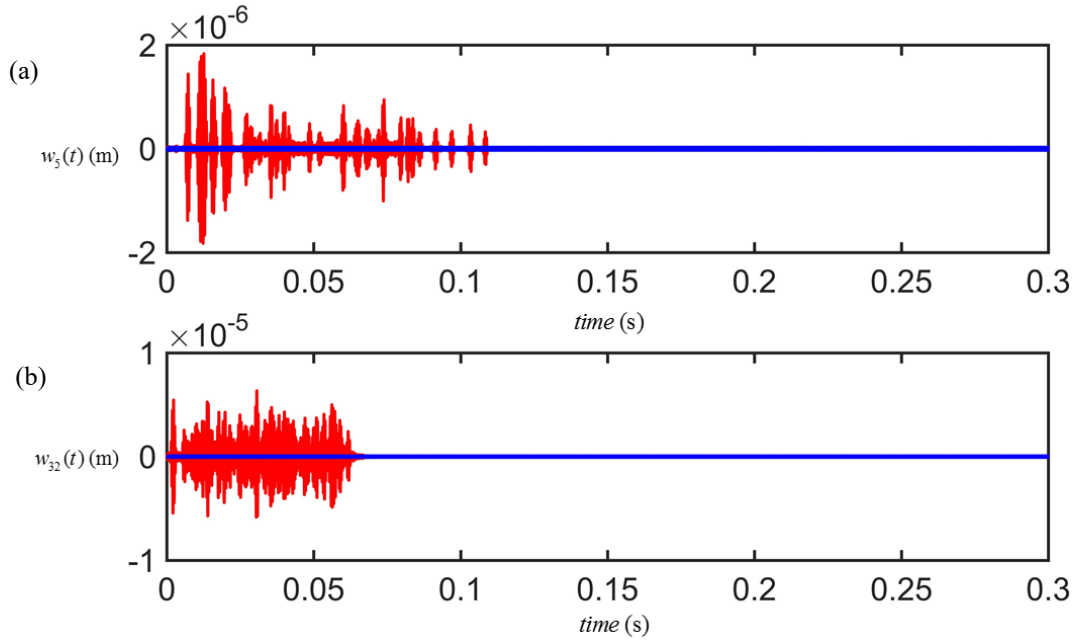

Fig. 6.50 Reconstructed displacement signals of case 3A.

The inaccurately captured motion by waving in front of the camera has been correct by reconstruction. Then, rotational angle signals can be computed by finite difference method based on the result displacement signals with a few reconstructions. Figure 6.51 gives the result rotational angle signals $\theta(t)$ computed based

on finite difference method.

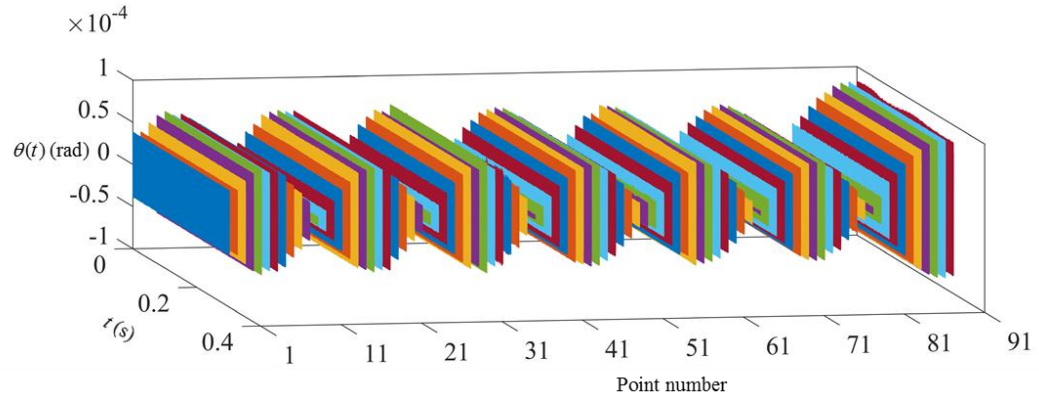

Fig. 6.51 Result rotational angle signals of case 3A.

Then the mass-CMM can be applied to compute the damage index at each time instant, and result damage index can be calculated as its average. Figure 6.52a gives the result damage index $\bar{q}_i$ in red curve with dots and the approximated baseline in blue dash curve. A window length of 8 elements is used for baseline computation. Figure 6.52b gives the filtered damage index $\hat{q}_i$ in blue lines and dots. With baseline exists in $\hat{q}_i$, a second-time baseline filtering has applied. The computed approximated baseline is given in magenta dash curve. While the same window length as 8 elements is used for most points, half window length is used for the first/last 4 points. Figure 6.52c gives the twice filtered damage index $\hat{q}_i'$ in magenta lines and dots. While the damage location is identified as elements before and after $\hat{q}_{37}'$ and marked by the grey area, the actual damage location (the 37th element) as marked by black dash lines is included in the identified damage range. The mass-CMM gives the accurate damage localization for this case.

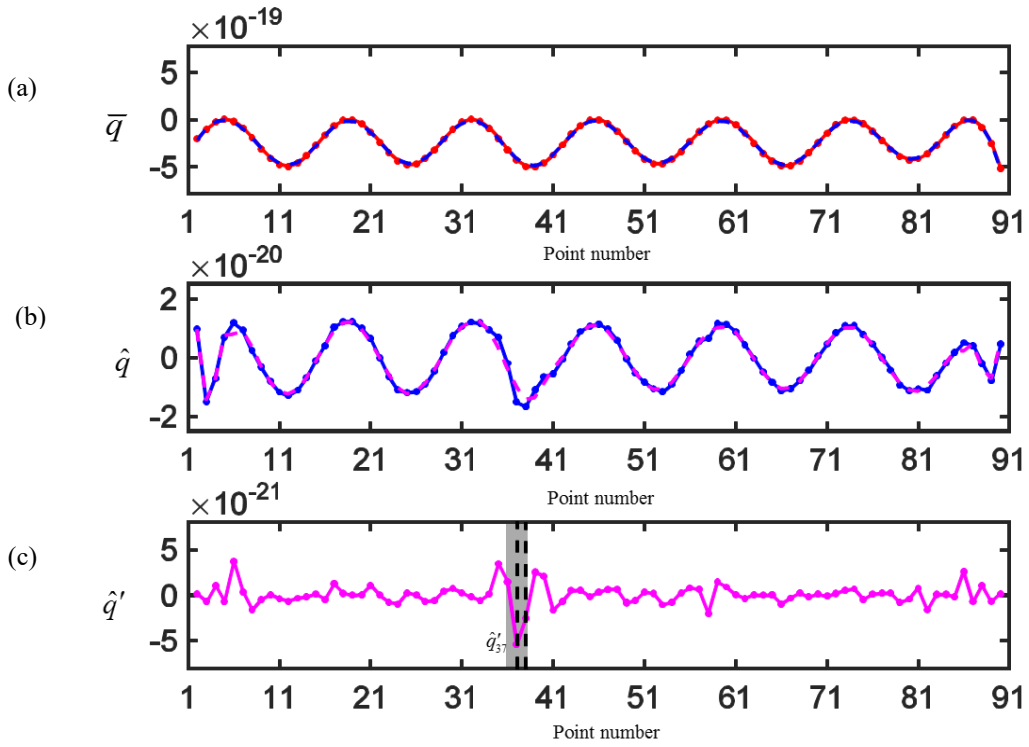

Fig. 6.52 (a) Result damage index $\bar{q}_i$ of case 3A using coefficient matrix from the elemental mass matrix, (b) corresponding filtered damage index $\hat{q}_i$ and (c) corresponding twice filtered damage index $\hat{q}_i'$.

6.4.2 ODSs Close to the 10th Mode Shape (case 3C)

The used exciting frequency is in the case 3C as $f_{10} = 3600Hz$. With the sampling rate of 51200Hz, only about 14 measured time instants fall in each period. The crack is located at the 37th element among the measured 91 points same as the case 3A. Measured velocity signals are given in Fig. 6.53a. With the bandpass filter applied to the measured velocity signals as 2400-4800Hz, Figure 6.53b gives the filtered velocity signals.

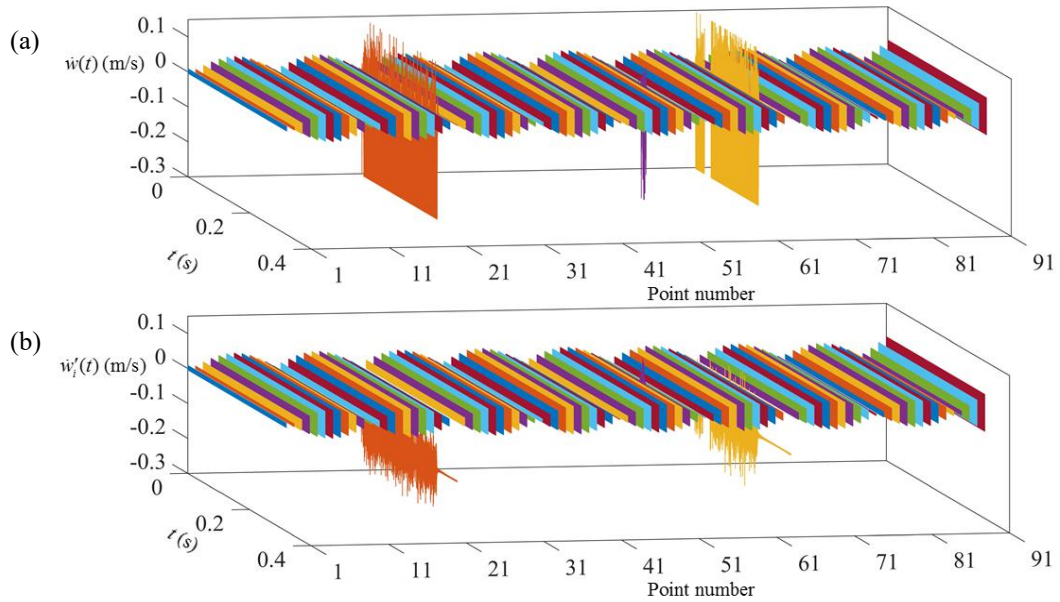

Fig. 6.53 (a) Measured velocity signals of the case 3Cand (b) filtered velocity signals of the case 3C.

Based on the measured velocity signals shown in Fig. 6.53a, most measured signals are relative consistent along the time trace except three points have relative large measuring noise as $\dot{w}_{23}(t)$ and $\dot{w}_{66}(t)$. Like case 3A, two points as 23 and 66 has relative small vibration amplitude, and the laser vibrometer treats the existed vibration as noise and stopped measuring. We waved several times in front of the camera to trigger the laser start to measure again, and the big noise is the captured waving. As shown in Fig. 6.53b, even with applied filter, the damaged signals still have an obvious nonlinear behavior, and some of them even have a nonzero moving average. A reconstruction may be necessary for later step. EMD has been applied to the filtered velocity signals and first/last few periods of shifted velocity signals have been eliminated to avoid the edge effect. Then, the result velocity signals $\bar{\dot{w}}_i(t)$ can be constructed by aligning signals with their local maximum/minimum based on the ODSs as shown in Fig. 6.54a. Integrate the result velocity signals, apply

the EMD to remove the nonzero moving average, shorten the shifted displacement signals and aligning by their local maximum/minimum based on the ODSs, the result displacement signals can be computed as shown in Fig. 6.54b.

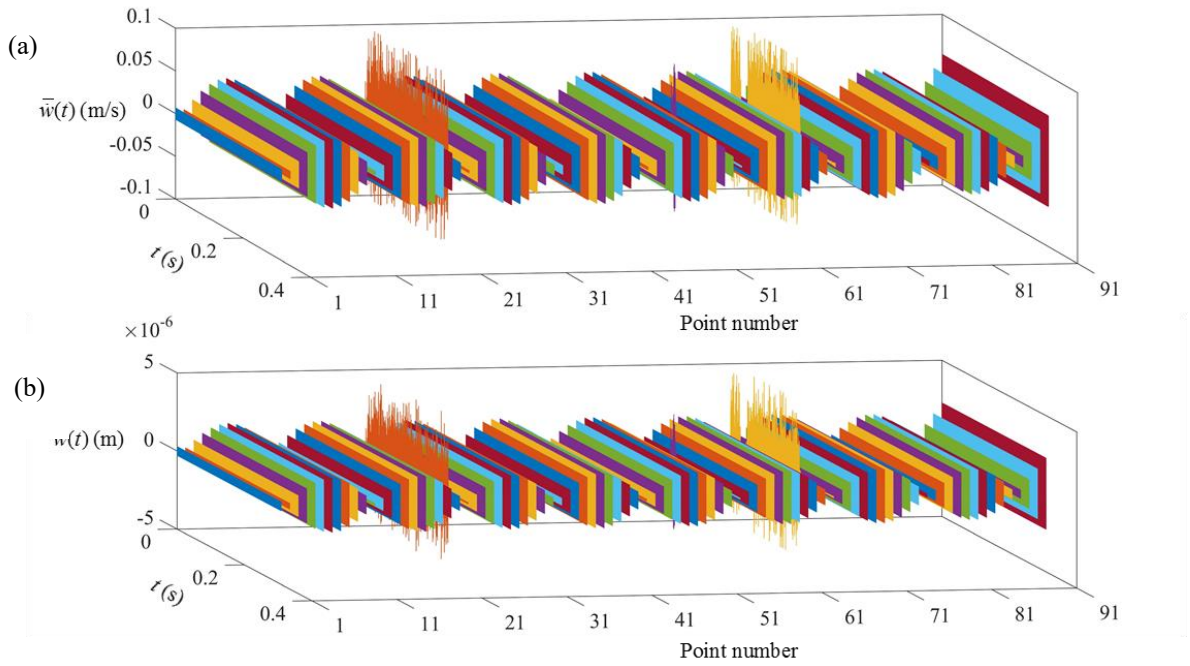

Fig. 6.54 (a) Result velocity signals of the case 3C and (b) result displacement signals of the case 3C.

Figure 6.55 gives the initial ODSs in red curve and dots, and the blue dash curve presents the curve fitting of the ODSs with a window length of 8 elements. Red circles marked the points need to be reconstructed, and blue circles marked the corresponding reference points. With the 'nodes' of mode shape located at: [1,2], [12,13],23, [33,34], 44, 55, 66, 77, [87,88], points need to be reconstructed is decided as: $\{r\} = \{23, 53, 55, 66\}$. And the used reference point can be located by $\{\Delta\} = \{1, -1, 1, 1\}$. The abnormal transient event existed in $w_{53}(t)$ is caused by noise from other interference signals. The abnormal transient events existed in $w_{23}(t), w_{66}(t)$ is caused by captured waving motion. The changing amplitude existed in

$w_{55}(t)$ is caused by inaccurate filtered velocity signal which caused by the relative large measuring noise (comparing to actual vibration signal) from the measured velocities. Figure 6.56 gives the displacement signals of the set $\{r\}$ before and after reconstruction in red curves and blue curves, respectively.

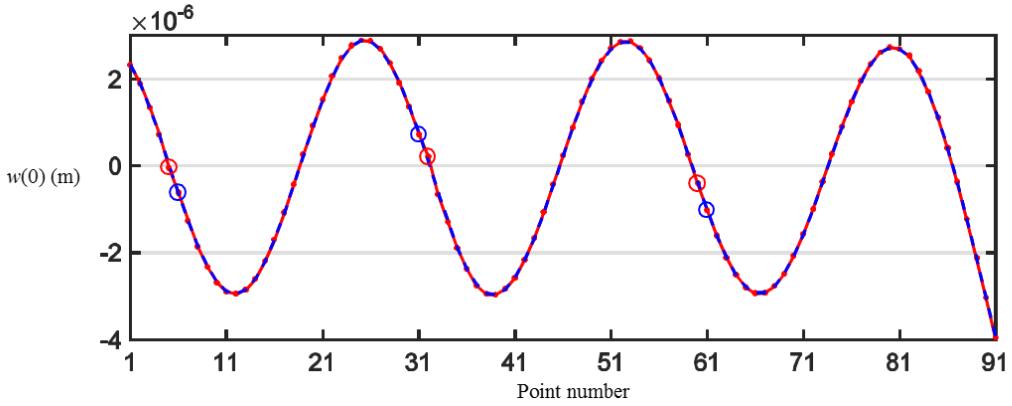

Fig. 6.55 The initial ODSs of result displacement signals.

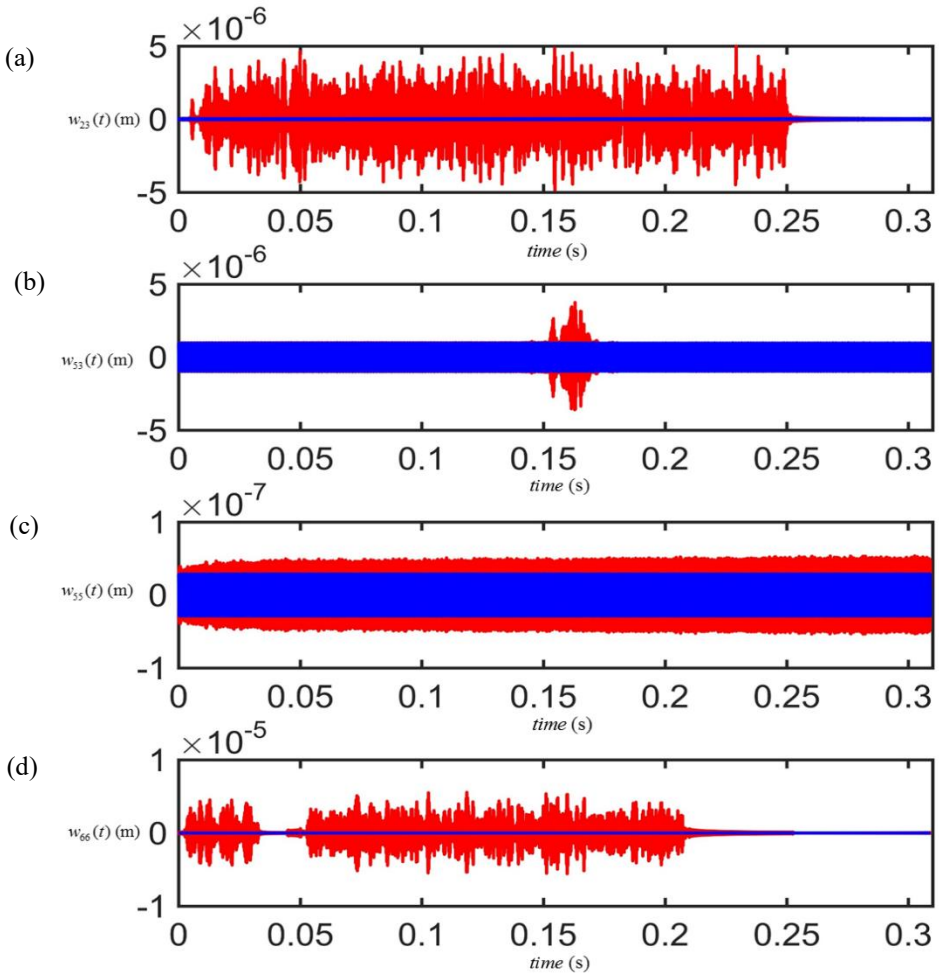

Fig. 6.56 Reconstructed displacement signals of case 3C.

With excited nonlinear behavior corrected by reconstruction, rotational angle signals can be computed by finite difference method based on the result displacement signals with a few reconstructions. Figure 6.57 gives the result rotational angle signals $\theta(t)$ computed based on finite difference method.

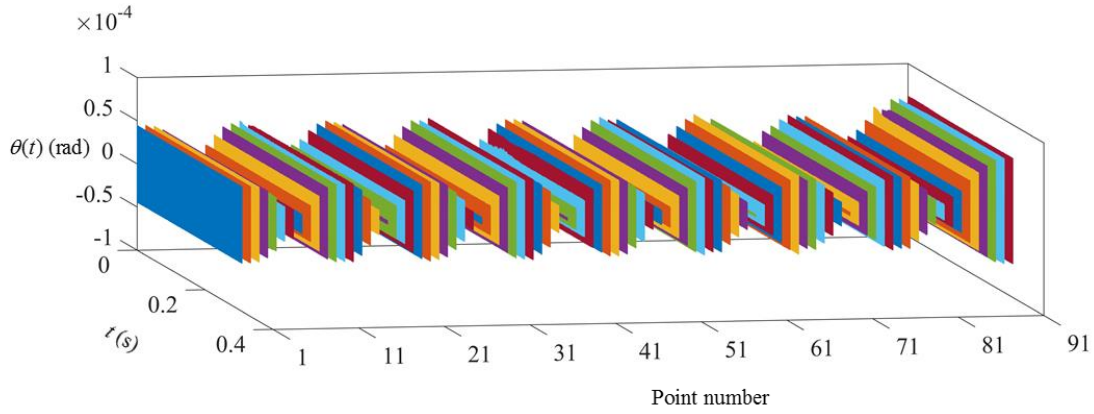

Fig. 6.57 Result rotational angle signals of case 3C.

Then the mass-CMM can be applied to compute the damage index at each time instant, and result damage index can be calculated as its average. Figure 6.58a gives the result damage index $\bar{q}_i$ in red curve with dots and the approximated baseline in blue dash curve. A window length of 8 elements is used for baseline computation. Figure 6.58b gives the filtered damage index $\hat{q}_i$ in blue lines and dots. With baseline exists in $\hat{q}_i$, a second-time baseline filtering has applied. The computed approximated baseline is given in magenta dash curve. While the same window length as 8 elements is used for most points, half window length is used for the first/last 4 points. Figure 6.58c gives the twice filtered damage index $\hat{q}_i'$ in magenta lines and dots. While the damage location is identified as elements before and after $\hat{q}_{37}'$ and marked by the grey area, the actual damage location (the 37th element) as marked by black dash lines is included in the identified damage range. The mass-CMM gives the accurate damage localization for this case.

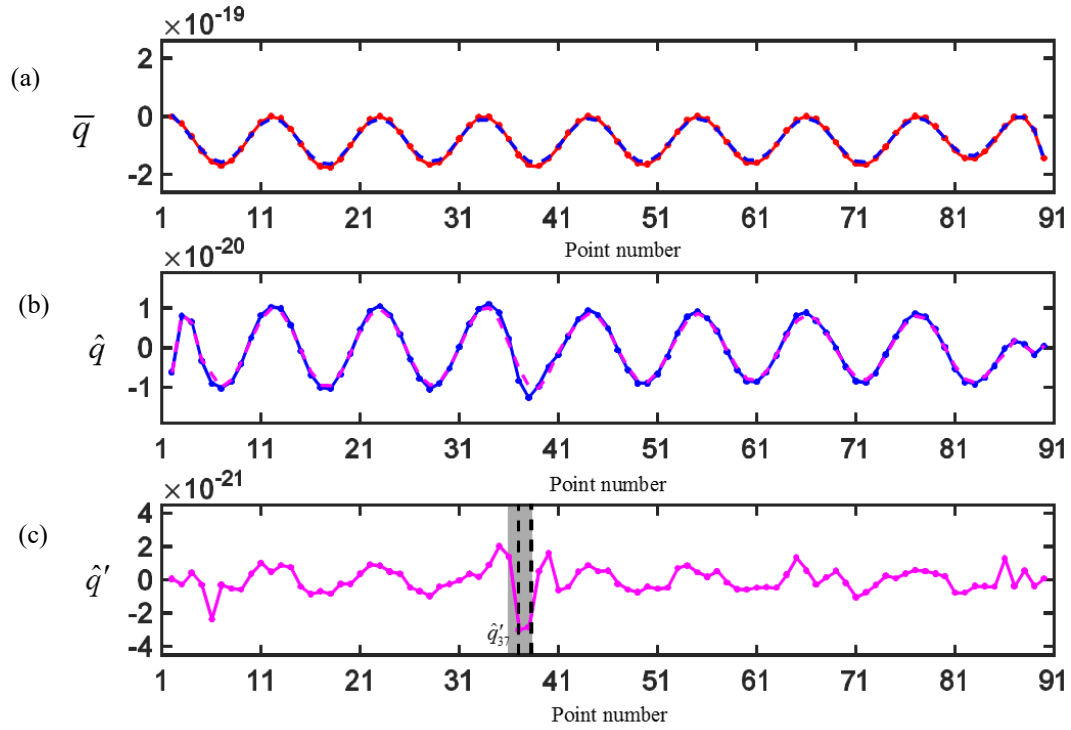

Fig. 6.58 (a) Result in damage index $\bar{q}_i$ of case 3C using coefficient matrix from the elemental mass matrix, (b) corresponding filtered damage index $\hat{q}_i$ and (c) corresponding twice filtered damage index $\hat{q}'_i$.

6.5 Rest experiments

Although the mass-CMM can identify the damage location accurately with different crack dimension and sampling rate, it does not work well with mode vibration with relative small natural frequency change ratio or free transient vibration. That is because, for mode vibration with relative small natural frequency change ratio, the existed crack is located close to the 'nodes'. With relative small vibration amplitude, even relative large noise existed at those locations will not show much difference in ODSs. In other words, the mode vibration is insensitive to signals at those locations. Therefore, it is hard to identify the discontinuous caused by existed small damage at those locations. Moreover, with relative small vibration amplitude, the measured signal at those locations usually contains measuring noise even larger than the actual vibration signal and

reconstruction usually necessary. Then, the information of existed damage will be buried either by the existed noise or be lost after reconstruction. And for free transient vibration, as shown in Fig. 6.3, with vibration amplitude, increases through the x-axis, the measuring noise will increase, too. Moreover, since the measured responses of free transient vibration are measured by the repeated experiments, although some factors can be controlled, the measured responses are clearly inconsistent along the x-axis and cannot be treated as responses to the same exciting.

Chapter 7 Conclusions and Future Work

7.1 Conclusions

This thesis develops/presents different methods for dynamical data computation, level 1 damage detection (detect the occurrence of damage) and proposed two methods for level 2 damage detection (detect the location of the damage) based on the use of velocity signals measured using a laser vibrometer. With measured velocities, the SG filter method is the best option for acceleration computation. It can be used to filter noise out of velocities and with least-square approximation it can provide accurate accelerations as the derivative of the determined velocity function. Moreover, the inverse calculation is independent with the time instant that it is very efficient when it comes to a large amount of data as in level 2 damage detection. The corresponding SG integration method is the best option for displacement signals computation. And the empirical mode decomposition can be used to remove the part due to non-zero initial conditions and the part due to the integration of noise. With adjustable n_L, n_R and M, a different approximation can be realized by the SG filter method. A relative larger n_L and n_R can be used for noise filtering to average out existed noise, but it is better to use a relatively small n_L and n_R for computing displacement and acceleration from the signal with noise to have less noise coupling.

Two direct time domain methods and two indirect time domain methods are discussed for level 1 damage detection. Direct time-domain methods based on processing the displacements, velocities, and accelerations without any sort of transformation. The least-square fitting method can provide accurate identification results for linear systems. As a point-by-point method, it is capable of capturing small transient

events and giving a fast feedback. Thus, it can be used for real-time monitoring and level 1 damage detection. Although the force separation method can provide accurate identification results for a nonlinear system, as a section-by-section method it cannot reveal a small change in system property or give a fast feedback. Thus, it cannot be used for level 1 damage detection. For indirect time domain methods, Hilbert-Huang transform (HHT) and conjugate-pair decomposition (CPD) are discussed. HHT uses empirical mode decomposition (EMD) and Hilbert transform (HT) for time-frequency analysis. EMD decomposes a signal into a few physically meaningful intrinsic mode functions (IMF), but it requires a high sampling rate and a long data length in order to have accurate decomposition. Moreover, because HT uses Fourier transform, it causes the edge effect and reduces the accuracy of HHT. Hence, with the requirement of data length, the HHT can only perform periodic analysis instead of real-time monitoring. And the time instant of occurrence of damage cannot be revealed clearly. On the other hand, CPD can provide accurate time-frequency analysis for a signal having a narrow frequency band. And because CPD requires only a few data points for sliding-window fitting to extract the instantaneous frequency and amplitude, it is capable of real-time monitoring and level 1 damage detection.

Based on the finite element model of beam structure using Euler-Bernoulli beam theory, two damage localization methods are developed as stiffness-characteristic matrix method (stiffness-CMM) and mass characteristic matrix method (mass-CMM). Measured signals are only processed in the spatial domain without any sort of transformation, and there is no requirement of the corresponding intact beam structure. Signals are processed in the elemental dimension that dynamical signals of two consecutive elements will be used as a pair to calculate the damage index by using a weighting matrix. The damage location will be

revealed by the damage index with the largest magnitude. The same algorithm is used for the two methods but only with a different weighting matrix which derived from the finite element model of Euler-Bernoulli beam. For the stiffness-CMM, since the weighting matrix is calculated based on the second derivative of the interpolation function, some information has been lost by the differentiation, and it is relative sensitive to existed measuring noise. The counting damage index can be used to interpolate the result and improve the result. On the other hand, the weighting matrix of the mass-CMM is based directly on the interpolation function and is more robust to signals with measuring noise. Methods can be used for localizing the damage based on both free-transient vibration and steady-state vibration. However, with laser vibrometer can only measuring one point at a time, it is hard to get consistent free-transient responses by experiments. It is not optimal for damage localization for reality. On the other hand, the steady state vibration is easy to perform and can have consistently measured responses. Cases with a relative larger natural frequency change ratio for its major mode vibration have been used for validation. While the stiffness-CMM can only give an accurately identified damage location for a case with relative small measuring error, the mass-CMM can give an accurately identified damage location for all discussed cases.

7.2 Future Work

From all the presented results and discussions, we recommend the following tasks for future research in order to improve the proposed methods:

1. The n_L, n_R and M used in the SG filter method and SG integration method needs to be adjusted for different use and different case. It is better to develop a general procedure to reach to

the better option of using n_L, n_R and M .

2. Hilbert transform can be computed in the time domain by following the definition shown in Eq. (3.17), instead of using the discrete Fourier transform. Then, the edge effect in HHT can be significantly reduced.

3. The noise tolerance of the stiffness-CMM needs to be improved.

4. The use of the stiffness-CMM and the mass-CMM of identifying beam structure with multi-crack is worth study.

5. The damage localization of the plate structure using similar algorithm used in the stiffness-CMM and the mass-CMM is worth study.

Reference:

1. Doebling, S.W., et al., Damage identification and health monitoring of structural and mechanical systems from changes in their vibration characteristics: A literature review, in Other Information: PBD: May 1996. 1996. p. Medium: ED; Size: 132 p.

2. Farrar, C. and S. Doebling, Damage detection and evaluation II, in Modal analysis and testing. 1999, Springer. p. 345-378.

3. Waldron, K., et al., Damage detection using finite element and laser operational deflection shapes. Finite Elements in Analysis and Design, 2002. **38**(3): p. 193-226.

4. Grafe, H., Model updating of large structural dynamics models using measured response functions. 1999, University of London.

5. Carden, E.P. and P. Fanning, Vibration based condition monitoring: A review. Structural Health Monitoring, 2004. **3**(4): p. 355-377.

6. Zou, Y., L. Tong, and G.P. Steven, VIBRATION-BASED MODEL-DEPENDENT DAMAGE (DELAMINATION) IDENTIFICATION AND HEALTH MONITORING FOR COMPOSITE STRUCTURES — A REVIEW. Journal of Sound and Vibration, 2000. **230**(2): p. 357-378.

7. Peeters, B. and G. De Roeck, Stochastic system identification for operational modal analysis: a review. Journal of Dynamic Systems, Measurement, and Control, 2001. **123**(4): p. 659-667.

8. Rytter, A., Vibration Based Inspection of Civil Engineering Structures, 1993. Aalborg University, Denmark, 1993.

9. Doebling, S.W., C.R. Farrar, and M.B. Prime, A summary review of vibration-based damage identification methods. Shock and vibration digest, 1998. **30**(2): p. 91-105.

10. Fan, W. and P. Qiao, Vibration-based Damage Identification Methods: A Review and Comparative Study. Structural Health Monitoring, 2011. **10**(1): p. 83-111.

11. West, W.M., Illustration of the use of modal assurance criterion to detect structural changes in an orbiter test specimen. 1986.

12. Allemang, R.J., The modal assurance criterion–twenty years of use and abuse. Sound and vibration, 2003. **37**(8): p. 14-23.

13. Heylen, W. and T. Janter, Extensions of the modal assurance criterion. ASME J. Vibr. Acoust, 1990. **112**(4): p. 468-472.

14. Brechlin, E., K. Bendel, and W. Keiper. A new scaled modal assurance criterion for eigenmodes containing rotational degrees of freedom. in Proceedings of the International Seminar on Modal Analysis. 1999. KATHOLIEKE UNIVERSITEIT LEUVEN.

15. Wei, J.J. and R.J. Allemang. Model correlation and orthogonality criteria based on reciprocal modal vectors. in 9th Conference International Modal Analysis Conference (IMAC). 1991.

16. Lieven, N. and D. Ewins. Spatial correlation of mode shapes, the coordinate modal assurance criterion (COMAC). in Proceedings of the sixth international modal analysis conference. 1988.

17. Hunt, D.L. Application of an enhanced coordinate modal assurance criterion. in 10th International modal analysis conference. 1992.

18. Hemez, F.M., Uncertainty quantification and the verification and validation of computational models.

Damage Prognosis for Aerospace, Civil and Mechanical Systems, 2004: p. 201-220.

19. Pawar, P.M., K. Venkatesulu Reddy, and R. Ganguli, Damage detection in beams using spatial Fourier analysis and neural networks. Journal of Intelligent Material Systems and Structures, 2007. **18**(4): p. 347-359.

20. Messina, A., E. Williams, and T. Contursi, Structural damage detection by a sensitivity and statistical-based method. Journal of sound and vibration, 1998. **216**(5): p. 791-808.

21. Khan, A., A.B. Stanbridge, and D.J. Ewins, Detecting damage in vibrating structures with a scanning LDV. Optics and Lasers in Engineering, 1999. **32**(6): p. 583-592.

22. Salawu, O. and C. Williams. Damage location using vibration mode shapes. in Proceedings of the 12th International Modal Analysis. 1994.

23. Huth, O., et al., Damage identification using modal data: Experiences on a prestressed concrete bridge. Journal of Structural Engineering, 2005. **131**(12): p. 1898-1910.

24. Pandey, A.K., M. Biswas, and M.M. Samman, Damage detection from changes in curvature mode shapes. Journal of Sound and Vibration, 1991. **145**(2): p. 321-332.

25. Chance, J., G. Tomlinson, and K. Worden. A simplified approach to the numerical and experimental modelling of the dynamics of a cracked beam. in Proceedings-SPIE the International Society for Optical Engineering. 1994. Citeseer.

26. Ratcliffe, C.P., Damage detection using a modified Laplacian operator on mode shape data. Journal of Sound and Vibration, 1997. **204**(3): p. 505-517.

27. Amaravadi, V.K., et al. Structural health monitoring using wavelet transforms. in SPIE's 8th Annual

International Symposium on Smart Structures and Materials. 2001. International Society for Optics and Photonics.

28. Kim, B.H., T. Park, and G.Z. Voyiadjis, Damage estimation on beam-like structures using the multi-resolution analysis. International Journal of Solids and Structures, 2006. **43**(14): p. 4238-4257.

29. Ratcliffe, C.P., A frequency and curvature based experimental method for locating damage in structures. TRANSACTIONS-AMERICAN SOCIETY OF MECHANICAL ENGINEERS JOURNAL OF VIBRATION AND ACOUSTICS, 2000. **122**(3): p. 324-329.

30. Wahab, M.A. and G. De Roeck, Damage detection in bridges using modal curvatures: application to a real damage scenario. Journal of Sound and Vibration, 1999. **226**(2): p. 217-235.

31. Schwarz, B.J. and M.H. Richardson, Introduction to operating deflection shapes. CSI Reliability Week, 1999. **10**: p. 121-126.

32. Vold, H., B. Schwarz, and M. Richardson. Measuring operating deflection shapes under non-stationary conditions. in 18th International Modal Analysis Conference. 2000. Citeseer.

33. Sundaresan, M., et al. Crack detection using a scanning laser vibrometer. in Second International Conference on Structural Health Monitoring. Stanford University, Stanford, California. 1999.

34. Sundaresan, M.J., et al. Damage detection on a wind turbine blade section. in Society for Experimental Mechanics, Inc, 17 th International Modal Analysis Conference. 1999.

35. Sohn, H., et al., A review of structural health monitoring literature: 1996–2001. Los Alamos National Laboratory, USA, 2003.

36. Frank Pai, P., Instantaneous frequency of an arbitrary signal. International Journal of Mechanical

Sciences, 2010. **52**(12): p. 1682-1693.

37. Luo, J., K. Ying, and J. Bai, Savitzky–Golay smoothing and differentiation filter for even number data. Signal Processing, 2005. **85**(7): p. 1429-1434.

38. Schafer, R.W. On the frequency-domain properties of Savitzky-Golay filters. in Proc. 2011 DSP/SPE Workshop. 2010. Citeseer.

39. Taubenbock, H., et al., Automated Allocation of Highly Structured Urban Areas in Homogeneous Zones From Remote Sensing Data by Savitzky&# 8211; Golay Filtering and Curve Sketching. Geoscience and Remote Sensing Letters, IEEE, 2006. **3**(4): p. 532-536.

40. Fung, T.C., Complex-time-step newmark methods with controllable numerical dissipation. International Journal for Numerical Methods in Engineering, 1998. **41**(1): p. 65-93.

41. Newmark, N.M. A method of computation for structural dynamics. in Proc. ASCE. 1959.

42. Huang, N.E., S.S. Shen, and ebrary Inc., Hilbert-Huang transform and its applications, in Interdisciplinary mathematical sciences v 5. 2005, World Scientific,: Singapore ; Hackensack, NJ ; London.

43. Rytter, A., Vibration based inspection of Civil Engineering Structures PhD Thesis Aalborg University Denmark. 1993.

44. Bayissa, W.L., N. Haritos, and S. Thelandersson, Vibration-based structural damage identification using wavelet transform. Mechanical Systems and Signal Processing, 2008. **22**(5): p. 1194-1215.

45. Michaels, J.E., Detection, localization and characterization of damage in plates with an in situ array of spatially distributed ultrasonic sensors. Smart Materials and Structures, 2008. **17**(3).

46. Yu, Q., J. Zhang, and Y. Jiang, Fatigue damage development in pure polycrystalline magnesium under

cyclic tension-compression loading. Materials Science and Engineering A, 2011. **528**(25-26): p. 7816-7826.

47. Chen, H.-L.R. and A.C. Kiriakidis, Stiffness evaluation and damage detection of ceramic candle filters. Journal of engineering mechanics, 2000. **126**(3): p. 308-319.

48. Hahn, S.L., Hilbert transforms in signal processing. 1996: Artech House on Demand.

49. Peng, Z.K., P.W. Tse, and F.L. Chu, An improved Hilbert-Huang transform and its application in vibration signal analysis. Journal of Sound and Vibration, 2005. **286**(1-2): p. 187-205.

50. Maragos, P., J.F. Kaiser, and T.F. Quatieri, Energy separation in signal modulations with application to speech analysis. Signal Processing, IEEE Transactions on, 1993. **41**(10): p. 3024-3051.

51. Ovanesova, A.V. and L.E. Suárez, Applications of wavelet transforms to damage detection in frame structures. Engineering Structures, 2004. **26**(1): p. 39-49.

52. Kerschen, G., et al., Past, present and future of nonlinear system identification in structural dynamics. Mechanical Systems and Signal Processing, 2006. **20**(3): p. 505-592.

53. Dutta, A. and S. Talukdar, Damage detection in bridges using accurate modal parameters. Finite Elements in Analysis and Design, 2004. **40**(3): p. 287-304.

54. Abdel Wahab, M.M. and G. De Roeck, DAMAGE DETECTION IN BRIDGES USING MODAL CURVATURES: APPLICATION TO A REAL DAMAGE SCENARIO. Journal of Sound and Vibration, 1999. **226**(2): p. 217-235.

55. Friswell, M.I. and J.E. Penny, Crack modeling for structural health monitoring. Structural Health Monitoring, 2002. **1**(2): p. 139-148.

56. Pai, P.F., Highly flexible structures: modeling, computation, and experimentation. 2007: AIAA

(American Institute of Aeronautics & Ast.

57. Pai, P.F., Time-frequency characterization of nonlinear normal modes and challenges in nonlinearity identification of dynamical systems. Mechanical Systems and Signal Processing, 2011. **25**(7): p. 2358-2374.

58. Rayleigh, J.W.S.B., The theory of sound. Vol. 2. 1896: Macmillan.

59. Adhikari, S. and A.S. Phani, Rayleigh's Classical Damping Revisited. 2004.

60. Guo, Z. and Z. Sun, Multiple cracked beam modeling and damage detection using frequency response function. Structural Longevity, 2011. **5**(2): p. 97-106.

61. Chondros, T.G. and A.D. Dimarogonas, Identification of cracks in welded joints of complex structures. Journal of Sound and Vibration, 1980. **69**(4): p. 531-538.

62. Chondros, T.G., A.D. Dimarogonas, and J. Yao, VIBRATION OF A BEAM WITH A BREATHING CRACK. Journal of Sound and Vibration, 2001. **239**(1): p. 57-67.

63. S. A. AMBARTSUMYAN, A.A.K., The different-modules theory of elasticity. Mechanics of Solids, 1966: p. 64-67.

64. Len'kov, V. and L. Tolokonnikov, Axisymmetric strains in materials with different moduli. International Applied Mechanics, 1969. **5**(1): p. 95-96.

65. Ibrahim, A., F. Ismail, and H. Martin, Modelling of the dynamics of a continuous beam including nonlinear fatigue crack. International Journal of Analytical and Experimental Modal Analysis, 1987. **2**(2): p. 76-82.

66. Pai, P.F., J. Liu, and M.J. Sundaresan. Dynamic characteristics and vibration-based damage inspection of structures with actual fatigue cracks. in SPIE Smart Structures and Materials+ Nondestructive Evaluation

and Health Monitoring. 2013. International Society for Optics and Photonics.

67. Pai, P.F. and L. Huang, Dynamics-and laser-based boundary effect evaluation method for damage inspection of one-and two-dimensional structures. Journal of Nondestructive Evaluation, 2006. **25**(2): p. 83-105.

68. Pai, P.F., Highly Flexible Structures: Modeling, Computation, and Experimentation. 2007: AIAA (American Institute of Aeronautics \\& Ast. 742.

VITA

Xuewei Ruan was born in June1991 at Shaoxing, China. She went to East China University of Science and Technology (ECUST), China for her BS degree in Engineering Mechanics from 2009. At her fourth year of college, she participated the exchange program between ECUST and University of Missouri-Columbia (MU). She came to the United States to finish her BS degree and pursue a master degree in MU. She graduated from the ECUST at 2013 and got her M.S. degree from MU at 2014. Right now, Xuewei Ruan is a Ph.D. candidate majoring in Mechanical and Aerospace Engineering at MU. During her study at MU, she works as a teaching assistant. She has gained extensive research experience in finite element analysis and teaching experience in applied numerical methods with MATLAB. By the time she writes her dissertation, she has submitted three journal papers.

From August 2013 to May 2014, Xuewei Ruan was a master student at MU working on research "Parametric and Nonparametric Dynamical System Identification Using Laser-Measured Velocities." She developed/presented different methods for parametric and nonparametric identifications of linear and nonlinear dynamical systems based on the use of velocity signals measured using a laser vibrometer. She proposed two time-domain system identification methods including one parametric method and a nonparametric method. By comparing proposed methods with other methods, numerical analysis and experimental validation have given. After finishing her master program in one year, Xuewei Ruan continued her Ph.D. study and switched her focus to damage detection. Her Ph.D. research topic is a signal procession of single measurand for dynamical system identification. Start with comparing different numerical

computation methods based on single measurand. She found the SG filter method and developed SG integration method works best for acceleration and displacement signal computation with efficiency and accuracy. And the SG filter method can also be used for noise filtering. Based on her master research, the developed/studied methods for system identification methods has been applied to level 1 damage detection. The least-square fitting method and conjugate-pair decomposition can realize real-time system identification (monitoring). They are both able to capture small transient events and give a fast feedback and are good for level 1 damage detection. And Based on the finite element modal of beam structure using Euler-Bernoulli beam theory she proposed two damage localization methods as stiffness-characteristic matrix method (stiffness-CMM) and mass-characteristic matrix method (mass-CMM). Different from traditional damage detection methods that require the corresponding intact structure/model for comparison, proposed methods only based on measured signals of the damaged structure. With signal only processed in the spatial domain, damage location can be identified in elemental dimension. With velocity signal measured by the laser vibrometer, a fine grid can be applied to the beam structure to have a relaitve accurate identifed damage location. Experiments of cantilever beams with harmonic input excitation have been used to verify the two proposed methods. While the stiffness-CMM is relatively sensitive to noise can only give an accurately identified damage location for a case with relative small measuring error, the mass-CMM that is more robust to noise can give an accurately identified damage location for all discussed cases.

From system identification to damage detection, Xuewei Ruan is experienced in the field of structural health monitoring. And from numerical analysis to experimental validation, she is skilled at building a numerical model for both single degree of freedom system and continuous system and setting up

corresponding experiments. With the proficient of finite element analysis, she is ready for her coming career in industry field.